UNIVERSITY OF SOUTHAMPTON

Faculty of Engineering and the Environment

National Centre for Advanced Tribology (nCATS)

INTERFACIAL INSTABILITY GENERATION IN DENTAL BIOFILMS BY HIGH-VELOCITY FLUID FLOW FOR BIOFILM REMOVAL AND ANTIMICROBIAL DELIVERY

Stefania Fabbri

Academic Supervisory Team: Paul Stoodley,
Julian Wharton.

Industrial Supervisory Team: Philips Oral Healthcare,
Marcelo Aspiras,
E. Michelle Starke,
Marilyn T. Ward.

THESIS SUBMITTED IN FULFILLMENT OF THE REQUIREMENT FOR THE DEGREE OF DOCTOR OF PHILOSOPHY

March 2016

UNIVERSITY OF SOUTHAMPTON

ABSTRACT

FACULTY OF ENGINEERING AND THE ENVIRONMENT

Thesis for the degree of Doctor of Philosophy

INTERFACIAL INSTABILITY GENERATION IN DENTAL BIOFILMS BY HIGH-VELOCITY FLUID FLOW FOR BIOFILM REMOVAL AND ANTIMICROBIAL DELIVERY

Stefania Fabbri

Oral biofilms play an important role in the development and the persistence of caries, gingivitis and periodontitis. The addition of antimicrobials to toothpastes and mouthwashes combined with biofilm mechanical disruption through dental cleaning devices is the most common way to control oral diseases. However, biofilms' complicated structure increases their resistance to antiplaque and/or antimicrobials by limiting the diffusion of dentifrices into and inside the biofilm. Studies showed that fluid-dynamic activity generated by power toothbrushes can enhance mass transfer inside the remaining biofilm compared to simple diffusional transport. Microsprays have the advantage in that they are low volume but also have an air/water interface which facilitates biofilm removal. The role of the hydrodynamics in the enhancement of dentifrices inside the biofilm has become a topic of interest since it has been shown that mechanical perturbation caused by fluid-dynamic activity can significantly weaken biofilm structure.

Here we showed that high-velocity microsprays enhance microparticles penetration and Chlorhexidine and Cetylpyridinium chloride antimicrobial activity inside *Streptococcus mutans* dental biofilms through the generation of hydrodynamic deformations. Using high-speed camera videography, we documented *S. mutans* biofilm extremely transient fluid behavior and the generation of ripple-like structures at the biofilm/fluid interface when exposed to water microsprays. Mathematical modelling demonstrated that ripples were Kelvin Helmotz Instabilities suggesting the development of fluid-like turbulent mixing in biofilms. Shear stresses generated at the biofilm/burst interface might have enhanced beads and antimicrobials delivery inside the remaining biofilm by combining forced advection into the biofilm matrix with the mixing of the biofilm itself. This project provided further insight into the mechanical behaviour of biofilms as complex liquids and how high-shear fluid-biofilm interaction can be induced to modulate biofilm survival and tolerance.

TABLE OF CONTENTS

LIST OF FIGURES

LIST OF TABLES

LIST OF ACCOMPANYING MATERIAL

A DVD has been attached with the high speed camera videos recorded during the experiments.

LIST OF PRESENTATIONS

- Rmaile A, **Fabbri S**, Carugo D, Capretto L, Ward MT, Aspiras M and Stoodley P. *Mechanical Characterization of the Viscoelastic Dental Plaque Bacterial Biofilms*. Poster presented at the IADR meeting (Seattle, March 20-23, 2013).
- **Fabbri S,** Rmaile A, Carugo D, Johnston DA, Ward MT, Aspiras M, De Jager M, Ward M, and Stoodley P. *Mucin influences mechanics and microspray detachment of Streptococcus mutans biofilms*. Accepted as oral presentation at the BSODR 2013 meeting (Bath, September 9-11, 2013).
- **Fabbri S**, Rmaile A, Carugo D, Capretto L, Ward MT, Aspiras M and Stoodley P. *Influence of mucin-bacterial interactions on Streptococcus mutans biofilm mechanical properties*. Poster presented at the EUROBIOFILM meeting (Ghent, September 9-12, 2013).
- **Fabbri S**, Rmaile A, Carugo D, Capretto L, Ward MT, Aspiras M and Stoodley P. *Microspray detachment of S. mutans dental biofilms*. Accepted as oral presentation at the nCATs conference (University of Southampton, October 23, 2013).
- **Fabbri S,** Rmaile A, Carugo D, Johnston DA, Aspiras M, De Jager M, Ward MT, and Stoodley P. *Streptococcus mutans biofilms microspray detachment using an in-vitro IP space model*. Poster presented at the Bioengineering and Human Factors Theme Conference (University of Southampton, May 2, 2014).
- **Fabbri S,** Rmaile A, Carugo D, Johnston DA, Aspiras M, De Jager M, Ward MT, and Stoodley P. *Streptococcus mutans biofilms microspray detachment using an in-vitro IP space model*. Poster presented at the BIOFILM6 meeting (Vienna, May 11-13, 2014).
- **Fabbri S,** Johnston DA, Ward MT, Aspiras M, De Jager M, Ward M, and Stoodley P. *Microspray technology as a potential antimicrobial delivery method for dental plaque biofilms*. Accepted as oral presentation at the MECbioeng14 Conference (London, 10-14 September, 2014).
- **Fabbri S,** Rmaile A, Carugo D, Johnston DA, Aspiras M, De Jager M, Ward MT, and Stoodley P. *Streptococcus mutans biofilms microspray detachment using an in vitro IP space model*. Poster presented at the nCATs conference (University of Southampton, October 23, 2014).
- **Fabbri S,** Rmaile A, Johnston DA, Aspiras M, De Jager M, Ward MT, and Stoodley P. *High-speed microspray effects on S. mutans dental biofilm mechanics and antimicrobial delivery*. Poster selected as a finalist at the SET FOR BRITAIN 2015 meeting at the House of Commons in London (March 9, 2015).

- **Fabbri S,** Johnston DA, Rmaile A Aspiras M, De Jager M, Ward MT, and Stoodley P. *High-Speed Microspray Effects on S. mutans Biofilms and Dentifrice Delivery*. Accepted as oral presentation at the IADR 2015 meeting (Boston, March 11-14, 2015).
- **Fabbri S,** Johnston DA, Rmaile A, Aspiras M, De Jager M, Starke EM, Ward MT, and Stoodley P *Dentifrice delivery into dental plaque biofilms via high-velocity microsprays*. Accepted as oral presentation at the BSODR 2015 meeting (Cardiff, September 14-16, 2015).
- **Fabbri S,** Rmaile A, Aspiras M, De Jager M, Starke EM, Ward MT, and Stoodley P *Discovery of High Velocity Interfacial Ripple Formation in S. mutans Biofilms: From Therapeutic Opportunities to Ancient Fossils*. Poster presented at the ASM Biofilms meeting (Chicago, October 24-29, 2015).
- Li J, **Fabbri S**, Rmaile A, De Jager M, Aspiras M, Starke EM, Ward M, Stoodley P, Cogan NG. *Mathematical Analysis of a Kelvin-Helmholtz Instability in Biofilms*. Poster presented at the ASM Biofilms meeting (Chicago, October 24-29, 2015).
- **Fabbri S**, Li J, Rmaile A, De Jager M, Aspiras M, Starke EM, Ward M, Stoodley P, Cogan NG. *Discovery of High Velocity Interfacial Ripple Formation in S. mutans Biofilms: From Therapeutic Opportunities to Ancient Fossils*. Poster presented at the AADR/CADR meeting (Los Angeles, 16-19 March 2016).
- **Fabbri S,** Johnston DA, Rmaile A, Aspiras M, De Jager M, E Starke M, Ward MT, and Stoodley P. *High-velocity microsprays enhance interproximal oral biofilms detachment and dentifrice penetration.* Poster presented at the AADR/CADR meeting (Los Angeles, 16-19 March 2016).
- **Fabbri S**, Li J, Rmaile A, De Jager M, Aspiras M, Starke EM, Ward M, Stoodley P, Cogan NG. *High Velocity Micro Water Sprays Create Ripple Formations in S. mutans Biofilms with Potential for Disrupting Acidic Gradients and Pathogenic Anaerobic Bacteria.* Poster presented at the AADR/CADR meeting (Los Angeles, 16-19 March 2016).

LIST OF PUBLICATIONS

- Howlin RP, **Fabbri S**, Offin DG, Symonds N, Kiang KS, Knee RJ, Yoganantham DC, Webb JS, Birkin PR, Leighton TG. 2015. Removal of dental biofilms with an ultrasonically activated water stream. Journal of dental research.0022034515589284.

  My contribution to the manuscript was performing high-speed camera videography in order to assess *Streptococcus mutans* dental biofilm removal when exposed to an Ultrasonically Activated Water Stream. A copy of the manuscript has been included in Appendix B.

- **Fabbri S**, Johnston DA, Rmaile A, Gottenbos B, De Jager M, Aspiras M, Starke ME, Ward MT, Stoodley P. 2016. Streptococcus mutans biofilm transient viscoelastic fluid behaviour during high-velocity microsprays. Journal of the mechanical behavior of biomedical materials. 59:197-206

  A copy of the manuscript has been included in Appendix C.

- **Fabbri, S.**, Stoodley, P. 2016. Mechanical properties of biofilms. In *The Perfect Slime: Microbial Extracellular Polymeric Substances (EPS)*, Flemming HC, Neu TR, Wingender J. (eds). IWA Publishing, London, UK. ISBN13: 9781780407418.

  Publication Date: 15/08/2016.

DECLARATION OF AUTHORSHIP

I, Stefania Fabbri

declare that this thesis and the work presented in it are my own and has been generated by me as the result of my own original research.

Interfacial instability generation in dental biofilms by high-velocity fluid flow for biofilm removal and antimicrobial delivery

I confirm that:

This work was done wholly or mainly while in candidature for a research degree at this University;

Where any part of this thesis has previously been submitted for a degree or any other qualification at this University or any other institution, this has been clearly stated;

Where I have consulted the published work of others, this is always clearly attributed;

Where I have quoted from the work of others, the source is always given. With the exception of such quotations, this thesis is entirely my own work;

I have acknowledged all main sources of help;

Where the thesis is based on work done by myself jointly with others, I have made clear exactly what was done by others and what I have contributed myself;

Parts of this work have been published as:

- Howlin RP, Fabbri S, Offin DG, Symonds N, Kiang KS, Knee RJ, Yoganantham DC, Webb JS, Birkin PR, Leighton TG. 2015. Removal of dental biofilms with an ultrasonically activated water stream. Journal of dental research.0022034515589284.
- Fabbri S, Johnston DA, Rmaile A, Gottenbos B, De Jager M, Aspiras M, Starke ME, Ward MT, Stoodley P. 2016. Streptococcus mutans biofilm transient viscoelastic fluid behaviour during high-velocity microsprays. Journal of the mechanical behavior of biomedical materials. 59:197-206
- Fabbri, S., Stoodley, P. 2016. Mechanical properties of biofilms. In The Perfect Slime: Microbial Extracellular Polymeric Substances (EPS), Flemming HC, Neu TR, Wingender J. (eds). IWA Publishing, London, UK. ISBN13: 9781780407418 (Publication Date: 15/08/2016.)

Signed: ....

Date: 8/6/16 ....

ACKNOWLEDGMENTS

First of all, I would like to thank my supervisor, Paul Stoodley for all the help and support.

I would acknowledge the Philips Oral Healthcare and the Eustace Award for founding my PhD project. I would like to thank also my other supervisors, Dr Julian Wharton, Dr Marcelo Aspiras, Dr. Michelle Starke, Dr Marko De Jager and Dr Marilyn Ward.

I will forever be thankful to Dr. Natalya Doroshenko, Dr. Robert Howlin, Caroline Duignan, Dr. Amir Rmaile, Dr. Lianne Niehaus for helping me in the laboratory.

I also thank Dr. David Johnston (BIU, SGH) for teaching me confocal and scanning microscope analysis; Dr. Janice Burton and Dr. Marco Longana (TSLR lab) for borrowing me the high speed camera set up.

I would like to thank all my Southampton friends, Vanesa, Jorge, Davide, Asim, Asad, Valentina, Stefano, Mirko, Federico, Ottavia, Laura and Simone, for all the hangouts and fun time. What an amazing 3 years it has been!! Also, I will always remember the great time I had with my officemates Jim, Jahnabi, Natalya, Vanesa, Viktorija and Kasia!

Finally, I would like to thank my family, my parents and my sister Letizia for their amazing support, and my amazing boyfriend Paolo always here for me when I needed.

Thanks

Stefania

LIST OF ABBREVIATIONS

AF - AirFloss

AIs – Autoinducers

AFM – Atomic-force microscopy

BHI – Brain Heart Infusion

CA – Cellula Automata

CHX – Chlorhexidine

CDF – Computational Fluid Dynamic

CLSM – Confocal Laser Scanning Microscopy

CPC – Cetylpyridinium chloride

DO – Dissolved oxygen

eDNA - Extracellular DNA

EPS - Extracellular polymeric substances

FHA – Fluorohydroxyapatite

FFT – Fast Fourier Transform

fps – Frames per second

GTF - Glucosyltransferase

HÁ - Hydroxyapatite

HSC - High-speed camera

IBM – Individual Based Model

IP – Interproximal

KHI – Kelvin-Helmotz Instability

MBC – Minimum bactericidal concentration

MIC – Minimum inhibitory concentration

MJI – Microjet Impingement

NO - Nitric Oxide

PBS – Phosphate-buffered saline

PCA – Principal Component Analysis

PFA - Paraformaldehyde

PI – Propidium Iodide

POH – Philips Oral Healthcare

PTM – Particle-tracking microrheology

QS – Quorum sensing

RD – Relative depth

SEM - Scanning Electron Microscope

TSB - Tryptic soy broth

UMCCA – Unified Multiple-Component Cellular Automaton

ZOC – Zone of clearance

LIST OF SYMBOLS

σ – Normal stress

σ^* – Yield normal stress

σ_A – Adhesive strength

σ_C – Cohesive strength

σ_R – Residual stress

τ – Shear stress

τ^* – Yield shear stress

τ_w – Shear stress acting at the wall

ε – Strain

ε_R – Residual strain

γ – Shear strain

E – Young modulus

E_{app} – Apparent Young modulus

G – Shear modulus

G_{app} – Apparent shear modulus

$G(t-t')$ – Relaxation modulus

$\hat{G}(\omega)$ – Complex modulus

G' – Storage modulus

G''– Loss modulus

ν – Poisson's ratio

ω – angular frequency

μ – Viscosity

μ_{app} – Apparent viscosity

η^* – Complex viscosity

tr – relaxation time coefficient

$\dot{\gamma}$ – Deformation rate

k_{cell} – cellular spring constant

u –Water microspray velocity

Re – Reynolds Number

A_{ZOC} – Area of the zone of clearance

d_{AF} – External diameter AirFloss nozzle

T – Biofilm thickness

A – Biofilm surface area

B – Biofilm biomass

%RT – Percent reduction biofilm thickness

%RB – Percent reduction biofilm biomass

%RA – Percent reduction biofilm surface area

u_{jet} – Air jet velocity

Q_{jet} – Volumetric air flow rate

A^* - Area nozzle of the air compressor

w_p – Wetted perimeter air compressor nozzle

λ_R – Ripples wavelength

w_R – Ripples width

u_R – Ripples velocity

RD_{BEADS} – Beads relative depth ratio

z_{BEAD} – Bead z-coordinate

$z_{BIOFILM}$ – Biofilm z-coordinate (or thickness)

N – Beads number

KD_{CHX} – CHX killing depth ratio

KD_{CPC} – CPC killing depth ratio

You will come to know that what appears today to be a sacrifice
will prove instead to be the greatest investment that you will ever make.

Gordon B. Hinckley

CHAPTER 1

1.1 GENERAL INTRODUCTION

Dental plaque biofilms are sessile heterogeneous oral bacterial communities attached to the surface of the teeth and embedded in an extracellular polysaccharide matrix (Donlan and Costerton 2002). Dental biofilms are often associated with the development of caries, gingivitis and periodontitis (Marsh 2004). Because of the complexity behind the biofilm structure, dental diseases are difficult to control and to eradicate, thus becoming a worldwide public health problem. Nowadays, dental caries still remains amongst the most important chronic disease of individuals worldwide. Approximately 36% of the global population has dental caries in their permanent teeth and about 90% of adults have been susceptible to this disease throughout their lifetime (Jin et al. 2016). Regarding the economic burden related with curative dental care, United Kingdom spends over £3.4 billion on primary and secondary care dental services per annum (Claxton et al. 2016) with the European Union almost € 79 billion between 2008 and 2012 (Patel 2012) and USA approximately $116.6 billion in 2013 (Thomas Wall et al. 2014). Recently it has been estimated that direct treatment costs related to dental diseases were approximately 4.6% of global health expenditure (Listl et al. 2015).

As of today, the mechanical disruption of dental biofilms through toothbrushes, oral irrigators or microsprays combined with the addition of anticaries agents to toothpastes and mouthwashes for killing biofilm bacteria is the most common way to control oral-related disease (Marsh 2010). The main goal of dental cleaning methods is to remove all dental plaque inside the mouth. However, this is not possible in many difficult-to-reach areas because brushes need to be in contact with the teeth surface. Also, powered toothbrushes, water jets and microsprays, which project fluid forces without direct contact of the device, leave some biofilm attached to the teeth surface. In parallel, biofilm complex structure increase its resistance to antiplaque agents by limiting the transport of dentifrices inside the biofilm (Socransky and Haffajee 2002).

The understanding of biofilm mechanical properties and detachment under different physical forces, such as hydrodynamic stresses or mechanical scraping, is essential in order to develop more effective strategies or dental cleaning devices for preventing and controlling dental biofilms. Despite a diversity of methods, research groups and types of biofilms tested their mechanical behaviour is consistently described as viscoelastic. Viscoelasticity means the material behaves either as an elastic solid or a viscous fluid depending how fast it is deformed and how quickly it recovers (Banks et al. 2010). The extracellular polysaccharides substances

(EPS) of the matrix, which are kept together by physicochemical interactions (electrostatic interactions, van der Waals forces and hydrogen bonding) appear to be the main contributors to biofilm viscoelasticity and mechanical stability (Korstgens 2001). Energy dissipation through viscoelasticity allows biofilms to tolerate rapidly-changing shear stresses without completely detaching from the surface.

Recently, investigators demonstrated that mechanical perturbation caused by the fluid-dynamic activity of power toothbrushes or low-volume high-velocity microsprays can significantly change the viscoelastic properties of unremoved biofilms (Busscher et al. 2010; Fabbri et al. 2016). Such a change in biofilm structure could leave the biofilm more susceptible to antimicrobials and antiplaque agents compared to simple topical application (He et al. 2014; Jongsma et al. 2015; Sjogren et al. 2004; Stoodley et al. 2007). Therefore, the role of the hydrodynamics in the enhancement of dentifrices inside the biofilm has become a topic of interest, since oral irrigators or water microsprays might be utilized to improve delivery to the tooth surface or the bacteria directly. Both the advances in microbiology and in the mechanical testing techniques have shown that is not only the biology of the EPS that contributes to viscoelasticity and structure but also the biophysical factors (e.g., strain, fluid flow and pressure) under which the biofilm is grown. Shear forces can influence biofilm structure and cause bacteria to undergo phenotypic adaptation (Stoodley et al. 2002). Biofilms have also been shown to be able to migrate in ripple- or stream-like structures when exposed to high-velocity flows (Stoodley et al. 1998). Fluid/structure interactions in biofilms can modulate the dynamics of biofilm growth, cell-signalling, tolerance to antibiotics, and virulence (Peterson et al. 2015; Stoodley 2016). Understanding the interaction between biofilm structure and chemical composition with their viscoelastic properties could open up new strategies for better controlling and preventing not only biofilms in the dental field but also in the industrial and medical sectors.

1.2 REFERENCES

Banks HT, Hu S, Kenz ZR. 2010. A brief review of elasticity and viscoelasticity for solids. Adv in Appl Math Mech. 3:1-51.

Busscher HJ, Jager D, Finger G, Schaefer N, Van Der Mei HC. 2010. Energy transfer, volumetric expansion, and removal of oral biofilms by non-contact brushing. European Journal of Oral Sciences. 118(2):177-182.

Claxton L, Taylor M, Kay E. 2016. Oral health promotion: The economic benefits to the nhs of increased use of sugarfree gum in the uk. British dental journal. 220(3):121-127.

Donlan RM, Costerton JW. 2002. Biofilms: Survival mechanisms of clinically relevant microorganisms. Clinical Microbiology Reviews. 15(2):167-193.

Fabbri S, Johnston DA, Rmaile A, Gottenbos B, De Jager M, Aspiras M, Starke ME, Ward MT, Stoodley P. 2016. Streptococcus mutans biofilm transient viscoelastic fluid behaviour during high-velocity microsprays. Journal of the mechanical behavior of biomedical materials. 59:197-206.

He Y, Peterson BW, Ren Y, van der Mei HC, Busscher HJ. 2014. Antimicrobial penetration in a dual-species oral biofilm after noncontact brushing: An in vitro study. Clin Oral Invest. 18(4):1103-1109.

Jin LJ, Lamster IB, Greenspan JS, Pitts NB, Scully C, Warnakulasuriya S. 2016. Global burden of oral diseases: Emerging concepts, management and interplay with systemic health. Oral diseases.Doi: 10.1111/odi.12428.

Jongsma MA, van de Lagemaat M, Busscher HJ, Geertsema-Doornbusch GI, Atema-Smit J, van der Mei HC, Ren Y. 2015. Synergy of brushing mode and antibacterial use on in vivo biofilm formation. Journal of dentistry. 43(12):1580-1586.

Korstgens V. 2001. Influence of calcium ions on the mechanical properties of a model biofilm of mucoid pseudomonas aeruginosa. Water Sci Technol. 43(6):49-57.

Listl S, Galloway J, Mossey PA, Marcenes W. 2015. Global economic impact of dental diseases. Journal of dental research. 94(10):1355-1361.

Marsh PD. 2004. Dental plaque as a microbial biofilm. Caries Research. 38:204-211.

Marsh PD. 2010. Controlling the oral biofilm with antimicrobials. Journal of Dentistry. 38, Supplement 1(0):S11-S15.

The state of oral health in europe: report commissioned by the platform for better oral health in europe. 2012. [accessed 21/05/2016]. http://www.oralhealthplatform.eu/our-work/the-state-of-oral-health-in-europe/.

Peterson BW, He Y, Ren Y, Zerdoum A, Libera MR, Sharma PK, van Winkelhoff A-J, Neut D, Stoodley P, van der Mei HC. 2015. Viscoelasticity of biofilms and their recalcitrance to mechanical and chemical challenges. FEMS microbiology reviews. 39(2):234-245.

Sjogren K, Lundberg AB, Birkhed D, Dudgeon DJ, Johnson MR. 2004. Interproximal plaque mass and fluoride retention after brushing and flossing--a comparative study of powered toothbrushing, manual toothbrushing and flossing. Oral health & preventive dentistry. 2(2):119-124.

Socransky SS, Haffajee AD. 2002. Dental biofilms: Difficult therapeutic targets. Periodontology 2000. 28(1):12-55.

Stoodley P. 2016. Biofilms: Flow disrupts communication. Nature Microbiology. 1:15012.

Stoodley P, A Nguyen D, A Longwell M, A Nistico L, A von Ohle C, A Milanovich N, A de Jager M. 2007. Effect of the sonicare flexcare power toothbrush on fluoride delivery through streptococcus mutans biofilms. Compendium of Continuing Educationin Dentistry. 28:15-22.

Stoodley P, Cargo R, Rupp CJ, Wilson S, Klapper I. 2002. Biofilm material properties as related to shear-induced deformation and detachment phenomena. Journal of industrial microbiology & biotechnology. 29(6):361-367.

Stoodley P, Lewandowski Z, Boyle JD, Lappin-Scott HM. 1998. Oscillation characteristics of biofilm streamers in turbulent flowing water as related to drag and pressure drop. Biotechnology and Bioengineering. 57(5):536-544.

Us dental spending remains flat through 2012. 2014. American Dental Association; [accessed 21/5/2016]. http://www.ada.org/~/media/ADA/Science%20and%20Research/Files/HPRCBrief_0114_1.ashx.

CHAPTER 2

Aims, objectives and thesis structure

2.1 AIMS AND OBJECTIVES

Dental biofilm removal using low-volume high-velocity microsprays has obtained positive results due the hydrodynamic shear stresses generated at the passage of an air-water interface over the biofilm surface (Parini and Pitt 2006; Rmaile et al. 2015). The aim of this work is to assess the potential for high-velocity microsprays to enhance antimicrobial penetrations inside dental biofilms via hydrodynamic shear forces. The microspray burst will both detach biofilm and enhance dentifrice delivery in the biofilm left behind (Figure 2.1). This work was completed using *Streptococcus mutans* UA159 strain (ATCC number 700610, www.atcc.org). *S. mutans* is a gram-positive and facultative anaerobic microorganism that is considered a causative agent of human dental decay (Loesche 1986). *S. mutans* biofilms have been widely used in research to investigate biofilm mechanical properties and detachment (Cense et al. 2006; Rmaile et al. 2012; Vinogradov et al. 2004).

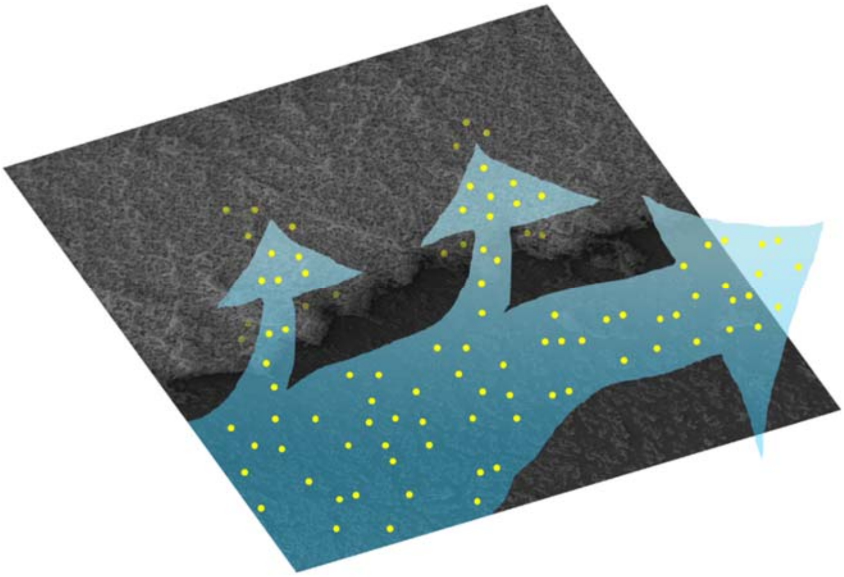

Figure 2.1. Schematic representation oral biofilm (grey) subjected to a fluid containing antimicrobial agents (yellow dots). The physic of the impact could change biofilm mechanical properties or mixing the biofilm up and enhance the delivery of a specific antiplaque or antimicrobial agent inside itself, thereby increasing the therapeutic effect.

The project aim has been addressed by:

Specific Aim # 1: Determine mechanism of removal of *S. mutans* biofilm by high velocity water sprays and air jets

Assessing *S. mutans* biofilm mechanical behaviour and biofilm/fluid interactions during the exposure of high-velocity microspray bursts using high-speed camera videography. An AirFloss interdental cleaning device was used to generate high-velocity microsprays or air-only microbursts. Since the device was designed to remove interproximal dental plaque we developed an *in vitro* interproximal space model which allowed the parallel insertion of two biofilm-colonized slides separated by a distance of 1 mm and enabled high-speed imaging of the biofilm/fluid interactions happening at the surface.

Specific Aim # 2: Determine the ability of high-velocity water microsprays to enhance mass transfer inside *S. mutans* dental biofilms

Quantifying mass transfer inside *S. mutans* biofilms using fluorescent microbeads incorporated in the AirFloss microspray. Biofilms were exposed to a 90° or 30° impact. For comparison, a 30 sec diffusive transport an *in vitro* mouthwashing were performed. Confocal Laser Scanning Microscopy (CLSM) complemented with COMSTAT and IMAGEJ were used to determine the relative bead penetration depth into the biofilm.

Specific Aim # 3: Determine the ability of high-velocity water microsprays to enhance dentifrice penetration inside *S. mutans* dental biofilms

Quantifying antimicrobials penetration into *S. mutans* biofilms using a 0.2% Chlorhexidine or 0.085% Cetylpyridinium chloride solution incorporated in the AirFloss microspray. For comparison, a 30 sec diffusive transport was performed. CLSM complemented with COMSTAT and IMAGEJ were used to determine the penetration depth calculated from the resultant zone of killing detected by live/dead viability staining.

2.2 THESIS STRUCTURE

This thesis consists of 8 chapters. The literature review can be found in Chapter 3 where the current state of knowledge and the scientific aspects related to this work are summarized. The Section relative to biofilm mechanical properties (Section 3.5) has already been published as “Mechanical properties of biofilms” in the book “The Perfect Slime: Microbial Extracellular Polymeric Substances (EPS)’, Flemming, H.C., Neu, T.R., Wingender, J. (eds). IWA Publishing, London, UK (publication date: 15/08/2016).

Chapters 4, 5, 6, and 7 were written in paper format since they were, or will, be submitted as manuscripts for publication in journals, where each chapter has its own introduction, materials and methods, results, discussion, conclusion and references sections. Some repetition may occur in these chapters when the same or similar techniques or methods were used.

In Chapter 4 we introduced the in vitro interproximal model which allowed high-speed camera videography of the biofilm-burst interactions and biofilm mechanical behaviour during the exposure to high-velocity water microsprays or air-only microbursts with respect to the removal process. We discovered that high-velocity fluid-biofilm interactions can cause the biofilm to behave like a viscoelastic fluid over very short times-scales. Biofilm fluidification can be the result of mixing processes occurring between the water and the biofilm structure. This chapter has already been published as a research paper in The Journal of Mechanical Behaviour of Biomedical Materials ((Fabbri et al. 2016) – see Appendix C).

Chapter 5 was based on the results obtained from the previous chapter. Here we documented the discovery of interfacial ripple-like structures forming at the biofilm-fluid interface during the exposure to high-velocity microsprays. We also collaborated with a mathematician, Nick Cogan at the University of Florida who developed and analysed a two-fluid model of a biofilm. He demonstrated that the ripples where actually Kelvin-Helmholtz instabilities providing further insight into the mechanical behaviour of biofilms as complex liquids and further go they can develop internal turbulence. The formation of these instabilities is common in many fluids but has never previously been documented in biofilms before. One of the reasons is that it happens so quickly and the ripple structures rapidly dissipate. This chapter has already been submitted for publication in ISME Journal.

In Chapter 6 we assessed the ability of high-velocity water microsprays to enhance mass transfer inside *Streptococcus mutans* dental biofilms using a 1-µm tracer beads solution (10^9 beads/mL), while in Chapter 7, we documented the ability of high-velocity microsprays to enhance delivery of antimicrobials into 3-days old *S. mutans* biofilms using a 0.2% Chlorhexidine or 0.085% Cetylpyridinium chloride solution. We related the physic of the microspray impact, which changed biofilm mechanical properties by generation of ripples instabilities (Chapter 5) and mixing the biofilm up (Chapter 4), with an increase in the beads and antimicrobial penetration. Chapter 6 and 7 are part of a research paper which has already been submitted for publication in the Journal of Dental Research.

Concluding remarks and future works are given in chapter 8.

2.3 AUTHORS CONTRIBUTIONS STATEMENT

The study in Chapter 4 was designed by the PhD student S. Fabbri under the general supervision of P. Stoodley. S. Fabbri conducted all laboratory experiments, performed data analysis and statistics. P. Stoodley gave feedback on experimental design and data handling D. A. Johnston trained S. Fabbri on confocal and SEM microscopy and gave input on sample preparation, staining and imaging. A. Rmaile, B. Gottenbos, M. De Jager, M. Aspiras and gave feedback on the experimental design. E. M. Starke and M. T. Ward gave input on clinical significance with respect to experimental design. The manuscript was written by SF and the final draft was commented by all co-authors.

The study in Chapter 5 was designed by the PhD student S. Fabbri under the general supervision of P. Stoodley. S. Fabbri conducted all laboratory experiments, performed data analysis and statistics J. Li constructed the mathematical model under the supervision of N. Cogan and performed data analysis. N. Cogan contributed with the results interpretation of the mathematical model. R. P. Howling assisted in laboratory experiments with *S. epidermidis* and *P. aeruginosa* and gave feedback on data interpretation regarding the microbiology aspects. P. Stoodley gave feedback on the general experimental design and data handling. A. Rmaile, B. Gottenbos, M. De Jager, M. Aspiras and gave feedback on the experimental design regarding the engineering aspects. E. M. Starke and M. T. Ward gave input on clinical significance with respect to experimental design. J. Li and N. Cogan wrote introduction, materials and methods, results and discussion relating to the mathematical modelling aspects. S. Fabbri wrote introduction, materials and methods for the laboratory experiments, figure composition and discussion. The final draft was commented by all co-authors.

The study in Chapter 6 was designed by the PhD student S. Fabbri under the general supervision of P. Stoodley. S. Fabbri conducted all laboratory experiments, performed data analysis and statistics. P. Stoodley gave feedback on experimental design and data handling D. A. Johnston trained S. Fabbri on confocal and SEM microscopy and gave input on sample preparation, staining and imaging. A. Rmaile, B. Gottenbos, M. De Jager, M. Aspiras and gave feedback on the experimental design. E. M. Starke and M. T. Ward gave input on clinical significance with respect to experimental design. The manuscript was written by SF and the final draft was commented by all co-authors.

The study in Chapter 7 was designed by the PhD student S. Fabbri under the general supervision of P. Stoodley. S. Fabbri conducted all laboratory experiments, performed data analysis and statistics. P. Stoodley gave feedback on experimental design and data handling D. A. Johnston trained S. Fabbri on confocal and SEM microscopy and gave input on sample preparation, staining and imaging. A. Rmaile, B. Gottenbos, M. De Jager, M. Aspiras and gave feedback on the experimental design. E. M. Starke and M. T. Ward gave input on clinical significance with respect to experimental design. The manuscript was written by SF and the final draft was commented by all co-authors.

2.4 REFERENCES

Cense A, Peeters E, Gottenbos B, Baaijens F, Nuijs A, Van Dongen M. 2006. Mechanical properties and failure of streptococcus mutans biofilms, studied using a microindentation device. Journal of microbiological methods. 67(3):463-472.

Fabbri S, Johnston DA, Rmaile A, Gottenbos B, De Jager M, Aspiras M, Starke ME, Ward MT, Stoodley P. 2016. Streptococcus mutans biofilm transient viscoelastic fluid behaviour during high-velocity microsprays. Journal of the mechanical behavior of biomedical materials. 59:197-206.

Loesche WJ. 1986. Role of streptococcus mutans in human dental decay. Microbiological reviews. 50(4):353-380.

Parini MR, Pitt WG. 2006. Dynamic removal of oral biofilms by bubbles. Colloids and Surfaces B: Biointerfaces. 52:39-46.

Rmaile A, Carugo D, Capretto L, Wharton JA, Thurner PJ, Aspiras M, Ward M, De Jager M, Stoodley P. 2015. An experimental and computational study of the hydrodynamics of high-velocity water microdrops for interproximal tooth cleaning. Journal of the Mechanical Behavior of Biomedical Materials. 46:148-157.

Rmaile A, Carugo D, Capretto L, Zhang X, Wharton JA, Thurner PJ, Aspiras M, Ward M, Stoodley P. 2012. Microbial tribology and disruption of dental plaque bacterial biofilms. Wear. 306(1-2):276–284.

Vinogradov AM, Winston M, Rupp CJ, Stoodley P. 2004. Rheology of biofilms formed from the dental plaque pathogen streptococcus mutans. Biofilms. 1(01):49-56.

CHAPTER 3

Literature Review

3.1 BIOFILMS

It's almost one century ago when microbiologists discovered that the majority of bacterial species in nature preferred to live attached to surfaces than in the planktonic state (Høiby 2014). Since then, a significant body of research has aimed at understanding the processes that lead bacteria to set up the complex structure called "biofilm". One of the most common definitions of biofilm was given by professor microbiologist Bill Costerton (Donlan and Costerton 2002):

"*A biofilm is a microbially derived sessile community characterized by cells that are irreversibly attached to a substratum and embedded in a matrix of extracellular polymeric substances that they have produced.*"

Biofilms grow in any environment in which there are nutrients, fluid flow and a surface. Both the solid-liquid interface and the stress caused by the flow provide the ideal habitat for the attachment and the maturation of sessile biofilm-structured bacteria. Once attached to the surface, microorganisms excrete extracellular polymeric substances (EPS) (mainly extracellular DNA, proteins, and polysaccharides) from the nutrients they metabolize. The EPS convey to the biofilm a three-dimensional (3D) structure (matrix) which allows bacteria to withstand stressful environmental events such as extreme temperatures, high-shear flows or environmental pH changes (Flemming and Wingender 2010). Bacteria within a biofilm become metabolically-organised communities of interacting species generating a spectrum of chemical communications which allow biofilms to adapt quicker to evolutionary changes than freely suspended bacteria populations (Konovalova and Sogaard-Andersen 2011). The matrix material surrounding and enclosing cells in close proximity to each other facilities cell-cell interactions which regulate biofilm formation, survival and protection (Rumbaugh and Armstrong 2014). Bacteria cooperation is a clever behaviour since it regulates biofilm biological fitness in any hostile environment enlightening even more biofilm complexity. Biofilms are ubiquitous in the modern natural environment (Stoodley et al. 2002b) and have been identified in the fossil record (Krumbein et al. 2003; Noffke et al. 2013). Astonishingly, the oldest known discovery of biofilms in the fossil records was a 3.5-billion-year-old stromatolite in Australia (Schopf and Packer 1987), suggesting that micro-organism growth as a biofilm might be an ancient survival mechanism. Biofilms are not only found in the natural environment, but they also play an important role in industry and healthcare sectors. Biofilm beneficial effects can be found in the waste treatment of drinking water (Nicolella et al. 2000), in the removal of mineral oil from marine systems (dos Santos et al. 2008), in the cleaning of fuel tanks (Srivastava et al. 2006), in the protection from corrosive agents in industry (Morikawa 2006) and lastly in the protective microflora in healthy human (Wilson 2001). On the other side, biofilms are also involved in biofouling issues such as water treatment systems (Salta et al. 2013), energy losses on ship hulls and in fluid pipelines (Schultz et al. 2011) causing serious complications in the industry sectors. In the medical and dental fields, biofilms play an important role in the development and persistence of infectious diseases (Costerton et al. 1999). Urinary tract, catheters, dental plaque, gingivitis, endocarditis, cystic fibrosis, permanent indwelling devices (joint prostheses, heart valves) are some examples of infections that are biofilm-based in the medical field (Costerton et al. 2005; Marsh et al. 2011). Biofilm communities are estimated to cause about 60% of the bacterial infections reported in developing countries (Donelli 2014) suggesting that virulence is favoured for the biofilm residents. In addition, biofilm persistence during antibiotic treatment also enjoy a greater antimicrobial tolerance than planktonic bacteria contributing to biofilm virulence.

3.2 FORMATION OF DENTAL PLAQUE

Dental plaque is one of the most complex biofilm bacterial communities found in the human body with around 1000 species present (Dewhirst et al. 2010). *Firmicutes*, *Bacteroidetes*, *Proteobacteria*, *Actinobacteria*, *Spirochaetes* and *Fusobacteria* form 96% of the dental plaque microbiota. Even after “cleaning”, the tooth enamel is not an absolutely clean surface but salivary molecules (glycoproteins, lipids and glycolipids) are immediately adsorbed on the surface forming a conditioning film called the *acquired pellicle* (Armstrong 1968; Hannig 2002). The main functions of the acquired pellicle are to reduce the demineralisation processes by acting as buffer for remineralizing ions and, act as a lubricant, antimicrobial and nutrient source for the oral microflora (Hannig et al. 2005). However, pellicle glycoproteins (such as mucin glycoproteins, amylase and proline-rich proteins) enhance bacterial attachment on the teeth surface through protein-protein or protein-carbohydrates interactions between the pellicle and the bacterial cell surface (Nobbs et al. 2011). Mucins are glycosylated proteins which are secreted from the human salivary glands. Two types of mucins are produced: the oligomeric mucins which are synthetized by mucous cells and the monomeric mucins which are synthetized by the serous cells (Zalewska et al. 1999). Since salivary mucins are able to form gels, they act as lubricants inside the mucosal surfaces avoiding desiccation, irritations and virus proliferation (Mandel 1987). In addition, mucins appear to enhance the aggregation of the microbes in order to facilitate their removal from the teeth (agglutination) (Marsh and Bradshaw 1995). Also enzymes, such as lysozyme, chitinase and amylase, are present in the salivary pellicle and play an important role in determining both the functions of the conditioning layer and the attachment of bacteria to the surface (Hannig et al. 2005). Bacteria attachment to the tooth surface and biofilm growth is not an instantaneous process but involves different and complex steps (Figure 3.1) (Soumya et al. 2012; Stoodley et al. 2002b) which are described in the following paragraphs.

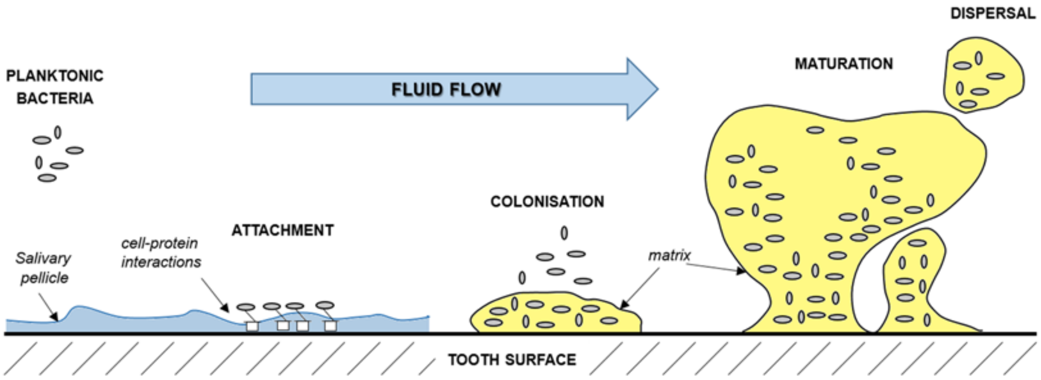

Figure 3.1. Schematic representation of the different stages involved in the formation process of oral biofilms on the teeth surface.

1. *Reversible attachment*

The saliva flow is responsible of the passive transport of planktonic bacteria to the teeth surface. Free-floating bacteria possess different structures in the outer membrane (such as flagella, fimbriae or curli) which are involved in the bacterial early stages of attachment (Prakash et al. 2003). The strength of the biofilm attachment depends directly on the properties of the pellicle conditioning film rather than on the tooth surface ones. A wide and complex range of physicochemical interactions take place during the first stage of microbial adhesion (Van Oss et al. 1986). Those interactions vary from long-range forces (50–100 nm), such as Coulomb interactions, Van der Waals forces, medium-range forces (10–50 nm) such as hydrophobic interactions and short-range forces (less than 5 nm), such as hydrogen bonds and Lewis interactions (Bos et al. 1999; Busscher et al. 2008). Due to the weak interactions that take place, the attachment is reversible.

2. *Irreversible attachment*

In order to transform the reversible interactions into a stronger and irreversible attachment, bacteria hydrophobic surfaces have to dehydrate the water film on the colonized surface. This happens when bacteria adhere to the surface thanks to proteins (such as curli) which are located on the outer membrane. In the case of dental biofilms, specific adhesins on the bacteria membrane are able to interact with specific receptors (complementary molecules expressed specifically to interact with a ligand*)* of the pellicle components (Marsh and Bradshaw 1995). The first colonisers of the teeth are mainly streptococci bacteria such as *S. sanguinis, S. oralis* and *S. mitis* (ten Cate 2006) which bind to acid proline-rich-proteins, glycoproteins and to other receptors in the acquired pellicle (Whittaker et al. 1996). Oral streptococci are gram positive bacteria and possess anionic polymers on the membrane which can interact with pellicle reactive components. Once attached, the bacteria start to duplicate and auto-produce the extracellular polymeric substances of the biofilm matrix (Flemming et al. 2007) (for a detailed description of the matrix please see Session 3.4.1). The EPS, polysaccharides, enzymes, extracellular DNA, RNA, and extracellular proteins, can also establish short-range interaction with surface (Götz 2002) and provide a stronger attachment to the surface.

3. Maturation

Later colonizers, such as *Aggregatibacter actinomycetemcomitans, Prevotella intermedia, Eubacterium spp., Treponema spp.,* and *Porphyromonas gingivalis* (Kolenbrander et al. 2002) interact via adhesins-receptors interactions with the early colonizers. Biofilm bacteria density quickly increases as late colonizers attach to the first biofilm layers and start to replicate. Extracellular components are continuously generated from the bacteria which build up the three dimensional structure of the biofilm .Voids and channels start to form thanks to the fluid flow and nutrients supply from the environment (Stoodley et al. 1998) Over time, different gradients of nutrients, pH or oxygen are formed because of the diversity of the bacteria species. This leads to different micro-environments enabling the co-existence and the co-aggregation of different species together (Marsh 2009; Rickard et al. 2003). Various bacteria cell-cell interactions start to take place helping biofilms to regulate themselves in function of both environmental changes or host defences (Miller and Bassler 2001). This communication is accomplished primarily through chemical cell-to-cell signalling called quorum sensing (QS). Bacteria secrete small signalling molecules called *autoinducers* (AIs) in order to control their behavior according to population density in the surrounding environment (Konovalova and Sogaard-Andersen 2011; Miller and Bassler 2001). The local concentration of signalling molecules released by a single bacterium into their environment would be low, however if sufficient bacteria are present, the autoinducers concentration reach a threshold, allowing the bacteria to activate or supress particular genes (Senadheera and Cvitkovitch 2008). Quorum sensing in biofilms regulates the movement of genetic information between and within microbes (horizontal gene transfer) which contribute to bacterial formation and evolution (Madsen et al. 2012). The complex community of bacteria will continue to grow according to a sigmoidal function and produce matrix until the mature plaque is formed and a maximum thickness reached.

4. Dispersal

Shear forces caused by saliva or liquids flow can remove microorganisms from oral surfaces and limit any further expansion of the dental plaque (Hall-Stoodley et al. 2004; Stoodley et al. 2001). Biofilm dispersal is of fundamental importance in the proliferation of biofilms, because detached cells, also known as dispersal cells, can colonize new places in the mouth and start a new biofilm cycle (Singh et al. 2002). The detachment process has also clinical issues because some bacteria species, such as *S. mutans*, can enter into the blood stream and cause bacteraemia and endocarditis. In general, biofilm dispersal can be divided in two main categories: a passive dispersal, where biofilm cell detachment is mediated by external forces or human intervention, and an active dispersal, where bacteria within biofilm can decide to escape in response to inter- or intra-bacterial communication, starvation or physical-chemical signals (Kaplan 2010). Since bacteria in biofilms are enclosed in an extracellular polymeric matrix, most detachment agents released are enzymes with degradative functions (Kaplan 2014). Kaplan and co-authors discovered that the oral bacterium *A. actinomycetemcomitans* produces a particular extracellular enzyme (Dispersin B) which regulate oral biofilm dispersal through the degradation of matrix components (N-acetyl-D-glucosamine) (Kaplan et al. 2003). *P. aeruginosa* biofilms detach in response to glucose or nitrogen depletion and to a carbon increase (Sauer et al. 2004; Sawyer and Hermanowicz 2000). Likewise, it has been demonstrated that the cyclic signalling of an intracellular nucleotide c-di-GMP through the modulation of polysaccharide biosynthesis and gene expression triggers biofilm dispersal (Cotter and Stibitz 2007). Depending on the oxygen concentration, nutrient levels and temperature of the surrounding environment, c-di-GMP can promote either biofilm attachment (high levels of c-di-GMP) or detachment (low levels of c-di-GMP) (McDougald et al. 2011). C-di-GMP also induces cell dispersal when low concentrations of Nitric Oxide (NO) are detected in many biofilm species such as *P. aeruginosa* and *E. coli* (Barraud et al. 2015; Barraud et al. 2009). Moreover, an interesting effect of NO-mediated dispersal is that *P. aeruginosa* or *S. pneumoniae* biofilms lose antimicrobial resistance to antimicrobial agents (Allan et al. 2016; Barraud et al. 2006). The discovery of a signalling molecule responsible for biofilm dispersion not only further demonstrates the complexity of biofilm structure and developmental mechanisms, but also the important implications in biofilm control and prevention. The combination of dispersion inducers with antimicrobials might enhance the activity of the treatment through the disruption of the existing biofilm. For instance, recently Kolderman et. al discovered that the amino acid L-arginine is able to destabilise oral multispecies biofilms (changes in community composition and architecture) leading to an increase of antimicrobial penetration and greater killing (Kolderman et al. 2015).

3.3 NEGATIVE EFFECTS OF PLAQUE

In general, in healthy individuals with a healthy diet, the plaque is stable (*microbial homeostasis*) (Marsh 2004) and plays an important role in the defence of the host (Marsh 2000). A perturbation of the environment, which could be for example the introduction of sugars in the diet, may break the commensal homeostasis and lead to the progression of caries, periodontitis and gingivitis (Marsh 2005). In particular, dental caries are defined as a localised loss of enamel caused by acids produced from the bacterial metabolism of sugars (Gibbons and Houte 1975). Dental enamel is composed of 90% crystals of carbonated calcium hydroxyapatite and 10% body fluids and impurities such as fluoride ions. Tooth enamel consist of prisms (3–6 μm in diameter) which are composed of hexagonal hydroxyapatite (HA) crystals with a mean width of 68.3 nm and a mean thickness of 26.3 nm (Lippert et al. 2004). HA, like all mineralised tissue, is sensitive to pH variations inside the mouth and thus, the solubility of the enamel is related to the HA solubility in the saliva fluid. The dissolution of HA in water consists in the generation of small amounts of calcium, phosphate and hydroxyl ions according to the following equation:

$$Ca_{10}(PO_4)_6(OH)_2 \leftrightarrow 10Ca^{2+} + 6PO_4^{3-} + 2OH^- \tag{3.1}$$

The dissolution of HA is governed by the pH of the solution and the ionic product (represented by calcium, phosphate and hydroxyl ions). If the pH becomes acidic, the HA starts to loose phosphates and dissolves (dissolution). When the pH returns to normal, phosphate recrystallizes into the HA (precipitation). The equilibrium is reached when there is no net loss/gain of ions in solution/in the solid phase. In acidic conditions, the concentrations of the calcium or phosphate ions have to increase in order to maintain saturation with respect to HA. Since saliva contains calcium, phosphate and hydroxyl ions, it maintains the solution supersaturated. Enamel dissolution occurs in saliva only if the pH goes below a critical pH value which is found to be equal to 5.5 (Dawes 2003). If the exposure to acid is short the saliva will raise the pH naturally so the enamel loss can be repaired through remineralisation (Stoodley et al. 2008). But, if the exposure to acid is prolonged or cyclic, the remineralisation rate may not be enough to repair the loss from demineralisation leading to a lower pH. Consequently, the acidic environment aids the proliferation of acidogenic (acid-producer) and aciduric (acid-tolerant) species at the expense of health-associated bacteria that live at neutral pH values (Marsh 2003). Mutans streptococci, bifidobacteria and lactobacilli, examples of acidogenic and aciduric species, enhance tooth demineralisation by the production of acids from dietary sugars and, in turn, lead to the development of caries (cariogenic bacteria). However, cariogenic bacteria in biofilms have also been found in healthy sites (Chen and Jiang 2015). As result a relationship between bacterial plaque and disease has been presented in the *Extended Ecological Plaque Hypothesis* (Figure 3.2*)* (Marsh et al. 2015; Takahashi and Nyvad 2008). The main hypothesis is that the pathogenicity of the bacteria is directly linked to changes in local environment conditions which might lead to an increase of disease-related bacteria in the new environment.

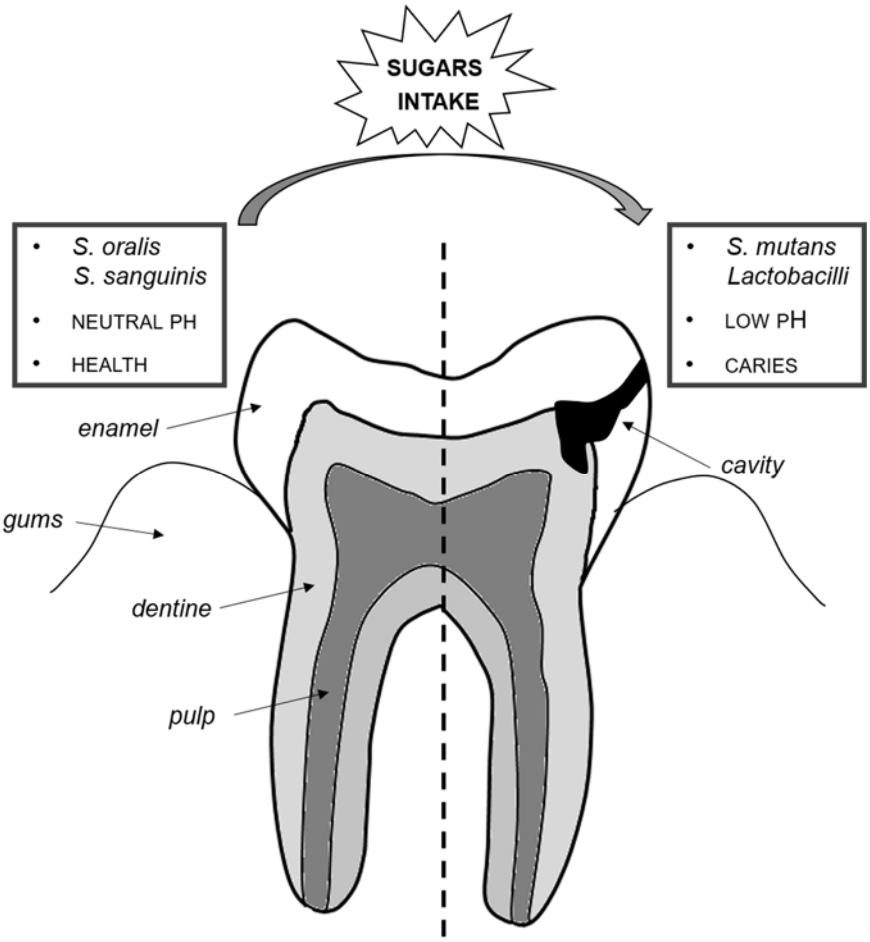

Figure 3.2 Schematic view of the tooth related with the Extended Ecological Plaque Hypothesis. Caries are a result of environmental changes due to acid production from the fermentation of sugars. The acidogenic environment leads to an ecological shift by favouring the proliferation of acidogenic and aciduric microbes such as mutans streptococci and lactobacilli.

3.3.1 *STREPTOCOCCUS MUTANS* DENTAL BIOFILM

Streptococcus mutans or *S. mutans* is a gram positive and facultative anaerobic microorganism which is considered, together with lactobacilli, the main causative agent of human dental decay (Hamada and Slade 1980). It has also been found associated with infective endocarditis caused by bacteria colonisation of damaged heart valves (Ajdic et al. 2002). *S. mutans* was first isolated from caries by J. K. Clark in 1924 and subsequently many studies have been made in order to understand the antigenic structure of this bacterium. In addition, *S. mutans* is widely used in dental and microbiology research as a biofilm model (Figure 3.3) for the study of caries, biofilm mechanical properties and detachment (Cense et al. 2006a; Rmaile et al. 2013; Vinogradov et al. 2004). Mutans streptococci colonize the tooth surface through the establishment of adhesion-receptors interactions with pellicle components (Vacca-Smith et al. 1996). For example, *antigen I/II* is a particular adhesin which is involved in the attachment of *S. mutans* with pellicle glycoproteins (Lemos et al. 2013; Senadheera and Cvitkovitch 2008). Interestingly, adhesin-mediated binding also stimulates cell signalling and immune response of mutans streptococci through the synthesis of proinflammatory cytokines contributing to increase the virulence of the bacterium in the oral microenvironment (Engels-Deutsch et al. 2011). In addition, *S. mutans* ability to form biofilms is also related to the glucosyltransferase (GTF) enzymes. GTF synthesizes soluble (α-1,3- glucan) and insoluble (α-1,6-glucan) glucans (or dextran) from monomeric sugars (sucrose) found in the acquired pellicle promoting cell adherence to the enamel surface and to other microbial cells (Krzyściak et al. 2014). Dextrans are also represent the majority of the exopolysaccharides which build the diffusion-limiting polymeric 3D matrix that protects embedded bacteria (Ajdic et al. 2002). In parallel, fructose, glucose, lactose are rapidly converted by *S. mutans* into various fermentation products (lactic acid, formate, ethanol and acetate) (Ajdic et al. 2002). This creates a highly acidic and low-pH environment which consequently cause localised demineralisation and tooth decay. *S. mutans* are aciduric bacteria and therefore are able to tolerate low pH stresses by maintaining the intracellular pH homeostasis (Quivey et al. 2001). This mechanism allows *S. mutans* to out-compete other non-pathogenic bacteria, which are not able to survive in acid environments, leading to cariogenic biofilm accretion and further acidification of the environment. All these functions and properties are regulated by complex quorum sensing interactions (Senadheera and Cvitkovitch 2008). In streptococci, the main QS system (called CSP-ComDE) is composed of the competence-stimulating peptide (CSP) pheromone and the ComDE signal transduction system. It has been shown that CSP can promote repair of damaged DNA or cellular damages (Spoering and Gilmore 2006). *S. mutans* actively produces CSP molecules as a response to various environmental stresses, including heat shock, oxidative stress, acidic pH, amino acid starvation, and even antibiotic treatment (Leung and Lévesque 2012; Perry et al. 2009).

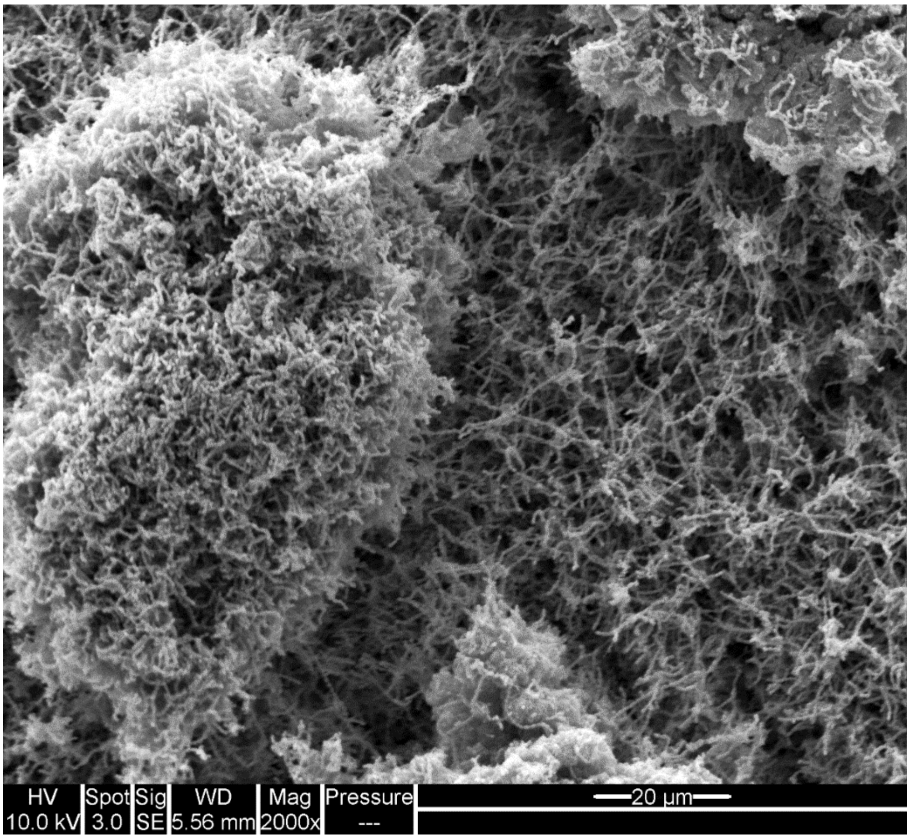

Figure 3.3. Scanning electron microscope image of a 3-days old biofilm formed from Streptococcus mutans UA159 strain. Original data.

3.4 BIOFILM ANTIMICROBIAL RESISTANCE

The chronicity of biofilm-related infections is mainly caused by the biofilm resistance to both antibiotics and antimicrobials agents. Biofilm antibiotic resistance is an outstanding clinical issue, considering that it is estimated that 65-80% of all infections worldwide are associated with biofilm formation (Donelli 2014). The majority of the biofilm related infections concerns the attachment and the colonisation of implanted medical devices surfaces (such as cardiac peacemaker, intravenous catheters, heart valves and joint prostheses) by pathogenic sessile bacteria (Stoodley et al. 2013). Microbes (such as *S. epidermidis*, *S. aureus* and *P. aeruginosa*) are able to enter in the bloodstream via the skin or the mouth and, consequently colonize not only biomedical implants but also damaged tissues (Hall-Stoodley et al. 2004). Endocarditis and cystic fibrosis pneumonia are two examples of biofilm colonisation of altered endothelial surfaces, in which pathogenic bacteria create a biofilm on the heart valves and the lungs respectively (Donlan and Costerton 2002; Lyczak et al. 2002). The common characteristic of biofilm-mediated infections is the ability of the bacterial community to withstand the antimicrobial intervention. Biofilm antimicrobial tolerance was, for the first time, discovered in a pacemaker patient with a *S. aureus* blood infection (Marrie et al. 1982). As the bacteraemia persisted after 6 weeks of antibiotic treatment, the pacemaker was removed and scanning electron microscope (SEM) images revealed *S. aureus* sessile bacteria attached on the implant surface. Since then, many studies have been on-going in order to understand the unique mechanisms behind biofilm formation and detachment. It is now recognized that biofilm cells are up to 1000 times more tolerant to antibiotics than the planktonic cells (Lewis 2001), highlighting both the complexity and the importance of the heterogeneous structure in which bacteria are protected. The main factors that contribute to increase a significant resistance to antimicrobial agents by pathogenic sessile microcosms are described in the following paragraphs (Sedgley and Dunny 2015).

3.4.1 THE EPS MATRIX

The EPS matrix constitutes the majority of the biofilm structure (90% of the biofilm dry mass) and provides the physical architecture and the solidity of the biofilm itself (Flemming and Wingender 2010). Interstitial voids and channels separate bacteria microcolonies embedded in the matrix allowing water flow (de Beer et al. 1994; Stoodley et al. 1994). This allows the exchange of oxygen and other nutritive elements and creates chemical gradient and different microenvironments (Hall-Stoodley et al. 2004a). The main components of the matrix are water (up to 97% (Sutherland 2001)), polysaccharides, glycoproteins, glycolipids and extracellular DNA (eDNA) (Flemming et al. 2007). The percentage of the EPS in the biofilm matrix depends on the organisms present and on the surrounding physicochemical environment (natural or human environment). Polysaccharides represent the major structural component of the matrix and many of which are strain specific (Decho 2013). For example, in gram-negative bacteria they are mostly polyanionic (i.e. anion having more than one negative charge) because of the high presence of uronic acids (the most common is the D-glucuronic acid) and ketal-linked pyruvates (Sutherland 2001). Instead, in gram-positive bacteria the polymeric substances are mostly negatively charged because of the presence of teichoic acids and eDNA (Allison 2003). Polysaccharides can also be hydrophilic or hydrophobic playing an important role in determining the matrix behaviour at the interface (Neu and Poralla 1990). Extracellular proteins have important structural and enzymatic functions. Enzymes, such as hydrolases, lyases, glycosidases, esterases, most important function is the degradation of biopolymers to provide carbon and energy sources or to serve biofilm dispersal (Flemming and Wingender 2010). Enzymes have also a role of virulence factors in medical and dental biofilms (Wingender et al. 2012). Another component of the biofilm matric is the extracellular DNA whose functions (adhesion, aggregation and exchange of genetic information) vary between biofilms strains. In *S. aureus* and *P. aeruginosa* eDNA has structural and regulatory function respectively, whereas it is almost absent in the *S. epidermidis* matrix (Izano et al. 2008). The EPS components, which are kept together by physicochemical interactions (electrostatic interactions, van der Waals forces and hydrogen bonding) appear to be the main contributors to biofilm mechanical stability, mechanical behaviour and antimicrobial resistance (Körstgens et al. 2001). In particular, the strong framework of the slime acts as a protective barrier against host defences and confers antimicrobial tolerance to the biofilm (Costerton et al. 1999). The porosity, density, charge and hydrophobicity of the exopolysaccharides might affect the penetration of antimicrobial agents into the biofilm inner layers. For instance positive charged antimicrobials could bind to negative charged polymers in the biofilm matrix (Mah et al. 2003; Rachid et al. 2000). Moreover, large molecules of antibiotics could fail to penetrate in the internal layers of the biofilm and, consequently not reach the living cells in the depths of the biofilm.

3.4.2 CELL-CELL COMMUNICATION AND GENE TRANSFER

It has been documented that quorum sensing, by regulating gene transfer processes, has potential implications for pathogenesis through the productions of virulence factors in both Gram-positive and Gram-negative commensal bacteria (Bassler and Miller 2013). Gene transfer can convert previously non-pathogenic bacteria into highly pathogen one causing serious problem for the human health (Molin and Tolker-Nielsen 2003). Moreover, when biofilms are subjected to a particular biocide, pathogenic bacteria can transfer antimicrobial resistance genes inside the biofilm community and promote the evolution of a more resistant biofilm phenotype (Broszat and Grohmann 2014). For example, different quorum sensing systems enhance pathogeny of *P. aeruginosa* biofilms in cystic fibrosis patients (Duan et al. 2003) and of oral pathogens in dental diseases (Jakubovics and Kolenbrander 2010; Rickard et al. 2008). Finally, multispecies biofilms are more resistant to antibiotics ant antimicrobials than single species biofilms enlightening the importance of bacteria communications for ensuring survival. For instance dual species *S. mutans* and *Veillonella parvula* were less susceptible to wide range of antimicrobials compared to single species biofilms (Kara et al. 2006). The mechanisms which related biofilm signalling with virulence and biocide resistance remain still unclear. However, studying quorum-sensing signalling process may help to identify inhibitors that can interfere with biofilm formation.

3.4.3 DORMANT AND PERSISTER CELLS

Nutrient and chemical (such as oxygen) gradients in concentrations lead to starved zones in which bacteria metabolism and replication slow leading to a dormant phase. Recent studies have shown that dormant phase bacteria increase in resistance to antibiotics, outlying the possible occurring of physiological changes in the biofilm (Brown et al. 1988; Wentland et al. 1996). In addition, bacterial species in a biofilm produce a diversity of phenotypes. It has been discovered that subpopulations of strains are able to survive prolonged antibiotics therapies and to coexist with cells that are antibiotic sensitive (Spoering and Lewis 2001). These cells (persister cells) are not phenotypic variants and are genetically identical to the susceptible cells.

3.5 BIOFILM MECHANICAL PROPERTIES

This Section has been published as" Mechanical properties of biofilms" in the book "The Perfect Slime: Microbial Extracellular Polymeric Substances (EPS)", Flemming, H.C., Neu, T.R., Wingender, J. (eds). IWA Publishing,

Mechanical properties have been widely studied in order to understand the physical behaviour of biofilms when subjected to physical forces. This could help not only to control and predict biofilm attachment and growth in either mechanical or medical environments, but also to understand biofilm structure and functions. Due to the high complexity and variability of the biofilm structure it is difficult to find a single well-defined mechanical behaviour and a narrow range of values for the materials parameters. Instead, it is more likely that different behaviours can be defined by changing the conditions to which the biofilm is subjected (such as mechanical instruments, type of loading, temperature or biofilm growing conditions). We divide the findings into two main groups: macrorheological and microrheological studies. Macrorheological studies give great insights on the biofilm mechanical properties at a macroscopic scale through the measurement of bulk material parameters such as biofilm elastic moduli, viscosity and relaxation times. These measurements commonly involve the application of a controlled external force through mechanical tests (for example indenters or rheometers) or hydrodynamic means (such as flow cells). But, because of the microscale heterogeneity in the biofilm structure macroscale properties can only provide averages of the bulk material. Therefore, new technologies have been used and improved in order to reveal spatial distribution of biofilm viscoelastic parameters at the microscale. These includes atomic force microscopy (AFM); micromanipulators, microindenters, micro-cantilever, microfluidics chambers and particle-tracking microrheology (PTM). In addition, microrheological studies allow measurements of biofilm adhesive and cohesive strengths which are important parameters for assessing biofilm failure. Cohesive failure happens when the applied deformation disrupt only biofilm top layers leaving the underlying biofilm attached at the surface, whereas adhesive failure results in a completely detachment of the biofilm (Flemming et al. 2011). For a deeper description of the mechanical methods and instruments we suggest the following excellent reviews (Böl et al. 2013; Guélon et al. 2011).

3.5.1 MECHANICAL BACKGROUND

Investigating the mechanical properties of a generic material requires describing how the material deforms when an external force is applied. The main goal is to find the relationship (known as the "constitutive law") between the state of stress inside the material and the corresponding deformation. Each material has its own behaviour which is explored through standardized techniques and instruments. Depending on the way the deforming force is applied (Figure 3.4A), two stresses and relative deformations (strains) are considered:

- *Normal stress* (σ), when the sample is either compressed or stretched. It is defined as the ratio between the perpendicular component of the applied force and the initial area of the sample:

$$\sigma = \frac{F_{\perp}}{A_0} \tag{3.2}$$

- *Shear stress* (τ), when the sample is twisted. It is defined as the ratio between the parallel component of the applied force and the initial area of the sample:

$$\tau = \frac{F_{\parallel}}{A_0} \tag{3.3}$$

- Strain (ε), defined as the ratio between the change in length and the initial length of the sample:

$$\varepsilon = \frac{\Delta l}{l_0} \tag{3.4}$$

- *Shear strain* (γ), defined as the tangent of the angle (Φ) between the loaded and unloaded configurations:

$$\gamma = \tan(\phi) \tag{3.5}$$

Hookean solids and Newtonian fluids

Generally the behaviour of many solids can be approximated as pure elastic (Hookean solids) for infinitesimal deformations and, many liquids as pure viscous (Newtonian fluids) for low strain rates (Banks et al. 2010). If a deforming force is applied to an elastic solid, it deforms and relax back to its original shape when the force ceases (stores energy). In contrast, if a stress is applied to a viscous fluid, it won't resist to the stress applied and it will flow (deform) indefinitely without recovering the initial shape (dissipates energy). For Hookean solids the measured strain is always directly proportional to the stress applied (Hosford 2010)(Figure 3.4B) according to:

$$\sigma = E\varepsilon \tag{3.6}$$

$$\tau = G\gamma \tag{3.7}$$

where E and G are the Young's (or elastic) and shear modulus respectively. The units of E and G in the metric system are Newton per square metre (N/m^2) or Pascal (Pa).

The elastic constants G and E are closely related to each other:

$$G = \frac{E}{2(1+\upsilon)} \tag{3.8}$$

where ν is the Poisson's ratio of the material considered. The intuitive interpretation of the elastic parameters is simple: the higher their value, the stiffer the material will be (to achieve the same relative deformation it is necessary to supply the specimen with a greater force). E and G are commonly used to characterize the stiffness of an elastic material. Ceramic and metals are usually considered elastic linear materials and the Young's moduli generally are in the range 200-500 GPa and 50-210 GPa respectively (Cotterell and Williams 2010).

On the other hand, when a fluid is subjected to an applied shear and starts to flow, frictional forces always take place in the fluid as a result of cohesion movements between fluid particles. These forces give rise to a fluid property called viscosity (μ) which is a measure of the liquid resistance to flow (Gresham 2008). It has been found experimentally that the velocity at which the fluid is deformed (deformation rate, $\dot{\gamma}$) is directly proportional to the shear stress applied by the viscosity (Batchelor 2000):

$$\tau = \mu\dot{\gamma} \tag{3.9}$$

For a Newtonian fluid the viscosity is independent of the stress or strain rate, therefore Eq. (3.9) is a straight line (Figure 3.4C). Most low molecular weight substances and gases exhibit Newtonian flow characteristics. Commonly viscosity measurement of linear viscous fluids is performed with a viscometer. The viscosity in the metric system is expressed as Pa·s. Typical values of viscosity for scores of common fluids (at 25 °C) are: air (18.6 μPa·s), water (8.90×10^{-4} Pa·s), ethanol (1.074 mPa·s), olive oil (81 mPa·s) and pitch (2.3×10^{8} Pa·s).

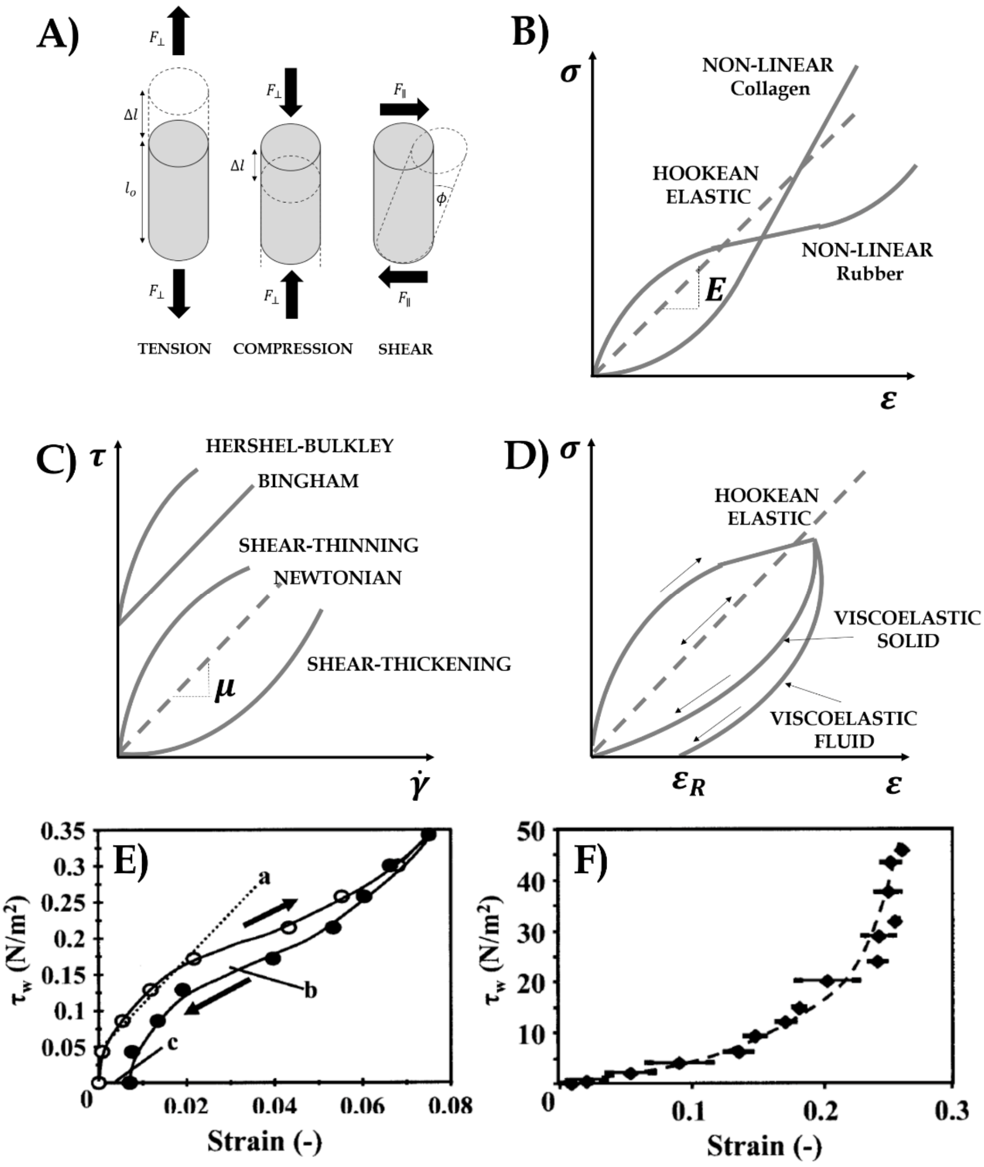

Figure 3.4. A) Schematic representation of a sample subjected to a normal stress, during compression or stretching, and to a shear stress. During a normal stress the force acts perpendicularly to the surface area (A_0) generating a compression (or stretching) of the sample (Δl). For a shear stress the force acts parallel to the surface area (A_0) creating a deformation angle Φ. B) Representation of stress-strain curves of Hookean-elastic and non-linear elastic materials for a compression (or tension) experiment. For a pure elastic material, the stress applied is proportional to the strain by the constant E (Eq. 3.6): the increase in its length (Δl) by an applied force doubles each time the force is doubled. Many biomaterials (such as collagen) display non-linear J-shaped curves: small increases in stress give large deformations, then at large deformations the material becomes stiffer. Many lightly cross-linked polymers (such as rubber) display an S-shaped curve. The initial part of the curve shows a decreasing in the stiffness with increasing load, than it shows the same behaviour as a J-shaped curve (adapted and redrawn from (Cambridge 2006)). C) Representation of stress-strain

curves of Newtonian and non-Newtonian fluids. For a pure viscous material, the viscosity μ doesn't vary with the shear rate as it happens for a non-Newtonian material. The "apparent" fluid viscosity (μ_{app}*) can decrease (shear-thinning) or increase (shear-thickening) with increasing* $\dot{\gamma}$*. Instead a visco-plastic fluid starts to flow only after a certain yield stress τ* is exceeded. The fluid then can show either linear (Bingham plastic) or non-Newtonian behaviour (Hershel-Bulkley) (adapted and redrawn from (Chhabra 2010)). D) Illustration of a pure elastic behaviour with full energy recovery compared to a viscoelastic behaviour. The energy dissipation generates hysteresis in a viscoelastic solid or a permanent deformation (*ε_R*) in a viscoelastic fluid (adapted and redrawn from (Meyers and Chawla 2009)). E) Stress-strain curve of P. aeruginosa FRD1 strain biofilm grown under laminar flow showing a non-linear S-shaped curve when exposed to low-shear stresses. Biofilm also exhibits viscoelastic energy dissipation in the loading (a) and unloading (b) curves and residual strain (c) (image used with permission of author (Klapper et al. 2002)). F) Stress-strain curve of the mucoid P. aeruginosa FRD1 cystic fibrosis isolate biofilm grown under laminar flow showing a non-linear elastic J-shaped curve when exposed to high-shear stresses (image used with permission of author (Klapper et al. 2002)).*

Non-linear behaviour

Hookean and Newtonian behaviour are idealizations. In reality, most solids and fluids, mainly for high stress or strains, present a non-linear behaviour, i.e. σ-ε or τ- relationships are not linear. Rubber and various living tissues are examples of non-linear elastic solids (Figure 3.4B). For small stresses or strains, the response will be linear and therefore linear elastic theory can be applied. "Apparent" elastic parameters (E_{app} and G_{app}) are estimated from the linear region of the stress-strain curves. For instance, E_{app} of polymers and rubbers range 1-3 GPa and 3-100 MPa respectively. For comparison, living tissues have the following "apparent" elastic moduli: pig brain (260–490 Pa), human liver (640 Pa), rat skeletal muscle (100 kPa) and bovine cartilage (950 kPa). On the other hand, biological fluids (blood, saliva), polymeric melts and solutions and fluid and semisolid foods (honey, peanut butter) are examples of non-linear viscous fluids (Figure 3.4C). This type of fluids shows an "apparent" viscosity (μ_{app}), which varies with the shear rate ($\dot{\gamma}$). The study of complex non-linear fluids is called rheology. Rheometers are the common instruments used to measure non-linear fluids behaviour and viscosity dependence on the applied stress (or strain). According to the η-relationship, we can classify this type of fluid into two classes (Chhabra 2010): 1) *shear-thinning* fluids, where the fluid viscosity falls with increasing $\dot{\gamma}$, and *shear-thickening* fluids, which exhibit an apparent viscosity which progressively rises with increasing $\dot{\gamma}$. Another peculiar non-linear behaviour is the so called *visco-plastic*, where a fluid behaves like an elastic solid below a certain threshold stress value (yield stress), but when the yield stress is exceeded, the fluid starts to behave like a fluid. For stresses beyond the yield stress, if the dependence between σ and $\dot{\gamma}$ is linear (Newtonian), the fluid is called *Bingham plastic*, instead if the dependence displays a shear-thinning behaviour, the fluid is called *Hershel-Bulkley*.

Viscoelasticity

Biofilms, as well as polymers, soft tissues and biological fluids present not only a non-linear behaviour but they are also viscoelastic. Viscoelasticity means the material behaves either as an elastic solid or a viscous fluid depending how fast it is deformed and how quickly it recovers (Banks et al. 2010). In other words, viscoelastic materials respond to an instantaneous stress with a deformation which varies in time. In literature, a viscoelastic material can be classified as viscoelastic fluid or viscoelastic solid. Despite the similarity of the two names, these material behaviours are quite different. A viscoelastic solid is a true solid that show a retarded response to stress (in this case “viscoelasticity” refers to viscous retardation), whereas a viscoelastic fluid is a material that acts like a solid on short time scales and a fluid on longer time scales (in this case “viscoelasticity” refers to adding elastic behaviour to a viscous fluid). Because of the viscous component, viscoelastic materials do not store 100% of the energy under deformation. For a viscoelastic solid the forward and backward deformation curves are different but initial and final deformation are the same (hysteresis) (Figure 3.4D). Instead, for a viscoelastic fluid the initial and final deformation don’t coincide and the material presents a residual deformation.

If the material is subjected to a small deformation (or stresses), the material response is considered to be linear viscoelastic or in the linear viscoelastic range (Ponnamma and Thomas 2014). Linear viscoelasticity is the simplest response of a viscoelastic material and is based on the Boltzmann superposition principle. According to this theory the material response is a function of the entire loading history and each loading makes independent contribution to the final behaviour. Following these principles, the stress-strain relationship for a linear viscoelastic material is expressed by the so called Boltzmann-Volterra equation (Liu 2013):

$$\sigma(t) = \int_{-\infty}^{t} G(t - t')\varepsilon(t')dt' \tag{3.10}$$

where G(t – t’) is the defined as the relaxation modulus. The stress is linked to the history of deformation: ε is a function of t’ and therefore represents the entire deformation from the past ($-\infty$) to the actual time (t). The way in which σ is linked to ε is determined by the function G which must obey the condition of “vanishing memory”: i.e., the more the deformation is in the past, less the material remembers (Banyavichyus et al. 1981).

Rheology of viscoelastic materials

The mechanical characterization of viscoelastic materials consists in performing specific tests in order to enable the observation of the time dependency and non-linearity of the material response. Three main rheological tests are commonly performed: creep, stress-relaxation and dynamic testing, and all of these tests have been performed on biofilms. Creep and stress-relaxation are used for studying material viscoelastic response over long time scales. For testing the short time response behaviour, dynamic tests which use oscillating loads are performed.

Creep and relaxation tests

The stress-relaxation test is achieved by producing a constant deformation to the material and measuring the relaxation of the internal stress which was built up during the initial deformation (Figure 3.5A). The resulting stress for a viscoelastic solids slowly relax and reach an equilibrium value (residual stress, σ_R), while for viscoelastic fluids the stress goes to zero (Irgens 2008). Instead the creep test consists of measuring the time dependent strain resulting from the application of a steady uniaxial stress (Figure 3.5B). In this case, the strain increases until approaching an asymptotic level. If the load is removed, the resulting strain slowly decreases until zero for a viscoelastic solid, while for viscoelastic fluid the resulting ε decreases until an equilibrium value (residual strain, ε_R) (Irgens 2008).

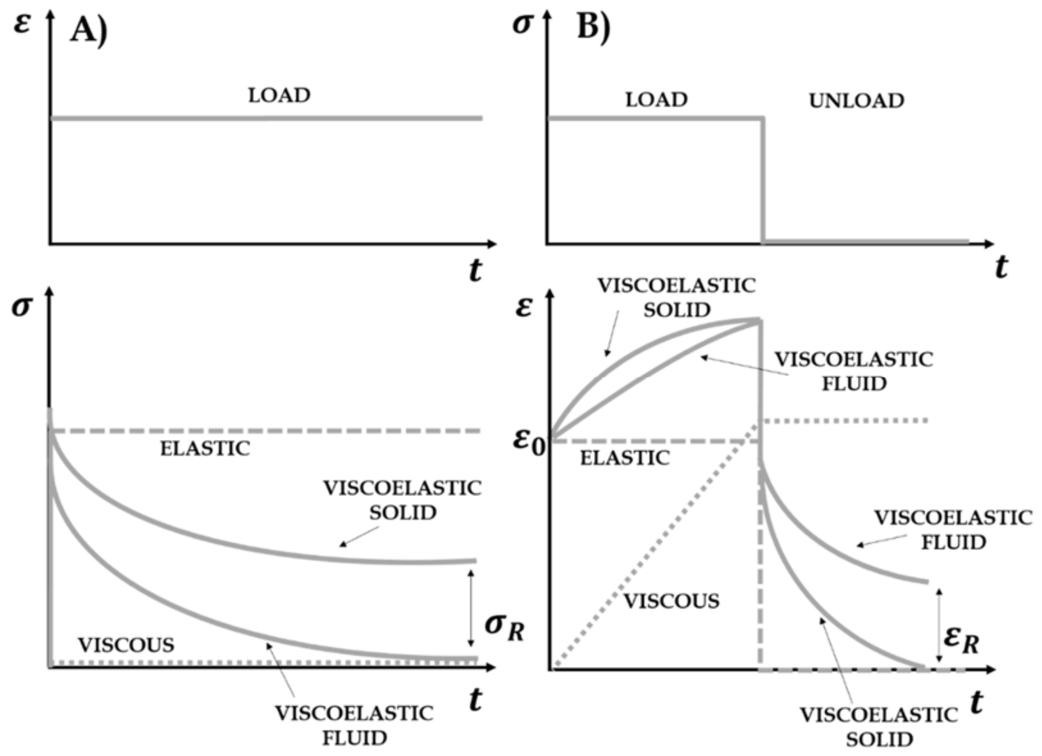

Figure 3.5. Schematic representation example of a stress relaxation test for a pure elastic, pure viscous and viscoelastic material. When a constant strain is applied (LOAD) over a period of time to a viscoelastic sample, the resulting stress decreases over time until it reaches an equilibrium value σ_R *(viscoelastic solid), or it goes to zero (viscoelastic fluid) (adapted and redrawn from (Lakes 1998) and (Irgens 2008)). B) Schematic representation example of a creep and recovery test for a pure elastic, pure viscous and viscoelastic material. When a constant stress is applied to a viscoelastic sample (LOAD), after an immediate elastic response (*ε_0*) the resulting strain increases over time (viscoelastic fluids) or approaches an asymptotic level (viscoelastic solid). When the stress is removed (UNLOAD), the strain immediately decreases (elastic behaviour) and then gradually decreases to a residual strain* ε_R *(viscoelastic fluid) or to zero (viscoelastic solid) (adapted and redrawn from (Lakes 1998) and (Irgens 2008)).*

Dynamic test

Dynamic tests consist in subjecting the sample to a controlled small, sinusoidal oscillatory strain and measuring the resulting stress. In purely elastic solids the stress and strain are in phase (store energy) (Figure 3.6A). On the other hand, in purely viscous fluids, the stress and strain have a 90º phase lag (dissipate energy). The reason for this 90º lag (known as the phase angle (δ)) is that, as we saw in Eq. (3.6) and (3.7), for an ideal elastic solid the maximum strain is proportional to the maximum stress. However, as we see in Eq. (3.9), for an ideal Newtonian liquid the maximum stress is proportional to the rate of strain. Since the rate of strain (i.e. the change in strain as a function of time) is effectively the first derivative of a sinusoidal oscillation (i.e. a cosine) then the rate of strain will be zero when the absolute value of strain is at a maximum. Viscoelastic materials behave somewhere in the middle and therefore display an intermediate phase angle (Schramm 1994). We can represent oscillatory stress and strain as:

$$\varepsilon(t) = \varepsilon_0 \sin(\omega t) \tag{3.11}$$

$$\sigma(t) = \sigma_0 \sin(\omega t + \delta) \tag{3.12}$$

By applying the Fourier Transform to Eq. (3.10) we obtain:

$$\hat{\sigma}(\omega) = \hat{G}(\omega) \cdot \hat{\varepsilon}(\omega) \tag{3.13}$$

All transformed functions are complex numbers. The term $\hat{G}(\omega)$ is the Complex modulus and can be rewritten as:

$$\hat{G}(\omega) = G' + i \cdot G'' \tag{3.14}$$

where the real part (Storage modulus) indicates the material ability to accumulate elastic energy while the Imaginary part (Loss modulus), describes the ability to dissipate energy.

Substituting Eq. (3.10) in Eq. (3.13) we obtain:

$$(t) = \varepsilon_0 [G' \sin(\omega t) + G'' \cos(\omega t)] \tag{3.15}$$

Using the formula for the sine of a sum Eq. (3.15) yields the following for the Storage and Loss moduli:

$$G' = \frac{\sigma_0}{\varepsilon_0} \cos(\delta) \tag{3.16}$$

$$G'' = \frac{\sigma_0}{\varepsilon_0} \sin(\delta) \tag{3.17}$$

By determining G’ and G”, we can understand if a viscoelastic material acts in a more viscous or more elastic manner in response to a given applied stress (Figure 3.6B).

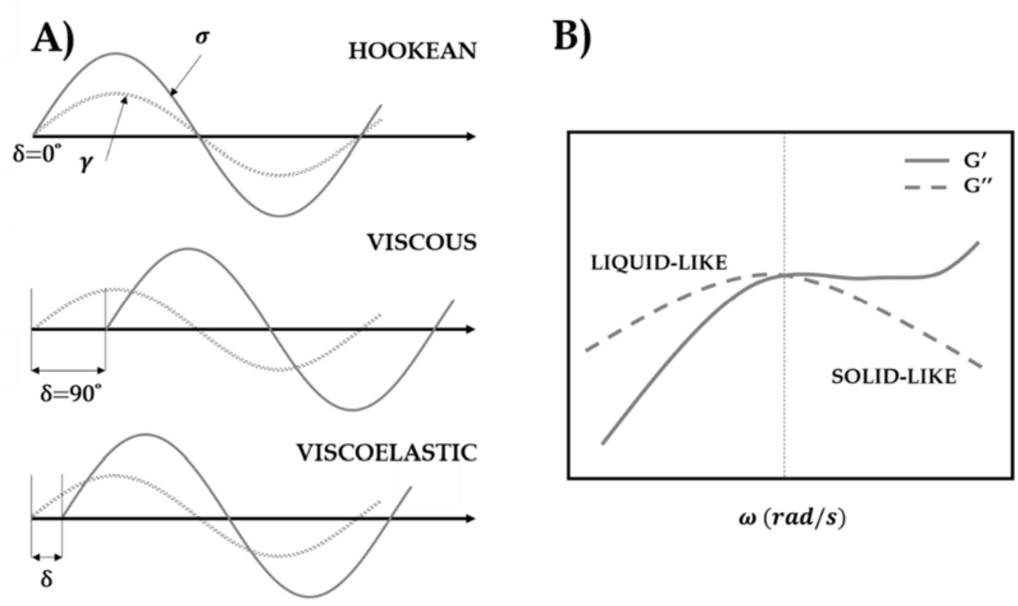

Figure 3.6. A) Schematic representation of the measured stress in response to an oscillatory strain for a Hookean solid, a Newtonian fluid and a viscoelastic material. For a pure elastic solid, the stress is in phase with the applied strain (δ=0º). For a pure viscous fluid, the strain and the stress are out of phase (δ=90º). For a viscoelastic materials the stress-strain response is between 0 º and 90º (adapted and redrawn from (Schramm 1994)). B) Frequency (ω) dependence of G’ and G’’ for a generic polymer solution. For low strain rates, the material behaves more like a liquid (G’’ > G’), instead for high strain rates the material response becomes solid-like (G'> G") (adapted and redrawn from (Mezger 2006)).

Modelling viscoelasticity

A mathematical model describing the response of a viscoelastic material (such as biofilms) during creep and relaxation experiments is essential for predicting deformation, failure and detachment. Such models, called rheological models, are linear networks of two fundamental elements: elastic solid “Hookean” springs () and viscous liquid “Newtonian” dashpots () (Barnes et al. 1989). The first represents the purely elastic response, expressed by Eq. (3.6), the second the dissipative and delayed response, expressed by Eq. (3.9). The simplest viscoelastic models consist of one single spring and one single dashpot in series (Maxwell model) or in parallel (Kelvin-Voigt model). The Kelvin-Voigt model displays an exponential strain creep (viscoelastic solids) (Figure 3.7A), whereas the Maxwell model exhibits an exponential relaxation (viscoelastic liquids) (Figure 3.7B). Maxwell and Kelvin models are adequate for qualitative and conceptual analyses. Complex viscoelastic materials like biofilms are modelled combining multiple elements of Kelvin-Voigt and Maxwell. The Burger's model and the generalized Maxwell model are the most used in literature. The Burger model, which results in a series combination of a Maxwell element with a Voigt element, is used to model the creep response (Figure 3.7C-D). The generalized Maxwell model, which is a combination of multiple Maxwell elements in parallel, is used to model the relaxation response (Figure 3.7E-F). As a result, a final stress relaxation time coefficient (t_r), which estimates the time necessary to pass from the initial stress at the beginning of the test to the asymptotic minimal value of the stress, is obtained.

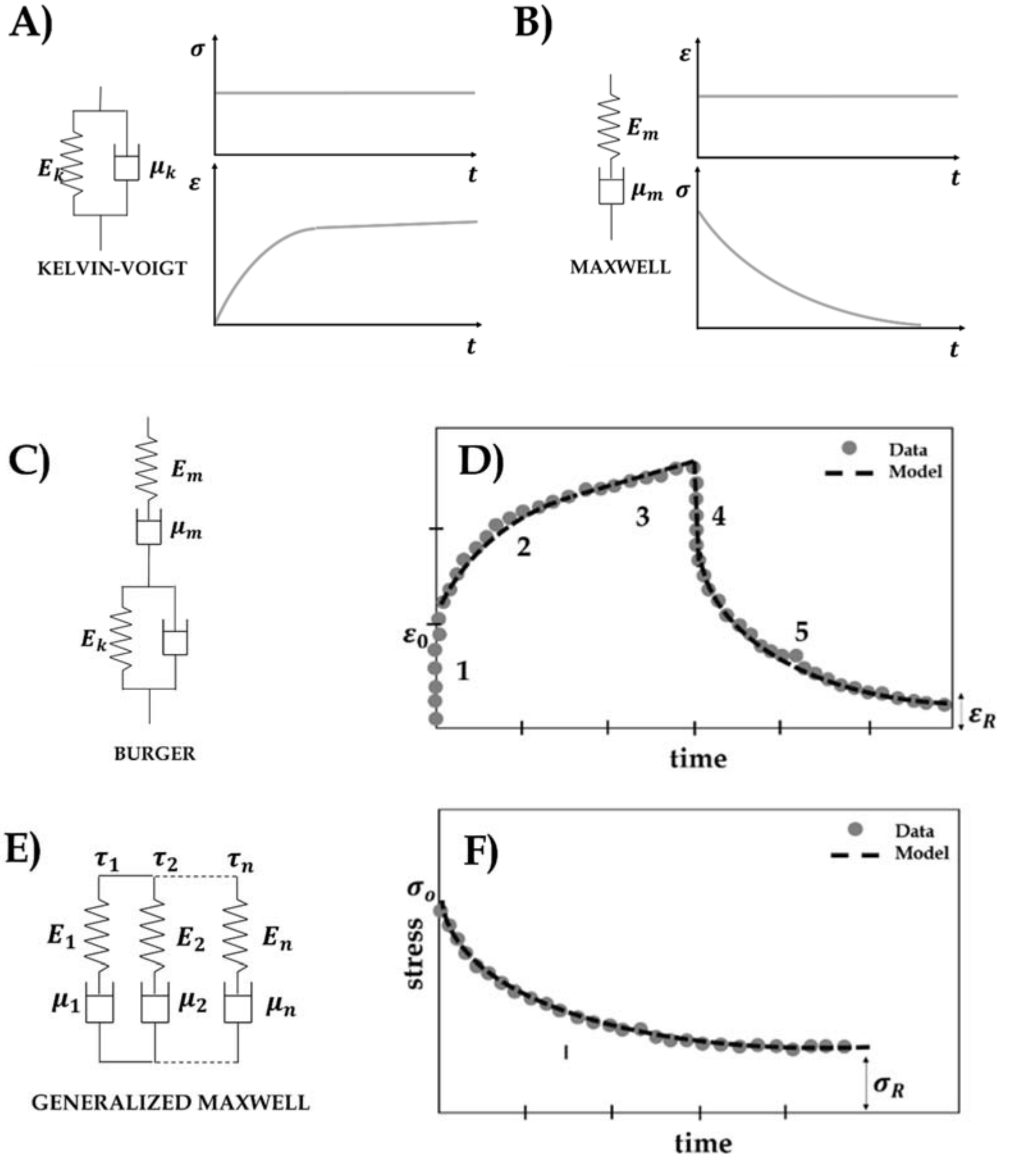

Figure 3.7. A) Schematic representation of Kelvin-Voigt model and the relative creep curve. When a constant stress is applied (upper graph), the dashpot μk in parallel with the spring E_k dampens the elastic response causing a retarded viscoelastic strain (adapted and redrawn from (Reddy 2013)). B) Schematic representation of the Maxwell model and the relative stress-relaxation curve. When a constant strain is applied (upper graph), there is an immediate elastic response (represented by the spring E_m) followed by a retarded relaxation in the stress (caused by the dashpot μ_m) until it reaches zero (adapted and redrawn from (Reddy 2013)). C) Graphic representation for Burger's model. This model is generated by putting a Maxwell model in series with a Kelvin-Voigt model. E_m and E_k are the elastic elements while μ_m and μ_k are the viscous ones. Spring respond instantaneously to an applied stress (or strain), instead dashpot reduces the reaction speed. D) Illustration of a creep and recovery curve of a mixed-culture biofilm after rheometer analysis fitted with the Burger model (adapted and redrawn from (Towler et al. 2003)). The instantaneous elastic strain and recovery (region 1 and 4)

corresponds to E_m and E_k. The retarded viscoelastic strain and recovery (region 2 and 5) are represented by $\mu 1$ and the Kelvin-Voigt model. The purely viscous response (region 3) is represented by μ_m. E) Schematics of a generalized n-element Maxwell model. En represent the spring constants and τn the relaxation time constants, which are equal to μ_n/E_n. F) Illustration of a measured stress relaxation of a P. aeruginosa biofilm fitted with five Maxwell elements (adapted and redrawn from(Peterson et al. 2013)).

3.5.2 MACRORHEOLOGICAL STUDIES

One of the first reports on biofilms viscoelasticity was in 1999 when Stoodley et al. performed rheological tests on mixed culture biofilms grown in a microfluids biofilm reactor (Stoodley et al. 1999a). They measured the elongation of biofilm clusters caused by elevations in liquid shear stress. Creep and stress-strain curves demonstrated biofilms behave as viscoelastic solids when the applied fluid shear stress is below or near the stresses at which the biofilm was grown (τ=5.09 N/m2), while at higher values of shear stress the biofilm can yield and behave as a viscoelastic fluid. This trend is similar to that of a non-Newtonian fluid. They also estimated G_{app} and E_{app} which were 27 Pa and in the range of 17 to 40 N/m^2 respectively. Biofilm viscoelastic fluid-like behaviour was also assessed on various *P. aeruginosa* biofilms grown in a flow cell subjected to laminar and turbulent flows (Klapper et al. 2002; Stoodley et al. 2002a). Stress-strain curves showed the biofilms had an elastic-solid behaviour for short time scales but a linear viscous fluid like behaviour for long time scales. In addition, *P. aeruginosa* FRD1 strain biofilm grown under laminar flow displayed viscoelastic behaviour showing non-linear S-shaped curved with hysteresis and residual strain for low-shear stresses (Figure 3.4E), and a non-linear J-shaped curve for high-shear stresses (Figure 3.4F). Instead, *P. aeruginosa* PAO1 strain grown under turbulent flow showed a linear elastic response for low-shear stresses, while a non-linear viscoelastic response at high-shear stresses. The measured apparent shear modulus varied from 1 to 280 N/m^2 and increased with the applied shear. These findings demonstrated the high dependence of the biofilm viscoelastic properties on the biofilm growing conditions, applied force and bacterial strain. Uniaxial compression experiments on *P. aeruginosa* biofilms (Körstgens et al. 2001), performed with a rheometer, showed elastic-Hookean behaviour (E_{app}= 6500 ± 500 Pa) for low loadings until a critical yield stress (σ^*= 980 ± 50 Pa), then fluid-like behaviour was observed afterwards. In 2003, Towler at al. performed rheometers shear creep tests on mixed culture biofilms (Towler et al. 2003). The creep curves obtained from the experiments presented a residual strain when the load was removed, indicating viscoelastic fluid behaviour (Figure 3.7D). The measured biofilm G_{app} and μ_{app} were in the range of 0.2-24 Pa and 10-3000 Pa respectively. In a study of Vinogradov et al. (Vinogradov et al. 2004) the static and dynamic (sinusoidal oscillations) responses of *S.*

mutans biofilms were studied performing rheological creep tests. Static creep curves showed a viscoelastic fluid behaviour with biofilm apparent shear modulus and viscosity values of 1.9 ± 3.8 x 10^2 Pa and 2.8 ± 6.4 x 10^2 Pa respectively. In addition, the decrease of the complex viscosity (η^*) with the frequency measured from dynamic creep tests suggested a shear-thinning viscoelastic fluid-like behaviour, similar to a polymeric solution (Menard, 1999). In 2005, a glass capillary system was used to assess the viscoelastic properties of *S. aureus* biofilms (Rupp et al. 2005) by measuring the deformation of individual biofilm clusters at different wall shear stresses values over a short time period. The resultant stress-strain and creep curves demonstrated biofilm viscoelastic behaviour in order to adapt the structure to different shear stresses. Stress-strain curves yielded a G_{app} of 4.9 ± 3.7 Pa and a μ_{app} of 3,500 ± 2,900 Pa/s. An interesting study of Lahaye and co-authors consisted in comparing the viscoelastic properties of extracted EPS solutions from *P. mirabili*s biofilms (Lahaye et al. 2007). They discovered that the water content inside the biofilm could vary the EPS viscoelastic behaviour by changing the types of interaction between the polymer chains. In 2009, Paramonova and co-authors performed low-load compression tests (with a LLCT instrument) on a wide range of biofilm species (Paramonova et al. 2009a; Paramonova et al. 2009b). In particular, stress-strain curves obtained from single or double species oral biofilms (Paramonova et al. 2009a) showed both a non-linear behaviour with E_{app} ranging from 17 to 62 Pa and 29 to 182 Pa respectively. In the same year, Koza et al. measured the viscoelastic properties of a *P. fluorescens* biofilm air–liquid interface through amplitude sweep tests with an oscillatory rheometer (Koza et al. 2009). A loss factor (which is the ratio between G' and G'') less than 1 determined biofilms viscoelastic solid-like behaviour until a threshold stress value of 0.028 Pa. In addition, an apparent storage modulus of 0.75±0.16 Pa and an apparent viscosity of 0.24±0.05 Pa were obtained from the linear viscoelastic region. Afterwards, the G' decreased with increasing the shear stress indicating a shear-thinning behaviour. Similar results were obtained from the group of Ribbeck on *P. aeruginosa* biofilms (Lieleg et al. 2011). They assessed biofilm viscoelastic behaviour at large deformations discovering that biofilms are able to fully regain their initial stiffness after a period of recovery. This observation can explain the biofilm capability of dispersing in clusters rather than totally detaching from surfaces when subjected to high shear forces. In addition, they assessed the influence of chemical perturbation on the properties of *P. aeruginosa* biofilms. They found that biofilm elasticity was increased when adding multivalent cations (such as Fe^{3+} or Al^{3+}), decreased when adding citric acid or unchanged when adding citric acid and Fe^{3+} together. An increase or decrease in the cross linking interactions between trivalent ions and negatively charged groups in the EPS could possibly strength or weaken biofilm structure. These results are crucial for developing new strategies which consider the use of chemicals for biofilms removal. In 2012, Rmaile et al. (Rmaile et al. 2013) tested *S. mutans* biofilm viscoelasticity performing uniaxial indentation test with a Bose machine. They also assessed the effect of sugar concentration, osmotic-inducing agent (PEG-8000) and chelating agent (EDTA) on biofilm elasticity. Non-linear force-displacement curves and stress-relaxation measurements confirmed the viscoelastic behaviour of the biofilm samples. The biofilm elastic modulus and relaxation time were approximately 280 Pa and 11 sec. Osmotic and higher sugar concentration in the growth medium caused an increase in biofilm stiffness, while chelating effects caused a decrease. Since biofilms metabolize sugars to produce EPS glucans, a higher sugar supply will lead to a higher EPS production and therefore to a stiffer biofilm. Increasing stiffness due to the osmotic effects can be explained by "dewatering" of the biofilm. Similar results were obtained from Waters and co-authors who studied the mechanical properties through dynamic rheological tests of *in situ S. mutans* biofilms grown in the presence or absence of sucrose (Waters et al. 2013). Complex moduli measurements showed biofilms grown in the presence of sucrose behaved more like soft elastic solid materials than viscoelastic fluids enhancing the importance of the EPS matrix composition on the biofilm mechanical properties. More recently, rheological characterisation of biofouling layers under steady shear flow demonstrated biofilms thixotropic, shear-thinning viscoelastic behaviour for which solid-like behaviour appeared below a yield stress (τ^*=10 Pa) and fluidity at elevated values of τ^* (Patsios et al. 2015). The G' values (40 - 200 Pa) were bigger than those of G″ (20 - 30 Pa) indicating the marked elastic behaviour of the biofouling layer. Hysteresis in the stress-strain curves of heterotopic biofilms performing time-lapsed deformation experiments at different shear stresses using optical coherence tomography confirmed a viscoelastic trend (Blauert et al. 2015). E_{app} (36.0 ± 2.6 Pa) was estimated from the linear part of the stress-strain curve while G_{app} (29.7 ± 1.7 Pa) from the OCT B-scans. *In situ* rheological characterisation of *S. epidermidis* biofilms probed through small-amplitude oscillatory deformation and non-linear creep tests showed that osmotic pressure (in terms of NaCl concentration) and temperature altered biofilm mechanical properties (Pavlovsky et al. 2013). In particular biofilms both showed a non-monotonic relationship between stiffness and the NaCl concentration and a hysteresis of the viscoelastic moduli with an increase in temperature. These finding advocates that biofilms viscoelastic properties are strongly determined by local environmental conditions. Researchers also showed that the storage modulus (G'~10 Pa), unlike the loss modulus (G''~1 Pa), exhibited a power-law increase at increasing angular frequency. Similar results were obtained from the same group which showed a significant decrease in the yield stress and *S. epidermidis* biofilm elastic modulus under increasing temperatures (Pavlovsky et al. 2015). In addition, they showed a correlation between the effect of temperature on cell viability (higher temperature caused a drastic decrease in cell viability) and the weakening of the biofilm. This could open new doors for controlling biofilm such as the development of non-invasive temperature-based strategies for the treatment of biofilm infections in the medical field.

3.5.3 MICROREHOLOGICAL STUDIES

In 1998, a micromanipulator with a T-shaped probe was developed by Chen and co-authors to measure the adhesive strength (σ_A), defined as the work required to detach the biofilm from the surface, of 29-days olds *P. fluorescens* biofilms grown under different fluid velocities (Chen et al. 1998). Investigators reported that the biofilm adhesive strength (σ_A = 0.05-0.2 J/m^2) increased as the fluid velocity increased (u=0.6–1.6 m/s). In a later study using the same technique, Chen and co-authors reported that the adhesive strength of *P. fluorescens* biofilms increased as the biofilm age, fluid velocity, pH and roughness increased (Chen et al. 2005). Interestingly, the biofilm adhesive strength also increased with an increase in the glucose concentration, but when it exceeded 30 mg/l the adhesive strength decreased again. The glucose-adhesive strength non-linear relationship was explained suggesting that a too high glucose concentration might inhibit the irreversible adhesion and lead to a lower adhesive strength. In 2006, Cense and co-authors, using a microindenter apparatus to measure *S. mutans* biofilms failure confirmed the extracellular polysaccharide matrix pivotal role in the biofilm tensile strength (Cense et al. 2006a). In addition, biofilms exhibited a viscoelastic solid-like behaviour during stress-relaxation tests. This conclusion differed from that of main macrorheological studies previously reported (where *S. mutans* biofilm was characterized as a viscoelastic liquid) enlightening the heterogeneity of the biofilm at different scales. They also discovered that the biofilm cells remained undamaged after testing enlightening EPS matrix role on the biofilm strength. One year later, particle-tracking microrheology (PTM) on *S. aureus* biofilms exhibited different mechanical environments between individual bacteria within the same biofilm and a dependence of the biofilm stiffness on the growth conditions – i.e. hardening during growth, and softening during starvation (Rogers et al. 2008). In 2009, Hohne et al. developed a flexible microfluidic rheometer which enabled measurements of *S. epidermidis* and *K. pneumonia* biofilms mechanical properties at the microscale (Hohne et al. 2009). Both biofilms exhibited typical non-linear exponential stress–strain trends but the *S. epidermidis* biofilm was much stiffer (E_{app}=3.2 kPa) than *K. pneumonia* biofilm (E_{app}=1.1 kPa) demonstrating the variability in the mechanical properties in changing biofilm strain. Video holographic PTM enabled the measurements of the mechanical properties of a water-soluble and -insoluble polysaccharides of *S. mutans* biofilms (Cheong et al. 2009). The biofilm's water-soluble polysaccharides formed a shear-thinning fluid roughly ten times more viscous than water. By contrast, the N- type fraction formed an elastic gel with a storage modulus of 10 Pa but strongly shear-thinning, as indicated by its dynamic viscosity. These studies show how the EPS functional roles are strictly connected with the macroscale biofilm physical and mechanical properties. Aggarwal et al. (Aggarwal et al. 2010) measured cohesive strength (σ_C) of *P. aeruginosa* and *S. epidermidis* performing tensile tests modifying the common microcantilever method of Poppele and Hozalski (Poppele and Hozalski 2003). The high variability of the measured cohesive strength values (59 - 18,900 Pa and 61 - 5,840 Pa for the *P. aeruginosa* and the *S. epidermidis* biofilms respectively) enlightened biofilm structural heterogeneity at the microscale. In another study, they measured the ultimate tensile strength and the elastic modulus of *S. epidermidis* biofilms using the same method (Aggarwal and Hozalski 2010; Aggarwal and Hozalski 2012). Results showed biofilm viscoelastic behaviour characterized by a non-constant Young modulus which increases with the strain rate applied. In 2012, using magnetic tweezers and micron-sized magnetic particles Galy et al. obtained a 3D mapping of *E. coli* biofilm viscoelastic properties (Galy et al. 2012). A significant variation in the local mechanical properties within the structure revealed the three-dimensional mechanical heterogeneity of a biofilm. More recently, Chew et al. tracking the Brownian motion of beads within the biofilm (particle-tracking microrheology) discovered that increasing or decreasing the amount of specific exopolysaccharides inside *P. aeruginosa* biofilms can change biofilm behaviour from more elastic to more viscous (Chew et al. 2014). One of the first AFM measurement on biofilms was performed by Fang and co-authors by measuring AFM tip-cell interaction forces of sulphate-reducing bacteria of an early stage 6h-old biofilm (Fang et al. 2000). Adhesion forces were found to be 25% higher at cell–cell and cell–substratum interface than on the middle of cells. Similar results were obtained in the study of Oh et al. on *E. coli* biofilms grown on glass slides (Oh et al. 2007). Force-distance curves showed a higher adhesion at the top of the bacterium surface (σ_A=122.65 pN) than at the glass surface (σ_A=51.79 pN). In addition, investigators also showed biofilm elasticity on the cell surface increased as biofilm became mature, suggesting that EPS could considerably enhancing the bacteria binding to surface. The elastic properties of three gram-negative (*E. coli* ML35, *E. coli* ZK1056 and *P. putida*) and two gram-positive (*B. subtilis* and *M. luteus*) bacterial strains were assessed calculating cellular spring constants (k_{cell}) from AFM force-distance curves (Volle et al. 2008). All the bacteria strains showed high k_{cell} values (0.16 to 0.41 N/m), demonstrating bacteria rigidity. In addition, extracellular polymeric substances were observed covering the biofilm cells outer layer, facilitating bacterial adhesion. In 2009, Oh end co-authors used AFM operating in a force mode to assess the influence of different substrates (aluminium, steel, rubber, and polypropylene) on 3 days-old *P. aeruginosa* biofilms attachment (Oh et al. 2009). The results demonstrated a higher bacteria adherence to polypropylene than to the other substrates (because of higher surface roughness). The researches also subjected biofilms to hot water treatment to measure changes in biofilm adhesion force which significantly decreased. Most of extra-cellular matrix was removed after water exposure, enlightening again matrix pivotal role in the biofilm attachment process. Lau et al combined microbead force spectroscopy with atomic force microscopy showing significant changes in adhesion and viscoelastic properties of a *P. aeruginosa* PAO1 strain compared to a derived mutant *wapR*, which has defective expression of lipopolysaccharides (Lau et al. 2009). Biofilm biophysical properties, genetic, growth and environmental factors are important aspects which need to be considered in order to understand bacterial biofilms persistence.

3.5.4 BIOFILM DETACHMENT

Environmental changes such as fluid velocity or shear stresses and chemical cues cause microbes in the biofilm to detach and disperse in the bulk fluid. Biofilm dispersal is of fundamental importance in the proliferation of biofilms, because detached cells could potentially transmit pathogens into the blood stream and cause bacteraemia and endocarditis (Lu 2009) or release contaminating bacteria into the environment as seen in showers and cooling towers with legionella. Viscoelastic features such as elongation and recoil allows biofilms to tolerate even high-velocity fluid flows without detaching from the surface (Figure 3.8). A wide range of mechanical parameters such as cohesive or adhesion strength have been quantified in order to understand how different hydrodynamic conditions affect biofilm detachment. Parallel plate flow chamber reactor systems represent the traditional technique to measure such values (Ohashi and Harada 1994; Stoodley et al. 2002a; Stoodley et al. 2001). Flow devices such as jet impingement (Deshpande and Vaishnav 1983; Vaishnav et al. 1983) and fluid dynamic gauging (Chew et al. 2004; Tuladhar et al. 2000) were developed to assess biofilm adhesion under well-defined hydrodynamic conditions. Micro jet impingement (MJI) on *S. mutans* biofilms grown in different sucrose concentrations (0.1%, 0.5% and 1%) demonstrated that sucrose affects biofilm adhesion strength (Kreth et al. 2004). In particular, the shear stress (measured from the zone of clearance) was about 20-fold higher between 0.1% and 0.5% sucrose and 1.6-fold between 0.5% and 1% sucrose. In 2005, Bayoudh and co-authors investigated the adhesion strength of *P. stutzeri* onto hydrophilic and hydrophobic glass surfaces using laminar microjet impingement at various Re numbers and exposure time combinations (Bayoudh et al. 2005). Researchers found that bacterial detachment strength decreased significantly with increasing exposure time and flow velocity. In addition, adhesion strength values measured for the biofilm grown onto the hydrophobic glass surface (343.9 Pa and 7,084 kPa at Re=500 and Re=1,500 respectively) were higher than those measured for the biofilm grown on hydrophilic ones (167.5 Pa and 3,347 kPa at Re=500and Re=1,500 respectively). Similar experiments were performed on *Synechococcus* biofilms grown on three different substrata over a 4-week period but exposed to a pressure mode fluid dynamic gauging in order to measure monitor biofilm strength (Salley et al. 2012). Interestingly, biofilm formed on stainless steel (SS) and on an indium tinoxide (ITO) on a polyethylene terephthalate (PET) substratum detached by cohesive mechanisms, whereas those on glass were removed by adhesive failure. Investigators related this difference to a change in substratum surface energies. Möhle et al. used fluid dynamic gauging to determine the cohesive strength of a heterotrophic mixed culture biofilms (Möhle et al. 2007). They found that biofilm thickness depended on biofilm hydrodynamic-growth conditions (shear stress) while biofilm cohesive strength (6.0 and 7.7 N $m^{-}2$) was independent. Interestingly, CLSM imaging after gauging showed a remaining layer of EPS glycoconjugates at the surface which could play an important role in biofilm mechanical strength. Paul and co-authors exposed biofilms grown under different hydrodynamic conditions to various shear stresses from a Couette Taylor Reactor (Paul et al. 2012). After a biofilm upper part detachment, which depended on the shear stress applied during biofilm grow, researchers discovered the presence of a basal layer that withstood shear stresses up to 13 Pa by compressing itself rather than detaching. Similar results were found by Hwang and co-authors on 64 and 116 h old *S. mutans* biofilms (Hwang et al. 2014). Researcher measured biofilm mechanical strength using a shear-induced biofilm mechanical strength testing combined with confocal microscopy and biomass measurements. After an initial 50% biofilm removal the remaining biofilm resistance increased considerably even with a 10-fold increase in the shear stress. Confocal images showing EPS spatial distribution particularly near the surface and mechanical strength testing on biofilms treated with dextranase demonstrated EPS matrix role in modulation of biofilm mechanical stability. In 2012, Abe and co-authors imaged young drinking water biofilms in order to quantify the mechanical detachment shear stress exerted by an AFM tip (Abe et al. 2012). They developed a new technique consisting of a consecutive AFM scan were the biofilm itself was removed "layer by layer" by increasing the applied force. Therefore, the cohesiveness of the biofilm removed layer was lower than the tip applied stress while the remaining biofilm was stronger. Interestingly, high shear stress values (τ=100 kPa) were measured for removing biofilm clusters greater than 200 μm^3 which means that biofilms cleaning in industrial sectors (pipes, hulls) might be not always efficient. The influence of surface roughness and temperature on *E. coli* biofilm detachment using a flow chamber was investigated by Fink at al. (Fink et al.

2015). Researchers found that more bacterial cells adhered on electro polished samples than on brushed samples and that the increasing liquid temperature and flow velocity increased biofilm detachment.

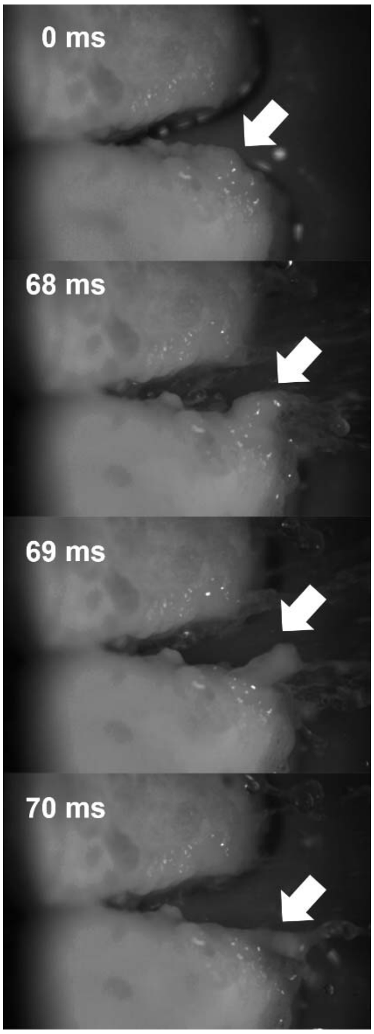

Figure 3.8. Four frames from a high-speed camera movie showing the viscoelastic elongation of a 3 days-old S. mutans dental biofilm, grown between two central incisors from a typodont model, during high-velocity (u>60 m/s) microspray exposure. A biofilm cluster (white arrow) elongated under shear-flow without detaching from the tooth surface. Original data.

3.5.5 MATERIAL MODELLING OF BIOFILM MECHANICS

From the previous paragraphs is evident that despite biofilm large physiological heterogeneity, which precluded the use of a single standard experimental procedure, researches produced a vast amount of useful data regarding biofilm materials properties. This, stimulated modellers to mathematical model biofilms mechanics which in turn can help the development of new experimental strategies for predicting and controlling biofilms behaviour. Mathematical models can be divided in those that focus only on the biofilm structure to measure mechanical and structural properties (here we call them “single-phase models”, where phase refers to just the biofilm as a bulk material) and those that couple fluid dynamic to assess biofilm/fluid interaction (multi-phase models, where phase can refer to the biofilm, the surrounding bulk liquid, the solid surface, the bacterial cells or the EPS).

Single-phase models

The earliest modelling approach of biofilm mechanical properties was presented by Klapper et al. who modelled *P. aeruginosa* biofilm bulk structure as cross-linked polymer viscoelastic gel using the linear Jeffrey’s stress-strain constitutive law (Klapper et al. 2002). The authors considered EPS responsible for the viscoelastic behaviour because of the internal and physicochemical bonds. In absence of an external stress the matrix remained in an isotropic configuration in which the attractive and repulsive forces between the chains are in balance. When a loading force is applied on the biofilm matrix, alignment and stretching of both polymer chains and intermolecular bonds took place until the yield limit is reached. After this point, intermolecular bonds broke and matrix polymers started flowing. Finally, when the shear is removed the intermolecular bonds reformed and the biofilm simulated a gel-like behaviour. Biofilm time-dependent strain and creep compliance responses at different scales of testing were interpreted using the Maxwell (Wloka et al. 2004) or Burger (Towler et al. 2003; Vinogradov et al. 2004) linear viscoelastic models or by combining multiple elements of Kelvin-Voigt and Maxwell (Figure 3.7) (Cense et al. 2006a; Ehret and Böl 2013; Lau et al. 2009; Pavlovsky et al. 2013). In particular, Lau et al. modelling the creep curves using a combined viscoelasticity model showed that the elastic parameters in *P. aeruginosa* biofilms were drastically reduced by a lipopolysaccharide deficiency (Lau et al. 2009). The good agreement between experimental data and the material models suggested biofilm viscoelastic behaviour similar to synthetic polymers (Janmey et al. 1990) and other biological fluids such as saliva and mucus (Fung 2013). However, due to the vast amount of biofilm materials models available in the literature, stress-relaxation constants covered a wide range of values (5 to 100 s) (Peterson et al. 2014). Peterson and co-authors performed principal component analysis (PCA) on a four-element Maxwell model showing that only three principal components are enough to model biofilms time-dependent behaviour: the fastest one (<3 s) was linked to the water due to its smallest viscosity; the intermediate one (3 to 70 s) was associated with the matrix polysaccharides; and the slowest component (10 to 25 s) incorporated eDNA structures (Peterson et al. 2013). Materials model were also used to investigate biofilm mechanical behaviour after the exposure to chemicals/antimicrobials (He et al. 2014; Jones et al. 2011). In particular, He and co-authors (He et al. 2014) assessed dental biofilm expansion caused after brushing and relative increased antimicrobials penetration using a three-element Maxwell model. Results showed an increase of the slow relaxation element which is related to a more open biofilm structure (after brushing). These results demonstrated that by changing oral biofilm mechanical properties we can enhance antimicrobial penetration inside the biofilm and have a better therapeutical effect.

A weakness of the dashpot and spring models is that it lacks capturing biofilm structural heterogeneity (such as density, porosity, bacterial growth and nutrient transfer). The advances in computing science have allowed the development of new complex and multidisciplinary models which combine microbiology, biochemistry. We can divide these models in two main categories: one-dimensional (1D) continuum biofilm models and advanced multi-dimensional biofilm models (which include Cellular Automata models (CA) and Individual-based models (IbM)). For a deeper mathematical description of these models we recommend the following reviews (Horn and Lackner 2014; Klapper and Dockery 2010; Wang and Zhang 2010). The first two categories are mainly centred to model biofilm growth dynamics, substrate concentration, bacterial reproduction and the cell-to-cell communication. Only a few studies have included simplified mechanical analysis in 1D models finding that shear-stress influences not only biofilm detachment but also microbial growth rate (Horn et al. 2003; Peyton and Characklis 1992; Stewart 1993). One particularly elegant two-dimensional CA model solved two different detachment processes (erosion and sloughing) at the biofilm surface caused by fluid-flow-induced stresses (Picioreanu et al. 2001). By treating the biofilm as elastic solid researchers showed that sloughing significantly increased biofilm-surface roughness compared to the erosion process. In addition, simulations showed that high-growth rates can cause a faster biofilm detachment compares to slow-growth ones. Three hypothetical mechanisms of detachment were incorporated into a 3D CA framework (Chambless and Stewart 2007). Results showed that detachment was highly related to the biofilm structure. In addition, nutrient depletion in the biofilm generated a higher amount of sloughing events. Towler et al. studied biofilm response to a turbulent flow field using FEA (Towler et al. 2007). Navier-Stokes equation were used to describe flow hydrodynamic while a single biofilm cluster was modelled using the linear viscoelastic Burger model. Results showed that biofilms with a lower Young modulus were more predisposed to lift forces and that biofilm induced-detachment was most effective during the initial relaxation period. In the same year Alpkvist and Klapper modelled biofilm bulk fluid-driven mechanical response and detachment by developing a ball-spring viscoelastic model (Figure 3.9A) (Alpkvist and Klapper 2007). A finite element model was created in order to assess the influence of the Young modulus, Re number and biofilm structure on biofilm detachment during fluid flow (Böl et al. 2009). Researchers used stacks from CLSM images to reconstruct the biofilm structure and St.

Venant-Kirchhoff and Arruda-Boyce models to represent the biofilm mechanics (Figure 3.9B). Interestingly, the biofilm detachment rate resulted to be independent from a change of Young modulus but was highly dependent on the biofilm structure (such as growth) and Re numbers. In another study, Laspidou and colleagues developed a unified multi-component cellular automata model (UMCCA) using finite element analysis (FEA) to test biofilm mechanical properties under compression, tension and shear tests (Laspidou et al. 2014).

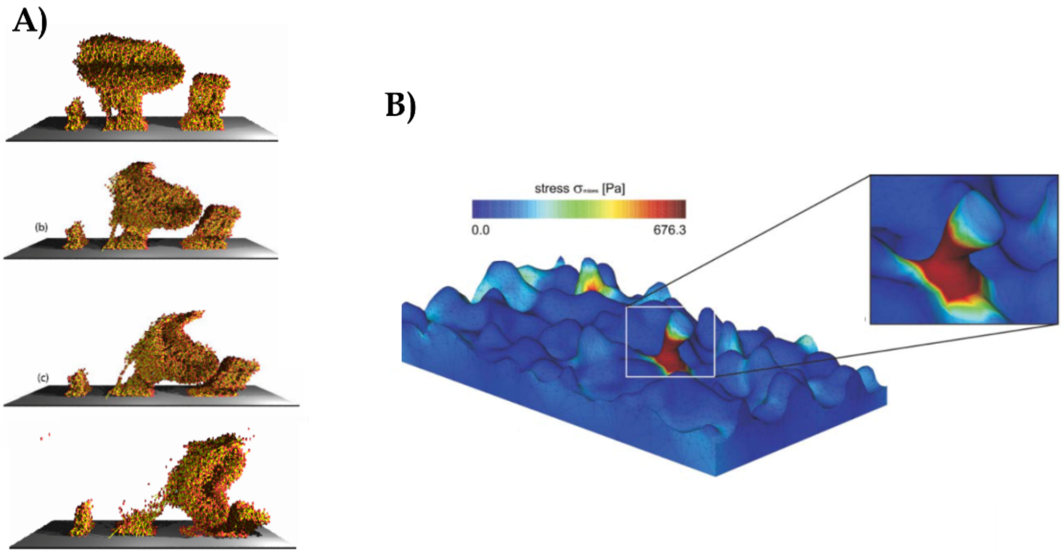

Figure 3.9. A) 3D simulation generated using the immersed boundary method showing biofilm detachment under impact of flow (image used with permission of author (Alpkvist and Klapper 2007)). B) 3D-finite element model of a biofilm showing shear-stresses distribution at the surface y (image used with permission of author (Böl et al. 2009)).

Multiphase models

Multiphase models are a new generation of models (Cogan and Guy 2010), where the physics of the biofilm system interacts with the surrounding bulk fluid in order to model biofilm viscoelasticity - biofilm/fluid interactions. In this model, each phase (in this case biofilm and the surrounding fluid) moves with its own velocity. The mixture's composition is defined by the volume fractions (ϕ_B and (ϕ_F) of the two phases (Figure 3.10) by:

$$\varphi_B + \varphi_F = 1; \tag{3.18}$$

Then the dynamics of the two phases are united by the Newton's laws equations. Researchers used a two-phase multiphase model to understand the combined motion of the fluid and the biofilm (Cogan and Keener 2004; Cogan 2008; Zhang et al. 2008a; Zhang et al. 2008b). In particular, Zhang et al. were able to simulate deformations, detachment phenomena, rippling and streaming events (Zhang et al. 2008a).

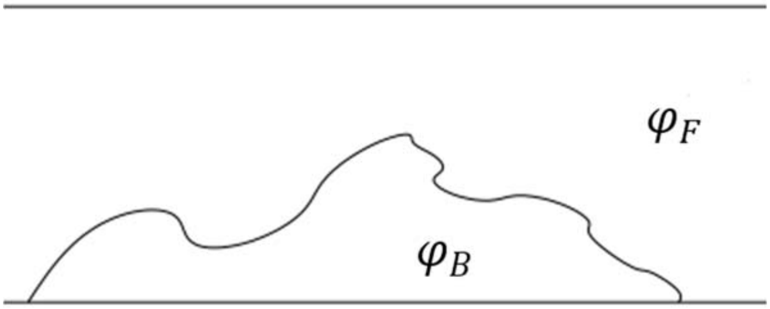

Figure 3.10.Schematic representation of a multiphase model of a biofilm coupled with its surrounding fluid. The region is separated into two phases, φ_B, the bulk fluid region, and φF), the biofilm region, by an interface (adapted from(Cogan 2008)).

3.5.6 BIOFILM/FLUID INTERACTIONS

The pertinent question to be addressed is: what happens at the interface between biofilm and the surrounding fluid when one is moving relative to the other? Wrinkle and ripple-like structures are the most documented patterns developing at the biofilm surface when subjected to shear flows (Noffke et al. 2001; Porada et al. 2008). In particular, it has been observed that ripples not only migrate downstream, which might affect biofilm colonisation on surfaces, but also their morphology varies with the flow velocity (Stoodley et al. 1999b). This fact, that ripples did not form under low flow, indicates that their formation must have a hydrodynamic origin. One of the firsts to explore this hypothesis were Thomas et al. who studied the ripples-structures formed on Kinneyia fossils. Kinneyia are fossilized microbial mats usually found in environments that have experienced heavy floods (Thomas et al. 2013). The researchers were able to model the ripples structures as Kelvin–Helmholtz Instabilities (KHII) caused by the ancient flowing of water above the mats. KH are one example of hydrodynamic instability which occurs at the interface between two fluids with different viscosities and flowing with different velocities (Miles 1959). A well-defined instability forms, giving rise to a harmonic interfacial corrugation (Figure 3.11). KHI occurs ubiquitously in Nature, such as in cloud layers, and are considered a prelude to mixing and turbulence (Geyer et al. 2010).

As the ripples build they can fold the two fluids into each other causing mixing. KHI implies the onset of turbulence in the flowing biofilm, providing further insight into the mechanical behaviour of biofilms as complex liquids.

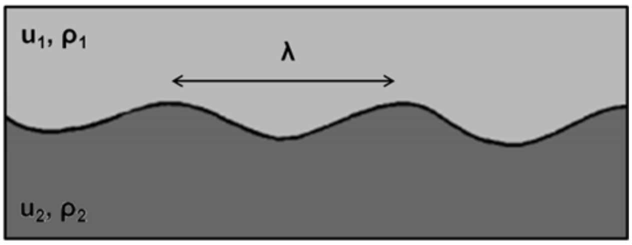

Figure 3.11. Schematic view of the formation of KHI in two-fluid systems that are stratified by density variations ($\rho_1 > \rho_2$) with a velocity differential between the fluids($u_1 > u_2$). Shear forces generated from the velocity difference lead to unstable vorticity which grows exponentially until the distorted interface overturns into a spiral forming rippled features of wavelength λ.

Herewith, biofilm mechanical properties are determined by an interaction between a structure's composition and external environmental changes which may have a possible survival meaning. These observations also provide the basis for future investigations into biofilm survival and control that can be developed and optimized with validated modelling coupled with state-of-the art experimentation.

3.6 DENTAL BIOFILM CONTROL STRATEGIES

Dental caries is one of the most important problems in the oral healthcare and a lot of research has been made in order to manage and to control dental plaque biofilms. The research on caries prevention has been deeply studied for a long time in order to define a standard method that helps to reduce caries risk in patients. In 1999 Featherstone et al. published for the first time the concept of *caries balance* as a protocol to follow in order to simplify the key factors involved in development of caries (Featherstone 1999). The caries balance consists of a proper balance between pathological factors and protective factors. Acid-producing bacteria, such as mutans streptococci, represent the pathological factors; instead saliva flow and anticaries agents represent the protective ones. If the pathological factors overcome the protective factors, then caries develop. The concept introduced by Featherstone could help dentists to determine the progression or the inhibition of dental caries in patients. Afterwards, a variety of clinical trials have been done to assess practical methods for caries management (Featherstone 2006). Nowadays, according to the primary oral health measures a balanced low sugar and acid diet not only helps to prevent the dental decay but also to avoid teeth erosion, which is the irreversible loss of dental hard tissue caused by the prolonged exposure of the enamel to the acids from foods such as fruit juice or commercial soft drinks (Al-Malik et al. 2001). The reduced frequency of sugar consumption should be combined with routine daily oral hygiene and periodical visits to the dentist in order to maintain a normal health oral microflora.

However, as it is difficult to alter established eating patterns and to maintain a high degree of oral hygiene, alternative preventive measures are being studied and developed.

3.6.1 MECHANICAL DISRUPTION

Toothbrushes

The most common way to mechanically disrupt and removal dental biofilms is routine tooth brushing. Manual toothbrushes remove biofilm by direct contact and movement of toothbrush bristles (filaments) across the teeth surface. From a mechanical point of view this can be imagined as an energy transfer into the biofilm through the shear forces created by the elastic deformations of the toothbrush filaments (Carter et al. 2007). In order to completely remove biofilm from the tooth surface, shear forces need to exceed both biofilm adhesion and cohesion forces otherwise biofilm is only disrupted (removal of only part of the biofilm) (Busscher et al. 2010). However, dental plaque is likely found in particular areas inside the mouth, such as fissures, interproximal space (IP) and subgingival areas, which can be inaccessible for toothbrush bristles. The introduction of powered toothbrushes (in which the bristle motion is produced by the device) with brush heads varying in shape, length and sizes has improved biofilm removal efficacy in the abovementioned hard-to-reach areas (Stanford et al. 1996; Van der Weijden et al. 2005). Powered toothbrushes have high-frequency moving bristles typically in the range of 73 Hz for oscillating-rotating brushes or 200-400 Hz for sonic brushes. Clinical trials, in which manual and electric toothbrushing were compared, discovered that powered toothbrushes removed more plaque and gingivitis than manual toothbrushing (Deacon et al. 2011; Heanue et al. 2005; Zimmer et al. 2005). The advantages of sonic toothbrushes are that the bristles oscillating motion not only helps to remove biofilm by direct contact but also by non-contact through the generation of turbulent fluid flows and air-bubbles (Busscher et al. 2003; Hope and Wilson 2003; Sharma et al. 2005). The fluid flow generates shear forces parallel to the tooth surface (Landau and Lifshitz 1987) enhancing energy transfer into the biofilm located in difficult to access areas. When bubbles are created, the flowing stream impacting the biofilm becomes three-phase (surface, liquid and gas) (Pitt et al. 1993). This generates interfacial forces that pull biofilms away from the substrate (Parini et al. 2005; Parini and Pitt 2006). Thus, with bubbles in a rapidly moving stream there are two forces that can remove the bacteria: the fast-moving fluid forces and the shear stress forces created when bubbles contact the biofilm. In addition, it has been shown that the powered toothbrushes may contributes to biofilm reduction through the generation of acoustic energy.

Interdental Cleansing

Detachment of dental plaque which was not in direct contact with the toothbrush bristles diminishes with distance (Adams et al. 2003), suggesting that the power of the bristles should be high enough in order to overcome the viscoelastic properties of the biofilm adhesive mass (Thomas and Nakaishi 2006). This is important when dealing with plaque removal in the proximal surfaces of the teeth, especially in the interproximal space, where unremoved bacteria can accumulate and increase the risk for dental caries or periodontal diseases. Traditional dental flossing has been the most common way to mechanically remove dental plaque in the IP areas to supplement tooth brushing. However, it has been considered time consuming and related to bleeding gums when used for a long time (Gough 2010). Therefore, a variety of different of power interdental devices which adopt continuous water jets (oral irrigators) have been developed and improved since the 1960s (Lyle 2012). Oral irrigators are a valid alternative to dental flossing for those patients who will not or cannot floss, providing significant reductions not only in plaque biofilm but also in bleeding and gingivitis (Fried 2012; Greenstein ; Husseini et al. 2008). A wide variety of head tips (conical, soft, straight) have been produced in order to remove dental biofilms in different parts of the teeth, such as the IP space or inside the subgingival pocket. The combination of pulsation and pressure, the two main mechanisms of a dental water jet, helps to remove a higher amount of supragingival plaque biofilm than a standard steam device, reducing calculus and gingivitis (Jahn 2010). In addition, when the water jet is driven into the narrowing gap constituting the interproximal space, increases its velocity and turbulence, therefore generating larger shear stresses at the biofilm interface.

Microsprays

More recently a new mechanical method for removing biofilm has been developed, which consists of applying high-velocity water microdroplets sprays to dental plaque (Cense et al. 2006b). Biofilm removal through the perpendicular impact (impingement) of many water droplets is the result of an erosion process (Ruff and Wiederhorn 1979), similar to water jet cleaning. Cense and co-authors found that the cleaning rate of droplets was almost twice that of a continuous jet suggesting that the droplets' impact pressure, hydrodynamic shear stresses and the surface tension effects of the passage of an air-water interface over a solid surface influence biofilm removal (Busscher et al. 2010). In 2011, Philips Oral Healthcare (POH) developed a new power interdental device (Sonicare AirFloss, AF) which adopts the micro droplets technology to deliver a high-velocity (ms) microburst of compressed air and water droplets. In contrast to the continuous water jets, which require large reservoirs of water and long cleaning times, the AF is completely portable and the microdroplets technology reduces water volume and cleaning times. Clinical studies showed that the microspray burst removed significantly more plaque (99%) than a manual toothbrush alone (Bruce 2013; de Jager et al. 2015; Holley et al. 2013). Rmaile and co-authors used high-speed camera videography in order to assess the AirFloss removal of laboratory grown interproximal *S. mutans* dental biofilms to high-velocity microsprays from the AF device (Rmaile et al. 2014; Rmaile et al. 2015; Rmaile et al. 2013). Interestingly, before detaching from the tooth surface, the biofilm was elongated to more than 9 times its original length. This phenomenon enlightens the viscoelastic nature of bacterial biofilms which has to be taken into consideration when applying shear forces to remove biofilms.

3.6.2 CHEMICAL DISRUPTION

Oral biofilm control through only mechanical means is not sufficient. For complementing mechanical removal methods, routine oral hygiene includes the use of toothpastes and/or moth rinses. Specific chemical compounds are present inside dentifrices to prevent biofilm formation and/or to enhance removal. Depending on mode of action chemicals are classified as antiplaque or antimicrobial agents. Antiplaque agents prevent the formation of the biofilm or remove already established biofilm, whereas antimicrobial agents inhibit bacterial growth or cell killing. Normally, for liquid grown planktonic bacteria the ability of an antibiotic to inhibit the growth or to kill a target bacteria is expressed in terms of Minimum inhibitory concentration (MIC) or Minimum bactericidal concentration (MBC), respectively (Olson et al. 2002). However, as discussed previously (Session 3.4) sessile bacteria biofilms are more tolerant to antimicrobial agents than planktonic cells, consequently affecting the mode of action and the efficacy of the biocide. The list of chemical compounds used into toothpastes and mouth rinses is long, thus in the following paragraphs we will comment the most commonly used.

Fluoride

Fluoride (F^-, molar mass ≈ 19 g/mol), a highly electronegative anion (electronegativity=3.98), is the most important and common chemical agent found inside mouth rinses, gums, and mouthwashes. Fluoride not only enhances the remineralisation and the solubility of the teeth, but also modulates the microbial physiology and has even an antimicrobial effect (Van Loveren 2001). Fluoride enhances the remineralisation of the teeth because supplied fluoride ions enter in the enamel framework by filling hydroxyl vacancies or moving hydroxyl ions (Young 1975). The high charge density of the fluoride ion stabilizes the crystal structure and creates the so called fluorohydroxyapatite (FHA). The resulting solubility product of the FHA is lower than the one of the enamel apatite, rendering the fluoridate-enamel more difficult to dissolve (ten Cate 1997). This behaviour is of crucial importance in the remineralisation aiding caries preventing. The penetration of fluoride inside the dental enamel is a diffusion-controlled process and is highly dependent on the exposure time (≈ 4 min, (Wei and Chik 1989)), the fluoride concentration and the demineralisation process (Ivanoff et al. 2013). In the majority of the studies, fluoride deposition on the teeth surface does not exceed 24 hrs. (Eakle et al. 2004). A clinical trial on high caries individuals showed that in order to both avoid the fluorosis disease and to have a therapeutic effect on caries, the fluoride concentration in saliva must be a continuous 0.1 ppm all day (Chandra et al. 1980). A fluoride concentration of 304 $\mu g/mm^3$ was able to reach an enamel depth of 150-300 µm (Rodrigues, Delbem et al. 2010). Interestingly, fluoride may have a positive interaction with dental plaque biofilm. Frequent exposure of fluoridate drinking water, mouth rinses or dentifrices helps fluoride to enters the plaque and possible bind to bacterial cells or EPS (Tenuta et al. 2006). In this case, the biofilm plaque acts as a reservoir for not only fluoride but also phosphate and calcium ion, possibly slowly releasing them over time and prolonging the anticaries activity. Duckworth et al reported significant increase of sodium fluoride (NaF) in measured plaque after 18 hours of treatment (Duckworth et al. 1987). Fluoride can also modulate the microbial physiology by leading to as a less acid environment and lower risk of caries. It is well documented that inside dental plaque biofilm there are different microenvironments which lead to chemical gradients such as pH or dissolved oxygen (Aspiras et al. 2010). Anoxic niches favour the proliferation of cariogenic bacteria in the inner layers of the biofilm causing a higher probability of caries development. Microelectrodes have been used extensively for measuring the physicochemistry of *in vitro* oral biofilms local environments (Aspiras et al. 2010; Stoodley et al. 2008). *S. mutans* is able to metabolize dissolved oxygen (DO) to generate more favourable conditions for its growth inside the inner layers of the biofilm (Nguyen et al. 2002). Microelectrodes measurements by Stoodley and colleagues determined the DO profile of an *in vitro S. mutans* dental biofilm grown in artificial saliva and 10 % of sucrose (Stoodley et al. 2008). The sucrose addition caused the creation of an anaerobic region inside the biofilm which is the perfect habitat for aciduric and acidogenic bacteria. Fluoride could influence the localized anaerobic environments and attenuate the proliferation of cariogenic bacteria, thereby decreasing the caries process. In 2007 Stoodley at al. used oxygen and pH electrode in order to measure the influence of NaF in the physiology of an *in vivo S. mutans* oral biofilm (Stoodley et al. 2008). The results showed that 1,000 mg/L of NaF can drastically increase both dissolved oxygen and pH levels leading to a less acidogenic habitat.

Chlorhexidine

As of today, Chlorhexidine (CHX) is the most effective antimicrobial agent for oral biofilm control (Frias-Lopez 2014). Used at high concentrations, this compound is a wide spectrum bactericide (i.e. kills bacteria) by damaging the bacterial cell membrane. CHX is a positively-charged molecule which likely binds to negatively charged molecules present in bacteria cell surfaces causing irreversible loss of cytoplasmic constituents (Russell and Day 1993). A concentration of 0.2 % of CHX in several oral biofilm models has shown bactericidal effect (Hope and Wilson 2004b). In addition 0.2 % of CHX in oral mouth rinses showed the best efficacy in clinical studies (von Ohle et al. 2010). Instead, at low concentrations Chlorhexidine is bacteriostatic (i.e. stops bacteria from reproducing while not necessarily killing them) through the inhibition of sugar transport and acid production in streptococci (Houari and Di Martino 2007; Modesto and Drake 2006). In addition, Chlorhexidine has the ability to inhibit bacterial attachment through the binding to the salivary pellicle (Rölla and Melsen 1975)

Cetylpyridinium chloride

Cetylpyridinium chloride (CPC), a cationic quaternary molecule, is another broad spectrum antimicrobial agent commonly incorporated into oral hygiene products (Haps et al. 2008). The high positive charge of CPC facilitates the binding to negatively charged bacteria which lead to the disruption of bacteria membrane functions (Scheie 1989). Clinical studies showed that both short-term and long-term exposure of CPC-containing dentifrices (between 0.045% and 0.10%) significantly reduced dental plaque and gingivitis in patients (Hernandez-Cott et al. 2008; Lotufo et al. 2008; Silva et al. 2008). I*n vitro* and *ex-vivo* studies on oral biofilms corroborated the clinical studies demonstrating CPC significant antimicrobial activity (Latimer et al. 2015; Pandit et al. 2015; Sreenivasan et al. 2013).

Triclosan

Triclosan, a chlorinated aromatic compound, has been widely formulated into dentifrices and mouthwashes as an antimicrobial and antiplaque agent. Triclosan binds with the bacterial cell membrane causing bacteriolysis or inhibits bacteria sugar metabolism and protease activity (Marsh et al. 2015).

Essential Oils

Menthol, eucalyptol, methyl salicylate and thymol into a mouthwash (commonly called “Listerine”) has demonstrated the ability to interfere with dental plaque biofilm formation (Marsh 2009). The main function of essential oils is thought to be the disruption of bacterial cell membranes and the inhibition of specific enzymes (Patel and Malaki 2007; Stoeken et al. 2007).

3.7 ANTIMICROBIAL PENETRATION

Because of biofilm high-cell density and the physicochemical properties of the matrix which normally does not allow advective fluid flow through the EPS, mass transport within the biofilm is limited to diffusion (Forier et al. 2014; Takenaka et al. 2009). Previous studies on oral biofilms showing that CHX and CPC antimicrobial efficacy decreased in biofilm deep layers (Hope and Wilson 2004a; Vitkov et al. 2005; von Ohle et al. 2010) with penetration timescales up to 20 mins to reach half of the biofilm thickness (Corbin et al. 2011). The retarded penetration is related with the EPS matrix structure which acts as a barrier towards the diffusion of particles and free antimicrobial agents into the biofilm (Flemming and Wingender 2010). Cetylpyridinium chloride and Chlorhexidine are positively-charged molecules which likely bind to negatively charged EPS matrix polymers or to cell surfaces, delaying penetration. Also fluoride penetration was found limited to the first layers of the biofilm (Pessan et al. 2014; Watson et al. 2005). It has been demonstrated that advection alone with no significant mechanical perturbation of the biofilm structure was not enough to drive particles inside the biofilm (de Beer et al. 1996; Stoodley et al. 1994). Busscher and co-authors pointed out that biofilm viscoelastic volumetric expansion documented after sonic brushing, which left unremoved biofilm “fluffed-up”, could enhance antimicrobials and antiplaque agents increasing their therapeutical effect (Busscher et al. 2010). Microelectrodes studies on *in vitro* oral biofilms showed that fluoride and CHX could influence the localized anaerobic environments and attenuate the proliferation of cariogenic bacteria (Aspiras et al. 2010; Stoodley et al. 2008; von Ohle et al. 2010). The role of the hydrodynamic in the enhancement of dentifrices inside the biofilm has become a topic of interest, since it might be utilized to improve delivery to the tooth surface or the cells themselves. Investigators demonstrated that fluid-dynamic activity generated by power toothbrushes can enhance antimicrobials/antiplaque delivery inside any remaining biofilm compared to simple diffusional transport (He et al. 2014; Jongsma et al. 2015; Sjogren et al. 2004; Stoodley et al. 2007). Low-volume high-velocity microsprays have the advantage in that they are low volume but also have an air/water interface moving over the solid surface which not only facilitates biofilm removal but also might change the mechanical properties of unremoved biofilm. This could open up new strategies for controlling and preventing biofilms such as using water microspray to increase antimicrobial delivery inside biofilms for better therapeutic control in medicine and industry.

3.8 REFERENCES

Abe Y, Skali-Lami S, Block J-C, Francius G. 2012. Cohesiveness and hydrodynamic properties of young drinking water biofilms. Water Research. 46(4):1155-1166.

Adams H, Winston MT, Heersink J, Buckingham-Meyer KA, Costerton JW, Stoodley P. 2003. Development of a laboratory model to assess the removal of biofilm from interproximal spaces by powered tooth brushing. Am J Dent. 15 Spec No:12B-17B.

Aggarwal S, Hozalski RM. 2010. Determination of biofilm mechanical properties from tensile tests performed using a micro-cantilever method. Biofouling. 26(4):479-486.

Aggarwal S, Hozalski RM. 2012. Effect of strain rate on the mechanical properties of staphylococcus epidermidis biofilms. Langmuir. 28(5):2812-2816.

Aggarwal S, Poppele EH, Hozalski RM. 2010. Development and testing of a novel microcantilever technique for measuring the cohesive strength of intact biofilms. Biotechnol Bioeng. 105(5):924-934.

Ajdic D, McShan WM, McLaughlin RE, Savic G, Chang J, Carson MB, Primeaux C, Tian R, Kenton S, Jia H et al. 2002. Genome sequence of *Streptococcus mutans* ua159, a cariogenic dental pathogen. Proc Natl Acad Sci U S A. 99:14434-14439.

Al-Malik MI, Holt RD, Bedi R. 2001. The relationship between erosion, caries and rampant caries and dietary habits in preschool children in saudi arabia. International Journal of Paediatric Dentistry. 11(6):430-439.

Allan RN, Morgan S, Brito-Mutunayagam S, Skipp P, Feelisch M, Hayes SM, Hellier W, Clarke SC, Stoodley P, Burgess A. 2016. Low concentrations of nitric oxide modulate streptococcus pneumoniae biofilm metabolism and antibiotic tolerance. Antimicrobial agents and chemotherapy.AAC-02432.

Allison DG. 2003. The biofilm matrix. Biofouling. 19:139-150.

Alpkvist E, Klapper I. 2007. Description of mechanical response including detachment using a novel particle model of biofilm/flow interaction. Water Sci Technol. 55(8-9):265-273.

Armstrong WG. 1968. Origin and nature of the acquired pellicle. Proceedings of the Royal Society of Medicine. 61(9):923-930.

Aspiras M, Stoodley P, Nistico L, Longwell M, de Jager M. 2010. Clinical implications of power toothbrushing on fluoride delivery: Effects on biofilm plaque metabolism and physiology. International journal of dentistry. 2010:651869.

Banks HT, Hu S, Kenz ZR. 2010. A brief review of elasticity and viscoelasticity. DTIC Document.

Banyavichyus R, Barauskas A, Marma A, Askadskii A. 1981. Features of viscoelastic behavior of materials based on heat-resistant polymers. Mechanics of Composite Materials. 16(6):644-649.

Barnes HA, Hutton JF, Walters K. 1989. An introduction to rheology. Elsevier.

Barraud N, Hassett DJ, Hwang S-H, Rice SA, Kjelleberg S, Webb JS. 2006. Involvement of nitric oxide in biofilm dispersal of pseudomonas aeruginosa. Journal of Bacteriology. 188(21):7344-7353.

Barraud N, J Kelso M, A Rice S, Kjelleberg S. 2015. Nitric oxide: A key mediator of biofilm dispersal with applications in infectious diseases. Current pharmaceutical design. 21(1):31-42.

Barraud N, Schleheck D, Klebensberger J, Webb JS, Hassett DJ, Rice SA, Kjelleberg S. 2009. Nitric oxide signaling in pseudomonas aeruginosa biofilms mediates phosphodiesterase activity, decreased cyclic di-gmp levels, and enhanced dispersal. Journal of Bacteriology. 191(23):7333-7342.

Bassler BL, Miller MB. 2013. Quorum sensing. The prokaryotes. Springer. p. 495-509.

Batchelor GK. 2000. An introduction to fluid dynamics. Cambridge university press.

Bayoudh S, Ponsonnet L, Ouada HB, Bakhrouf A, Othmane A. 2005. Bacterial detachment from hydrophilic and hydrophobic surfaces using a microjet impingement. Colloids and Surfaces A: Physicochemical and Engineering Aspects. 266(1):160-167.

Blauert F, Horn H, Wagner M. 2015. Time-resolved biofilm deformation measurements using optical coherence tomography. Biotechnology and bioengineering. 112(9):1893-1905.

Bos R, van der Mei HC, Busscher HJ. 1999. Physico-chemistry of initial microbial adhesive interactions – its mechanisms and methods for study. FEMS Microbiology Reviews. 23(2):179-230.

Broszat M, Grohmann E. 2014. Horizontal gene transfer in planktonic and biofilm modes. In: Rumbaugh PK, Ahmad I, editors. Antibiofilm agents: From diagnosis to treatment and prevention. Berlin, Heidelberg: Springer Berlin Heidelberg. p. 67-95.

Brown MRW, Allison DG, Gilbert P. 1988. Resistance of bacterial biofilms to antibiotics a growth-rate related effect? Journal of Antimicrobial Chemotherapy. 22(6):777-780.

Bruce JD. 2013. Effect of philips sonicare airfloss on plaque index, gingival index, and bleeding index in patients with fixed orthodontic appliances. SAINT LOUIS UNIVERSITY.

Busscher HJ, Jager D, Finger G, Schaefer N, Van der Mei HC. 2010. Energy transfer, volumetric expansion, and removal of oral biofilms by non-contact brushing. European journal of oral sciences. 118(2):177-182.

Busscher HJ, Norde W, van der Mei HC. 2008. Specific molecular recognition and nonspecific contributions to bacterial interaction forces. Applied and Environmental Microbiology. 74(9):2559-2564.

Busscher HJ, Rustema-Abbing M, Bruinsma GM, De Jager M, Gottenbos B, Van der Mei HC. 2003. Non-contact removal of coadhering and non-coadhering bacterial pairs from pellicle surfaces by sonic brushing and de novo adhesion. European journal of oral sciences. 111(6):459-464.

Böl M, Ehret AE, Bolea Albero A, Hellriegel J, Krull R. 2013. Recent advances in mechanical characterisation of biofilm and their significance for material modelling. Critical reviews in biotechnology. 33(2):145-171.

Böl M, Möhle RB, Haesner M, Neu TR, Horn H, Krull R. 2009. 3d finite element model of biofilm detachment using real biofilm structures from clsm data. Biotechnology and Bioengineering. 103(1):177-186.

Elasticity in biological materials. 2006. Cambridge University Press; [accessed May 2016]. http://www.doitpoms.ac.uk/tlplib/bioelasticity/index.php.

Carter K, Landini G, Walmsley AD. 2007. Influence of compressive and deflective force on powered toothbrush filaments. Quintessence International. 38(5).

Cense A, Peeters E, Gottenbos B, Baaijens F, Nuijs A, Van Dongen M. 2006a. Mechanical properties and failure of *Streptococcus mutans* biofilms, studied using a microindentation device. Journal of microbiological methods. 67(3):463-472.

Cense AW, Van Dongen MEH, Gottenbos B, Nuijs AM, Shulepov SY. 2006b. Removal of biofilms by impinging water droplets. Journal of Applied Physics. 100(12):124701-124701-124708.

Chambless JD, Stewart PS. 2007. A three-dimensional computer model analysis of three hypothetical biofilm detachment mechanisms. Biotechnology and bioengineering. 97(6):1573-1584.

Chandra S, Sharma R, Parshuram Thergaonkar V, Chaturvedi SK. 1980. Determination of optimal fluoride concentration in drinking water in an area in india with dental fluorosis. Community Dentistry and Oral Epidemiology. 8(2):92-96.

Chen H, Jiang W. 2015. Application of high-throughput sequencing in understanding human oral microbiome related with health and disease. Recent Discoveries in Evolutionary and Genomic Microbiology.76.

Chen M, Zhang Z, Bott T. 1998. Direct measurement of the adhesive strength of biofilms in pipes by micromanipulation. Biotechnology Techniques. 12(12):875-880.

Chen MJ, Zhang Z, Bott TR. 2005. Effects of operating conditions on the adhesive strength of pseudomonas fluorescens biofilms in tubes. Colloids and Surfaces B: Biointerfaces. 43(2):61-71.

Cheong F, Duarte S, Lee S-H, Grier D. 2009. Holographic microrheology of polysaccharides from *Streptococcus mutans* biofilms. Rheol Acta. 48(1):109-115.

Chew J, Paterson W, Wilson D. 2004. Fluid dynamic gauging for measuring the strength of soft deposits. Journal of Food Engineering. 65(2):175-187.

Chew SC, Kundukad B, Seviour T, van der Maarel JRC, Yang L, Rice SA, Doyle P, Kjelleberg S. 2014. Dynamic remodeling of microbial biofilms by functionally distinct exopolysaccharides. MBio. 5(4):e01536-01514.

Chhabra RP. 2010. Non-newtonian fluids: An introduction. Rheology of complex fluids. Springer. p. 3-34.

Cogan N, Keener JP. 2004. The role of the biofilm matrix in structural development. Mathematical Medicine and Biology. 21(2):147-166.

Cogan NG. 2008. Two-fluid model of biofilm disinfection. Bulletin of Mathematical Biology. 70(3):800-819.

Cogan NG, Guy RD. 2010. Multiphase flow models of biogels from crawling cells to bacterial biofilms. HFSP Journal. 4(1):11-25.

Corbin A, Pitts B, Parker A, Stewart PS. 2011. Antimicrobial penetration and efficacy in an in vitro oral biofilm model. Antimicrobial agents and chemotherapy. 55(7):3338-3344.

Costerton JW, Montanaro L, Arciola CR. 2005. Biofilm in implant infections: Its production and regulation. The International journal of artificial organs. 28:1062-1068.

Costerton JW, Stewart PS, Greenberg E. 1999. Bacterial biofilms: A common cause of persistent infections. Science. 284(5418):1318-1322.

Cotter PA, Stibitz S. 2007. C-di-gmp-mediated regulation of virulence and biofilm formation. Current opinion in microbiology. 10(1):17-23.

Cotterell B, Williams JG. 2010. Fracture and life. World Scientific.

Dawes C. 2003. What is the critical ph and why does a tooth dissolve in acid? Journal (Canadian Dental Association). 69(11):722-724.

de Beer D, Stoodley P, Lewandowski Z. 1996. Liquid flow and mass trasport in heterogeneous biofilms. Biotechnology and Bioengineering. 44:636-641.

de Beer D, Stoodley P, Roe F, Lewandowski Z. 1994. Effects of biofilm structures on oxygen distribution and mass transport. Biotechnology and Bioengineering. 43:1131-1138.

de Jager M, Jain V, Schmitt P, DeLaurenti M, Jenkins W, Milleman J, Milleman K, Putt MJ. 2015. Effect of philips sonicare airfloss on interproximal plaque and gingivitis.

Deacon SA, Glenny AM, Deery C, Robinson PG, Heanue M, Walmsley AD, Shaw WC. 2011. Different powered toothbrushes for plaque control and gingival health. Australian Dental Journal. 56(2):231-233.

Decho AW. 2013. The eps matrix as an adaptive bastion for biofilms: Introduction to special issue. International journal of molecular sciences. 14:23297-23300.

Deshpande MD, Vaishnav RN. 1983. Wall stress distribution due to jet impingement. Journal of Engineering Mechanics. 109(2):479-493.

Dewhirst FE, Chen T, Izard J, Paster BJ, Tanner ACR, Yu W-H, Lakshmanan A, Wade WG. 2010. The human oral microbiome. Journal of bacteriology. 192(19):5002-5017.

Donelli G. 2014. Biofilm-based healthcare-associated infections. Springer.

Donlan RM, Costerton JW. 2002. Biofilms: Survival mechanisms of clinically relevant microorganisms. Clinical Microbiology Reviews. 15(2):167-193.

dos Santos VAPM, Yakimov MM, Timmis KN, Golyshin PN. 2008. Genomic insights into oil biodegradation in marine systems. Caister Academic Press

Duan K, Dammel C, Stein J, Rabin H, Surette MG. 2003. Modulation of pseudomonas aeruginosa gene expression by host microflora through interspecies communication. Molecular microbiology. 50(5):1477-1491.

Duckworth RM, Morgan SN, Murray AM. 1987. Fluoride in saliva and plaque following use of fluoride-containing mouthwashes. Journal of dental research. 66(12):1730-1734.

Eakle WS, Featherstone JD, Weintraub JA, Shain SG, Gansky SA. 2004. Salivary fluoride levels following application of fluoride varnish or fluoride rinse. Community Dentistry and Oral Epidemiology. 32(6):462-469.

Ehret AE, Böl M. 2013. Modelling mechanical characteristics of microbial biofilms by network theory. Journal of the Royal Society Interface. 10(78):20120676.

Engels-Deutsch M, Rizk S, Haïkel Y. 2011. *Streptococcus mutans* antigen i/ii binds to α5β1 integrins via its a-domain and increases β1 integrins expression on periodontal ligament fibroblast cells. archives of oral biology. 56(1):22-28.

Fang HHP, Chan K-Y, Xu L-C. 2000. Quantification of bacterial adhesion forces using atomic force microscopy (afm). Journal of Microbiological Methods. 40(1):89-97.

Featherstone J. 1999. Prevention and reversal of dental caries: Role of low level fluoride. Community Dent Oral Epidemiol. 27:31 - 40.

Featherstone JD. 2006. Caries prevention and reversal based on the caries balance. Pediatric dentistry. 28(2):128-132; discussion 192-128.

Fink R, Oder M, Rangus D, Raspor P, Bohinc K. 2015. Microbial adhesion capacity. Influence of shear and temperature stress. International journal of environmental health research. (ahead-of-print):1-14.

Flemming H-C, Neu TR, Wozniak DJ. 2007. The eps matrix: The “house of biofilm cells”. Journal of Bacteriology. 189(22):7945-7947.

Flemming H-C, Wingender J. 2010. The biofilm matrix. Nature Reviews Microbiology. 8:623-633.

Flemming H-C, Wingender J, Szewzyk U. 2011. Biofilm highlights. Springer.

Forier K, Raemdonck K, De Smedt SC, Demeester J, Coenye T, Braeckmans K. 2014. Lipid and polymer nanoparticles for drug delivery to bacterial biofilms. Journal of Controlled Release. 190:607–623.

Frias-Lopez J. 2014. Biofilm control strategies in dental health. In: Rumbaugh PK, Ahmad I, editors. Antibiofilm agents: From diagnosis to treatment and prevention. Berlin, Heidelberg: Springer Berlin Heidelberg. p. 291-326.

Fried JL. 2012. Interdental cleansing. Access. 2:22-25.

Fung Y-C. 2013. Biomechanics: Mechanical properties of living tissues. Springer Science & Business Media.

Galy O, Latour-Lambert P, Zrelli K, Ghigo J-M, Beloin C, Henry N. 2012. Mapping of bacterial biofilm local mechanics by magnetic microparticle actuation. Biophysical journal. 103(6):1400-1408.

Geyer WR, Lavery AC, Scully ME, Trowbridge JH. 2010. Mixing by shear instability at high reynolds number. Geophysical Research Letters. 37(22).

Gibbons RJ, Houte JV. 1975. Dental caries. Annual Review of Medicine. 26(1):121-136.

Gough N. 2010. Dental hygiene theory and practice. Vital. 7(2):7-7.

Greenstein G. Position paper: The role of supra- and subgingival irrigation in the treatment of periodontal diseases. (0022-3492 (Print)).

Gresham B. 2008. Viscosity: A fluid's resistance to flow. Tribology & lubrication technology. 64(11):55-57.

Guélon T, Mathias J-D, Stoodley P. 2011. Advances in biofilm mechanics. In: Flemming H-C, Wingender J, Szewzyk U, editors. Biofilm highlights. Springer Berlin Heidelberg. p. 111-139.

Götz F. 2002. Staphylococcus and biofilms. Molecular microbiology. 43(6):1367-1378.

Hall-Stoodley L, Costerton JW, Stoodley P. 2004. Bacterial biofilms: From the natural environment to infectious diseases. Nat Rev Micro. 2:95-108.

Hamada S, Slade HD. 1980. Biology, immunology, and cariogenicity of *Streptococcus mutans*. Microbiol Rev. 44:331-384.

Hannig C, Hannig M, Attin T. 2005. Enzymes in the acquired enamel pellicle. European journal of oral sciences. 113(1):2-13.

Hannig M. 2002. The protective nature of the salivary pellicle. International Dental Journal. 52(S5):417-423.

Haps S, Slot De Fau - Berchier CE, Berchier Ce Fau - Van der Weijden GA, Van der Weijden GA. 2008. The effect of cetylpyridinium chloride-containing mouth rinses as adjuncts to toothbrushing on plaque and parameters of gingival inflammation: A systematic review. International Journal of Dental Hygiene. 6(3):290-303.

He Y, Peterson BW, Ren Y, van der Mei HC, Busscher HJ. 2014. Antimicrobial penetration in a dual-species oral biofilm after noncontact brushing: An in vitro study. Clin Oral Invest. 18(4):1103-1109.

Heanue M, Deacon SA, Deery C, Robinson PG, Walmsley AD, Worthington HV, Shaw WC. 2005. Manual versus powered tooth brushing for oral health. Australian Dental Journal. 50(2):123.

Hernandez-Cott PL, Elias BA, Stewart B, DeVizio W, Proskin HM. 2008. Clinical investigation of the efficacy of a commercial mouthrinse containing 0.05% cetylpyridinium chloride in reducing dental plaque. The Journal of clinical dentistry. 20(2):39-44.

Hohne DN, Younger JG, Solomon MJ. 2009. Flexible microfluidic device for mechanical property characterization of soft viscoelastic solids such as bacterial biofilms. Langmuir. 25(13):7743-7751.

Holley TJ, Ross JA, Hottel TL. 2013. Efficacy of philips sonicare airfloss compared to manual brushing and flossing: An in vitro study. The Journal of the Tennessee Dental Association. 94(1):34-36.

Hope C, Wilson M. 2004a. Analysis of the effects of chlorhexidine on oral biofilm vitality and structure based on viability profiling and an indicator of membrane integrity. Antimicrobial agents and chemotherapy. 48(5):1461-1468.

Hope CK, Wilson M. 2003. Effects of dynamic fluid activity from an electric toothbrush on in vitro oral biofilms. Journal of clinical periodontology. 30(7):624-629.

Hope CK, Wilson M. 2004b. Analysis of the effects of chlorhexidine on oral biofilm vitality and structure based on viability profiling and an indicator of membrane integrity. Antimicrobial agents and chemotherapy. 48(5):1461-1468.

Horn H, Lackner S. 2014. Modeling of biofilm systems: A review. Productive biofilms. Springer. p. 53-76.

Horn H, Reiff H, Morgenroth E. 2003. Simulation of growth and detachment in biofilm systems under defined hydrodynamic conditions. Biotechnology and Bioengineering. 81(5):607-617.

Hosford WF. 2010. Mechanical behavior of materials. Cambridge University Press.

Houari A, Di Martino P. 2007. Effect of chlorhexidine and benzalkonium chloride on bacterial biofilm formation. Letters in applied microbiology. 45(6):652-656.

Husseini A, Slot DE, Van der Weijden GA. 2008. The efficacy of oral irrigation in addition to a toothbrush on plaque and the clinical parameters of periodontal inflammation: A systematic review. International journal of dental hygiene. 6(4):304-314.

Hwang G, Klein MI, Koo H. 2014. Analysis of the mechanical stability and surface detachment of mature *Streptococcus mutans* biofilms by applying a range of external shear forces. Biofouling. 30(9):1079-1091.

Høiby N. 2014. A personal history of research on microbial biofilms and biofilm infections. Pathogens and disease. 70:205-211.

Irgens F. 2008. Continuum mechanics. Springer Science & Business Media.

Ivanoff CS, Swami Ns Fau - Hottel TL, Hottel Tl Fau - Garcia-Godoy F, Garcia-Godoy F. 2013. Enhanced penetration of fluoride particles into bovine enamel by combining dielectrophoresis with ac electroosmosis. Electrophoresis. 34(20-23):2945-2955.

Izano EA, Amarante MA, Kher WB, Kaplan JB. 2008. Differential roles of poly-n-acetylglucosamine surface polysaccharide and extracellular dna in staphylococcus aureus and staphylococcus epidermidis biofilms. Applied and Environmental Microbiology. 74:470-476.

Jahn CA. 2010. The dental water jet: A historical review of the literature. American Dental Hygienists Association. 84(3):114-120.

Jakubovics NS, Kolenbrander PE. 2010. The road to ruin: The formation of disease-associated oral biofilms. Oral diseases. 16(8):729-739.

Janmey PA, Hvidt S, Lamb J, Stossel TP. 1990. Resemblance of actin-binding protein/actin gels to covalently crosslinked networks.

Jones WL, Sutton MP, McKittrick L, Stewart PS. 2011. Chemical and antimicrobial treatments change the viscoelastic properties of bacterial biofilms. Biofouling. 27(2):207-215.

Jongsma MA, van de Lagemaat M, Busscher HJ, Geertsema-Doornbusch GI, Atema-Smit J, van der Mei HC, Ren Y. 2015. Synergy of brushing mode and antibacterial use on in vivo biofilm formation. Journal of dentistry. 43(12):1580-1586.

Kaplan JB. 2014. Biofilm matrix-degrading enzymes. Microbial Biofilms: Methods and Protocols.203-213.

Kaplan JB, Ragunath C, Ramasubbu N, Fine DH. 2003. Detachment of actinobacillus actinomycetemcomitans biofilm cells by an endogenous β-hexosaminidase activity. Journal of bacteriology. 185(16):4693-4698.

Kaplan Já. 2010. Biofilm dispersal: Mechanisms, clinical implications, and potential therapeutic uses. J Dent Res. 89:205-218.

Kara D, Luppens SBI, Cate JM. 2006. Differences between single-and dual-species biofilms of *Streptococcus mutans* and veillonella parvula in growth, acidogenicity and susceptibility to chlorhexidine. European journal of oral sciences. 114(1):58-63.

Klapper I, Dockery J. 2010. Mathematical description of microbial biofilms. SIAM review. 52(2):221-265.

Klapper I, Rupp CJ, Cargo R, Purvedorj B, Stoodley P. 2002. Viscoelastic fluid description of bacterial biofilm material properties. Biotechnology and Bioengineering. 80(3):289-296.

Kolderman E, Bettampadi D, Samarian D, Dowd SE, Foxman B, Jakubovics NS, Rickard AH. 2015. L-arginine destabilizes oral multi-species biofilm communities developed in human saliva. PloS one. 10(5):e0121835.

Kolenbrander PE, Andersen RN, Blehert DS, Egland PG, Foster JS, Palmer RJ. 2002. Communication among oral bacteria. Microbiology and Molecular Biology Reviews. 66(3):486-505.

Konovalova A, Sogaard-Andersen L. 2011. Close encounters: Contact-dependent interactions in bacteria. Molecular microbiology. 81(2):297-301.

Koza A, Hallett PD, Moon CD, Spiers AJ. 2009. Characterization of a novel air–liquid interface biofilm of pseudomonas fluorescens sbw25. Microbiology. 155(5):1397-1406.

Kreth J, Hagerman E, Tam K, Merritt J, Wong DTW, Wu BM, Myung NV, Shi W, Qi F. 2004. Quantitative analyses of *Streptococcus mutans* biofilms with quartz crystal microbalance, microjet impingement and confocal microscopy. Biofilms. 1(4):277-284.

Krumbein WE, Paterson DM, Zavarzin GA. 2003. Fossil and recent biofilms: A natural history of life on earth. Springer Science & Business Media.

Krzyściak W, Jurczak A, Kościelniak D, Bystrowska B, Skalniak A. 2014. The virulence of *Streptococcus mutans* and the ability to form biofilms. European Journal of Clinical Microbiology & Infectious Diseases. 33(4):499-515.

Körstgens V, Flemming HC, Wingender J, Borchard W. 2001. Uniaxial compression measurement device for investigation of the mechanical stability of biofilms. Journal of Microbiological Methods. 46(1):9-17.

Lahaye E, Aubry T, Kervarec N, Douzenel P, Sire O. 2007. Does water activity rule p. Mirabilis periodic swarming? I. Biochemical and functional properties of the extracellular matrix. Biomacromolecules. 8(4):1218-1227.

Lakes RS. 1998. Viscoelastic solids. CRC press.

Landau LD, Lifshitz EM. 1987. Fluid mechanics, vol. 6. Course of Theoretical Physics.227-229.

Laspidou C, Spyrou L, Aravas N, Rittmann B. 2014. Material modeling of biofilm mechanical properties. Mathematical biosciences. 251:11-15.

Latimer J, Munday JL, Buzza KM, Forbes S, Sreenivasan PK, McBain AJ. 2015. Antibacterial and anti-biofilm activity of mouthrinses containing cetylpyridinium chloride and sodium fluoride. BMC microbiology. 15(1):169.

Lau PC, Dutcher JR, Beveridge TJ, Lam JS. 2009. Absolute quantitation of bacterial biofilm adhesion and viscoelasticity by microbead force spectroscopy. Biophys J. 96:2935-2948.

Lemos JA, Quivey RG, Jr., Koo H, Abranches J. 2013. *Streptococcus mutans*: A new gram-positive paradigm? Microbiology. 159(Pt 3):436-445.

Leung V, Lévesque CM. 2012. A stress-inducible quorum-sensing peptide mediates the formation of persister cells with noninherited multidrug tolerance. Journal of bacteriology. 194(9):2265-2274.

Lewis K. 2001. Riddle of biofilm resistance. Antimicrobial Agents and Chemotherapy. 45(4):999-1007.

Lieleg O, Caldara M, Baumgärtel R, Ribbeck K. 2011. Mechanical robustness of pseudomonas aeruginosa biofilms. Soft Matter. 7(7):3307-3314.

Lippert F, Parker DM, Jandt KD. 2004. In vitro demineralization/remineralization cycles at human tooth enamel surfaces investigated by afm and nanoindentation. Journal of colloid and interface science. 280(2):442-448.

Liu IS. 2013. Continuum mechanics. Springer Science & Business Media.

Lotufo R, Calil CM, Feng HS, Sekiguchi RT, Stewart B, DeVizio W, Proskin HM. 2008. Clinical investigation of the efficacy of a commercial mouthrinse containing 0.05% cetylpyridinium chloride in preventing dental plaque. The Journal of clinical dentistry. 20(2):50-54.

Lu J. 2009. Defect of cell wall construction may shield oral bacteria's survival in bloodstream and cause infective endocarditis. Med Hypotheses. 73(6):1055-1057.

Lyczak JB, Cannon CL, Pier GB. 2002. Lung infections associated with cystic fibrosis. Clinical Microbiology Reviews. 15(2):194-222.

Lyle DM. 2012. Relevance of the water flosser: 50 years of data. Compendium of continuing education in dentistry (Jamesburg, NJ: 1995). 33(4):278-280.

Madsen JS, Burmølle M, Hansen LH, Sørensen SJ. 2012. The interconnection between biofilm formation and horizontal gene transfer. FEMS Immunology & Medical Microbiology. 65(2):183-195.

Mah T-F, Pitts B, Pellock B, Walker GC, Stewart PS, O'Toole GA. 2003. A genetic basis for pseudomonas aeruginosa biofilm antibiotic resistance. Nature. 426(6964):306-310.

Mandel ID. 1987. The functions of saliva. Journal of dental research. 66:623-627.

Marrie TJ, Nelligan J, Costerton J. 1982. A scanning and transmission electron microscopic study of an infected endocardial pacemaker lead. Circulation. 66(6):1339-1341.

Marsh PD. 2000. Role of the oral microflora in health. Microbial Ecology in Health and Disease. 12(3):130-137.

Marsh PD. 2003. Are dental diseases examples of ecological catastrophes? Microbiology. 149:279-294.

Marsh PD. 2004. Dental plaque as a microbial biofilm. Caries Research. 38:204-211.

Marsh PD. 2005. Dental plaque: Biological significance of a biofilm and community life-style. Journal of Clinical Periodontology. 32:7-15.

Marsh PD, Bradshaw DJ. 1995. Dental plaque as a biofilm. Journal of Industrial Microbiology. 15(3):169-175.

Marsh PD, Head DA, Devine DA. 2015. Dental plaque as a biofilm and a microbial community—implications for treatment. Journal of Oral Biosciences. 57(4):185-191.

Marsh PD, Martin, M V. 2009. Oral microbiology. Elsevier.

Marsh PD, Moter A, Devine DA. 2011. Dental plaque biofilms: Communities, conflict and control. Periodontology 2000. 55:16-35.

McDougald D, Rice SA, Barraud N, Steinberg PD, Kjelleberg S. 2011. Should we stay or should we go: Mechanisms and ecological consequences for biofilm dispersal. Nature Reviews Microbiology. 10(1):39-50.

Meyers MA, Chawla KK. 2009. Mechanical behavior of materials. Cambridge university press Cambridge.

Mezger TG. 2006. The rheology handbook: For users of rotational and oscillatory rheometers. Vincentz Network GmbH & Co KG.

Miles JW. 1959. On the generation of surface waves by shear flows part 3. Kelvin-helmholtz instability. Journal of Fluid Mechanics. 6(04):583-598.

Miller MB, Bassler BL. 2001. Quorum sensing in bacteria. Annual review of microbiology. 55(1):165-199.

Modesto A, Drake DR. 2006. Multiple exposures to chlorhexidine and xylitol: Adhesion and biofilm formation by *Streptococcus mutans*. Current microbiology. 52(6):418-423.

Molin S, Tolker-Nielsen T. 2003. Gene transfer occurs with enhanced efficiency in biofilms and induces enhanced stabilisation of the biofilm structure. Current opinion in biotechnology. 14(3):255-261.

Morikawa M. 2006. Beneficial biofilm formation by industrial bacteria< i> bacillus subtilis</i> and related species. Journal of bioscience and bioengineering. 101(1):1-8.

Möhle RB, Langemann T, Haesner M, Augustin W, Scholl S, Neu TR, Hempel DC, Horn H. 2007. Structure and shear strength of microbial biofilms as determined with confocal laser scanning microscopy and fluid dynamic gauging using a novel rotating disc biofilm reactor. Biotechnology and bioengineering. 98(4):747-755.

Neu TR, Poralla K. 1990. Emulsifying agents from bacteria isolated during screening for cells with hydrophobic surfaces. Applied microbiology and biotechnology. 32(5):521-525.

Nguyen PTM, Abranches J, Phan T-N, Marquis RE. 2002. Repressed respiration of oral streptococci grown in biofilms. Curr Microbiol. 44(4):262-266.

Nicolella C, Van Loosdrecht M, Heijnen J. 2000. Wastewater treatment with particulate biofilm reactors. Journal of biotechnology. 80(1):1-33.

Nobbs AH, Jenkinson HF, Jakubovics NS. 2011. Stick to your gums mechanisms of oral microbial adherence. Journal of dental research. 90(11):1271-1278.

Noffke N, Decho AW, Stoodley P. 2013. Slime through time: The fossil record of prokaryote evolution. PALAIOS. 28(1):1-5.

Noffke N, Gerdes G, Klenke T, Krumbein WE. 2001. Microbially induced sedimentary structures: A new category within the classification of primary sedimentary structures. Journal of Sedimentary Research. 71(5):649-656.

Oh Y, Jo W, Yang Y, Park S. 2007. Influence of culture conditions on escherichia coli o157: H7 biofilm formation by atomic force microscopy. Ultramicroscopy. 107(10):869-874.

Oh Y, Lee N, Jo W, Jung W, Lim J. 2009. Effects of substrates on biofilm formation observed by atomic force microscopy. Ultramicroscopy. 109(8):874-880.

Ohashi A, Harada H. 1994. Adhesion strength of biofilm developed in an attached-growth reactor. Water Science and Technology. 29(10):281-288.

Olson ME, Ceri H, Morck DW, Buret AG, Read RR. 2002. Biofilm bacteria: Formation and comparative susceptibility to antibiotics. Canadian journal of veterinary research = Revue canadienne de recherche veterinaire. 66(2):86-92.

Pandit S, Cai JN, Jung JE, Lee YS, Jeon JG. 2015. Effect of brief cetylpyridinium chloride treatments during early and mature cariogenic biofilm formation. Oral Diseases. 21(5):565-571.

Paramonova E, Kalmykowa OJ, van der Mei HC, Busscher HJ, Sharma PK. 2009a. Impact of hydrodynamics on oral biofilm strength. Journal of dental research. 88(10):922-926.

Paramonova E, Krom BP, van der Mei HC, Busscher HJ, Sharma PK. 2009b. Hyphal content determines the compression strength of candida albicans biofilms. Microbiology. 155(6):1997-2003.

Parini MR, Eggett DL, Pitt WG. 2005. Removal of *Streptococcus mutans* biofilm by bubbles. Journal of clinical periodontology. 32(11):1151-1156.

Parini MR, Pitt WG. 2006. Dynamic removal of oral biofilms by bubbles. Colloids and Surfaces B: Biointerfaces. 52:39-46.

Patel RM, Malaki Z. 2007. The effect of a mouthrinse containing essential oils on dental plaque and gingivitis. Evid-based Dent. 9(1):18-19.

Patsios SI, Goudoulas TB, Kastrinakis EG, Nychas SG, Karabelas AJ. 2015. A novel method for rheological characterization of biofouling layers developing in membrane bioreactors (mbr). Journal of Membrane Science. 482(0):13-24.

Paul E, Ochoa JC, Pechaud Y, Liu Y, Liné A. 2012. Effect of shear stress and growth conditions on detachment and physical properties of biofilms. Water research. 46(17):5499-5508.

Pavlovsky L, Sturtevant RA, Younger JG, Solomon MJ. 2015. Effects of temperature on the morphological, polymeric, and mechanical properties of staphylococcus epidermidis bacterial biofilms. Langmuir. 31(6):2036-2042.

Pavlovsky L, Younger JG, Solomon MJ. 2013. In situ rheology of staphylococcus epidermidis bacterial biofilms. Soft matter. 9(1):122-131.

Perry JA, Cvitkovitch DG, Lévesque CM. 2009. Cell death in *Streptococcus mutans* biofilms: A link between csp and extracellular dna. FEMS microbiology letters. 299(2):261-266.

Pessan JP, Alves KMRP, Italiani FdM, Ramires I, Lauris JRP, Whitford GM, Toumba KJ, Robinson C, Buzalaf MAR. 2014. Distribution of fluoride and calcium in plaque biofilms after the use of conventional and low-fluoride dentifrices. International Journal of Paediatric Dentistry. 24(4):293-302.

Peterson BW, Busscher HJ, Sharma PK, Van Der Mei HC. 2014. Visualization of microbiological processes underlying stress relaxation in pseudomonas aeruginosa biofilms. Microscopy and Microanalysis. 20(03):912-915.

Peterson BW, van der Mei HC, Sjollema J, Busscher HJ, Sharma PK. 2013. A distinguishable role of edna in the viscoelastic relaxation of biofilms. MBio. 4(5):e00497-00413.

Peyton BM, Characklis W. 1992. Kinetics of biofilm detachment. Water Science & Technology. 26(9-11):1995-1998.

Picioreanu C, Van Loosdrecht MC, Heijnen JJ. 2001. Two-dimensional model of biofilm detachment caused by internal stress from liquid flow. Biotechnology & Bioengineering. 72(2):205-218.

Pitt WG, McBride MO, Barton AJ, Sagers RD. 1993. Air-water interface displaces adsorbed bacteria. Biomaterials. 14(8):605-608.

Ponnamma D, Thomas S. 2014. Non-linear viscoelasticity of rubber composites and nanocomposites: Influence of filler geometry and size in different length scales. Springer.

Poppele EH, Hozalski RM. 2003. Micro-cantilever method for measuring the tensile strength of biofilms and microbial flocs. Journal of Microbiological Methods. 55(3):607-615.

Porada H, Ghergut J, Bouougri EH. 2008. Kinneyia-type wrinkle structures—critical review and model of formation. PALAIOS. 23:65-77.

Prakash B, Veeregowda B, Krishnappa G. 2003. Biofilms: A survival strategy of bacteria. Current science. 85(9):1299-1307.

Quivey RG, Kuhnert WL, Hahn K. 2001. Genetics of acid adaptation in oral streptococci. Critical Reviews in Oral Biology & Medicine. 12(4):301-314.

Rachid S, Ohlsen K, Witte W, Hacker J, Ziebuhr W. 2000. Effect of subinhibitory antibiotic concentrations on polysaccharide intercellular adhesin expression in biofilm-forming staphylococcus epidermidis. Antimicrobial agents and chemotherapy. 44(12):3357-3363.

Reddy JN. 2013. An introduction to continuum mechanics. Cambridge university press.

Rickard AH, Campagna SR, Kolenbrander PE. 2008. Autoinducer-2 is produced in saliva-fed flow conditions relevant to natural oral biofilms. Journal of applied microbiology. 105(6):2096-2103.

Rickard AH, Gilbert P, High NJ, Kolenbrander PE, Handley PS. 2003. Bacterial coaggregation: An integral process in the development of multi-species biofilms. Trends in microbiology. 11(2):94-100.

Rmaile A, Carugo D, Capretto L, Aspiras M, De Jager M, Ward M, Stoodley P. 2014. Removal of interproximal dental biofilms by high-velocity water microdrops. Journal of Dental Research. 93(1):68-73.

Rmaile A, Carugo D, Capretto L, Wharton JA, Thurner PJ, Aspiras M, Ward M, De Jager M, Stoodley P. 2015. An experimental and computational study of the hydrodynamics of high-velocity water microdrops for interproximal tooth cleaning. Journal of the Mechanical Behavior of Biomedical Materials. 46:148-157.

Rmaile A, Carugo D, Capretto L, Zhang X, Wharton JA, Thurner PJ, Aspiras M, Ward M, Stoodley P. 2013. Microbial tribology and disruption of dental plaque bacterial biofilms. Wear. 306(1):276-284.

Rogers S, Van Der Walle C, Waigh T. 2008. Microrheology of bacterial biofilms in vitro: Staphylococcus aureus and pseudomonas aeruginosa. Langmuir. 24(23):13549-13555.

Ruff AW, Wiederhorn SM. 1979. Erosion by solid particle impact. DTIC Document.

Rumbaugh KP, Armstrong A. 2014. The role of quorum sensing in biofilm development. Antibiofilm agents. Springer. p. 97-113.

Rupp CJ, Fux CA, Stoodley P. 2005. Viscoelasticity of staphylococcus aureus biofilms in response to fluid shear allows resistance to detachment and facilitates rolling migration. Applied and Environmental Microbiology. 71(4):2175-2178.

Russell AD, Day MJ. 1993. Antibacterial activity of chlorhexidine. Journal of Hospital Infection. 25(4):229-238.

Rölla G, Melsen B. 1975. On the mechanism of the plaque inhibition by chlorhexidine. Journal of Dental Research. 54(2 suppl):B57-B62.

Salley B, Gordon P, McCormick A, Fisher A, Wilson D. 2012. Characterising the structure of photosynthetic biofilms using fluid dynamic gauging. Biofouling. 28(2):159-173.

Salta M, Wharton JA, Blache Y, Stokes KR, Briand J-F. 2013. Marine biofilms on artificial surfaces: Structure and dynamics. Environmental Microbiology. 15:2879-2893.

Sauer K, Cullen M, Rickard A, Zeef L, Davies D, Gilbert P. 2004. Characterization of nutrient-induced dispersion in pseudomonas aeruginosa pao1 biofilm. Journal of Bacteriology. 186(21):7312-7326.

Sawyer L, Hermanowicz S. 2000. Detachment of aeromonas hydrophila and pseudomonas aeruginosa due tovariations in nutrient supply. Water Science and Technology. 41(4-5):139-145.

Scheie AA. 1989. Modes of action of currently known chemical anti-plaque agents other than chlorhexidine. Journal of Dental Research. 68:1609-1616.

Schopf JW, Packer BM. 1987. Early archean (3.3-billion to 3.5-billion-year-old) microfossils from warrawoona group, australia. Science (New York, NY). 237(4810):70-73.

Schramm G. 1994. A practical approach to rheology and rheometry. Haake Karlsruhe.

Schultz M, Bendick J, Holm E, Hertel W. 2011. Economic impact of biofouling on a naval surface ship. Biofouling. 27(1):87-98.

Sedgley C, Dunny G. 2015. Antimicrobial resistance in biofilm communities. In: Chávez de Paz EL, Sedgley MC, Kishen A, editors. The root canal biofilm. Berlin, Heidelberg: Springer Berlin Heidelberg. p. 55-84.

Senadheera D, Cvitkovitch DG. 2008. Quorum sensing and biofilm formation by *Streptococcus mutans*. Advances in experimental medicine and biology. 631:178-188.

Sharma PK, Gibcus MJ, Van Der Mei HC, Busscher HJ. 2005. Microbubble-induced detachment of coadhering oral bacteria from salivary pellicles. European journal of oral sciences. 113(4):326-332.

Silva MF, dos Santos NB, Stewart B, DeVizio W, Proskin HM. 2008. A clinical investigation of the efficacy of a commercial mouthrinse containing 0.05% cetylpyridinium chloride to control established dental plaque and gingivitis. The Journal of clinical dentistry. 20(2):55-61.

Singh PK, Parsek MR, Greenberg EP, Welsh MJ. 2002. A component of innate immunity prevents bacterial biofilm development. Nature. 417(6888):552-555.

Sjogren K, Lundberg AB, Birkhed D, Dudgeon DJ, Johnson MR. 2004. Interproximal plaque mass and fluoride retention after brushing and flossing--a comparative study of powered toothbrushing, manual toothbrushing and flossing. Oral health & preventive dentistry. 2(2):119-124.

Soumya EA, Koraichi IS, Madani K, Hassan L, Fatima H. 2012. Scanning electron microscopy (sem) and environmental sem: Suitable tools for study of adhesion stage and biofilm formation.

Spoering AL, Gilmore MS. 2006. Quorum sensing and dna release in bacterial biofilms. Current opinion in microbiology. 9(2):133-137.

Spoering AL, Lewis K. 2001. Biofilms and planktonic cells of pseudomonas aeruginosa have similar resistance to killing by antimicrobials. J Bacteriol. 183(23):6746-6751.

Sreenivasan PK, Haraszthy VI, Zambon JJ. 2013. Antimicrobial efficacy of 0· 05% cetylpyridinium chloride mouthrinses. Letters in applied microbiology. 56(1):14-20.

Srivastava R, Awasthi M, Upreti M, Mathur G. 2006. Studies on aureobasidium pullulans forming biofilm on high strength aluminium alloy, a structural component, in aircraft fuel tanks. Indian Journal of Engineering and Materials Sciences. 13(2):135.

Stanford CM, Srikantha R, Wu CD. 1996. Efficacy of the sonicare toothbrush fluid dynamic action on removal of human supragingival plaque. The Journal of clinical dentistry. 8(1 Spec No):10-14.

Stewart PS. 1993. A model of biofilm detachment. Biotechnology and Bioengineering. 41(1):111-117.

Stoeken JE, Paraskevas S, Van Der Weijden GA. 2007. The long-term effect of a mouthrinse containing essential oils on dental plaque and gingivitis: A systematic review. Journal of periodontology. 78(7):1218-1228.

Stoodley P, A Nguyen D, A Longwell M, A Nistico L, A von Ohle C, A Milanovich N, A de Jager M. 2007. Effect of the sonicare flexcare power toothbrush on fluoride delivery through *Streptococcus mutans* biofilms. Compendium of Continuing Educationin Dentistry. 28:15-22.

Stoodley P, Cargo R, Rupp CJ, Wilson S, Klapper I. 2002a. Biofilm material properties as related to shear-induced deformation and detachment phenomena. Journal of industrial microbiology & biotechnology. 29(6):361-367.

Stoodley P, deBeer D, Lewandowski Z. 1994. Liquid flow in biofilm systems. Applied and Environmental Microbiology. 60(8):2711-2716.

Stoodley P, Dodds I, Boyle JD, Lappin-Scott HM. 1998. Influence of hydrodynamics and nutrients on biofilm structure. Journal of Applied Microbiology. 85(S1):19S-28S.

Stoodley P, Hall-Stoodley L, Costerton B, DeMeo P, Shirtliff M, Gawalt E, Kathju S. 2013. Biofilms, biomaterials, and device-related infections. App Med and Medical Devices.77-102.

Stoodley P, Lewandowski Z, Boyle JD, Lappin-Scott HM. 1999a. Structural deformation of bacterial biofilms caused by short-term fluctuations in fluid shear: An in situ investigation of biofilm rheology. Biotechnol Bioeng. 65(1):83-92.

Stoodley P, Lewandowski Z, Boyle JD, Lappin-Scott HM. 1999b. The formation of migratory ripples in a mixed species bacterial biofilm growing in turbulent flow. Environmental microbiology. 1(5):447-455.

Stoodley P, Sauer K, Davies DG, Costerton JW. 2002b. Biofilms as complex differentiated communities. Annual review of microbiology. 56:187-209.

Stoodley P, Wefel J, Gieseke A, deBeer D, von Ohle C. 2008. Biofilm plaque and hydrodynamic effects on mass transfer, fluoride delivery and caries. The Journal of the American Dental Association. 139(9):1182-1190.

Stoodley P, Wilson S, Hall-Stoodley L, Boyle JD, Lappin-Scott HM, Costerton J. 2001. Growth and detachment of cell clusters from mature mixed-species biofilms. Applied and Environmental Microbiology. 67(12):5608-5613.

Sutherland IW. 2001. Biofilm exopolysaccharides: A strong and sticky framework. Microbiology. 147:3-9.

Takahashi N, Nyvad B. 2008. Caries ecology revisited: Microbial dynamics and the caries process. Caries research. 42(6):409-418.

Takenaka S, Pitts B, Trivedi HM, Stewart PS. 2009. Diffusion of macromolecules in model oral biofilms. Applied and Environmental Microbiology. 75:1750-1753.

ten Cate JM. 1997. Review on fluoride, with special emphasis on calcium fluoride mechanisms in caries prevention. European journal of oral sciences. 105(5 Pt 2):461-465.

ten Cate JM. 2006. Biofilms, a new approach to the microbiology of dental plaque. Odontology / the Society of the Nippon Dental University. 94(1):1-9.

Tenuta LMA, Del Bel Cury AA, Bortolin MC, Vogel GL, Cury JA. 2006. Ca, pi, and f in the fluid of biofilm formed under sucrose. Journal of dental research. 85(9):834-838.

Thomas JG, Nakaishi LA. 2006. Managing the complexity of a dynamic biofilm. The Journal of the American Dental Association. 137(suppl 3):10S-15S.

Thomas K, Herminghaus S, Porada H, Goehring L. 2013. Formation of kinneyia via shear-induced instabilities in microbial mats. Philosophical Transactions of the Royal Society A: Mathematical, Physical and Engineering Sciences. 371:20120362.

Towler BW, Cunningham A, Stoodley P, McKittrick L. 2007. A model of fluid–biofilm interaction using a burger material law. Biotechnology and bioengineering. 96(2):259-271.

Towler BW, Rupp CJ, Cunningham AB, Stoodley P. 2003. Viscoelastic properties of a mixed culture biofilm from rheometer creep analysis. Biofouling. 19(5):279-285.

Tuladhar TR, Paterson WR, Macleod N, Wilson DI. 2000. Development of a novel non-contact proximity gauge for thickness measurement of soft deposits and its application in fouling studies. The Canadian Journal of Chemical Engineering. 78(5):935-947.

Vacca-Smith AM, Venkitaraman AR, Quivey Jr RG, Bowen WH. 1996. Interactions of streptococcal glucosyltransferases with α-amylase and starch on the surface of saliva-coated hydroxyapatite. Archives of Oral Biology. 41(3):291-298.

Vaishnav R, Patel D, Atabek H, Deshpande M, Plowman F, Vossoughi J. 1983. Determination of the local erosion stress of the canine endothelium using a jet impingement method. Journal of biomechanical engineering. 105(1):77-83.

Van der Weijden GA, Timmerman MF, Danser MM, Piscaer M, Ijzerman Y, Van der Velden U. 2005. Approximal brush head used on a powered toothbrush. Journal of clinical periodontology. 32(3):317-322.

Van Loveren C. 2001. Antimicrobial activity of fluoride and its in vivo importance: Identification of research questions. Caries Res. 35 Suppl 1:65-70.

Van Oss C, Good R, Chaudhury M. 1986. The role of van der waals forces and hydrogen bonds in “hydrophobic interactions” between biopolymers and low energy surfaces. Journal of Colloid and Interface Science. 111(2):378-390.

Vinogradov AM, Winston M, Rupp CJ, Stoodley P. 2004. Rheology of biofilms formed from the dental plaque pathogen *Streptococcus mutans*. Biofilms. 1(01):49-56.

Vitkov L, Hermann A, Krautgartner WD, Herrmann M, Fuchs K, Klappacher M, Hannig M. 2005. Chlorhexidine-induced ultrastructural alterations in oral biofilm. Microsc Res Tech. 68(2):85-89.

Volle C, Ferguson M, Aidala K, Spain E, Nunez M. 2008. Spring constants and adhesive properties of native bacterial biofilm cells measured by atomic force microscopy. Colloids and Surfaces B: Biointerfaces. 67(1):32-40.

von Ohle C, Gieseke A, Nistico L, Decker EM, deBeer D, Stoodley P. 2010. Real-time microsensor measurement of local metabolic activities in ex vivo dental biofilms exposed to sucrose and treated with chlorhexidine. Applied and Environmental Microbiology. 76(7):2326-2334.

Wang Q, Zhang T. 2010. Review of mathematical models for biofilms. Solid State Communications. 150(21):1009-1022.

Waters MS, Kundu S, Lin NJ, Lin-Gibson S. 2013. Microstructure and mechanical properties of in situ *Streptococcus mutans* biofilms. ACS applied materials & interfaces. 6(1):327-332.

Watson PS, Pontefract HA, Devine DA, Shore RC, Nattress BR, Kirkham J, Robinson C. 2005. Penetration of fluoride into natural plaque biofilms. Journal of dental research. 84(5):451-455.

Wei S, Chik F. 1989. Fluoride retention following topical fluoride foam and gel application. Pediatric dentistry. 12(6):368-374.

Wentland EJ, Stewart PS, Huang C-T, McFeters GA. 1996. Spatial variations in growth rate within klebsiellapneumoniae colonies and biofilm. Biotechnology Progress. 12(3):316-321.

Whittaker CJ, Klier CM, Kolenbrander PE. 1996. Mechanisms of adhesion by oral bacteria. Annual review of microbiology. 50(1):513-552.

Wilson M. 2001. Bacterial biofilms and human disease. Science progress. 84(3):235-254.

Wingender J, Neu TR, Flemming H-C. 2012. Microbial extracellular polymeric substances: Characterization, structure and function. Springer Science & Business Media.

Wloka M, Rehage H, Flemming HC, Wingender J. 2004. Rheological properties of viscoelastic biofilm extracellular polymeric substances and comparison to the behavior of calcium alginate gels. Colloid Polym Sci. 282(10):1067-1076.

Young R. 1975. Biological apatite vs hydroxyapatite at the atomic level. Clinical orthopaedics and related research. 113:249-262.

Zalewska A, Zwierz K, Zółkowski K, Gindzieński A. 1999. Structure and biosynthesis of human salivary mucins. Acta Biochimica Polonica. 47(4):1067-1079.

Zhang T, Cogan N, Wang Q. 2008a. Phase field models for biofilms. Ii. 2-d numerical simulations of biofilm-flow interaction.

Zhang T, Cogan NG, Wang Q. 2008b. Phase field models for biofilms. I. Theory and one-dimensional simulations. SIAM Journal on Applied Mathematics. 69(3):641-669.

Zimmer S, Strauss J, Bizhang M, Krage T, Raab WM, Barthel C. 2005. Efficacy of the cybersonic in comparison with the braun 3d excel and a manual toothbrush. Journal of Clinical Periodontology. 32(4):360-363.

CHAPTER 4

Streptococcus mutans biofilm transient viscoelastic fluid behaviour during high-velocity microsprays

S. Fabbri[1], D.A. Johnston[2], A. Rmaile[3], B. Gottenbos[3], M. De Jager[3], M. Aspiras[4], E. M. Starke[5], M. T. Ward[5] and P. Stoodley[1, 6]

[1]National Centre for Advanced Tribology at Southampton (nCATS), University of Southampton, Southampton SO17 1BJ, United Kingdom.
[2]Biomedical Imaging Unit, School of Medicine, University of Southampton, Southampton SO16 6YD, UK.
[3]Philips Research, High Tech Campus, Eindhoven 5656 AE, The Netherlands.

[4]Wrigley, Chicago, Illinois 60613, USA.

[5]Philips Oral Healthcare, Bothell, Washington 98021, USA.

[6]Department of Microbial Infection and Immunity and the Department of Orthopaedics, Centre for Microbial Interface Biology, The Ohio State University, Columbus, Ohio 43210, USA.

ABSTRACT

Using high-speed imaging we assessed *Streptococcus mutans* biofilm-fluid interactions during exposure to a 60-ms microspray burst with a maximum exit velocity of 51 m/sec. *S. mutans* UA159 biofilms were grown for 72 h on 10 mm-length glass slides pre-conditioned with porcine gastric mucin. Biofilm stiffness was measured by performing uniaxial-compression tests. We developed an in-vitro interproximal model which allowed the parallel insertion of two biofilm-colonized slides separated by a distance of 1 mm and enabled high-speed imaging of the removal process at the surface. *S. mutans* biofilms were exposed to either a water microspray or an air-only microburst. High-speed videos provided further insight into the mechanical behaviour of biofilms as complex liquids and into high-shear fluid-biofilm interaction. We documented biofilms extremely transient fluid behaviour when exposed to the high-velocity microsprays. The presence of time-dependent recoil and residual deformation confirmed the pivotal role of viscoelasticity in biofilm removal. The air-only microburst was effective enough to remove some of the biofilm but created a smaller zone of clearance underlying the importance of water and the air-water interface of drops moving over the solid surface in the removal process. Confocal and COMSTAT analysis showed the high-velocity water microspray caused up to a 99.9 % reduction in biofilm thickness, biomass and area coverage, within the impact area.

4.1 INTRODUCTION

Dental plaque biofilms are the heterogeneous bacterial communities attached to teeth and soft tissues and embedded in a matrix composed mainly of extracellular DNA, proteins, and polysaccharides (Marsh and Bradshaw 1995). Oral biofilms are associated with the development of caries, gingivitis and periodontitis (Costerton et al. 1995; Donlan and Costerton 2002). Dental caries occurs through the dissolution of the enamel by acidogenic bacteria such as *Streptococcus mutans*, *Streptococcus sobrinus*, and lactobacilli (Featherstone 1999). Biofilm complex structure makes dental diseases difficult to control and to eradicate, thus becoming a worldwide public health problem (Selwitz et al. 2007). When biofilms are subjected to different flow conditions, they mechanically behave as viscoelastic fluids (Peterson et al. 2015; Towler et al. 2003; Wilking et al. 2011). This means that at low-shear rates biofilms have a "solid-like" behaviour and are able to store energy, while at high-shear rates they become "fluid-like" and lose their ability to store elastic energy. Energy dissipation through viscoelasticity is an important characteristic because it allows biofilms to tolerate rapidly-changing shear stresses without detaching from the surface. In dentistry, fluid shear stresses generated via either non-contact toothbrushing or fluid flow play a major role in biofilm detachment (Hope et al. 2003; Hope and Wilson 2003; Paramonova et al. 2009) since dental plaque mainly accumulates in particular areas inside the mouth (such as pits, fissures, interproximal (IP) spaces and subgingival areas) inaccessible for toothbrush bristles and dentifrices (Fried 2012). Therefore, the understanding of biofilm mechanical properties under various hydrodynamic flows represents an important part for the design of more effective strategies to remove and to control dental plaque biofilms. Oral irrigators, which generate a continuous pulsating or steady water jet designed to remove interdental and subgingival plaque are widely used as a supplement to toothbrushing, or to replace traditional flossing (Barnes et al. 2005; Jahn 2010). More recently, mechanical biofilm removal either using low volume, high-velocity water droplets (Cense et al. 2006) or by entrained air bubbles (Parini and Pitt 2006; Sharma et al. 2005b) has shown positive results due to the droplets' impact pressure, hydrodynamic shear stresses and the surface tension effects of the passage of an air-water interface over a solid surface (Busscher et al. 2010).

In previous studies we grew *S. mutans* biofilms on and between two central incisors of a periodontal model to recreate the realistic geometry of the IP space (Rmaile et al. 2013). Then we performed high-speed imaging to assess biofilm removal and viscoelastic behaviour during the exposure to high-velocity microbursts (Rmaile et al. 2014). We also performed Computational Fluid Dynamics (CFD) simulations to predict wall shear stresses generated over the tooth surface during the burst (Rmaile et al. 2015). However, due to the opaque nature of the surface we could not see the details of biofilm removal process at the surface. Here we developed an *in vitro* IP model allowing the parallel insertion of two biofilm-colonized glass slides which could be monitored through the side of the slide by a high-speed camera (HSC). Biofilms were exposed to high-velocity water microsprays or air-only microbursts to assess the effects of these different fluid flows on the biofilm-burst interactions and biofilm viscoelastic mechanical behaviour with respect to the removal process.

4.2 MATERIALS AND METHODS

4.2.1 Bacteria and growth media

Biofilms were inoculated with a *S. mutans* UA159 (ATCC 700610) adjusted overnight culture (10^6 cfu/mL) grown in a 2 % sucrose-supplemented brain-heart infusion (BHI+S medium) (Sigma-Aldrich). 1% porcine gastric mucin (Type II, Sigma-Aldrich) was added to the BHI+S medium (BHI+SM medium). Petri plates or microscope glass slides were conditioned with 10 mL of the BHI+SM medium for 24 h to allow mucins to cover the surface. Then, biofilms were grown in static conditions for 72 h at 37 °C and 5 % CO_2 with BHI+SM medium replacement every 24 h. We also grew biofilms on non-mucin conditioned plates and in BHI+S medium (control *S. mutans* biofilms) to assess the influence of mucin on the mechanical properties.

4.2.2 Uniaxial compression tests

Uniaxial compression experiments were performed on control *S. mutans* biofilms and on *S. mutans* biofilms grown on mucin-conditioned petri plates and with mucin-supplemented medium using an Electroforce 3200 testing instrument (Bose). Since biofilms are known to be viscoelastic materials and their mechanical behaviour varies with the strain rate applied, we performed uniaxial compression experiments at a constant rate of 0.05 mm/s. An upper cylindrical plunger of a diameter (D) of 7.75 mm compressed the biofilm and a 5 N capacity load cell (Honeywell Sensotec, Columbus, OH, USA) recorded the resulted force. Biofilm stiffness under constant strain rate was measured calculating the Young’s modulus (E) from the stress-strain curves as previously described (Rmaile et al. 2013). Six independent replicate experiments were performed (n=6). Statistical analysis was performed using unpaired two samples t-test for normally distributed data and difference considered significant where $p < 0.05$.

4.2.3 In vitro IP model and high-velocity microsprays

To allow high-speed camera imaging at the surface we developed an *in vitro* IP model (Figure 4.1). The model consisted of a rectangular clear plastic holder, in which two grooves were made for the parallel insertion of two *S. mutans* biofilm-colonized slides at a distance of 1 mm. Slides were cut at 10 mm (10 mm-length slice) as a representative length, in the outside-in direction, of the proximal surface of the human molars. Since most of the biofilm was rapidly cleared from the 10 mm length of the slide we also grew *S. mutans* biofilms on full-length slides (75 mm × 25 mm) in order to more clearly assess the fluid nature of the biofilm which was most evident at the interface between the spray and the biofilm. Prior to the insertion into the IP model, the initial thickness of the biofilm was 51.8 ± 9.1 µm (mean ± 1SD, n=9), measured by COMSTAT from 3D confocal images (see Section 4.2.6). A Philips Sonicare AirFloss (AF) commercially available oral hygiene device was used to generate high-velocity microsprays. The device was filled either with water to generate a water microspray, as per normal use of the device, or was left empty in order to generate an air-only microburst.

4.2.4 ***S. mutans*** **biofilms exposure to high-speed microsprays**

The dental cleaning device was positioned in order to have the tip centred between the two biofilm-covered slides inside the IP model (Figure 4.1). The shooting was recorded at 8000 frames per seconds (fps) with a high-speed camera MotionPro X3 (IDT) equipped with a Sigma 105 mm f/2.8 EX DG Macro lens. To characterize the hydrodynamic of the flow during the water microspray, high-speed images were also taken of the burst into open air.

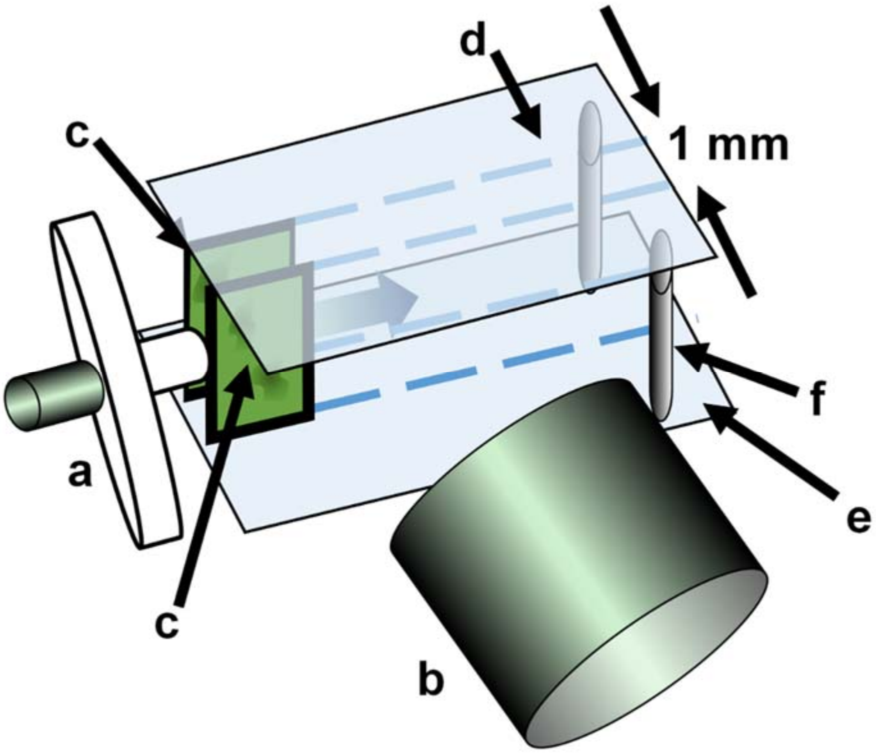

Figure 4.1. Schematic showing the juxtaposition of the IP model, the tip of the AirFloss (a) and the lens of the hyperspectral camera (b). The IP model was made up of two biofilm-colonized microscope slides (in green) (c) held in parallel grooves in top and bottom plates (d and e) to make a 1-mm gap. The slides length represented in this schematic is 10 mm. Two support pillars were placed at the back of the holder (f). The collar holding the AirFloss neck to the bottom plate (e) so that the tip was firmly abutted to the IP gap is not shown for clarity. The direction of the microspray though the IP space is indicated by the blue arrow.

4.2.5 High-speed video post-processing

The HSC videos were converted in Fiji (freely downloadable in http://fiji.sc/Fiji, (Schindelin et al. 2012)) to a stack with each frame in the stack being a different time (T) so that the volume could be represented as XYT co-ordinates. The external diameter of the nozzle tip (d_{AF} = 2 mm) was used as an internal scale to calibrate pixels with microns.

In order to characterize the water microspray hydrodynamic, a water microspray average velocity (u) was defined as $u = \Delta X / \Delta T$ (4.1), where ΔX is the microspray length variation along the X axis and ΔT is the time interval between the two adjacent frames. A Reynolds number (Re) was also measured using the Reynolds equation for free jets:

$$\mathrm{Re} = \frac{u\rho \mathrm{D}}{\mu} \tag{4.2}$$

where ρ and μ are the density (998 kg/m^3) and the viscosity (1.003 x 10^{-3} Pa·s) of water at 20°C and D is the Airfloss tip internal diameter (1 mm). Videos were analysed from five independent experiments (n=5).

The microsprays generated a zone of clearance (ZOC) in the area where the biofilm was removed. The area of the zone of clearance (A_{ZOC}) was measured as a function of the time in each frame every 5 ms. Using the Threshold function in Fiji only the cleared zone was selected in each frame. Then A was measured using the Measure function. Videos were analysed from three independent experiments (n=3). Statistical analysis was performed using unpaired two samples t-test for normally distributed data and difference considered significant where $p < 0.05$.

Biofilm recoil was measured using the reslice function which creates a time-trace along a defined line. As the biofilm recoiled towards the cleared zone it makes a continuous curve from the left to the right. Biofilm total recoil was defined as the difference between the final and initial length. Videos were analysed from three independent experiments (n=5 measurements per repeat). Statistical analysis was performed using unpaired two samples t-test for normally distributed data and difference considered significant where $p < 0.05$.

4.2.6 Confocal and scanning electron microscope analysis

The thickness of the control biofilms (unexposed to a spray or air jet) and those biofilms on the 1 cm slide immediately after the shooting were carefully transferred to petri plates filled with 1 % (wt/vol) phosphate-buffered saline (PBS) solution (Sigma-Aldrich). Then, the samples were fixed by the addition of 100 µL of 4 % (wt/vol) paraformaldehyde (PFA) solution (Agar Scientific) and left for 1 h inside the fridge. Afterwards, the biofilm slides were rinsed twice with 1 % PBS in order to disrupt loosely-adherent bacteria. To visualize dead cells in the biofilm, slides were immersed in a 0.2 % solution of Propidium iodide (PI, Live/Dead BacLight Bacterial Viability Kit, Invitrogen) for 30 minutes, washed three times with 1 % PBS and then covered immediately with mowiol mounting medium (20 gr of mowiol powder, 88 mL of 1 % PBS solution, 40 mL of Glycerol and 2.4 mL of 5 % Citifluor solution). Mowiol mounting medium is not only optically appropriate (non-absorbing, containing no autofluorescence, or light scattering), but also has an anti-fade agent which is capable of reducing light-induced fading of the fluorophore. Immediately after, the samples slides were covered with a microscope coverslip and left in the fridge for 24 h in order to settle the mountant uniformly over the whole slide. Then, the samples were imaged using an inverted Leica DMI600 SP5 confocal scanning laser microscope (CSLSM, Leica Microsystems) using a HCX PL APO CS 63x/1.3 NA glycerol immersion lens. Three random confocal images were taken on each of three independent replicate control (not exposed to the spray) biofilm slides to establish the thickness of the biofilm prior to the shooting (Figure 4.2A). For the independent triplicate spray-exposed biofilm slides, confocal images were taken inside the zone of clearance, at 1, 5 and 8 mm distances directly downstream from the nozzle, from the leading edge of the slide (Figure 4.2B). Thus the experiments were replicated three times with triplicate repeated confocal images for each position within each replicate.

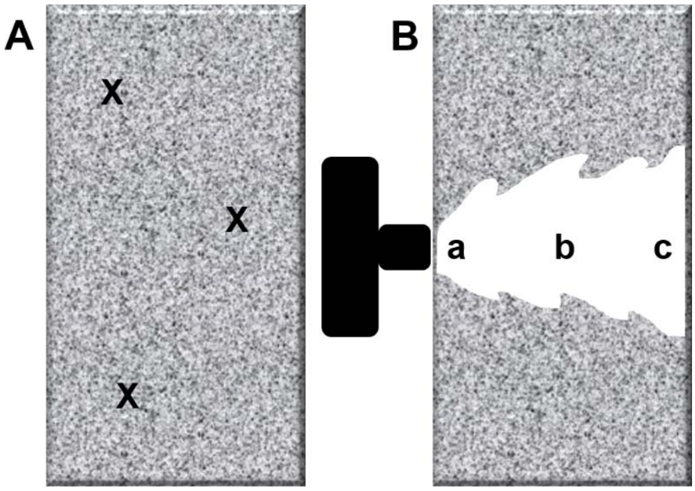

Figure 4.2. A) Schematic illustrating a S. mutans biofilm covered slide (10 mm × 25 mm) prior the shooting. Three random confocal images (X) were taken on the non-exposed slide. B) Schematic illustrating a S. mutans biofilm covered slide (10 mm × 25 mm) after the shooting. Confocal images were taken at 1 mm (a), 5 mm (b) and 8 mm (c) from the leading edge of the slide. Biofilm is depicted grey while the biofilm zone of clearance white.

The amount of biofilm removed by the water microspray was quantified by comparing biofilm thickness (T), surface area (A) and biomass (B) of non-exposed control slides and slides after the shooting by analysing the confocal images with the Matlab plugin COMSTAT (Heydorn et al. 2000). The percent reduction in biofilm thickness (%RT), biomass (%RB) and surface area (%RA) were also measured as:

$$\%\,\mathrm{RT} = \frac{\mathrm{T}_0 - \mathrm{T}_{CZ}}{\mathrm{T}_0} \times 100 \tag{4.3}$$

$$\% \text{ RB} = \frac{B_0 - B_{CZ}}{B_0} \times 100 \tag{4.4}$$

$$\% \text{ RA} = \frac{A_0 - A_{CZ}}{A_0} \times 100 \tag{4.5}$$

where T_0, B_0, A_0 and T_{CZ}, B_{CZ}, A_{CZ} are biofilm thickness, surface area and biomass prior the and after the shooting respectively.

We compared the thickness of the control (un-shot) biofilm with that at each of these distances using a t-test on an n=3 for the control and an n=3 for the experiment biofilms. In addition, we did a t-test to establish that there was no significant difference between the biofilm thicknesses at the three different distances from the nozzle after shooting ($p>0.05$) and so also grouped these values to compare the mean thickness within the cleared area with that of the thickness in the unexposed control biofilm (n=9).

A Scanning Electron Microscope (SEM, FEI Quanta-200) was also used to qualitatively assess biofilm removal in high resolution.

4.3 RESULTS

4.3.1 *S. mutans* biofilm structure and mechanical properties

The biofilm structure was similar to that reported previously (Rmaile et al. 2014; Rmaile et al. 2013) and consisted of a dense base layer of cells interspersed with prominent clusters separated by water channels. At 3 days, the unexposed *S. mutans* biofilm was 51.8 ± 4.9 µm (n=9) thick. The load-displacement curves under constant strain rate showed a linear behaviour (Figure 4.3) with a Young's modulus of 760 ± 201 kPa for the mucin grown biofilm and 800 ± 200 kPa for the non-mucin grown biofilm. These differences were not significant ($p > 0.05$, n=6).

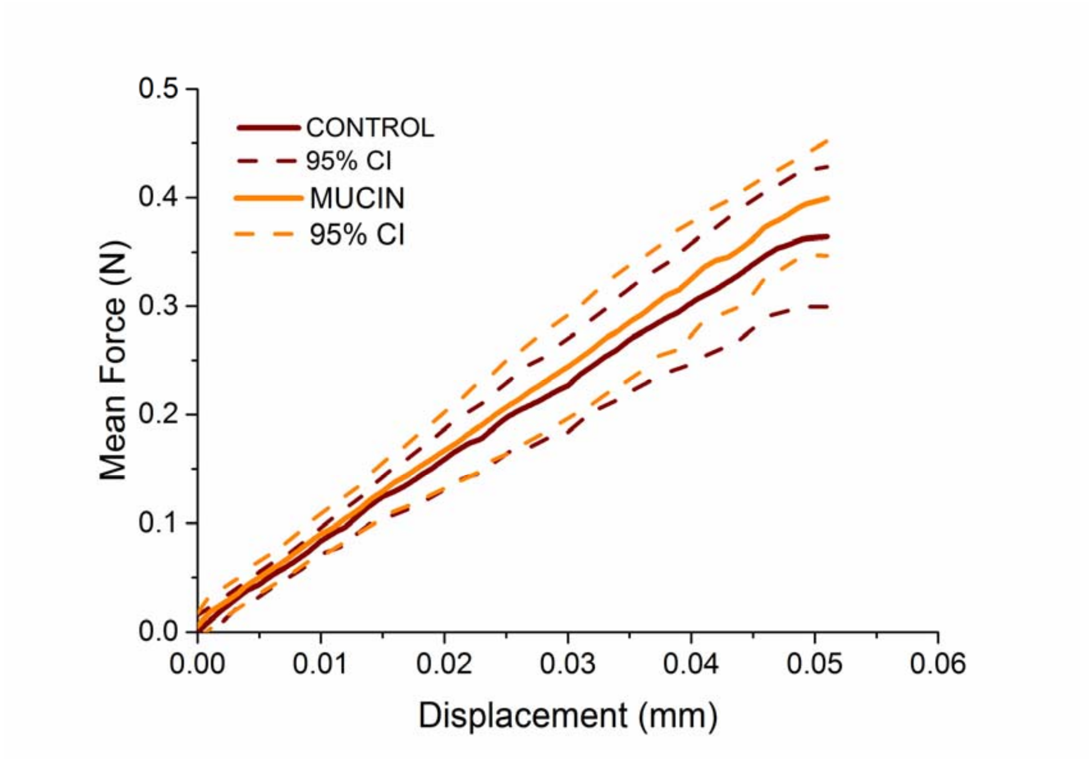

Figure 4.3. Load-versus-displacement curves of 3-days old S. mutans biofilms grown on mucin-conditioned plates or non-mucin conditioned plate from uniaxial compression experiments performed under a constant strain rate of 0.05 mm/s. The solid lines are the average of 5 mechanical tests and the dashed lines are the 95% confidence intervals.

4.3.2 High-velocity water microspray hydrodynamics

High-speed videos of the water microspray into air showed two distinct phases (Movie 1). The first phase was a 10.5 ms (± 0.3 ms, n=5) water jet, while the second phase was a 45.9 ms (± 0.8 ms, n=5) water spray (Figure 4.4A). The total microspray time interval (Δt) was 56.8 ms (± 0.6 ms, n=5). For the jet phase, the water microspray average velocity (u) started from a value of 36.6 m/s (± 6.2 m/s, n=5) and decreased to a minimum value of 31.7 m/s (± 6.8 m/s, n=5) before increasing to a maximum value of 51.1 m/s (± 6.3 m/s, n=5) (Figure 4.4B). The exit-velocity profile of the spray phase was less variable over time, and started from a maximum of 12.9 m/s (± 1.7 m/s, n=5) decreasing to 10.9 m/s (± 3.9 m/s, n=5). The Re number calculated for the jet phase ranged from 30,000 to 50,000 predicting fully-developed turbulent flow.

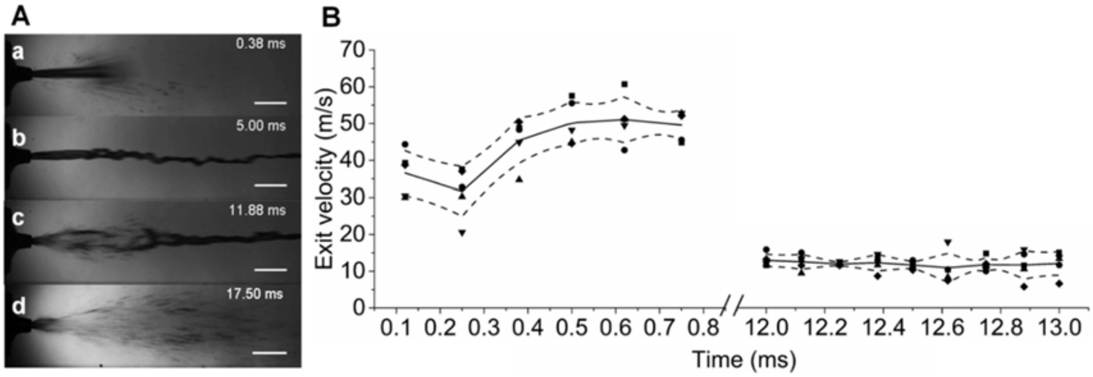

Figure 4.4. A) Individual frames from a high-speed camera video of the AirFloss water microspray as a free-jet into air at different time points. a) Initiation of the burst. b) Fully-developed jet phase. c) Transition phase from water jet to water spray. d) Spray phase. Scale bar = 5 mm. B) Water microspray exit velocity as a function of the time for the first part of the jet phase (0-0.8 ms) and the spray phase (12-13 ms). The solid lines is the average exit velocity and the dashed lines are 95% confidence intervals. Individual data from 5 independent runs shown as various symbols.

4.3.3 *S. mutans* biofilm viscoelastic fluid-like behaviour

High-speed videos of biofilms exposed to high-velocity microsprays revealed that the water microspray and the air-only microburst rapidly entered the IP channel pushing the biofilm outwards towards the distal end of the slide, creating a biofilm cleared zone. The microsprays appeared to cause the biofilms to liquefy and flow over the slide in an extremely short period of time (< 60 ms). We observed wave-like structures forming at the biofilm/fluid interface for the entire burst duration (Figure 4.5A and Movie 2). Also vortices were seeing developing in a very short time (<5 ms) at the edges of the remaining biofilm (Figure 4.5B and Movie 3). When the microspray ended, these structures disappeared and left no trace of their formation on the slide surface, suggesting biofilm fluidisation can be an extremely transient mechanical behaviour.

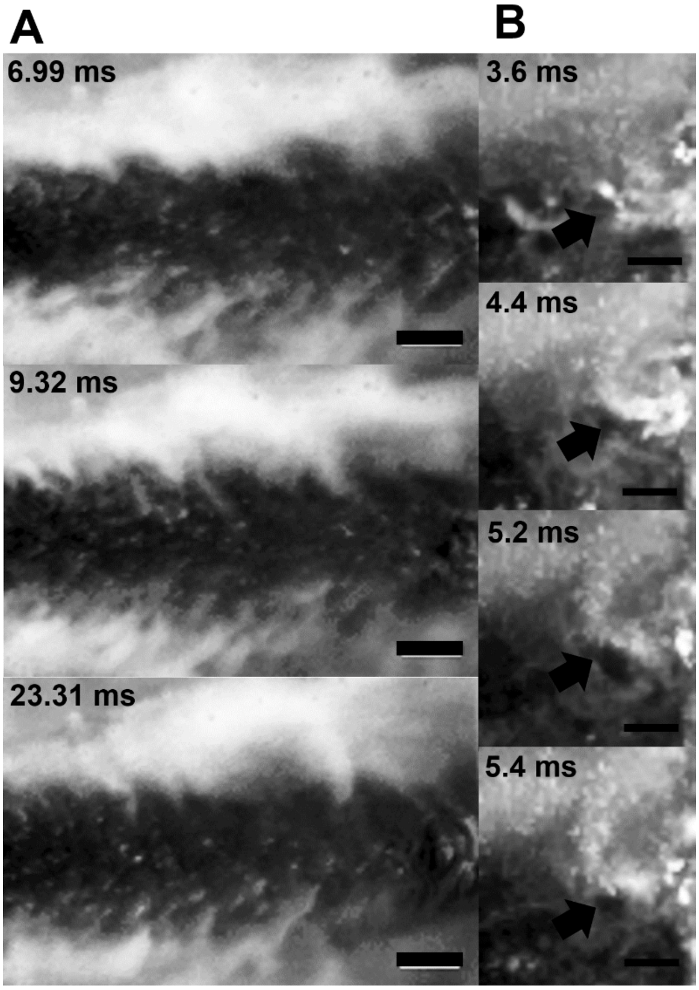

Figure 4.5. Cropped areas from individual frames from two high-speed camera videos showing S. mutans biofilm fluid behaviour when exposed to a high-velocity water microspray. The S. mutans biofilm appeared whitish grey and the zone of clearance was black. The flow was left to right. The microspray caused the transient formation of wave-like patterns (A) or vortices (B) at the biofilm/fluid interface. Scale bars are 1 mm and 0.5 mm for panels A and B respectively.

Biofilm fluid behaviour was also observed at the edge of the microscope slides where biofilm was seen dripping out and creating droplets which were pushed out of the IP space (Figure 4.6 and Movie 4). Biofilm drops were seen first stretching and then breaking off.

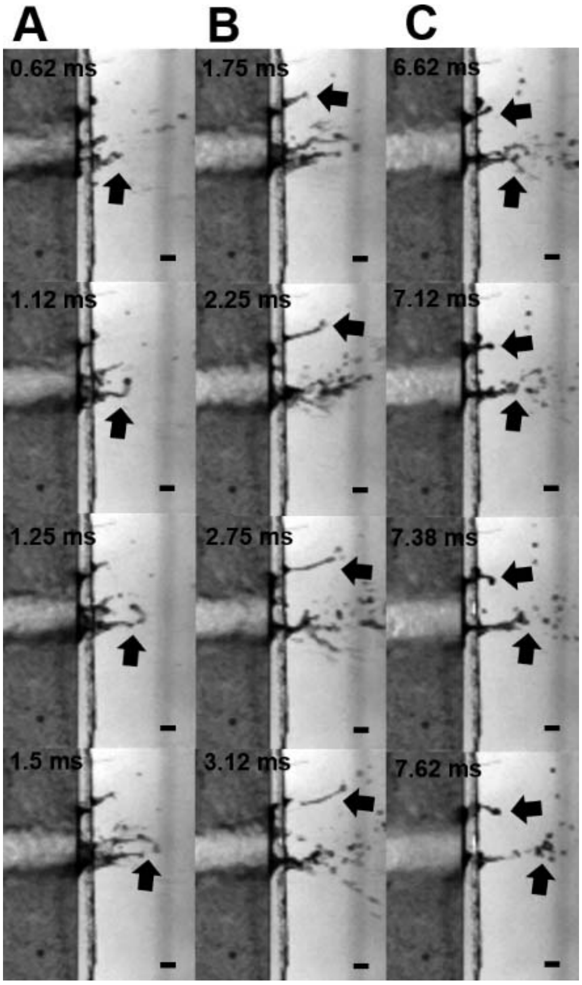

Figure 4.6. Cropped area from individual frames from a high-speed camera video showing three different sequences (A, B and C) of S. mutans biofilm fluid behaviour during the exposure to an air-only microburst. The flow was left to right. As the biofilm was pushed out of the IP space, it formed droplets which first elongated and then broke off (black arrows). Scale bar is 1 mm.

Immediately after the microspray ended, the biofilms exhibited viscoelastic behaviour by undergoing a time-dependant elastic recoil, which caused a reduction in the width of the cleared channel (Figure 4.7A and Movie 5). Reslice graphs showed an exponential increase in biofilm elongation (recoil) across the spray direction (Figure 4.7B). The rate of recoil was similar to that of a viscoelastic creep recovery (Towler et al. 2003). Biofilm total recoil was 0.41 mm (± 0.22, n=15 from three independent replicates) in approximately 15 ms.

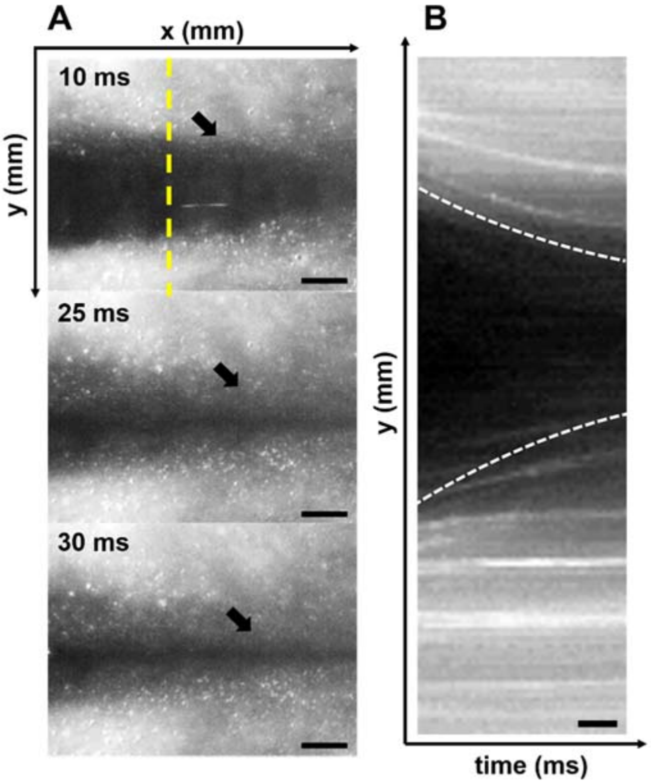

Figure 4.7. Images from a high-speed camera video showing biofilm viscoelastic recoil after the air-only microburst spray. A) Subsequent frames show the biofilm move back into back into the previously cleared channel. Scale bar = 1 mm. B). Time trace using the FIJI "reslice function" taken perpendicularly across the cleared channel (indicated by the yellow dashed line in panel A) showing the time-dependant biofilm recoil. Scale bar = 10 mm. The recovery of back into the cleared channel from both sides of the channel is indicated by the white-dashed lines and appears similar to that of an exponential decay function characteristic of viscoelastic creep recovery

4.3.4 *S. mutans* biofilm removal

High-speed camera videos of *S. mutans* biofilms removal from the 1-cm length slides showed a different removal process when exposed to a water microspray or an air-only microburst (Figure 4.8A-C and Movie 6 and Movie 7). Biofilm cleared area caused by the water microspray initial "jet" phase (Δt ~ 10 ms) created a relatively straight channel through the biofilm clearing an area of 32.6 mm^2 (± 6.3 mm^2, n=3) at a constant rate of removal. In the second "spray" phase (Δt ~ 45 ms) the zone of clearance flared out thus that a further area of 8.2 mm^2 (± 2.1 mm^2, n=3) was removed over an additional 20 ms. There was little further clearance over the remaining 25 ms of the burst. A total area of 40.8 mm^2 (± 0.9 mm^2, n=3) was cleared of biofilm at the end of the water microspray (Δt ~ 55 ms). In contrast, the air-only microburst only generated a straight channel through the biofilm, with less biofilm being "forced" off the edge of the slide, resulting in a cleared area of 11.7 ± 0.9 mm^2 after approximately 30 ms (Figure 4.8D). The final biofilm zone of clearance generated by the water microspray was approximately 20 times greater than the one created by the air-only microburst ($p < 0.05$, n=3).

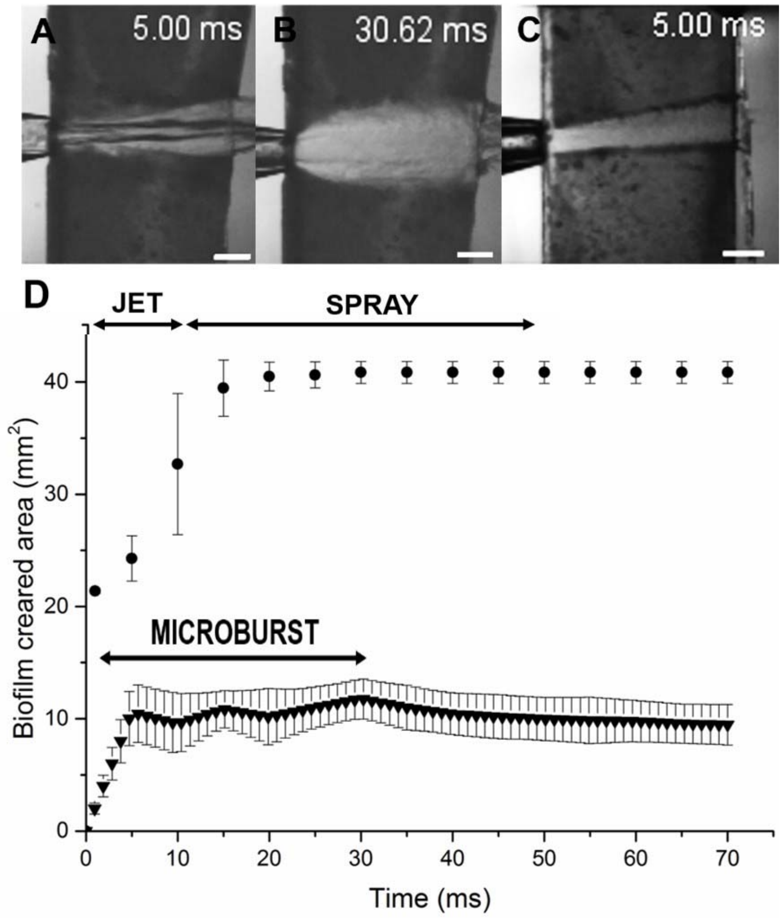

Figure 4.8. Individual frames showing S. mutans biofilm exposure to a high-speed water microspray (A-B) or air-only microburst (C) into the IP model space. Frames show S. mutans biofilm-colonized slide proximal to the camera (biofilm depicted as dark grey and biofilm zone of clearance depicted as white). The AirFloss nozzle tip was located at the left edge of the slide. A) Jet phase creating a straight zone of clearance. B) Spray phase generating a conical zone of clearance. C) Air-only microburst generating a straight zone of clearance. Scale bar = 2 mm. D) Mean biofilm cleared area as a function of the time during the water microspray (dots) and the air-only microburst (triangles). Data points represent the mean of triplicate experimental repeats with standard error bars. Data were statistically different in each time point ($p < 0.05$, n=3).

4.3.5 Microscopic evaluation of biofilm removal

SEM micrographs of biofilms grown on a 1-cm length slide and exposed to a single microburst revealed a zone of clearance with well-defined edges (Figure 4.9A). Higher magnification revealed that there were some small clusters and single bacterial cells remaining on the surface in the centre of the cleared area. Confocal micrographs were in agreement with SEM images and allowed the remaining biofilm to be quantified from the 3D stack (Figure 4.9B).

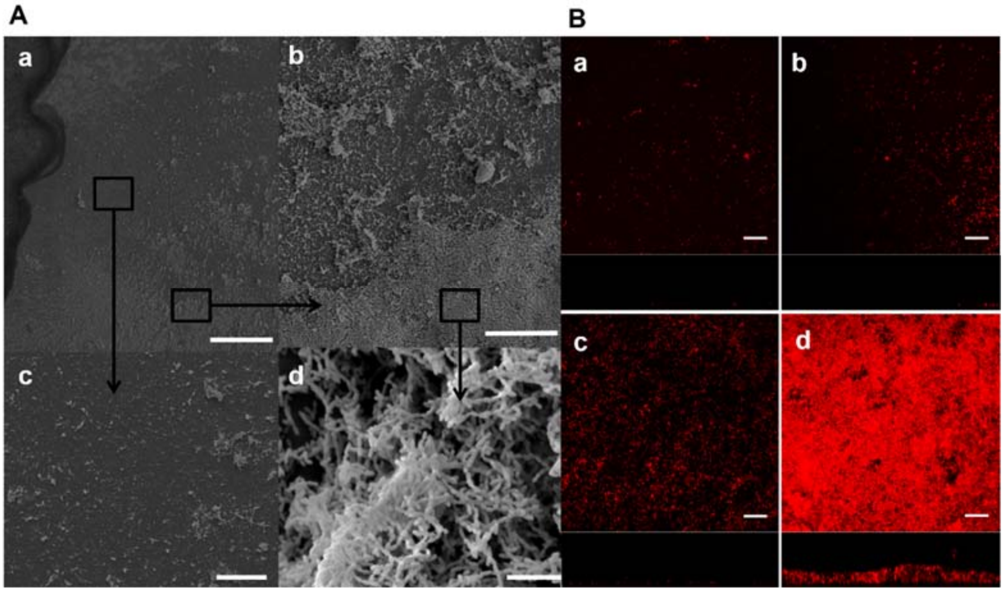

Figure 4.9. A) Scanning electron microscopy images of a representative slide exposed to a single water microspray burst. a) Lower magnification of the zone of clearance. The leading edge of the slide was located at the left as represented in Figure S2. Scale bar = 500 µm. b) Higher magnification SEM of the edge delimiting the zone of clearance showing a reduction of biofilm but with remaining clusters and single cells. Scale bar = 100 µm. c) Inside the zone of clearance only small clusters and single cells remained. Scale bar = 100 µm. d) Biofilm composed of dense clusters and chains of cocci in the unexposed area away from the microburst. Scale bar = 50 µm. B) Confocal images in x-y plan view with x-z cross section below at distances of a) 1 mm, b) 5 mm and c) 8 mm from the microspray inlet (see Figure 4.2B) An image of the biofilm in an unexposed area. Scale bar = 100 µm.

Quantification of *S. mutans* biofilms removal in the exposed area caused by the high-speed water microspray showed a significant reduction in terms of thickness, biomass and surface area compared to the unshot sample (Table 4.1). No statistical difference was observed between the 1 mm, 5 mm and 8 mm positions in terms of biofilm thickness, biomass and area coverage ($p < 0.05$, n=3). Therefore, we measured thickness, biomass and surface area in the exposed zone by grouping together the data from the different positions (n=9 from three independent replicates).

Sample	**Location**	**THICKNESS (µm)**	**BIOMASS (µm^3/µm^2)**	**AREA (10^5 x µm^2)**	**RT (%)**	**RB (%)**	**RA (%)**
Unexposed control	**Random (n=9)**	51.79±9.01	28.53±5.86	0.41±0.14	-	-	-
Exposed	**1 mm from nozzle (n=3)**	**0.38 ±0.49**	**0.25±0.29**	**0.11±0.10**	99.2±0.9	99.1±1.0	99.4±0.4
	5 mm from nozzle (n=3)	**0.03±0.03**	**0.03±0.02**	**0.25±0.21**	99.9±0.1	99.9±0.1	99.7±0.2
	8 mm from nozzle (n=3)	**0.13±0.14**	**0.07±0.06**	**41.05±13.22**	99.7±0.26	99.7±0.2	99.3±0.5
	Combined (n=9)	**0.16 ±0.24**	**0.10±0.15**	**0.20±0.15**	99.7±0.5	99.6±0.5	99.5±0.4

Table 4.1. Thickness, biomass, surface area and relative percent reductions of S. mutans biofilms prior and after the high-speed microspray exposure. Experimental data reported as mean and 1 standard deviation. Values marked in bold were statistically different from the unexposed controls ($p < 0.05$).

4.4 DISCUSSION

The *in vitro* IP model successfully simulated a simplified geometry of an interproximal biofilm and allowed high-speed imaging of the biofilm on the surface during the shooting. We are aware that this model represents a departure from a dental clinical relevant model; however, it allowed us to add a direct real-time biofilm imaging at the surface to the previous tests on typodonts (Rmaile et al. 2014; Rmaile et al. 2015). In particular, here we show that high-speed microsprays caused biofilm fluidization on the surface in a highly transient manner (Figure 4.5 and Figure 4.6). This phenomenon was extremely quick (< 60 ms) and cannot be seen with regular videography or microscopic imaging techniques. Biofilm fluidification can be the result of mixing processes occurring between the water and the biofilm structure. Since high Re numbers measured for the water-jet phase suggested turbulent behaviour, it might be possible that the vortices observed at the edges of the remaining biofilm can be turbulent eddies. Turbulent mixing together with biofilm fluid behaviour could possibly enhance the mass transfer inside the unremoved biofilm. This phenomenon could, in future, help antimicrobial delivery inside dental biofilms for a better therapeutical effect. In the oral cavity, dental biofilm removal under non-contact brushing is subjected to different shear forces which can cause an expansion in the structure of unremoved biofilms due to its viscoelastic nature (Busscher et al. 2010; Peterson et al. 2015). Investigators demonstrated that fluid-dynamic activity generated by power toothbrushes can change biofilm viscoelastic properties which in turn enhance antimicrobials penetration inside the remaining biofilm (He et al. 2014; Sjogren et al. 2004; Stoodley et al. 2007).

In addition to fluid behaviour we also demonstrated biofilm viscoelastic behaviour showing biofilm time-dependent recoil and residual strain when the shear-stress caused by the microsprays was removed (Figure 4.7). Other studies have reported that biofilms exhibit both elastic recoil and residual strain caused by viscous flow (Klapper et al. 2002; Rupp et al. 2005; Shaw et al. 2004; Towler et al. 2003). Conventional “before” and “after” imaging would not have revealed this behaviour and the drawn conclusion would be that a device had failed to remove biofilm from the surface in the first place. Thus, when dealing with dental biofilm removal, the shear forces should be high enough and sustained for a sufficient time to overcome the recoil effect and be able to detach the biofilm completely off the surface.

It is known from the literature that *S. mutans* specifically bind salivary mucins present in the dental pellicle which cover the tooth surface (Gibbons and Hay 1989). Therefore, we added type II porcine gastric mucin to the biofilm growth medium as a substitute for salivary mucin (Kolenbrander 2011). Then we conditioned microscope slides with the mucin medium prior the inoculation in order to simulate *S. mutans*/mucin interactions. We then performed uniaxial compression test to assess how mucin in the medium might influence biofilm mechanical properties and thus biofilm behaviour. Although mucins have been shown to be important in the adhesion of *S. mutans*, in both promoting attachment (Kishimoto et al. 1989) or inhibiting attachment and biofilm formation (Frenkel and Ribbeck 2015; Marsh et al. 2009) we found the presence of mucin as a slide preconditioned pellicle or in the growth medium had no significant effect on rigidity ($p > 0.05$), suggesting that it did not influence matrix production, or was not incorporated at all into the matrix. It is important to mention that mucin in the growth medium was a simplified model of the dental pellicle. Human saliva contains not only mucins but a complex mixture of proteins, electrolytes and antibacterial compounds. For our work we used commercially available mucin since it is more consistent and easier to work with than high viscosity human saliva, but in order to have a more complete picture, mechanical experiments should be performed with human saliva as the growth medium. However, we also discovered that increasing the growth period from 2 days in previous studies

(Rmaile et al. 2013) to 3 days significantly increased the rigidity of the biofilm from 0.280 kPa to 760 kPa, a factor of ~ 10^3. This is consistent with findings showing that the elastic modulus of dental biofilms is positively correlated with the amount (and density) of matrix components (Hwang et al. 2014; Klein et al. 2015; Waters et al. 2013), and stresses the importance of frequent and consistent oral hygiene to continually remove and disrupt plaque biofilm before it gets stiffer.

The initial jet phase blasted a channel through the biofilm and the second spray phase extended the zone of clearance, thus the combination of these two phases appear complimentary. The water microspray cleared approximately four times of the area of biofilm than the air-only microburst ($p < 0.05$) (Figure 4.8B). Although interestingly the force of the air alone was strong enough to remove some biofilm. This suggests that water inside the microspray plays a crucial role in the detachment mechanisms possibly because of the higher shear stresses caused by the more viscous water drops as well as the surface tension effect of the moving air-water interface of the drop over the biofilm-colonized surface (Sharma et al. 2005a). Previous studies demonstrated that, when water shear stresses inside flow cells reached a critical value between 5 and 12 Pa, biofilm macroscopic clusters detached from the surface (Ohashi and Harada 1994; Stoodley et al. 2002). Although high-speed camera videos of the water microspray developing inside the IP space model demonstrated the complexity and the turbulence of the flow (Movie 1), we made a rough estimate of the magnitude of the shear stresses (τ_w) acting over the surface of the biofilm for the water microspray first phase (i.e. water jet) and the air-only microburst, making two simplifying assumptions: a) when bursts developed inside the channel formed by the two *S. mutans* biofilm slides, the biofilm exposed area can be approximated to a square channel having a depth and a width of 1 mm; b) the air-only microburst had the same maximum velocity as the water jet (51.1 m/s). The corresponding wall shear stresses values were 7.4 kPa and 0.016 kPa for the water microspray and air-only microburst, respectively. These results were consistent with the values found by Rmaile et al., where a computed $\tau_w = 3$ kPa was required to remove 95 % of the biofilm by shooting water micro-drops from a prototype AirFloss at a velocity of 60 m/sec (Rmaile et al. 2014). Quantification of *S. mutans* biofilm removal in different positions along the 10-mm slide showed a reduction in biofilm thickness, biomass and area coverage up to 99.9 % (Table 4.1), similar to our previous studies (Rmaile et al. 2014; Rmaile et al. 2015; Rmaile et al. 2013). We are aware that one of the limitations of confocal analysis is that it is limited in being able to map in high resolution over larger areas. In this case the relevant area would be that of the tooth surface in the IP space which will be on the order of 0.5 to 1 cm^2. Future work will consider Optical Coherence Tomography as a complimentary technology to achieve both high resolution and a more complete mapping of the zone of clearance.

SEM images indicated that there was still some biofilm remaining in the zone of clearance (Figure 4.9A), underlining the importance of the adhesive viscoelastic forces which develop between the biofilm and the surface. Similar findings were obtained in a recent study on shear-induced detachment of 64 h *S. mutans* biofilms which showed a decrease in the biomass removal rate close to the surface because of the presence of a dense layer of EPS (Hwang et al. 2014). In addition, the authors also demonstrated that biofilm treated with EPS-digesting dextranase were easier to detach. Therefore, a possible new therapeutical approach can be the combination of high-speed fluid forces with specific matrix-digesting agents that facilitate the mechanical cleaning of dental biofilms.

4.5 REFERENCES

Barnes CM, Russell CM, Reinhardt RA, Payne JB, Lyle DM. 2005. Comparison of irrigation to floss as an adjunct to tooth brushing: Effect on bleeding, gingivitis, and supragingival plaque. *Journal of Clinical Dentistry*. 16(3):71.

Busscher HJ, Jager D, Finger G, Schaefer N, Van der Mei HC. 2010. Energy transfer, volumetric expansion, and removal of oral biofilms by non-contact brushing. European journal of oral sciences. 118(2):177-182.

Cense AW, Van Dongen MEH, Gottenbos B, Nuijs AM, Shulepov SY. 2006. Removal of biofilms by impinging water droplets. Journal of Applied Physics. 100(12):124701-124701-124708.

Costerton JW, Lewandowski Z, Caldwell DE, Korber DR, Lappin-Scott HM. 1995. Microbial biofilms. Annual review of microbiology. 49(1):711-745.

Donlan RM, Costerton JW. 2002. Biofilms: Survival mechanisms of clinically relevant microorganisms. Clinical Microbiology Reviews. 15(2):167-193.

Featherstone JDB. 1999. Prevention and reversal of dental caries: Role of low level fluoride. Community Dentistry and Oral Epidemiology. 27(1):31-40.

Frenkel ES, Ribbeck K. 2015. Salivary mucins protect surfaces from colonization by cariogenic bacteria. Applied and Environmental Microbiology. 81(1):332-338.

Fried JL. 2012. Interdental cleansing. Access. 2:22-25.

Gibbons R, Hay D. 1989. Adsorbed salivary acidic proline-rich proteins contribute to the adhesion of *Streptococcus mutans* jbp to apatitic surfaces. Journal of dental research. 68(9):1303-1307.

He Y, Peterson BW, Ren Y, van der Mei HC, Busscher HJ. 2014. Antimicrobial penetration in a dual-species oral biofilm after noncontact brushing: An in vitro study. Clin Oral Invest. 18(4):1103-1109.

Heydorn A, Nielsen AT, Hentzer M, Sternberg C, Givskov M, Ersbøll BK, Molin S. 2000. Quantification of biofilm structures by the novel computer program comstat. Microbiology. 146(10):2395-2407.

Hope CK, Petrie A, Wilson M. 2003. In vitro assessment of the plaque-removing ability of hydrodynamic shear forces produced beyond the bristles by 2 electric toothbrushes. Journal of periodontology. 74(7):1017-1022.

Hope CK, Wilson M. 2003. Effects of dynamic fluid activity from an electric toothbrush on in vitro oral biofilms. J Clin Periodontol. 30(7):624-629.

Hwang G, Klein MI, Koo H. 2014. Analysis of the mechanical stability and surface detachment of mature *Streptococcus mutans* biofilms by applying a range of external shear forces. Biofouling. 30(9):1079-1091.

Jahn CA. 2010. The dental water jet: A historical review of the literature. American Dental Hygienists Association. 84(3):114-120.

Kishimoto E, Hay DI, Gibbons RJ. 1989. A human salivary protein which promotes adhesion of *Streptococcus mutans* serotype c strains to hydroxyapatite. Infection and Immunity. 57(12):3702-3707.

Klapper I, Rupp CJ, Cargo R, Purvedorj B, Stoodley P. 2002. Viscoelastic fluid description of bacterial biofilm material properties. Biotechnology and Bioengineering. 80(3):289-296.

Klein M, Hwang G, Santos P, Campanella O, Koo H. 2015. *Streptococcus mutans*-derived extracellular matrix in cariogenic oral biofilms. Frontiers in Cellular and Infection Microbiology. 5(10).

Marsh PD, Bradshaw DJ. 1995. Dental plaque as a biofilm. Journal of Industrial Microbiology. 15(3):169-175.

Marsh PD, Martin MV, Lewis MA, Williams D. 2009. Oral microbiology. Elsevier Health Sciences.

Ohashi A, Harada H. 1994. Adhesion strength of biofilm developed in an attached-growth reactor. Water Science and Technology. 29(10):281-288.

Paramonova E, Kalmykowa OJ, van der Mei HC, Busscher HJ, Sharma PK. 2009. Impact of hydrodynamics on oral biofilm strength. Journal of dental research. 88(10):922-926.

Parini MR, Pitt WG. 2006. Dynamic removal of oral biofilms by bubbles. Colloids and Surfaces B: Biointerfaces. 52(1):39-46.

Peterson BW, He Y, Ren Y, Zerdoum A, Libera MR, Sharma PK, van Winkelhoff A-J, Neut D, Stoodley P, van der Mei HC. 2015. Viscoelasticity of biofilms and their recalcitrance to mechanical and chemical challenges. FEMS microbiology reviews. 39(2):234-245.

Rmaile A, Carugo D, Capretto L, Aspiras M, De Jager M, Ward M, Stoodley P. 2014. Removal of interproximal dental biofilms by high-velocity water microdrops. Journal of dental research. 93(1):68-73.

Rmaile A, Carugo D, Capretto L, Wharton JA, Thurner PJ, Aspiras M, Ward M, De Jager M, Stoodley P. 2015. An experimental and computational study of the hydrodynamics of high-velocity water microdrops for interproximal tooth cleaning. Journal of the Mechanical Behavior of Biomedical Materials. 46:148-157.

Rmaile A, Carugo D, Capretto L, Zhang X, Wharton JA, Thurner PJ, Aspiras M, Ward M, Stoodley P. 2013. Microbial tribology and disruption of dental plaque bacterial biofilms. Wear. 306(1):276-284.

Rupp CJ, Fux CA, Stoodley P. 2005. Viscoelasticity of staphylococcus aureus biofilms in response to fluid shear allows resistance to detachment and facilitates rolling migration. Applied and Environmental Microbiology. 71(4):2175-2178.

Schindelin J, Arganda-Carreras I, Frise E, Kaynig V, Longair M, Pietzsch T, Preibisch S, Rueden C, Saalfeld S, Schmid B et al. 2012. Fiji: An open-source platform for biological-image analysis. Nat Methods. 9(7):676-682.

Selwitz RH, Ismail AI, Pitts NB. 2007. Dental caries. The Lancet. 369(9555):51-59.

Sharma PK, Gibcus MJ, van der Mei HC, Busscher HJ. 2005a. Influence of fluid shear and microbubbles on bacterial detachment from a surface. Applied and Environmental Microbiology. 71(7):3668-3673.

Sharma PK, Gibcus MJ, Van Der Mei HC, Busscher HJ. 2005b. Microbubble-induced detachment of coadhering oral bacteria from salivary pellicles. European journal of oral sciences. 113(4):326-332.

Shaw T, Winston M, Rupp CJ, Klapper I, Stoodley P. 2004. Commonality of elastic relaxation times in biofilms. Physical Review Letters. 93(9):098102.

Sjogren K, Lundberg AB, Birkhed D, Dudgeon DJ, Johnson MR. 2004. Interproximal plaque mass and fluoride retention after brushing and flossing--a comparative study of powered toothbrushing, manual toothbrushing and flossing. Oral health & preventive dentistry. 2(2):119-124.

Stoodley P, A Nguyen D, A Longwell M, A Nistico L, A von Ohle C, A Milanovich N, A de Jager M. 2007. Effect of the sonicare flexcare power toothbrush on fluoride delivery through *Streptococcus mutans* biofilms. Compendium of Continuing Educationin Dentistry. 28:15-22.

Stoodley P, Cargo R, Rupp CJ, Wilson S, Klapper I. 2002. Biofilm material properties as related to shear-induced deformation and detachment phenomena. Journal of industrial microbiology & biotechnology. 29(6):361-367.

Towler BW, Rupp CJ, Cunningham AB, Stoodley P. 2003. Viscoelastic properties of a mixed culture biofilm from rheometer creep analysis. Biofouling. 19(5):279-285.

Waters MS, Kundu S, Lin NJ, Lin-Gibson S. 2013. Microstructure and mechanical properties of in situ *Streptococcus mutans* biofilms. ACS applied materials & interfaces. 6(1):327-332.

Wilking JN, Angelini TE, Seminara A, Brenner MP, Weitz DA. 2011. Biofilms as complex fluids. MRS Bulletin. 36:385-391.

CHAPTER 5

High-velocity Kelvin-Helmholtz Instability Formation in Biofilms

S. Fabbri[1], J. Li[2], R.P. Howlin[3,4], A. Rmaile[5], B. Gottenbos[5], M. De Jager[5], E. M. Starke[6], M. Aspiras[7], M.T. Ward[6], N.G. Cogan[2], and P. Stoodley[1, 8*]

[1]National Centre for Advanced Tribology at Southampton (nCATS), University of Southampton, Southampton SO17 1BJ, United Kingdom.

[2]Department of Mathematics, Florida State University, Tallahassee, FL 32306

[3]National Institute for Health Research Southampton Respiratory Biomedical Research Unit, Southampton Centre for Biomedical Research, University Hospital Southampton NHS Foundation Trust, Southampton SO17 1BJ, United Kingdom.

[4]Centre for Biological Sciences, Faculty of Natural and Environmental Sciences and Institute for Life Sciences, University of Southampton, Southampton SO17 1BJ, United Kingdom.

[5]Philips Research, Eindhoven 5656 AE, The Netherlands.

[6]Philips Oral Healthcare, Bothell, Washington 98021, USA.

[7]Wrigley, Chicago, Illinois 60613, USA.

[8]Department of Microbial Infection and Immunity and the Department of Orthopaedics, Centre for Microbial Interface Biology, The Ohio State University, Columbus, Ohio 43210, USA.

ABSTRACT

Biofilms are thin layers of bacteria embedded within a slime matrix that live on surfaces. They are ubiquitous in nature and responsible for many chronic medical and dental infections, industrial fouling and are also evident in ancient fossils. Biofilms are viscoelastic which is thought to enable them to survive surface shear. The interaction between biofilm structure and hydrodynamics remains one of the fundamental questions concerning biofilm dynamics. Here we use high-speed imaging to document that high-velocity water sprays and air jets can induce rapidly flowing interfacial ripples in *Streptococcus mutans* and *Staphylococcus epidermidis* biofilms and wrinkle-like structures in *Pseudomonas aeruginosa* biofilms. Classical linear stability analysis suggests that ripples were Kelvin-Helmholtz Instabilities implying the onset of turbulence in the flowing biofilm, providing further insight into the mechanical behaviour of biofilms as complex liquids. This behavior may have far reaching implications for our understanding of how fluid flow influences biofilm biology since it will likely disrupt metabolic and signal gradients as well as community stratification and can explain energy dissipation in pipe systems and ship hulls, and the formation of Kinneyia fossils.

5.1 INTRODUCTION

Biofilms are surface-attached microbial communities surrounded by a self-produced matrix of extracellular polymeric substances (EPS), which include polysaccharides, proteins, lipids and nucleic acids (Flemming and Wingender 2010). Biofilms can colonize all man-made surfaces such as ship hulls, industrial pipelines, and biomedical implants, as well as human tissues and oral surfaces (Costerton et al 1999, Lappin-Scott and Costerton 1989, Marsh 2004, Schultz et al 2011). Biofilms are also ubiquitous in the modern natural environment (Stoodley et al 2002) and have been identified in the fossil record (Krumbein et al 2003, Noffke et al 2013). Biofilms behave as viscoelastic materials whose viscous or elastic responses dominates depending on the environmental and growth conditions (Billings et al 2015, Peterson et al 2015, Wilking et al 2011). The EPS matrix gives flexibility to the biofilm structure by changing shape in response to an applied force. For instance, in mature biofilms compressive stresses can generate wrinkled and ridges structures which depend on the inherent elasticity of the EPS matrix (Trejo et al 2013).When biofilms are subjected to steady or transient fluid flows, energy dissipation through viscoelasticity allows them to tolerate rapidly-changing shear stresses without completely detaching from the surface. Ripple- or stream-like structures have been discovered at the surface of in vitro biofilms when exposed to high-velocity flows (Battin et al 2003, Stoodley et al 1999). The fossil record suggests that this might be an ancient survival mechanism. Ripple-like structures, similar to those seen in flow cells (Battin et al 2003, Stoodley et al 1999), have been observed in microbially-induced sedimentary structures (MISS) (Noffke et al 2001, Porada et al 2008). Recent studies have raised the hypothesis that such structures may be the result of Kelvin-Helmholtz Instabilities (KHI) between the viscoelastic microbial biofilm and the overlying fluid flow (Thomas et al 2013). The KHI manifests in two-fluid systems (such as water-air) that are stratified by density variations with a velocity differential between the fluids (Miles 1959). Shear forces generated from the velocity difference lead to unstable vorticity which grows exponentially until the distorted interface overturns into a spiral forming rippled features (Funada and Joseph 2001). Whether the interaction between biofilms and hydrodynamic forces is an adaptation of biofilms as multicellular entities remains a fundamental research question (Drescher et al 2013). The formation of similar structures in biofilms grown under a broad range of natural and *in vitro* environments has stimulated modellers to describe this behaviour from a materials perspective to shed light on the underlying function of the viscoelasticity of bacterial biofilms and to identify novel removal strategies.

Streptococcus mutans is a gram-positive and facultative anaerobic microorganism that is considered a causative agent of human dental decay (Loesche 1986). *S. mutans* biofilms have been widely used in research to investigate biofilm mechanical properties and detachment (Cense et al 2006, Rmaile et al 2012, Vinogradov et al 2004). We previously performed high-speed camera (HSC) videography during the exposure of *in vitro S. mutans* interproximal dental biofilms to high-velocity (60 m/s) impacts from micro water jets and sprays using an interdental cleaning device (AirFloss (AF), Philips) (Fabbri et al 2016, Rmaile et al 2014, Rmaile et al 2015). We demonstrated that biofilms exhibited fluid-like behaviour on the order of milliseconds in response (Fabbri et al 2016). The videos not only recorded a quasi-instant biofilm fluidisation, but also suggested the formation of migratory ripple-like structures. Here we report for the first time that ripple-like structures in *Streptococcus mutans* and *Staphylococcus epidermidis* biofilms and wrinkle-like structures in *Pseudomonas aeruginosa* biofilms can form extremely rapidly. In addition, we provide direct experimental evidence supported by mathematical modelling that ripples structures are KHI developing from an overlying fluid flow. The work described here is motivated by the fact that KHI are a prelude to mixing and turbulence (Geyer et al 2010). The development of fluid-like turbulent mixing in biofilms has implications for gradient dependent processes such as cell signalling, the formation of anaerobic microniches, as well as antibiotic delivery and mechanical removal strategies.

5.2 MATERIALS AND METHODS

5.2.1 Bacteria and growth media

Streptococcus mutans biofilms UA159 (ATCC 700610) were grown for 72 hrs on microscope glass slides as previously described (see Section 4.2.1). Overnight cultures of *S. epidermidis* (ATCC 35984) were grown in 100% tryptic soy broth (TSB) (Oxoid). Overnight cultures of *P aeruginosa* PAO1 were grown in M9 medium (Sigma-Aldrich). The M9 medium consisted of the following:500 ml of 1xM9 salts solution (Formedium), 1 ml of 1M $MgSO_4$ (Sigma-Aldrich), 50 µl of 1M $CaCl_2$ (Sigma-Aldrich) and 10 mL of 20% Glucose (Sigma-Aldrich). Each overnight culture was diluted in fresh media to an optical density value corresponding to 10^6 cfu/mL. Autoclaved microscope glass slides were placed in petri dishes and filled with 15 mL of the adjusted overnight culture. *S. epidermidis* and *P. aeruginosa* biofilms were grown for 72 hrs or 7 days respectively at 37 °C in a humidified incubator with media replacement every 24 h. After the growth period biofilm covered-slides were gently rinsed in 1 % (wt/vol) phosphate-buffered saline (1% PBS) solution (Sigma-Aldrich) before placing them in the IP model.

5.2.2 *In vitro* IP model

An *in vitro* interproximal (IP) model previously developed (see Section 4.2.3) to study the removal mechanism of dental biofilms by high velocity jets and sprays allowed the parallel insertion of two biofilm-colonized slides separated by a distance of 1 mm. The glass enabled high-speed imaging of the rippling phenomenon at the surface. After the growth period biofilm covered-slides were gently rinsed in 1 % (wt/vol) phosphate-buffered saline (1% PBS) solution (Sigma-Aldrich) before placing them in the IP model.

5.2.3 *S. mutans* biofilms exposure to high-velocity microsprays

To assess the influence of fluids with different viscosities on the rippling phenomenon, *S. mutans* biofilms were exposed to either a water microspray burst or an air only burst from the AF device as previously described (see Section 4.2.4). The shooting was recorded at 8000 frames per seconds (fps) with a high-speed camera MotionPro X3 (IDT) equipped with a Sigma 105 mm f/2.8 EX DG Macro lens.

5.2.4 *S. mutans* biofilms exposure to air-jets

The microsprays had a very complex flow hydrodynamics ((Fabbri et al. 2016) or Chapter 4) and could not be readily controlled or modelled. Consequently, *S. mutans* biofilms were exposed to a controlled jet generated from an air piston compressor (ClassicAir 255, Metabo) at different flow velocities (Table 5.1). Instead *S. epidermidis* and *P. aeruginosa* biofilms were exposed only to the jet at a velocity of 85.5 m/s. The average air jet velocities (u_{jet}) and Reynolds numbers (Re_{jet}) entering the IP space were estimated from the volumetric air flow rate (Q_{jet}), measured using a rotameter (FR2000; Key Instruments), using:

$$u_{jet} = \frac{Q_{jet}}{A^*} \tag{5.1}$$

$$D_h = \frac{A^*}{wp} \tag{5.2}$$

$$Re_{jet} = \frac{\rho u_{jet} D_h}{\mu} \tag{5.3}$$

where A* (1.92×10^{-3} m^2) and w_p (5.57×10^{-3} m) are the area and the wetted perimeter of the entry geometry (Figure 5.1), ρ and η are the viscosity (Pa·s) and density (kg/m^3) of air at 20°C and 1 atm.

U_{jet} (m/s)*	Re_{jet}^*
7.2	660
24.6	2244

44.9	4092
68.1	6205
85.5	7790
110	10034

*Table 5.1. Air jet velocities and Reynolds numbers developing into the IP space model. Experimental data reported as mean of three independent replicates (n=3). * All SDs were below 34% of the means.*

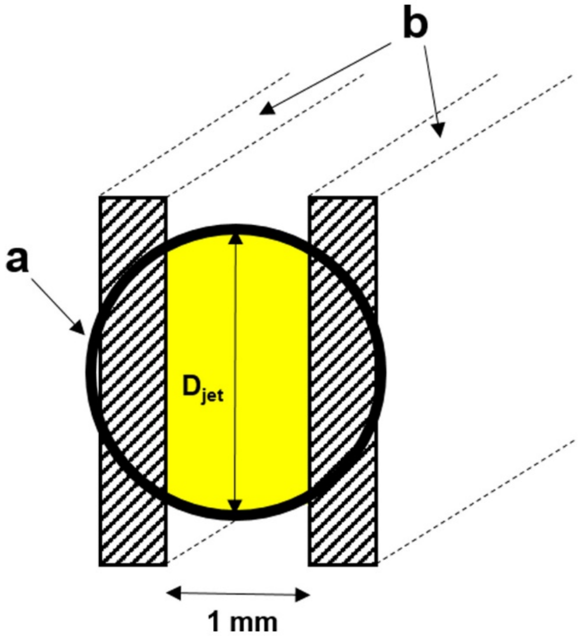

Figure 5.1. Schematic representation of the air jet entry geometry in the IP space. The air compressor nozzle (a) was positioned in the middle of the IP channel created by two microscope glass slides (b). The calculated area of the entry geometry is shown in yellow.

5.2.5 High-speed video post-processing

The high-speed camera videos were analysed with the image processing package Fiji (Schindelin et al. 2012)). The videos were converted to a stack with each frame in the stack being a different time (T) so that the volume could be represented in XYT co-ordinates. Ripples wavelength (λ_R) and width (w_R) were measured using the plot profile function (Figure 5.2A-B). A line was traced along three or more well-defined ripples in one frame. The plot profile graph obtained had the pixel values of the image along the traced line as a function of the line length. The distance between two reverse peaks was defined as λ_R and the width of one peak as w_R. The ripples velocity (u_R) was measured using the reslice function which creates a time-trace along the line (Figure 5.2C**)**. As a ripple moves across the surface the advancing edge makes a continuous line from the left to the right. The slope described by a ripple was defined as u_R. A stationary ripple would have a vertical line; an extremely fast moving object would approach a horizontal line.

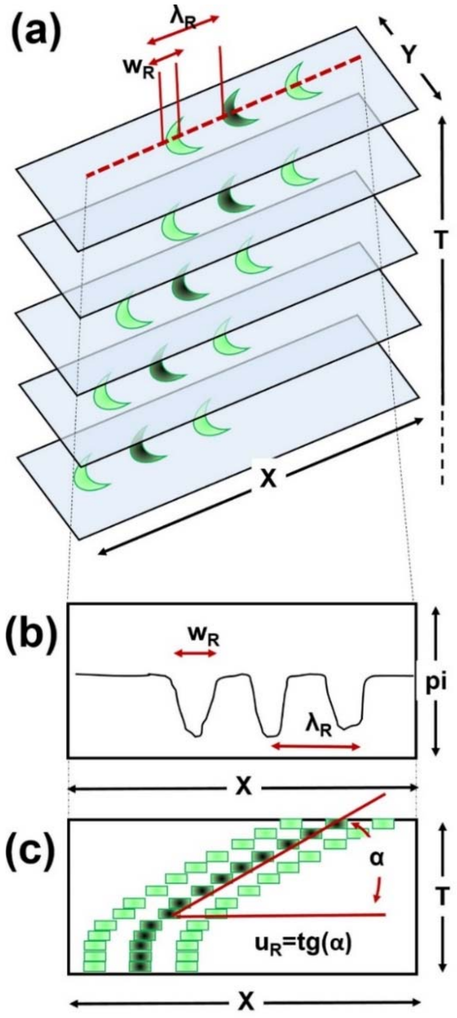

Figure 5.2. Schematic showing how the ripple width, wavelength and velocity are measured from successive frames from a high speed movie. (a) Five consecutive frames from a high-speed camera videos showing three biofilm ripples (green crescents) moving along the glass slide (light blue). The middle ripple has been highlighted to show how it would appear as a dark line in the reslice time-trace. A line was traced along three or more well defined ripples (red dashed line) to measure ripples wavelength, width and velocity. (b) Representation of a plot profile graph showing the grey scale values (pi) of the image along the traced line as a function of the length (X). The distance between two reverse peaks was defined as λ_R and the width of one peak as w_R. (c) Representation of a reslice function graph showing the time-traces along the traced line formed by the moving ripples. The slope of the line was defined as u_R.

5.2.6 Fast Fourier analysis

Fast Fourier Transform (FFT) was used to determine the dominant wavelengths of transient ripples formed during the *S. mutans* biofilm exposure to air jets. Frames from the videos were analysed in Fiji using the plot profile function as explained previously. Then Fast Fourier analysis was performed on the plot profile graph. Since the FFT algorithm imposes a fixed interval range ($N= 2^m$, where N is the number of samples and m a positive integer), we selected N=128. Wavelengths were obtained by from the inverse of the relative peak frequencies.

5.2.7 Confocal microscope analysis

Prior to the experiments, *S. mutans* biofilms slides were fluorescently stained with Live/Dead BacLight (Invitrogen) in the dark for 20 mins. Following a rinse in 1% PBS solution for 5 secs, the slides were gently covered with a cover slip and inverted. Confocal scanning laser microscopy (CSLM) was performed using an inverted Leica DMI600 SP5 confocal scanning laser microscope (CSLSM, Leica Microsystems) using a HCX PL APO CS 63x/1.3 NA glycerol immersion lens. Quantification of biofilm thickness was carried out using COMSTAT (Heydorn et al. 2000).

5.2.8 Scanning microscope analysis

A Scanning Electron Microscope (SEM, FEI Quanta-200) was used to qualitatively assess *S. mutans* biofilms structure in high resolution prior and after the water microspray exposure. Biofilm slides were processed for SEM by firstly immersing the slides in 200 µL of an initial fixative solution (3 % glutaraldehyde, 0.1 M sodium cacodylate and 0.15 % alcian blue). After 1 h of incubation inside the fridge the samples were washed with 0.1 M sodium cacodylate and incubated for 1 h at room temperature. Afterwards, the samples were incubated for 1 h with 200 µL of secondary buffer solution (0.1 M osmium tetroxide and 0.1 M sodium cacodylate). The solution was then replaced with 0.1 M sodium cacodylate and the samples were incubated for 1 h at room temperature. Finally, the samples were placed though an ethanol series (30, 50, 70, 95 and (two times) 100 %), adding and replacing 1 mL of each concentration. All the concentrations were incubated at room temperature for 15 min, except for 100% which was incubated for 20 min. After processing, the samples were first critical point dried and then sputter coated with gold.

5.2.9 Statistical analysis

Statistical comparisons with respect to the experimental biofilm measurements were made using an unpaired two-sample T-test (Origin 8.5). Differences were reported as statistically different for $p < 0.05$.

5.2.10 Mathematical modelling

Biofilm multiphase model

We focus on a single region of the physical experiment and conceptualize it as a two-fluid system (Figure 5.3).

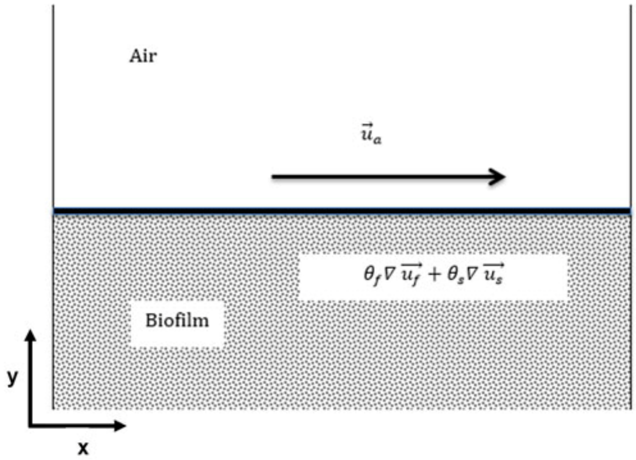

Figure 5.3. Schematic of the mathematical domain

The top fluid (air) is moving initially horizontally with velocity $\vec{u}_a$ while the bottom fluid (biofilm) is initially stationary. We assume that the dynamics of the air layer can be described using Euler equations:

$$\frac{\partial \vec{u}_a}{\partial t} + \vec{u}_a \cdot \nabla \vec{u}_a = -\frac{1}{\rho_a} \nabla p_a, \tag{5.4}$$

$$\nabla \cdot \vec{u}_a = 0 \tag{5.5}$$

where the velocity is denoted $\vec{u}_a$, the pressure in the upper layer is denoted p_a and the air density is denoted ρ_a. The physical parameters used in our analysis are shown in (Table 5.2).

Parameter	Units	Value
Integration Constant (B)	$\frac{m}{s}$	7[a]
Air Density (ρ_a)	$\frac{kg}{m^3}$	1.27[b]
Biofilm Viscosity (μ)	$Pa \cdot s$	6.5×10^{5} [c]
Surface Tension (γ)	$\frac{N}{m}$	0.04[a]

Table 5.2. Parameters used in the simulations. [a] Fitting, [b]Assumed, [c]Reference (Hall-Stoodley et al. 2004)

The biofilm layer was modelled using a simplified version of the multiphase model previously reported (Cogan and Keener 2004). The underlying assumption is that any infinitesimal volume of the biofilm can be separated into solid, occupying a fraction of the volume, θ_s. Since the biofilm consists entirely of either solid or fluid, the fluid volume fraction (θ_f) and the solid volume fraction must sum to one. Therefore $\theta_f = 1 - \theta_s$. We also assume that the solid and liquid components of the biofilm have the same density, allowing us to neglect buoyancy forces within the biofilm. This also implies that conservation of mass is equivalent to conservation of volume fraction. The governing dynamical equations are derived from conservation of mass/volume and momentum, where the latter assumes that the biofilm material is in force balance (i.e. neglecting inertial terms similar to the reduction from Navier-Stokes equations to Stokes' equation). The equations of motion are:

$$\frac{\partial \theta_f}{\partial t} + \nabla \cdot \left(\theta_f \nabla \overrightarrow{u_f}\right) = 0, \tag{5.6}$$

$$\frac{\partial \theta_f}{\partial t} + \nabla \cdot \left(\theta_s \nabla \overrightarrow{u_s}\right) = 0, \tag{5.7}$$

$$\mu_f \nabla \cdot \left(\theta_f \nabla \overrightarrow{u_f}\right) + \frac{1}{\rho_f} \theta_f \nabla p + \xi \theta_f \theta_s \left(\overrightarrow{u_f} - \overrightarrow{u_s}\right) = 0, \tag{5.8}$$

$$\mu_s \nabla \cdot \left(\theta_s \nabla \overrightarrow{u_s}\right) + \frac{1}{\rho_s} \theta_s \nabla p - \xi \theta_f \theta_s \left(\overrightarrow{u_f} - \overrightarrow{u_s}\right) = 0, \tag{5.9}$$

$$\theta_s + \theta_f = 1. \tag{5.10}$$

The first two equations represent conservation of mass/volume. Adding these and using Eq.(5.10), we find that the average material is incompressible:

$$\nabla \cdot \left(\theta_f \nabla \overrightarrow{u_f} + \theta_s \nabla \overrightarrow{u_s}\right) = 0. \tag{5.11}$$

Eqs. (5.8-5.9) are force balance equations between viscous (inter-phase viscosity), hydrostatic pressure, and friction (intra-phase viscosity). By adding these equations, we find that the average momentum obeys a Stokes'-like equation. Osmotic pressure was neglected in the model. The motion that is induced by the air shear was on a considerably shorter time-scale than growth so we do not expect the osmotic pressure to play a significant role (Cogan and Keener 2004). We assumed that all variables are periodic in the x-direction. All velocities tend towards zero in the far-field, as do the pressure gradients. There must be some matching conditions at the interface in order to have a well-posed problem. It is relatively standard practice to assume continuity in the tangential velocities, but as the dynamics evolve, we expect the interface between the materials to change in response to the motion. The motion of the interface, viewed from either side of the interface must be consistent (as we do not expect cavitation) so the boundary dynamics must be continuous. Additionally, we assume that there is a jump in the normal component of the stress that is balanced by surface tension, which is related to the curvature of the interface. This is often referred to as Bernoulli's theorem(Joseph 2003).

Linear stability analysis

We then conducted a linear stability analysis based of the two-fluid model developed. It is evident that $\overrightarrow{u_a} = (\alpha, 0)$ and $p = \hat{p}$ satisfy the equations in the air domain. Similarly, constant volume fractions (that sum to one) with zero velocity and constant pressure satisfy the equations in the biofilm domain. These flows also satisfy periodic boundary conditions, far-field conditions and continuity conditions at the interface, trivially. Since there is no vertical velocity, the interface motion is also consistent. Additionally, the normal stresses are continuous at the interface (as long as the pressure is continuous). Therefore, we have obtained a leading order solution to the system of equations.

To determine the stability of the solution, we consider the behaviour near this solution. Beginning with the air-layer, we define:

$$\widehat{u_a} = \alpha + \epsilon u_a'(x, z, t), \tag{5.12}$$

$$\widehat{w_a} = \alpha + \epsilon w_a'(x, z, t), \tag{5.13}$$

$$\hat{p} = p_0 + \epsilon p'(x, z, t), \tag{5.14}$$

where $\overrightarrow{u_a} = (u_a, w_a)$ denotes the velocity field in two dimensions. Substituting this into the equations, collecting in powers of ϵ and neglecting the ϵ^2-terms and higher, lead to a system of linear equations. Additionally, since we know the leading order terms are solutions, we find a linear system for the perturbations (prime variables):

$$\nabla \cdot (u_a' + w_a') = 0, \tag{5.15}$$

$$\frac{\partial u_a'}{\partial t} + \alpha \frac{\partial u_a'}{\partial x} = -\frac{1}{\rho_a} \frac{\partial p'}{\partial x}, \tag{5.16}$$

$$\frac{\partial w_a'}{\partial t} + \alpha \frac{\partial w_a'}{\partial x} = -\frac{1}{\rho_a} \frac{\partial p'}{\partial z}. \tag{5.17}$$

Taking the derivative of Eqs. (5.16-5.17) with respect to x and z, respectively, and adding the result we find that the pressure must be harmonic - $\Delta p' = 0$. The equations are separable, so the perturbation solutions are broken down to spatial and temporal contributions. Moreover, since the solutions are periodic in the x- direction, we use the expansion,

$$u_a' = \bar{u}(z) e^{i(kx - \omega t)}, \tag{5.18}$$

$$w_a' = \bar{w}(z) e^{i(kx - \omega t)}, \tag{5.19}$$

$$p' = \bar{p}(z) e^{i(kx - \omega t)}. \tag{5.20}$$

Since the pressure is harmonic, we find that $\bar{p}(z) = A_1 e^{-kz} + A_2 e^{kz}$ but since the pressure is bounded in the far field (as $z \to \infty$), $A_2 = 0$. We can use this solution in Eq. (5.20) to find that $\bar{w} = \frac{A_1 k\, e^{-kz}}{i(k\alpha - \omega)}$. In principle we could obtain a similar solution for the horizontal component, but we are interested in the growth of the perturbed interface location r'. The leading order term of the z- component of the material velocity of the interface viewed from the air-side depends on the z-component of the velocity, evaluated at the interface ($z = 0$) which is

$$r' = -\frac{A_1 k}{(k\alpha - \omega)^2}. \tag{5.21}$$

This must be consistent with the similar calculation from the biofilm side. We proceed in a straightforward manner by considering perturbations of the base solutions in the biofilm domain:

$$\theta_f = \Theta_f + \epsilon \theta_f', \tag{5.22}$$

$$\theta_s = \Theta_s + \epsilon \theta_s', \tag{5.23}$$

$$\overrightarrow{u_f} = \epsilon\, \overrightarrow{u_f'} \tag{5.24}$$

$$\overrightarrow{u_s} = \epsilon\, \overrightarrow{u_s'}, \tag{5.25}$$

$$p = p_0 + \epsilon p', \tag{5.26}$$

By plugging them into Eq. (5.6-5.10), dropping the nonlinear terms we have a linear system for the perturbed variables:

$$\nabla \cdot (\Theta_f \overrightarrow{u_f'} + \Theta_s \overrightarrow{u_s'}) = 0, \tag{5.27}$$

$$\mu_f\, \Theta_f \Delta \overrightarrow{u_f'} + \Theta_f \frac{1}{\rho_f} \nabla p' + \xi \Theta_f \Theta_s \left(\overrightarrow{u_f'} - \overrightarrow{u_s'} \right) = 0, \tag{5.28}$$

$$\mu_s\, \Theta_s \Delta \overrightarrow{u_s'} + \Theta_s \frac{1}{\rho_s} \nabla p' + \xi \Theta_f \Theta_s \left(\overrightarrow{u_f'} - \overrightarrow{u_s'} \right) = 0, \tag{5.29}$$

$$\theta_f' + \theta_s' = 0. \tag{5.30}$$

We assume a separation of variables form of the solutions,

$$\overrightarrow{u_f'} = \overline{\overrightarrow{u_f}}(z)\, e^{i(kx - \omega t)}, \tag{5.31}$$

$$\overrightarrow{u_s'} = \overline{\overrightarrow{u_s}}\,(z) e^{i(kx - \omega t)}, \tag{5.32}$$

$$\theta_f' = \overline{\theta_f}(z) e^{i(kx - \omega t)}, \tag{5.33}$$

$$\theta_s' = \bar{\theta}_s(z) e^{i(kx - \omega t)}, \tag{5.34}$$

$$p' = \bar{p}(z) e^{i(kx - \omega t)}. \tag{5.35}$$

Again, the pressure is harmonic and we find that $\bar{p} = Be^{kz}$ which remains bounded as $z \to -\infty$. Unfortunately, the intra-phase friction couples the system and there is no nice way to obtain closed form solutions for the velocities. We proceed by assuming that the frictional coefficient is of order ϵ, which is a relatively common assumption. In this way, we find an asymptotic approximation for the vertical components of the fluid and solid phase velocities,

$$\overline{w_f} = C_1 e^{kz} + \frac{B}{2\mu_f} z e^{kz}, \tag{5.36}$$

$$\overline{w_s} = C_2 e^{kz} + \frac{B}{2\mu_s} z e^{kz}. \tag{5.37}$$

Just as before, the displacement measured from the biofilm side are obtained by matching the interface velocity with the sum of the phase velocities. Additionally, we require that the displacements from above and below must match – giving a dispersion relation between the modes and the growth rates,

$$\frac{C}{i\omega} = \frac{A_1 k}{(ku_1 - \omega)^2}. \tag{5.38}$$

Bernoulli's relation completes the relationship,

$$-\omega^2 + M\omega + N = 0\,, \tag{5.39}$$

where the coefficients are

$$M = 2ku_1 - i\,B\,k - 2\,i\,k^2(\mu_f + 2\mu_s), \tag{5.40}$$

$$N = -k^2u_1^2 + \gamma k^3. \tag{5.41}$$

The peak of the dispersion curve indicates the most unstable mode and is used to estimate the ripples wavelength and velocity.

5.3 RESULTS

5.3.1 Microsprays induce ripples formation in *S. mutans* biofilms

At 3 days, *S. mutans* biofilms were approximately 65 µm thick and consisted of denser clusters of aggregated cells interspersed in an underlying basal layer (Figure 5.4).

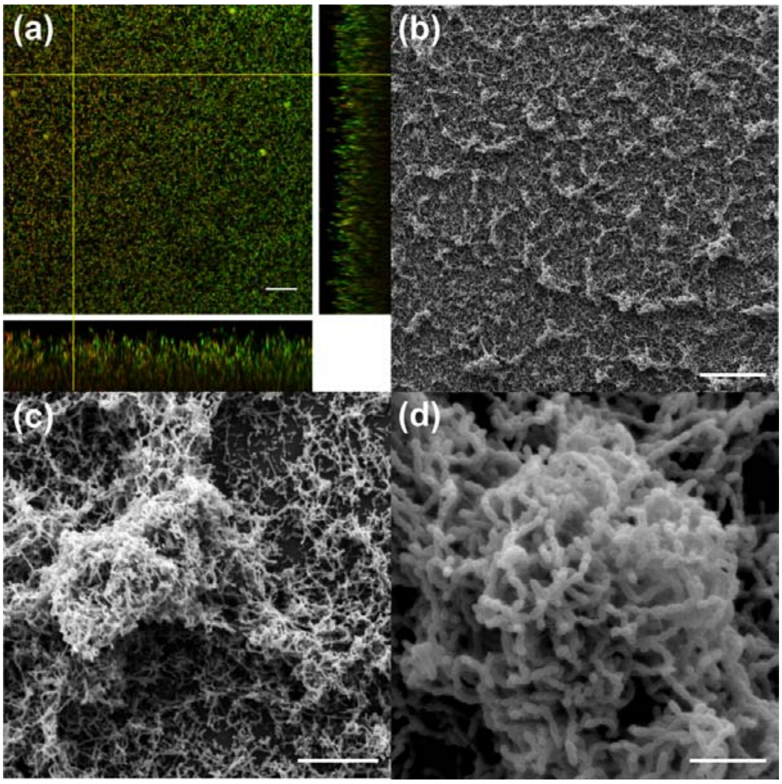

Figure 5.4. S. mutans biofilm prior to exposure to high velocity fluid disruption. (a) Confocal laser scanning micrograph of a fully hydrated biofilm. The main panel is an x-y plan view and the side panels are x-z and y-z cross sections. Viable bacteria were stained green and non-viable bacteria were stained yellowish/red. Scale bar = 25 µm. (b) Low magnification scanning electron microscope image showing a background layer interspersed with larger cell clusters. Scale bar = 100 µm. (c) and

(d) Higher magnification scanning electron microscope images of the biofilm clusters showing they were composed of dense clusters and chains of cocci. Scale bars = 20 μm and 5 μm respectively.

High-speed camera movies of *S. mutans* biofilms exposed to high-velocity microsprays revealed that the water microspray and air-only burst rapidly entered the IP model forcing *S. mutans* biofilm towards the end of the slide as it created a clearance zone through the biofilm (Movie 8 and Movie 9). Migratory ripple-like structures were seen developing at the fluid-biofilm interface (Figure 5.5) which travelled over the glass surface with an average velocity of 1.87 ± 0.27 m/s and 2.69 ± 0.07 m/s during the water spray and air bursts respectively. After the exposure to the burst (duration ~ 60 ms), the biofilm clearance zone covered an area of 130.1 ± 13.1 mm^2 and 32.6 ± 7.6 mm^2 for the water spray and air bursts respectively. Interestingly, after the burst, the ripples dissipated within milliseconds leaving little trace of their formation.

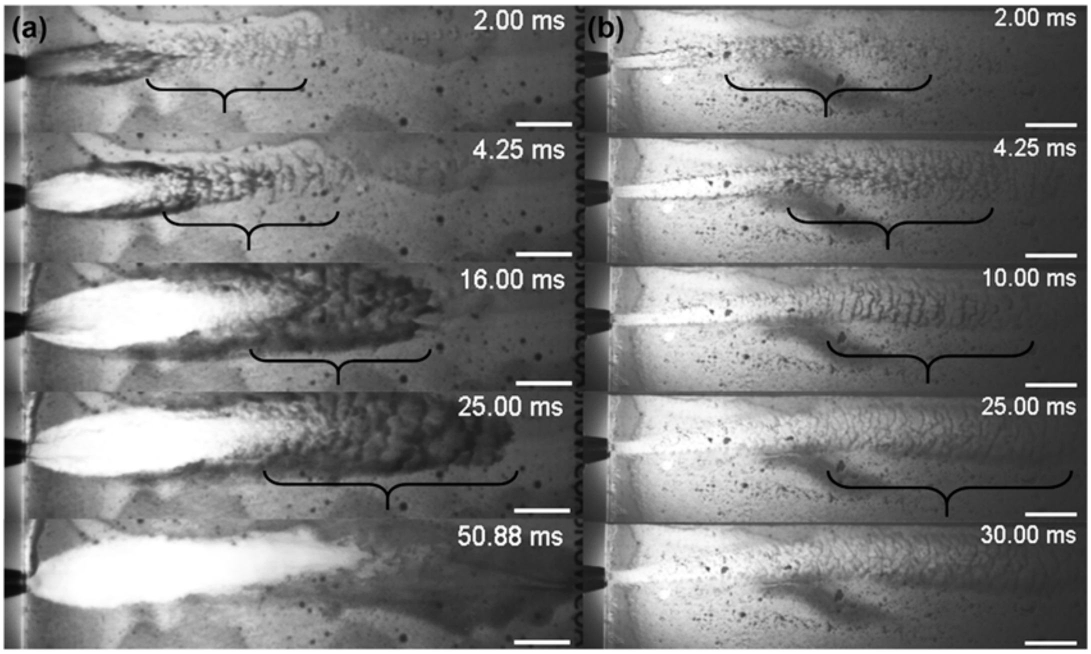

Figure 5.5. Consecutive frames from high-speed camera videos illustrating S. mutans biofilm removal and spatial migration of ripples during the exposure to a high-velocity water microspray burst (a) and air only burst (b). Frames show biofilm-colonized slide proximal to the camera (biofilm is grey and the zone of clearance is white). The nozzle tip was located at the left edge of the slide. Flow was left to right. Curly brackets illustrate ripples formation and movement along the slide during the microbursts. A biofilm clearance zone was created at the end of the microsprays and ripples disappeared. Scale bars are 5 mm.

Different ripple morphologies were observed at different phases of the bursts. The water microspray generated patterns of isolated and arcuate crests (linguoid ripples) at the front edge of the burst (Figure 5.6a) with an average wavelength of 1.85 ± 0.02 mm and a width of 0.31 ± 0.03 mm. In contrast, the air burst firstly produced transverse linguoid ripples protruding from the biofilm with an average amplitude of 0.57 ± 0.11 mm (Figure 5.6 (b)). Then, linguoid ripples alternated to straight-sinuous ripples at the front edge of the air microspray (Figure 5.6 (c)).

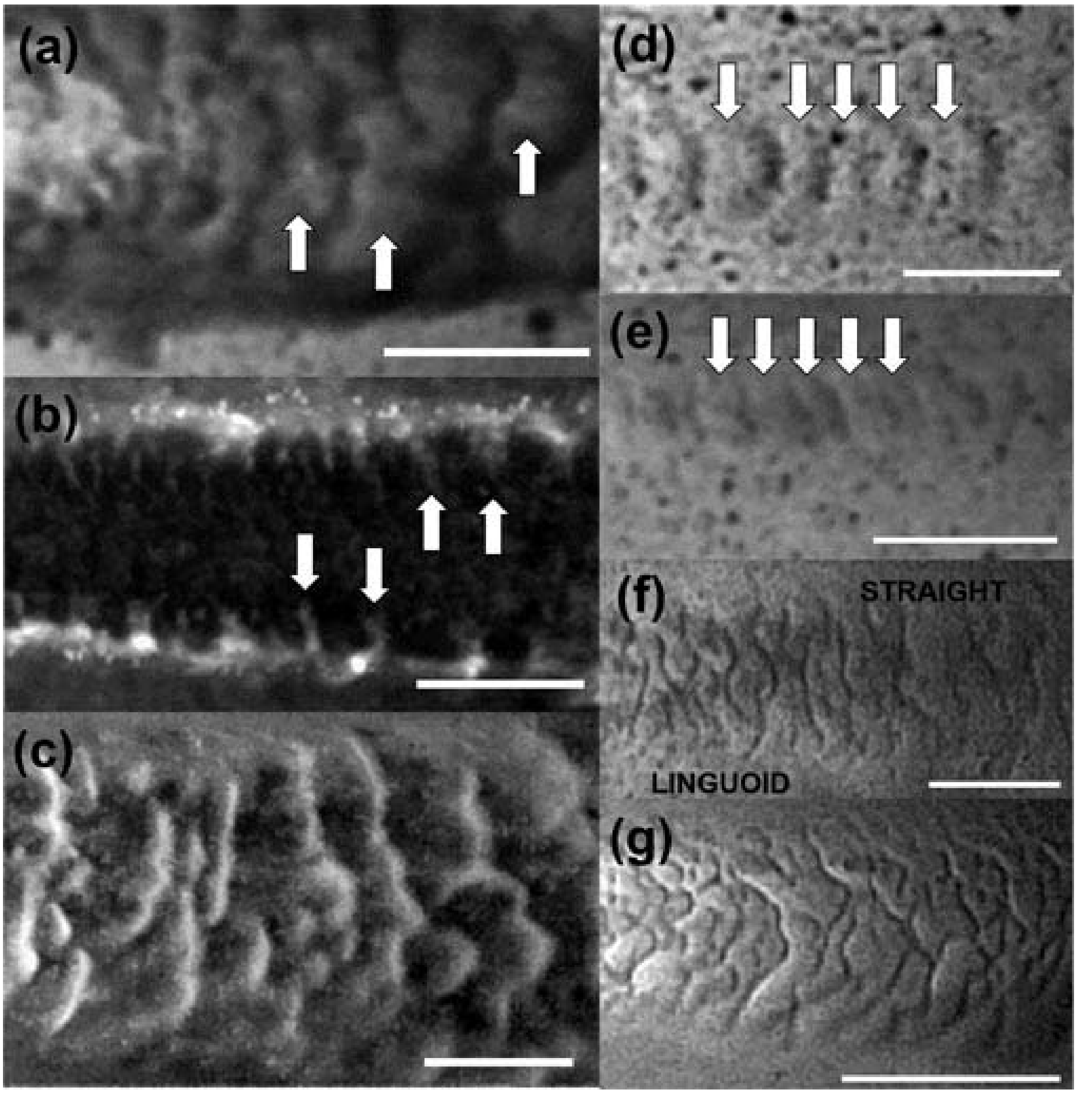

Figure 5.6. (a)-(c) High magnification pictures from high-speed camera videos of different ripples morphologies during S. mutans biofilms exposure to high-velocity bursts. (a) The water microspray burst generated isolated linguoid ripples (white arrows) at the front edge of the burst. Instead, the air only burst generated transverse linguoid ripples (white arrows) at the edges of the clearance zone (b) or a mixture of linguoid and straight-sinuous ripples at the front edge of the burst (c). Flow was left to right. Scale bar = 2 mm. (d) – (g) Different ripples morphologies during biofilm exposure to a compressed air jet of 24.6 m/s (d), 44.9 m/s (e), 68.1 m/s (f), 85.5 m/s (g). The ripples pattern changed as air jet velocity increased. Panel (d) and (e) show straight-sinuous ripples appeared during low-

velocity air jets (24.6 m/s and 44.9 m/s). (c) Straight-sinuous transition to linguoid at 85.5 m/s. (g) Linguoid ripples at high velocities (110.1 m/s). Flow from left to right. Scale bar = 5 mm.

Scanning electron microscope analysis of the biofilm after the perturbation confirmed the presence of residual ripples which clearly demonstrate the rearrangement of the biofilm structure while it was flowing (Figure 5.7).

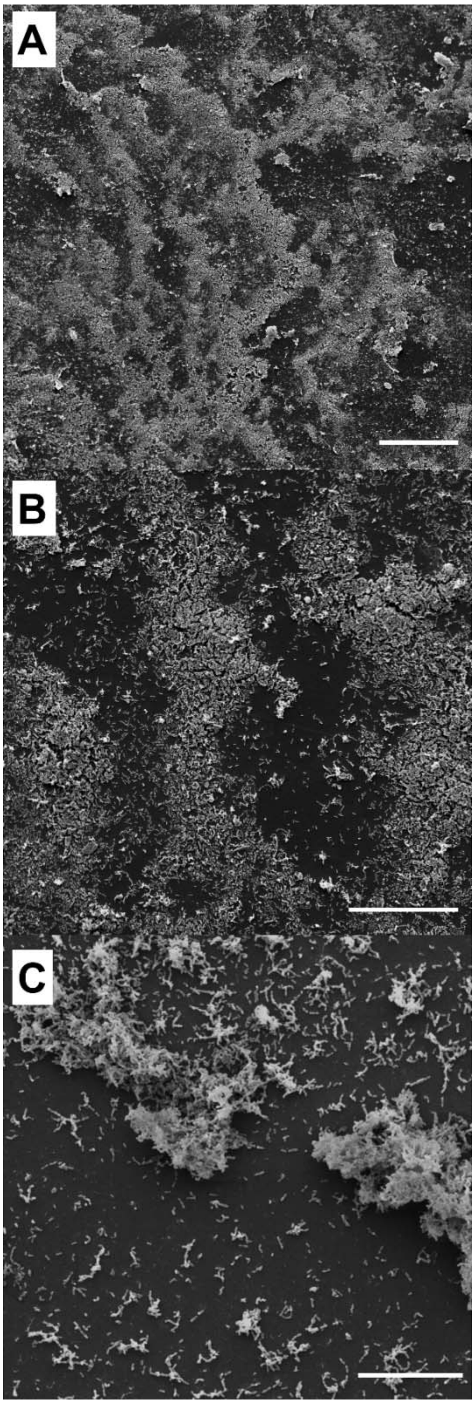

Figure 5.7. Scanning electron microscopy images of a S. mutans biofilm after exposure to a single water microspray burst showing residual ripples. Panels (a), (b) and (c) are at successively higher magnifications. Scale bars = 200, 50 and 20 μm respectively.

5.3.2 Air jets induce ripples formation in *S. mutans* biofilms

High-speed camera movies of *S. mutans* biofilms exposed to air jets showed there was no ripple formation at the lowest air flow of 7.2 m/s (Re = 660.1) but they did occur at flows greater than 24.6m/s (Re = 2244) (Movie 10 and Movie 11). Ripples generated at low-velocity jets (< 44.9 m/s) were similar to straight sinuous ripples (Figure 5.6d and Figure 5.6e), whereas high-velocity jets (>68.1 m/s) formed linguoid ripples (Figure 5.6f and Figure 5.6g). Our data suggest that the ripples formation and morphology might be linked to the onset of turbulence (predicted between Re 2,300 and 4,000 in the air flow (Rajaratnam 1976)). From the analysis of the high-speed camera videos, we found that the measured ripples velocity increased exponentially from 0.22 ± 0.02 m/s to 2.13 ± 0.41 m/s with increasing air jet velocity from 24.6 m/s to 110.2 m/s (Figure 5.8a). On the contrary, the measured ripples wavelength exponentially decayed from a value of 1.68 ± 0.13 mm to 0.68 ± 0.07 mm as u_{jet} increased (Figure 5.8b).

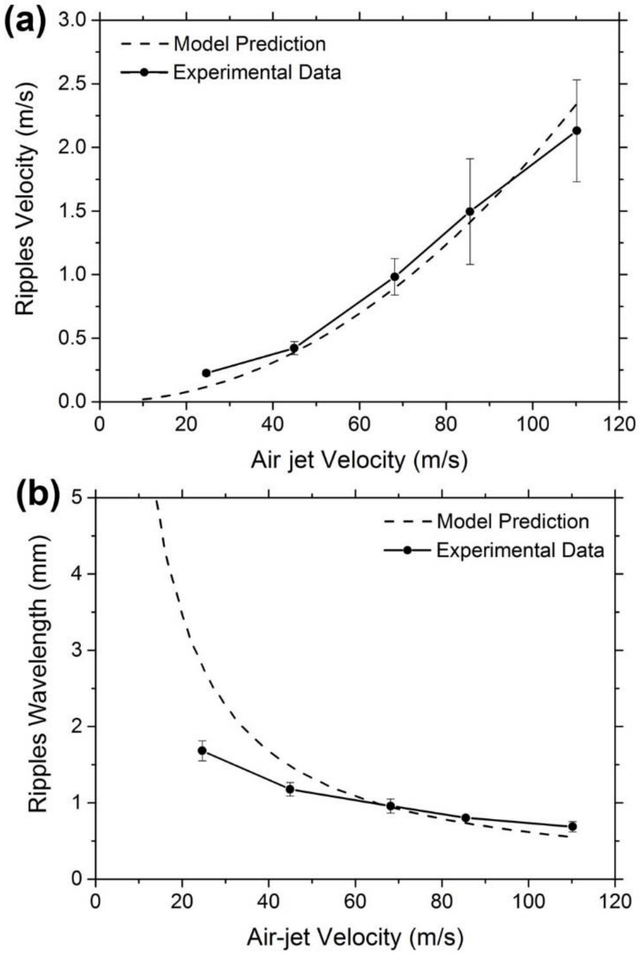

Figure 5.8. Comparison between the theoretical prediction (dashed lines) and experimental measurements (dot-solid lines) of ripples velocity and wavelength as a function of the air jet velocity. (a) The measured ripples velocity increased exponentially ($R^2 = 0.957$ for exponential fit) with the air jet velocity. Predicted values agreed well with the experimental data ($R^2=0.989$). (b) The measured ripples wavelength decreased exponentially ($R^2 = 0.989$ for exponential fit) with the air jet velocity. Predicted values agreed well with the experimental data ($R^2=0.986$). Experimental data reported as mean and 1 standard deviation, n = three independent replicates.

To further investigate apparent periodicity in the ripple structures, we manually measured the distance between individual ripples and also performed Fast Fourier Transform (FFT) analysis on the ripple patterns. The FFT provided a power spectrum (amplitude vs. frequency) for each of the air flow settings (Figure 5.9). Interestingly, below an air jet velocity of 68.1 m/s, the spectrum was relatively simple and the main peaks were easily identified by eye. However, at higher velocities (85.5 m/s and 110.1 m/s) there was a lot of fluctuation in the spectrum and an accurate identification of dominant peaks was more difficult. Studies showed that a transition to turbulence is bordered by an instability (Joseph and Renardy 2013) which can increase the randomness of the FFT spectra. Amplitude peaks occurring at frequencies which corresponded to wavelengths values similar to the ones measured using Fiji were easily identified.

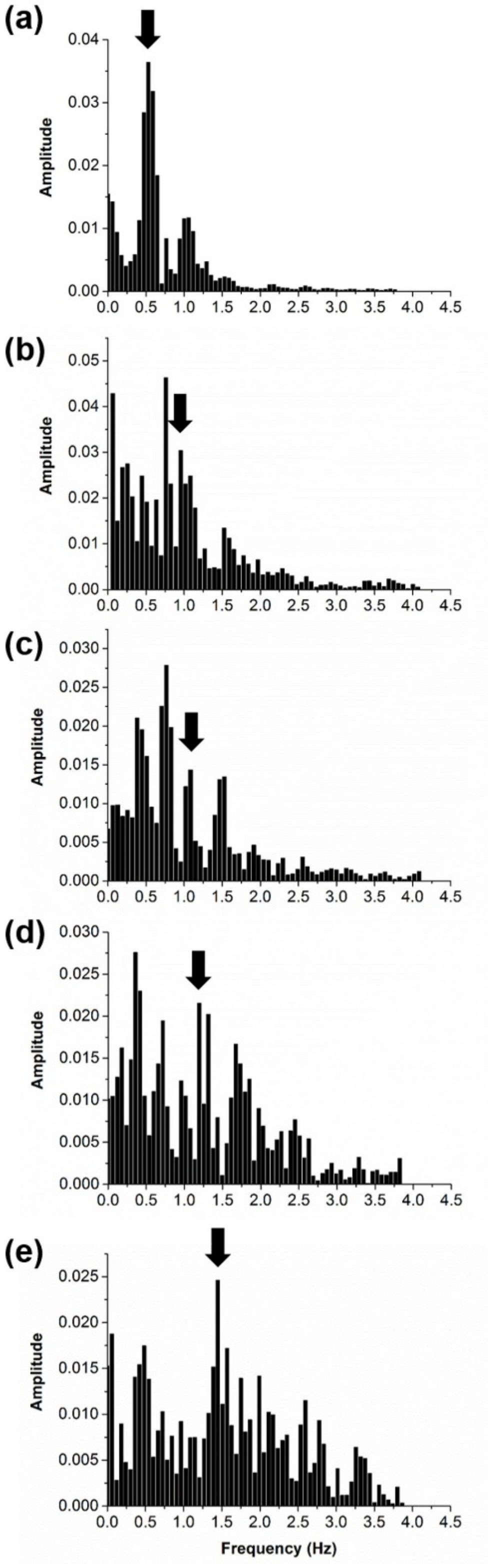

Figure 5.9. Power spectra of ripples patterns generated from FFT analysis after S. mutans biofilm exposure to air jets at 24.6 m/s (a), 44.9 m/s (b), 68.1 m/s (c), 85.5 m/s (d) and 110.1 m/s (e). Well-defined peaks represent periodicities in the distance between the ripples (wavelength). Black arrows indicate the position of the peak frequency relative to the wavelength measured manually.

5.3.3 Ripples modeled as Kelvin-Helmholtz Instabilities

We took a mathematical approach in modelling our experimental data to explore our hypothesis that the ripples were KHI formed at the interface between the biofilm and the air jet. Because the physical system of interest consists of materials of vastly different Reynolds numbers, we choose to treat the two-fluid system (air, biofilm) as Euler-flow over a Stokes-like multiphase material (Cogan and Keener 2004). The former is ‘infinite Reynolds number’, also referred to as inviscid since the viscous stress terms are neglected. The latter is ‘zero Reynolds number’ and the inertial terms are neglected. Because the materials are quite different we expect there to be surface tension on the interface. Then, we carried out linear stability analysis for the two-fluid model of a biofilm. Classical theory linearizes the equations and considers the stability of the interface to perturbations. Similar analysis shows how water waves develop, certain cloud patterns, and the bifurcation from laminar to turbulent mixing. We found a non-trivial dispersion curve relating the perturbation wavelength and the growth rate of the perturbation to a unique maximum that depends on the air velocity. From a pattern formation standpoint, we expect that the observed wavelength will correspond to this maximum since it is growing the fastest. At some stage nonlinear behavior takes over, but the peak gives a reasonable estimate for the observable wavelength. Additionally, the ratio of the growth rate, ω, to the frequency, k, provides an estimate for the velocity of the peaks. Comparing these for varying air jet velocities provides the match shown in Figure 5.8. R-squared values over 98% were estimated for both the ripples velocity and wavelength, which indicates an excellent agreement between the experimental measurements and the data obtained from the analysis. It appears from the analysis that although surface tension is required to stabilize the system, it does not play a strong role in selecting the wavelength or velocity of the ripples. Additionally, since there is a monotonic relationship between the ripple and air velocity, the generation of instabilities is limited primarily by the fluid speeds that may be achieved.

5.3.4 Ripples and wrinkles formation in *S. epidermidis* and *P. aeruginosa* biofilms

High-speed camera movies of *S. epidermidis* biofilms captured the formation of ripple-like structures migrating at a velocity of 2.4 m/s (±0.5, n=5) similar to the ones we documented for *S. mutans* biofilms (Movie 12 and Figure 10a). However, the *P. aeruginosa* biofilms formed wrinkle-like structures which developed from biofilm pelicle growth over a constrained surface (Movie 13 and Figure 10b). Under the forces of the air jet some wrinkles showed elastic behaviour as the stretched before breaking. Unlike the ripples, the wrinkles didn’t migrate over the surface but initially resisted the air jet until the whole film detached after a further 150 ms, and flowed over the surface in waves. The velocity was approx. 0.2 m/s.

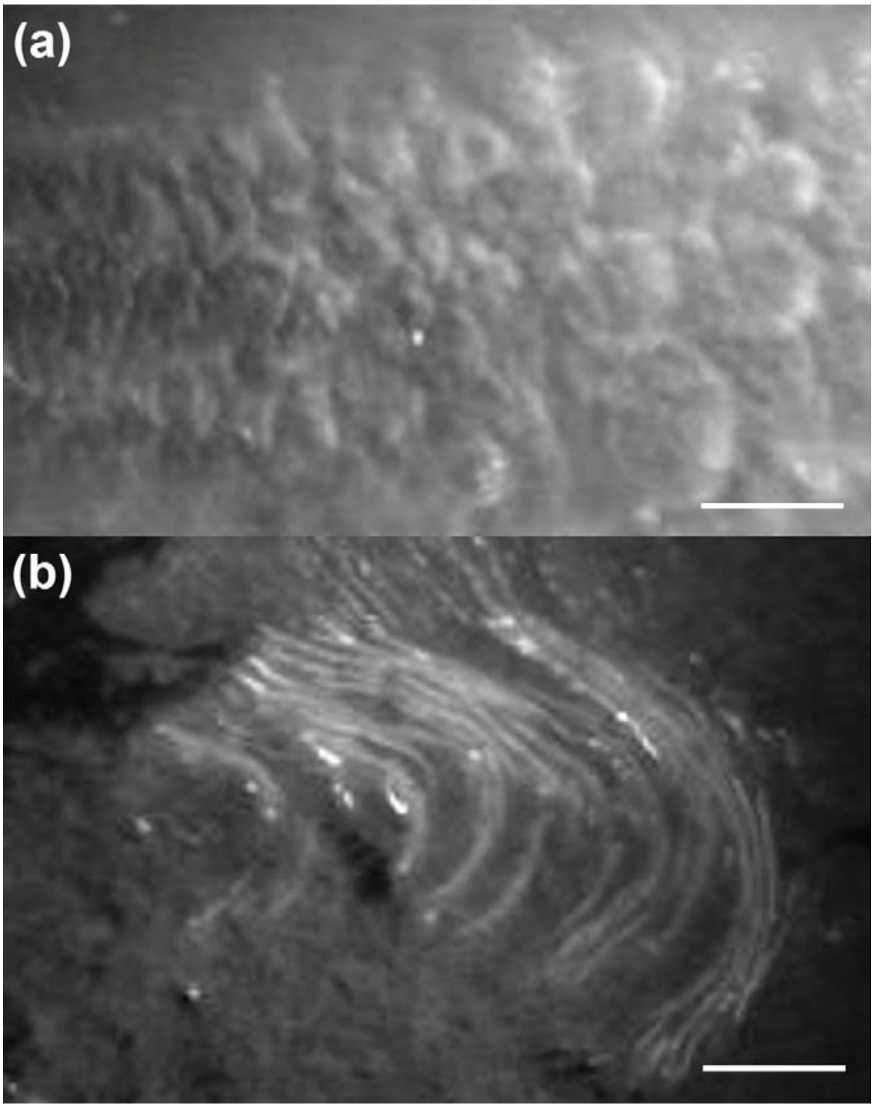

Figure 10. (a) High magnification picture from high-speed camera videos of ripples formed during S. epidermidis biofilm exposure to an air jet of 85.5 m/s. (b) High magnification picture from high-speed camera videos of wrinkles formed during P. aeruginosa biofilm exposure to an air jet of 85.5 m/s. Flow was left to right. Scale bars are 2 mm.

5.4 DISCUSSION

High-speed camera videography on laboratory-grown *S. mutans* biofilms exposed to high-velocity microbursts allowed the discovery of transient ripples-like structures which migrated over the biofilm surface. The ripples would not have been discovered without the benefit of the high-speed video. This phenomenon indicates that the biofilm has incredible flexibility to cope with environmental stresses without detaching due to the inherent characteristics of viscoelasticity. We noticed similarities in the ripple morphology of these high-velocity ripples to the slow moving, long-lived ripples observed in previous studies (Purevdorj et al. 2002; Stoodley et al. 1999). Our high-speed videos demonstrate that ripples can form, migrate and dissipate at extremely fast time scales (ms).

The microsprays generated by the interdental cleaning device had complex flow hydrodynamics ((Fabbri et al. 2016) or Chapter 4)) and could not be readily controlled or modelled. Consequently, we next assessed ripple formation in *S. mutans* biofilms using a steady compressed air jet at which the flow velocity could be controlled (u_{jet}). We found similarities in the shapes and forms also with sedimentary structures or sand beds which are moulded by external physical forces such as winds or currents (Porada et al. 2008). There is evidence that changes in the ripples morphology from two-dimensional to linguoid on sand beds is related to an increase in the bulk flow velocity (Robert 2014; Robert and Uhlman 2001). Ripples have been observed in gas-liquid flows demonstrating an instability nature (Cohen and Hanratty 1965; Craik 1966). In particular, our ripples morphology was similar to the ones discovered in annular thin (~ 147 μm) liquid films exposed to high gas velocities (> 20 m/s) (Asali and Hanratty 1993). From the analysis of the high-speed camera videos, we found that the measured ripples velocity increased exponentially with increasing air jet velocity, whereas, the measured ripples wavelength exponentially decayed u_{jet} increased (Figure 5.8). Although our wavelength values were lower by a factor of ~ 10^{-1} than the ones measured by Asali et al. (Asali and Hanratty 1993), the same ($R^2 = 0.976$) trend was observed. Stoodley and co-authors also reported a variation in the ripples morphology with temporary changes in the flow velocity (Stoodley et al. 1999).

Given the conserved nature of biofilm viscoelasticity (Shaw et al. 2004) we hypothesised that the formation of interfacial instabilities will likewise be a general phenomenon given the right set of biological and environmental conditions. We tested our hypothesis exposing 3-days old biofilms grown from *Staphylococcus epidermidis* (a skin isolate and opportunistic biofilm pathogen in orthopaedic device related infections (Otto 2009)) or *Pseudomonas aeruginosa* (*a* common nosocomial biofilm pathogen infecting wounds, medical devices and the upper respiratory tract*)* strain to a steady compressed air jet. High-speed camera movies of *S. epidermidis* biofilms captured the formation of ripple-like structures similar to the ones we documented for *S. mutans* biofilms. However, the *P. aeruginosa* biofilms formed wrinkle-like structures which appeared similar to those described by Trejo,et al. (Trejo et al. 2013) which developed from biofilm pelicle growth over a constrained surface. Whether a biofilm is more likely to flow in ripples or form more solid-like wrinkles is likely a function of a number of factors including adhesion strength, density, surface tension and viscoelastic moduli.

Interfacial instabilities in biofilms have been conjectured but never directly demonstrated (Klapper et al 2002, Thomas et al 2013). Despite the limited number of studies on ripples formation in laboratory-grown biofilms, an extensive number of authors have described the appearance of ripples-marks in both modern and ancient microbial mats (Noffke et al 2013, Porada et al 2008). Previous studies correlate the Kinneyia ripple fossils to high shear stresses caused by extreme environmental conditions such as high wind storms or water floods. Thus, recent evidence of highly-transient, high-velocity interfacial ripples offers a framework to test and validate mathematical models. Thomas et al. 2013 (Thomas et al 2013) hypothesized that Kinneyia ripples in Proterozoic fossils were Kelvin-Helmholtz Instabilities in microbial mats and used data from cross-linked gels to support their hypothesis. Here, using a detailed physics-based model and classical mathematical analysis, we provide support for the evidence of Kelvin-Helmholtz generated instabilities in microbial biofilms. We found an excellent match between the theoretical prediction and the experimental observations. The predictions are accurate enough to provide confidence that our model is capturing the most important material properties required to understand the mechanisms behind the phenomenon. We are aware that the use of a Newtonian fluid model contradicts most of the rheological data on biofilms as multiple groups have reported a viscoelastic shear-thinning behavior for different bacterial biofilms (Billings et al 2015, Peterson et al 2015, Wilking et al 2011). However, Newtonian models are routinely used for biofilm behavior at this scale (Cogan and Keener 2004, Cogan 2008, Klapper et al 2002). At the flow velocities that we are observing, shear thinning likely occurs quite quickly, which is why we treat the biofilm as a viscous fluid. Certainly, visco-elastic effects will play a role in the initial stages but this is transient at the scale of the experiments. The fact that we get excellent correlation between the theory and experiment supports the idea that visco-elastic effects are negligible for the comparisons made here.

Showing that transient high-velocity biofilm-fluid interactions can cause the extremely rapid generation of wrinkles and ripples travelling at high velocities provides further insight into the mechanical behaviour of biofilms as complex materials (Persat et al. 2015). In addition, fluid/structure interactions in biofilms are known to modulate the dynamics of biofilm growth, tolerance to antibiotics, and virulence. There are a number reasons for the interest in this newly developing field. 1) The biological perspective of being able to relate the emergent properties of form and biomechanics of biofilms with survival functions, in a manner similar to that used to study multicellular plants and animals (Vogel 1996). 2) The ability of biofilm to flow over surfaces has important consequences for mechanical removal control strategies in the medical field as evidenced by the wave-like pattern biofilms have been found inside endotracheal tubes

(Inglis 1993) and venous catheters (Rusconi et al. 2010). 3) Viscoelastic ripples migration can be related to the large pressure drops and drag associated with biofilms in systems ranging from industrial pipelines (Lappin-Scott and Costerton 1989) to ship hulls (Schultz et al. 2011). 4) Interfacial instabilities in biofilms may enhance mass and heat transport (Chen et al. 1997; Vazquez-Una et al. 2000). Furthermore this biofilm particular behaviour could be induced deliberately to increase antimicrobial delivery inside biofilms for better therapeutic control in medicine and industry (Davies et al. 1998). Moreover, our discovery of different observable patterns in biofilms offer the opportunity for theoretical models to be tested against specific and repeatable observations. These models are used, in turn, to quantify important features of biofilms (such as the role of surface tension (Picioreanu et al. 2001)), explore aspects of biofilms not available for experimental studies (Cogan 2010; Friedman 2015), and to optimize removal protocols (De Leenheer and Cogan 2009).

5.5 REFERENCES

Asali J, Hanratty T. 1993. Ripples generated on a liquid film at high gas velocities. International journal of multiphase flow. 19(2):229-243.

Battin TJ, Kaplan LA, Newbold JD, Cheng X, Hansen C. 2003. Effects of current velocity on the nascent architecture of stream microbial biofilms. Applied and Environmental Microbiology. 69(9):5443-5452.

Billings N, Birjiniuk A, Samad TS, Doyle PS, Ribbeck K. 2015. Material properties of biofilms—a review of methods for understanding permeability and mechanics. Reports on Progress in Physics. 78(3):036601.

Cense A, Peeters E, Gottenbos B, Baaijens F, Nuijs A, Van Dongen M. 2006. Mechanical properties and failure of *Streptococcus mutans* biofilms, studied using a microindentation device. Journal of microbiological methods. 67(3):463-472.

Chen Z, Chen X, Chen J. 1997. Effects of an oscillating interface on heat transfer. Chemical engineering science. 52(19):3265-3275.

Cogan N. 2010. An extension of the boundary integral method applied to periodic disinfection of a dynamic biofilm. SIAM Journal on Applied Mathematics. 70(7):2281-2307.

Cogan N, Keener JP. 2004. The role of the biofilm matrix in structural development. Mathematical Medicine and Biology. 21(2):147-166.

Cohen LS, Hanratty TJ. 1965. Generation of waves in the concurrent flow of air and a liquid. AIChE Journal. 11(1):138-144.

Costerton JW, Stewart PS, Greenberg E. 1999. Bacterial biofilms: A common cause of persistent infections. Science (New York, NY). 284(5418):1318-1322.

Craik AD. 1966. Wind-generated waves in thin liquid films. Journal of Fluid Mechanics. 26(02):369-392.

Davies DG, Parsek MR, Pearson JP, Iglewski BH, Costerton JW, Greenberg EP. 1998. The involvement of cell-to-cell signals in the development of a bacterial biofilm. Science. 280(5361):295-298.

De Leenheer P, Cogan N. 2009. Failure of antibiotic treatment in microbial populations. Journal of mathematical biology. 59(4):563-579.

Drescher K, Shen Y, Bassler BL, Stone HA. 2013. Biofilm streamers cause catastrophic disruption of flow with consequences for environmental and medical systems. Proceedings of the National Academy of Sciences. 110(11):4345-4350.

Fabbri S, Johnston DA, Rmaile A, Gottenbos B, De Jager M, Aspiras M, Starke ME, Ward MT, Stoodley P. 2016. *Streptococcus mutans* biofilm transient viscoelastic fluid behaviour during high-velocity microsprays. Journal of the mechanical behavior of biomedical materials. 59:197-206.

Flemming H-C, Wingender J. 2010. The biofilm matrix. Nature Reviews Microbiology. 8(9):623-633.

Friedman A. 2015. Free boundary problems in biology. Phil Trans R Soc A. 373(2050):20140368.

Funada T, Joseph D. 2001. Viscous potential flow analysis of kelvin–helmholtz instability in a channel. Journal of Fluid Mechanics. 445:263-283.

Geyer WR, Lavery AC, Scully ME, Trowbridge JH. 2010. Mixing by shear instability at high reynolds number. Geophysical Research Letters. 37(22).

Hall-Stoodley L, Costerton JW, Stoodley P. 2004. Bacterial biofilms: From the natural environment to infectious diseases. Nat Rev Micro. 2:95-108.

Heydorn A, Nielsen AT, Hentzer M, Sternberg C, Givskov M, Ersbøll BK, Molin S. 2000. Quantification of biofilm structures by the novel computer program comstat. Microbiology. 146(10):2395-2407.

Inglis T. 1993. Evidence for dynamic phenomena in residual tracheal tube biofilm. British journal of anaesthesia. 70(1):22-24.

Joseph D. 2003. Viscous potential flow. Journal of Fluid Mechanics. 479:191-197.

Joseph DD, Renardy Y. 2013. Fundamentals of two-fluid dynamics: Part i: Mathematical theory and applications. Springer Science & Business Media.

Krumbein WE, Paterson DM, Zavarzin GA. 2003. Fossil and recent biofilms: A natural history of life on earth. Springer Science & Business Media.

Lappin-Scott HM, Costerton JW. 1989. Bacterial biofilms and surface fouling. Biofouling. 1(4):323-342.

Loesche WJ. 1986. Role of *Streptococcus mutans* in human dental decay. Microbiological reviews. 50(4):353-380.

Marsh PD. 2004. Dental plaque as a microbial biofilm. Caries Research. 38(3):204-211.

Miles JW. 1959. On the generation of surface waves by shear flows part 3. Kelvin-helmholtz instability. Journal of Fluid Mechanics. 6(04):583-598.

Noffke N, Decho AW, Stoodley P. 2013. Slime through time: The fossil record of prokaryote evolution. PALAIOS. 28(1):1-5.

Noffke N, Gerdes G, Klenke T, Krumbein WE. 2001. Microbially induced sedimentary structures: A new category within the classification of primary sedimentary structures. Journal of Sedimentary Research. 71(5):649-656.

Otto M. 2009. Staphylococcus epidermidis—the'accidental'pathogen. Nature Reviews Microbiology. 7(8):555-567.

Persat A, Nadell CD, Kim MK, Ingremeau F, Siryaporn A, Drescher K, Wingreen NS, Bassler BL, Gitai Z, Stone HA. 2015. The mechanical world of bacteria. Cell. 161(5):988-997.

Peterson BW, He Y, Ren Y, Zerdoum A, Libera MR, Sharma PK, van Winkelhoff A-J, Neut D, Stoodley P, van der Mei HC. 2015. Viscoelasticity of biofilms and their recalcitrance to mechanical and chemical challenges. FEMS microbiology reviews. 39(2):234-245.

Picioreanu C, Van Loosdrecht MC, Heijnen JJ. 2001. Two-dimensional model of biofilm detachment caused by internal stress from liquid flow. Biotechnology & Bioengineering. 72(2):205-218.

Porada H, Ghergut J, Bouougri EH. 2008. Kinneyia-type wrinkle structures—critical review and model of formation. PALAIOS. 23(2):65-77.

Purevdorj B, Costerton JW, Stoodley P. 2002. Influence of hydrodynamics and cell signaling on the structure and behavior of pseudomonas aeruginosa biofilms. Applied and Environmental Microbiology. 68(9):4457-4464.

Rajaratnam N. 1976. Turbulent jets. Elsevier.

Rmaile A, Carugo D, Capretto L, Aspiras M, De Jager M, Ward M, Stoodley P. 2014. Removal of interproximal dental biofilms by high-velocity water microdrops. Journal of dental research. 93(1):68-73.

Rmaile A, Carugo D, Capretto L, Wharton JA, Thurner PJ, Aspiras M, Ward M, De Jager M, Stoodley P. 2015. An experimental and computational study of the hydrodynamics of high-velocity water microdrops for interproximal tooth cleaning. Journal of the Mechanical Behavior of Biomedical Materials. 46:148-157.

Rmaile A, Carugo D, Capretto L, Zhang X, Wharton JA, Thurner PJ, Aspiras M, Ward M, Stoodley P. 2012. Microbial tribology and disruption of dental plaque bacterial biofilms. Wear. (0).

Robert A. 2014. River processes: An introduction to fluvial dynamics. Routledge.

Robert A, Uhlman W. 2001. An experimental study on the ripple–dune transition. Earth Surface Processes and Landforms. 26(6):615-629.

Rusconi R, Lecuyer S, Guglielmini L, Stone HA. 2010. Laminar flow around corners triggers the formation of biofilm streamers. Journal of The Royal Society Interface. 7(50):1293-1299.

Schindelin J, Arganda-Carreras I, Frise E, Kaynig V, Longair M, Pietzsch T, Preibisch S, Rueden C, Saalfeld S, Schmid B et al. 2012. Fiji: An open-source platform for biological-image analysis. Nat Methods. 9(7):676-682.

Schultz M, Bendick J, Holm E, Hertel W. 2011. Economic impact of biofouling on a naval surface ship. Biofouling. 27(1):87-98.

Shaw T, Winston M, Rupp CJ, Klapper I, Stoodley P. 2004. Commonality of elastic relaxation times in biofilms. Physical Review Letters. 93(9):098102.

Stoodley P, Lewandowski Z, Boyle JD, Lappin-Scott HM. 1999. The formation of migratory ripples in a mixed species bacterial biofilm growing in turbulent flow. Environmental Microbiology. 1(5):447-455.

Stoodley P, Sauer K, Davies DG, Costerton JW. 2002. Biofilms as complex differentiated communities. Annual review of microbiology. 56:187-209.

Thomas K, Herminghaus S, Porada H, Goehring L. 2013. Formation of kinneyia via shear-induced instabilities in microbial mats. Philosophical Transactions of the Royal Society A: Mathematical, Physical and Engineering Sciences. 371(2004):20120362.

Trejo M, Douarche C, Bailleux V, Poulard C, Mariot S, Regeard C, Raspaud E. 2013. Elasticity and wrinkled morphology of bacillus subtilis pellicles. Proceedings of the National Academy of Sciences. 110(6):2011-2016.

Vazquez-Una G, Chenlo-Romero F, Sanchez-Barral M, Perez-Munuzuri V. 2000. Mass transfer enhancement due to surface wave formation at a horizontal gas–liquid interface. Chemical engineering science. 55(23):5851-5856.

Vinogradov AM, Winston M, Rupp CJ, Stoodley P. 2004. Rheology of biofilms formed from the dental plaque pathogen *Streptococcus mutans*. Biofilms. 1(01):49-56.

Vogel S. 1996. Life in moving fluids: The physical biology of flow. Princeton University Press.

Wilking JN, Angelini TE, Seminara A, Brenner MP, Weitz DA. 2011. Biofilms as complex fluids. MRS Bulletin. 36(05):385-391.

CHAPTER 6

High-velocity microsprays enhance mass transfer in *S. mutans* biofilms

S. Fabbri[1], D.A. Johnston[2], A. Rmaile[3], B. Gottenbos[3], M. De Jager[3], M. Aspiras[4], E. M. Starke[5], M. T. Ward[5] and P. Stoodley[1, 6]

[1]National Centre for Advanced Tribology at Southampton (nCATS), University of Southampton, Southampton SO17 1BJ, United Kingdom.
[2]Biomedical Imaging Unit, School of Medicine, University of Southampton, Southampton SO16 6YD, UK.
[3]Philips Research, High Tech Campus, Eindhoven 5656 AE, The Netherlands.

[4]Wrigley, Chicago, Illinois 60613, USA.

[5]Philips Oral Healthcare, Bothell, Washington 98021, USA.

[6]Department of Microbial Infection and Immunity and the Department of Orthopaedics, Centre for Microbial Interface Biology, The Ohio State University, Columbus, Ohio 43210, USA.

ABSTRACT

Oral biofilms, also known as dental plaque biofilms, are among the most complex microbial communities in nature. They cause dental caries, gingivitis and periodontitis, and are also associated with low birth weight and endocarditis. We assessed the ability of high-velocity water microsprays to enhance mass transfer inside *Streptococcus mutans* dental biofilms using a 1-µm tracer beads solution (10^9 beads/mL). Biofilms were exposed to microsprays shooting at a 90° or 30° angle. For comparison, a 30 sec diffusive transport and simulated mouth washing were also performed. Samples were imaged with confocal laser scanning microscopy to determine the relative bead penetration depth into the biofilm. We demonstrated that the microspray was able to deliver significantly more microbeads deeper in the biofilm compared to a simple 30-sec diffusion assay and simulated mouth-washing. Interestingly the 30° impact in the distal position delivered approximately 16 times more microbeads than the 90° impact. Using high-speed camera videography, we also documented the formation of migratory ripple-like structures at the biofilm/liquid interface. High shear stresses generated at the biofilm/burst interface might have possibly enhanced beads delivery inside the remaining biofilm by combining forced advection into the biofilm matrix with the mixing of the biofilm itself.

1.1 INTRODUCTION

Oral biofilms, sessile communities of bacteria embedded in an extracellular polysaccharide matrix, have a key role in cavities development, gingivitis and periodontitis (Marsh 2004). Both the heterogeneous structure and the mechanical properties are responsible for biofilm resistance to mechanical cleaning and dentifrices penetration. Current methods used to remove dental plaque biofilms consist in applying low volume, high-velocity water droplets (Cense et al. 2006) or entrained air bubbles (Parini et al. 2005; Parini and Pitt 2006). In particular, exposing *Streptococcus mutans* dental biofilms to high-velocity (ms) microbursts, investigators demonstrated not only biofilm viscoelastic behaviour (Rmaile et al. 2014; Rmaile et al. 2015), but also fluid-like behaviour on the order of milliseconds in response (see Chapter 4 or (Fabbri et al. 2016)). These techniques have shown positive results due to the droplets' impact pressure, hydrodynamic shear stresses and the surface tension effects of the passage of an air-water interface over a solid surface (Busscher et al. 2010).

Recently, the role of the hydrodynamic in the enhancement of mass transfer inside biofilms has become a new area of research. Because of biofilm high-cell density and the physiochemical properties of the matrix which normally does not allow advective fluid flow through the EPS, mass transport within the biofilm is limited to diffusion (Forier et al. 2014; Takenaka et al. 2009). In addition, it has been demonstrated that advection alone with no significant mechanical perturbation of the biofilm structure was not enough to drive particles inside the biofilm (de Beer et al. 1996; Stoodley et al. 1994). We previously discovered biofilm fluid-like behaviour could physically "churn up" the biofilm (see Chapter 4 or (Fabbri et al. 2016)) or generate fast-moving ripple-like structures during the exposure to the high-speed microsprays (see Chapter 5). We also provided evidence, supported by mathematical modelling, that these structure were Kelvin Helmotz Instabilities (KHI). Interfacial instabilities in biofilms may enhance mass and heat transport (Chen et al. 1997; Vazquez-Una et al. 2000) since KHI a prelude to mixing and turbulence (Geyer et al. 2010).

We think that high-velocity water microspray by inducing such deformations in the biofilm structure might enhance mass transfer into the biofilm itself. To test this hypothesis, we used 1-μm-size fluorescents beads as tracer particles. Delivery into the biofilm by the high-velocity water microspray was compared with a static (diffusion only) delivery and a simulated mouth-washing. We also performed high-speed camera videography in order to assess biofilm/fluid interaction during the shooting.

6.2 MATERIALS AND METHODS

6.2.1 Biofilm growth conditions

Streptococcus mutans biofilms UA159 (ATCC 700610) were grown for 72 hrs. on microscope glass slides as previously described (see paragraph 4.2.1). After the growth period biofilm covered-slides were gently rinsed in 1 % (wt/vol) phosphate-buffered saline (1% PBS) solution (Sigma-Aldrich) before placing them in petri plates.

6.2.2 Microbeads delivery

1-µm-size carboxylate-modified polystyrene yellow/green-fluorescent beads ($\lambda_{ex}/\lambda_{em}$: 470/505, density= 2.5%, charge density ≥ 0.008 mEq, Sigma-Aldrich, L4655) stock solution was diluted down to 10^9 beads/mL (beads working solution, BWS). A Philips Sonicare AirFloss (AF) commercially available oral hygiene device was used to generate high-velocity water microsprays. A micromanipulator was used in order to hold the Airfloss device in a vertical position. The AF device was filled with 3 mL of the beads working solution. The BWS volume dispensed in each microspray was 130 ± 0.03 µL (n=11), therefore the amount of beads in each burst was approximately 1.3 x 107 beads. First, *S. mutans* biofilm-covered slides were exposed to a microburst shot at either a 90° or a 30° angle with the tip held a distance of 5 mm from the biofilm (microspray experiments). Then, we compared the microspray-induced delivery with a simple diffusion transport (static experiments) and simulated mouth-washing (shaking experiments). Static experiments consisted in pouring the same amount of BWS over the biofilm and let to diffuse for 30 secs. Instead for the shaking experiments, petri plates were filled with BWS until cover the biofilm and then shaken for 30 secs at 200 rpm. After the experiments, the slide samples were washed once with 1% PBS solution for removing the floating beads. Three independent replicates were performed for each experiment.

6.2.3 Confocal microscopy

Control biofilms (unexposed to beads) and those biofilms immediately after the microbeads experiments were carefully transferred to petri plates filled with 1 % (wt/vol) phosphate-buffered saline (PBS) solution (Sigma-Aldrich). Then the samples were fixed with 4% PFA and subsequently stained with Syto 63 ($\lambda_{ex}/\lambda_{em}$: 657⁄673) to stain the cells. Samples were imaged by confocal laser scanner microscope (CLSM, Leica TCS SP5). Three random 3D stacks were taken on each of three independent replicate for the diffusion and shaking experiments (Figure 6.1D). The microsprays generated a zone of clearance (ZOC) in the area where the biofilm was removed (Figure 6.1A). The 90° impact generated a circular ZOC of approximately 300 mm^2, as the flow pattern was axisymmetric. Instead, the 30° impact created an elliptical ZOC of approximately 450 mm^2 because the liquid flow over the surface became asymmetric and less biofilm was removed behind the point of impact (proximal zone, with respect to the direction of the flow). For the independent triplicate spray-exposed biofilm slides (90° and 30° microsprays) confocal images were taken 1-2 mm outside the zone of clearance to represent the unimpacted biofilm. For the 90° microspray, three random images where taken around the circular zone (Figure 6.1B). Instead for the 30° microspray, to assess whether the symmetry of the flow influenced beads and/or antimicrobial penetration three random images were taken at the proximal and at the distal positions (Figure 6.1C). Three random images were also taken inside the zone of clearance (interior zone). To establish the thickness of the biofilm prior the microbeads experiments, three random confocal images were taken on each of three independent replicate control biofilm slides. The thickness of the control biofilms was measured by COMSTAT from the confocal images. The experiments were replicated three times with triplicate repeated confocal images for each position within each replicate.

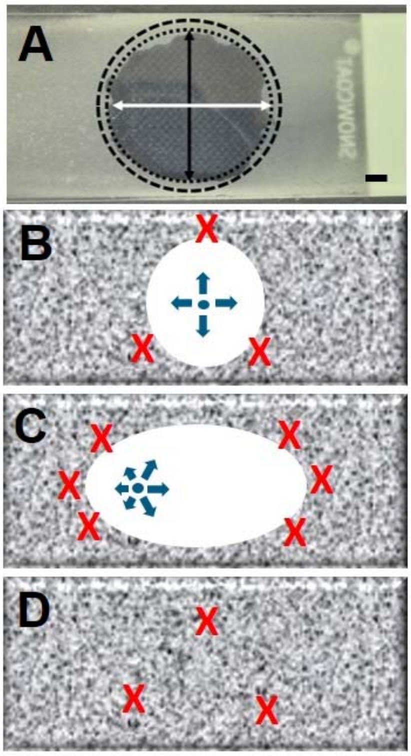

Figure 6.1. A) Microscope slide covered with S. mutans biofilm (light grey) after being exposed to a high velocity PBS microspray at 90º impact. A well-defined circular shaped zone of clearance (ZOC) in the area where biofilm was removed reveals the darker background surface. The black and white arrows show the diameters of the ZOC in the x- and y-axes respectively (major and minor axes lengths for the 30º impact). The dotted circle marks the edge of the ZOC and the measurements of transport and killing in the remaining biofilm were made no further than 200 µm from outside this edge (dashed circle). Scale bar is 5 mm. Representation of one biofilm-covered slide (biofilm depicted as grey and the zone of clearance as white) showing the confocal images positions taken after the 90° microspray shot (B), the 30° microspray shot (C) the diffusion and the shaking experiments (D). Images were taken 1-2 mm after the edge of the zone of clearance. Blue arrows show the direction of the flow from the impact centre.

6.2.4 Quantification of beads penetration

Biofilm surface is highly irregular and not only varies along z (thickness) but also along x and y. Therefore, in order to relate the beads position within the biofilm with respect to the thickness of the biofilm at any one location we used a relative depth ratio (RD_{BEADS}) (Miller et al. 2013), defined as:

$$RD_{BEADS}(\%) = \left(1 - \frac{z_{BEAD}(x_i, y_i)}{z_{BIOFILM}(x_i, y_i)} \times\right) 100 \qquad (6.1)$$

where z_{BEAD} was the bead z-coordinate (depth) and $z_{BIOFILM}$ was the biofilm thickness relative to each bead position (x_i, y_i). Therefore, A RD = 0 % corresponded to a bead located near the biofilm surface, while a RD = 100 % corresponded to a bead located in the biofilm substratum. Z_{BEAD} values were measured using Fiji (Schindelin et al. 2012) using the 3D Object Counter plug-in. Instead $z_{BIOFILM}$ values were obtained using COMSTAT (Heydorn et al. 2000)). A Matlab function was implemented in order to measure the RD_{BEADS} for all the beads found in one confocal image ($A=0.6 \times 10^{-3}$ cm^2) (see Appendix A for a more detailed explanation of the Materials and Methods).

The beads number (N) in each confocal image was measured using the Analyse Particles function of Fiji. We then measured a beads per cm square area dividing N with the area of one confocal image. Statistical analysis was performed using an unpaired t-test on log-transformed data and difference considered significant where $p < 0.05$.

6.2.5 Biofilms exposure to high-velocity microsprays and air-jets

S. mutans biofilms were exposed either to a water microspray burst or a jet generated from an air piston compressor (ClassicAir 255, Metabo) at a 90° angle with the tip held a distance of 5 mm from the biofilm. The shooting was recorded at 5000 or 2000 frames per seconds (fps) with a high-speed camera MotionPro X3 (IDT) placed in order to record the back view of a biofilm covered microscope slide. Experiments were performed in triplicates (n=3). A rotameter was used to estimate the average air jet velocity outside the nozzle ($u_{jet}=41.7 \pm 1.5$ m/s, n=3) and the relative Reynolds number (Re=5516 ± 203, n=3) using:

$$u_{jet} = \frac{Q_{jet}}{A} \tag{6.2}$$

$$Re_{jet} = \frac{\rho u_{jet} D}{\mu} \tag{6.3}$$

where Q_{jet} is the volumetric air flow rate (8±0.3 lpm, n=3), A (3.14×10^{-6} m^2) and D (2×10^{-3} m) are the area and internal diameter of the nozzle tip, ρ and η are the viscosity (Pa·s) and density (kg/m^3) of air at 20°C and 1 atm.

6.2.6 High-speed video post-processing

The high-speed camera videos were analysed with the image processing package Fiji (Schindelin et al. 2012)). Ripples wavelength (λ_R), width (w_R) and velocity (u_R) were measured using the same protocol as previously described (See paragraph 5.2.5). Statistical analysis was performed using an unpaired t-test and difference considered significant where $p < 0.05$.

6.2.7 Fast Fourier analysis

Fast Fourier Transform (FFT) was used to determine the dominant wavelengths of transient ripples formed during the *S. mutans* biofilm exposure to air jets. Frames from the videos were analysed in Fiji using the plot profile function as explained previously. Then Fast Fourier analysis was performed on the plot profile graph. Since the FFT algorithm imposes a fixed interval range ($N= 2^m$, where N is the number of samples and m a positive integer), we selected N=128. Wavelengths were obtained by from the inverse of the relative peak frequencies.

6.3 RESULTS

6.3.1 Biofilm structure and thickness

Biofilm samples imaged by confocal microscopy were heterogeneous in the structure showing channels and voids (Figure 6.2A). The thickness of the untreated biofilm (control) was 51.8±4.9 µm. Addition of the beads made no significant difference (55.9±3.5 µm) but the shaking and the exposure to a microspray (30° or 90°) reduced it a further 11.6±2.9 µm and 27.4±5.4 µm respectively ($p < 0.05$). Statistical difference was found between the biofilm thickness after the 90° microspray ($t_{90°}$=33.8±9.6 µm) and the biofilm thickness after a 30° microspray in the distal position ($t_{30°,d}$=23.1±3.9 µm) but not in the proximal one ($t_{30°,p}$ =28.7±5.2 µm). All the thicknesses were statistically different from the biofilm thickness in the interior zone (0.005±0.003 µm).

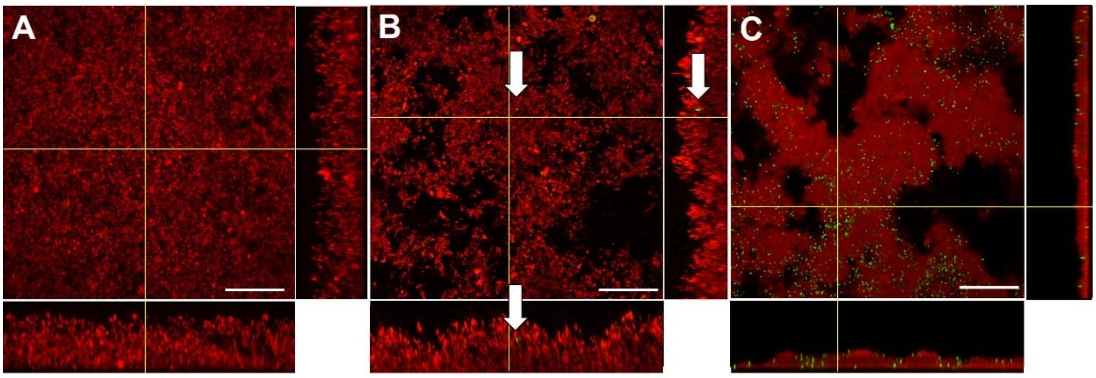

Figure 6.2. Confocal images in x–y plan view with x–z cross section below of S. mutans biofilm without any treatment (control) (A), after the static (B) and after the 30° microspray (C). Dead biofilm was stained red (Syto 63) and the beads were fluorescent green. The white arrows show one bead entrapped inside biofilm. Scale bars are 50 µm.

6.3.2 Microbeads delivery

CLSM images of the beads experiments exhibited a higher amount of beads after exposure to the microspray than after static or shaking conditions (Figure 6.2). Beads were also observed in the confocal cross-sections images, confirming their penetration inside the biofilm. Both microsprays (90° and 30°) delivered significantly more beads ($N_{90°}$ =1.3 x 10^5 ± 8.3 x 10^4 beads/cm^2, $N_{30°,D}$=1.9 x 10^6 ± 4.5 x 10^5 beads/cm^2 and $N_{30°,P}$=2.7 x 10^5 ± 1.2 x 10^5 beads/cm^2)

into the biofilm than static transport ($N_D=925.9 \pm 185.2 \times 10^4$, n=3) or shaking assay ($N_S=6.6 \times 10^3 \pm 1.6 \times 10^3$, n=3). We also found significantly more beads in the distal zone ($N_{30°,D}=1.9 \times 10^6 \pm 4.5 \times 10^5$ beads/cm^2) than in the proximal zone ($N_{30°,P}=2.7 \times 10^5 \pm 1.2 \times 10^5$ beads/cm^2). The 30° microspray in the distal zone delivered approximately 16 times more microbeads than the 90° microspray ($p < 0.05$, n=3) but it was not in the proximal zone. shows the beads distribution inside the biofilm in each relative depth "slice" (0-25%, 25-50%, 50-75% and 75-100%). Both 90º and 30º microsprays delivered the microbeads significantly deeper into the biofilm ($RD_{90}{}^{o}=92.5\pm3.1$, $RD_{30}{}^{o}{}_{,P}=93.1\pm2.2$ and $RD_{90}{}^{o}{}_{,D}=94.6\pm1.1$, n=3) compared to a diffusion transport ($RD_D=30.4\pm10.1$, n=3) and shaking ($RD_S=56.6\pm 3.6$, n=3).

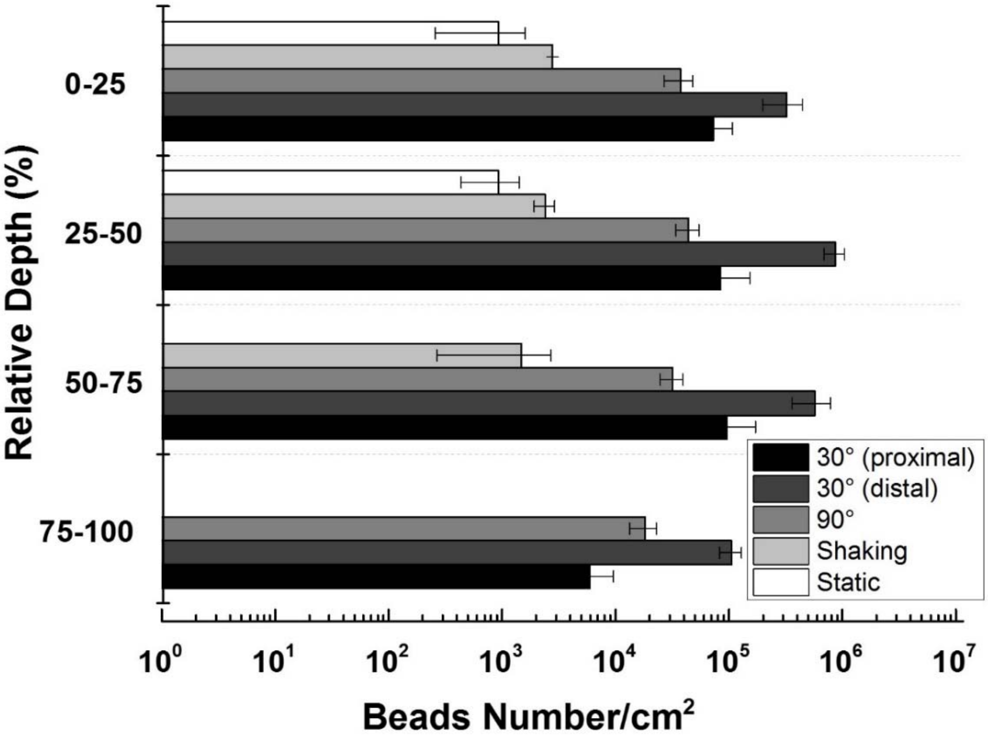

Figure 6.3. Bar chart (logarithmic scale) showing beads distribution (N/cm^2) inside S. mutans biofilm in terms of relative depth ratio for the static, shaking, 90 º and 30 º experiments. Data represented as mean and 1SE from three independent replicates. A RD value of 0–25% corresponded to a bead located near the biofilm surface, while a relative depth of 75–100% corresponded to a bead located in the biofilm substratum.

6.3.3 Ripple formation during high-speed microsprays

High-speed camera movies of *S. mutans* biofilms exposed to high-velocity microsprays at a 90º angle revealed that the water microspray rapidly impacted the biofilm creating a zone of clearance (Movie 14). After the exposure to the burst (duration ~ 60 ms), the biofilm clearance zone covered an area of approximately 300 mm^2 (Figure 6.1A). Migratory ripple-like structures were seen developing at the fluid-biofilm interface which travelled radially from the centre of the burst impact towards the outside with an average velocity of u_R=3.2 m/s (± 0.8 m/s, n=3) (Figure 6.4). Interestingly, after the burst, the ripples dissipated within milliseconds leaving little trace of their formation.

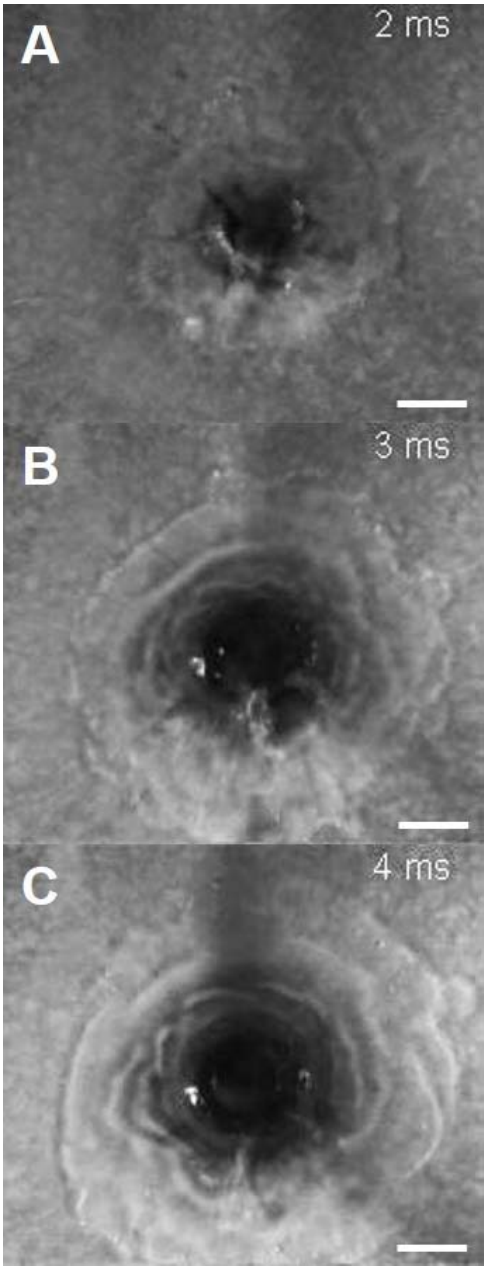

Figure 6.4. Subsequent frames from a high-speed camera video illustrating S. mutans biofilm removal and spatial migration of ripples trains during the exposure to a high-velocity water microspray. Frames show S. mutans biofilm-colonized slide proximal to the camera (biofilm depicted light grey) at 2 ms A), 3 ms B) and 4 ms C). The AirFloss nozzle tip was located perpendicularly to the slide at a distance of 5 mm. Scale bars are 1 mm.

The ripples morphology alternated straight-sinuous ripples to linguoid ripples (arcuate crests) with an average wavelength of λ_R=0.5 mm (± 0.08 mm, n=3) and a width of w_R=0.3 mm (± 0.03 mm, n=3) (Figure 6.5).

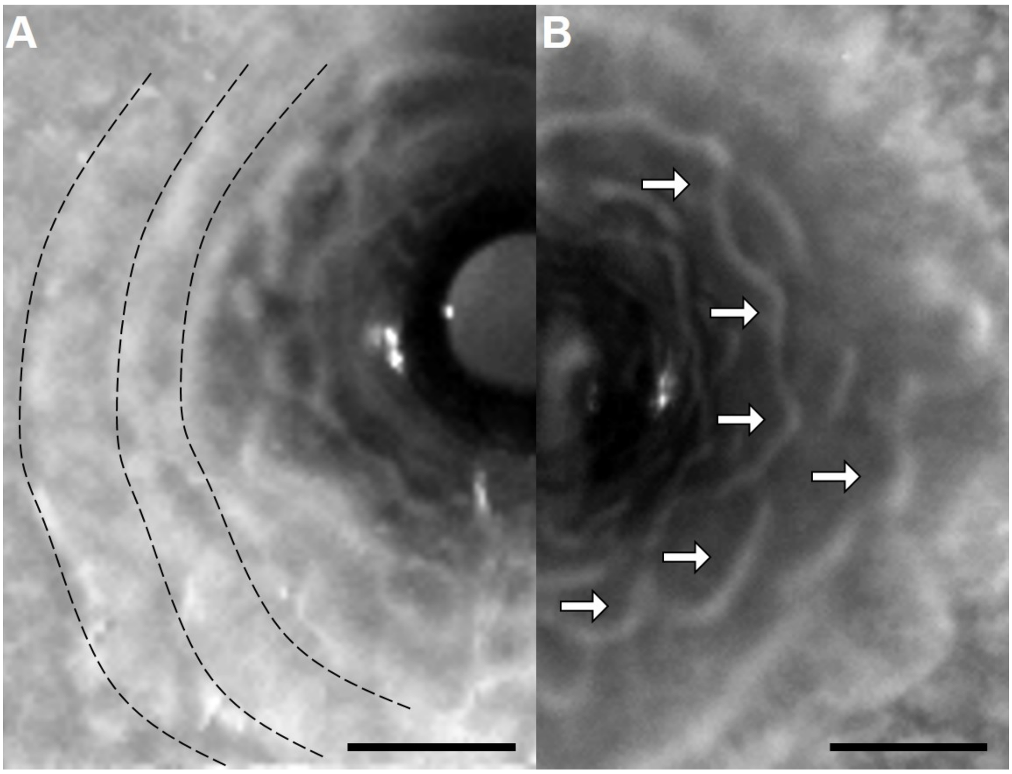

Figure 6.5. High magnification pictures from high-speed camera videos of different ripple morphologies during S. mutans biofilms exposure to a 90 º impact from a high-velocity water microspray. A) Straight-sinuous ripples (black dashed lines). Scale bar = 1 mm. B) Linguoid ripples (white arrows). Scale bar = 0.5 mm.

6.3.4 Ripple formation during air-jets

High-speed camera videos of *S. mutans* biofilms exposed to a perpendicular air jet showed the air flow travelling radially outwards from the impact point along the surface thereby dragging the biofilm into motion (Movie 15). Immediately after the impact, ripples-like structures were seen developing at the biofilm/air interface and propagating radially outwards. Ripples velocity increased linearly reaching a maximum average velocity of u_R=2.3 m/s (± 0.5 m/s, n=3) for the first approximately 50 ms for then exponentially decreasing until stationary as the biofilm was completely removed from the surface. Ripples morphology changed as they migrated outwards from the impact centre starting from linguoid ripples for merging together into circular straight sinuous ripples (Figure 6.6A-B). Ripples wavelength and width were λ_R=0.9 mm (± 0.3 mm, n=3) and w_R=0.2 mm (± 0.06 mm, n=3) respectively. A biofilm zone of clearance of A=278 mm (± 8.1 mm, n=3) was created at the end of the air jet exposure where residual ripples remained (Figure 6.6C).

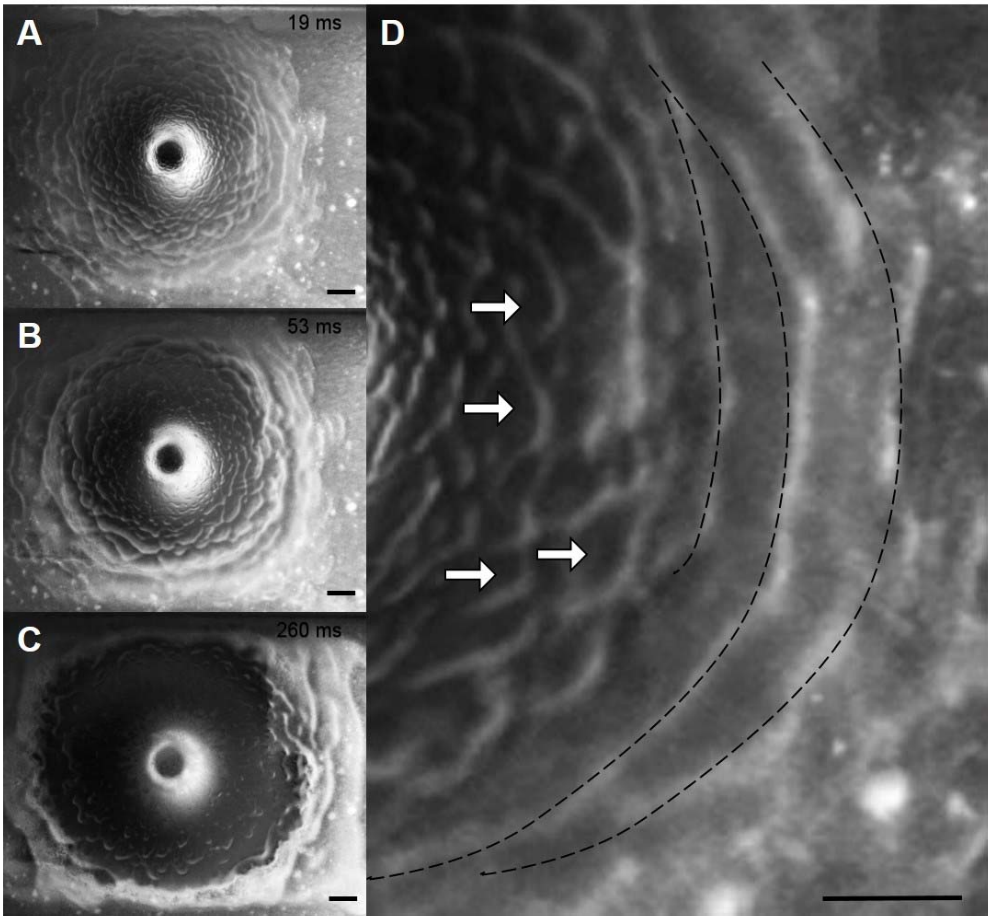

Figure 6.6. A-C) Subsequent frames from a high-speed camera video illustrating spatial migration of ripples during the exposure of S. mutans biofilms to an air-jet at a velocity of 41.7 m/s. Frames show biofilm-colonized slide proximal to the camera (biofilm is grey and the ZOC is black). The nozzle tip was located at the centre of the ZOC and air flow was moved radially from the centre towards the outside. A biofilm clearance zone was created at the end of the microsprays and residual ripples remained inside and at the edges (C). D) High magnification pictures from high-speed camera videos showing different ripples morphologies. Linguoid ripples formed at the centre of the ZOC (white arrows) which merged together into circular straight sinuous ripples (dashed black lines) as they migrated outwards. Scale bars are 2 mm.

To further investigate apparent periodicity in the ripple structures, we also performed Fast Fourier Transform (FFT) analysis on the ripple patterns. The FFT provided a power spectrum (amplitude vs. frequency) (Figure 6.7). Amplitude peaks were easily identified in the spectrum and occurred at an average frequency of f=1.1 Hz (± 0.07 Hz, n=3) which corresponded to a wavelength value of λ_R=0.8 mm (± 0.05 mm, n=3). No statistical difference was found between the wavelength values measured using FFT and the ones measured using Fiji (λ_R=0.9 mm ± 0.3 mm, n=3).

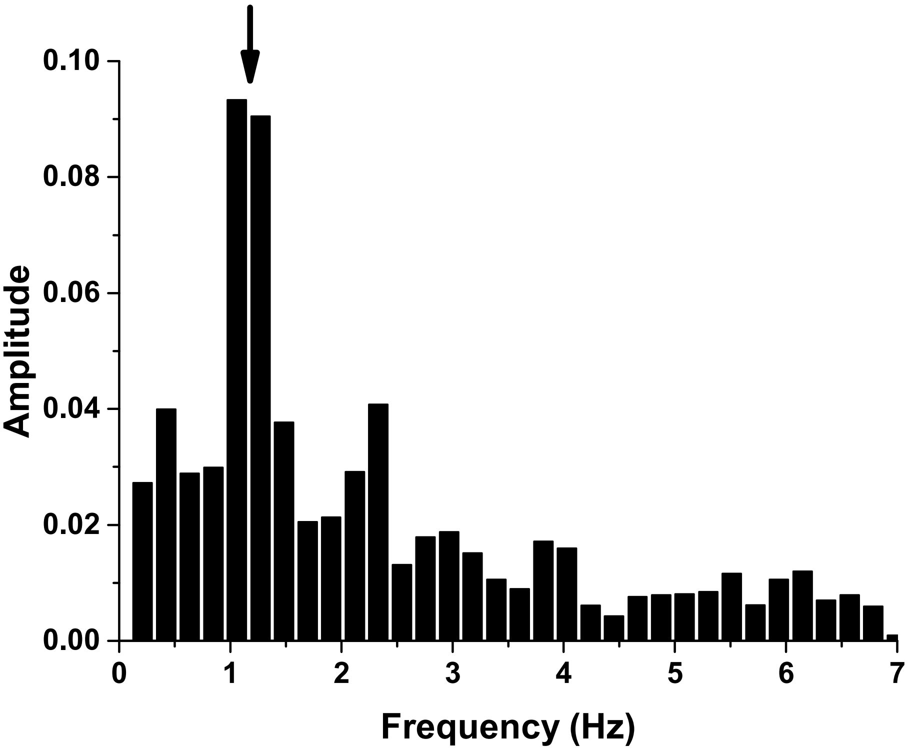

Figure 6.7. Power spectrum of ripples patterns generated from FFT analysis after S. mutans biofilm exposure to air jets at 41.7 m/s. Well-defined peaks represent periodicities in the distance between the ripples (wavelength). Black arrow indicates the position of the peak frequency relative to the wavelength measured manually.

6.4 DISCUSSION

The ability of high-velocity water microsprays generated by a commercially-available interdental cleaner to delivery micro particles inside *S. mutans* dental biofilms has been investigated. We demonstrated that the water microspray delivered significantly more microbeads in the biofilm compared to static transport or *in vitro* simulated-mouthwash (Figure 6.3). The AirFloss microburst is a turbulent burst of water and air (see Chapter 4 and (Fabbri et al. 2016)). High shear stresses are generated at the biofilm/burst interface which have possibly enhanced beads delivery inside the remaining biofilm. The microspray 90° impact on the biofilm can be simplified by modelling as a spray impingement on a flat surface covered with a thin film layer (Stanton and Rutland 1998). Once the spray impacts the surface the flow can be divided in two regions: an impingement region in the centre of the impact followed by a two-phase wall-jet region where the flow spreads radially outward everywhere.

Shear stresses generated at the jet/film interface rise as a function of radial distance, reaching a maximum value for decreasing again afterwards (Deshpande and Vaishnav 1983; Phares et al. 2000; Tu and Wood 1996). The maximum stress generated is not only responsible for the biofilm detachment but also for structural deformations (such as biofilm "churning up" up) of the unremoved biofilm at edges of the clearance zone. In addition, studies on rinsing flows where a water jet impinges on a flat surface coated with a second fluid at higher viscosity, demonstrated the formation of recirculation zones downstream at the interface between the two liquids (circular hydraulic jump (Liu 1993)) (Hsu et al. 2011; Walker et al. 2012) possibly increasing heat and mass transfer (Zuckerman and Lior 2006)**.**

Next, using high-speed camera videography we showed that a water microspray bursts at a 90° angle (perpendicular impact) can induce migratory ripple-like structures in *S. mutans* biofilms (Figure 6.4 and Figure 6.5) similar to the ones we documented for a parallel impact (see Chapter 5). It is known that rippling phenomenon is related to the viscoelastic properties of the EPS matrix which undergoes rapid structural changes in order to withstand external removal shear forces (He et al. 2013). Studies on gas jet impingement into a liquid documented the formation of ripples which advanced radially outward (Forrester and Evans 1997). The microspray burst is composed of two phases: the first phase is a well-defined jet, while the second phase is a complex spray of air and water droplets (see Chapter 4 or (Fabbri et al. 2016)). The combination of these two phases is complimentary when dealing with biofilm removal however the second phase was difficult to control. Therefore, we exposed *S. mutans* biofilms to controlled air jets and similar ripples structures were observed propagating radially along the circular clearance zone (Figure 6.6). Our wavelength, width and velocity values were the same order of magnitude as the ones measured after a parallel impact (see Chapter 5). FFT analysis also demonstrated periodicity in the ripple structures suggesting a possible analogy with the Kelvin Helmotz Instabilities previously modelled (Chapter 5) but this time generated by the normal impingement in a more viscous material (biofilm). Therefore, such instabilities could possibly enhance mixing with the biofilm increased the mixing between the remaining biofilm and the beads solution.

Interestingly a nozzle 30° inclination was more powerful in the distal part of the exposed area compared to the proximal part and to a 90° microspray. In the 30° microspray shooting there is an increase in the velocity in the direction of which the nozzle is inclined (i.e., distal position) and a reduction in the opposite direction (i.e., proximal position) (Kate et al. 2007). Such asymmetrical velocity distribution can have possibly enhanced microspray power in the distal position.

After the static experiment only 925 beads per cm^2 penetrated 30% of the biofilm depth. Presumably these entered via channels in the biofilm. Studies in biofilm permeability using fluorescent micro or nano beads are consistent with our data showing that the beads penetration was limited to the outer biofilm layers (20-30% of the biofilm thickness) (Drury et al. 1993a; Drury et al. 1993b) or needed timescales up to hours to reach up 90-95% biofilm substratum by diffusion alone (Miller et al. 2013). However, shaken biofilms showed a higher penetration (RD ~57%) compared to diffusion (RD ~30%). It is possible that shaken biofilms may have become more open, allowing beads to penetrate better. On the other hand, since the average biofilm thickness during shacking experiments was significantly lower compared to the control, we could also hypothesize that shearing forces "washed out" parts of the biofilm which might have enclosed some beads as well.

In conclusion, low volume high-velocity water microsprays were able to deliver microbeads inside *S. mutans* dental biofilms when exposed to a 90° impact. We believe that the physic of the microspray impact which changed biofilm mechanical properties (by generation of ripples instabilities and mixing the biofilm up) caused an increase in the beads penetration. Concerning dental plaque biofilms, this might have important consequences on gum health by enhancing the "washing out" of toxins compared to a simple mouth rinse. In future this will open up new strategies for controlling and preventing biofilms such as using water microspray to increase antimicrobial delivery inside biofilms for better therapeutic control in medicine and industry.

6.5 REFERENCES

Cense AW, Van Dongen MEH, Gottenbos B, Nuijs AM, Shulepov SY. 2006. Removal of biofilms by impinging water droplets. Journal of Applied Physics. 100(12):124701-124701-124708.

Chen Z, Chen X, Chen J. 1997. Effects of an oscillating interface on heat transfer. Chemical engineering science. 52(19):3265-3275.

de Beer D, Stoodley P, Lewandowski Z. 1996. Liquid flow and mass trasport in heterogeneous biofilms. Biotechnology and Bioengineering. 44:636-641.

Deshpande MD, Vaishnav RN. 1983. Wall stress distribution due to jet impingement. Journal of Engineering Mechanics. 109(2):479-493.

Drury WJ, Characklis WG, Stewart PS. 1993a. Interactions of 1 μm latex particles with pseudomonas aeruginosa biofilms. Water Research. 27(7):1119-1126.

Drury WJ, Stewart PS, Characklis WG. 1993b. Transport of 1-μm latex particles in pseudomonas aeruginosa biofilms. Biotechnology and Bioengineering. 42(1):111-117.

Fabbri S, Johnston DA, Rmaile A, Gottenbos B, De Jager M, Aspiras M, Starke ME, Ward MT, Stoodley P. 2016. Streptococcus mutans biofilm transient viscoelastic fluid behaviour during high-velocity microsprays. Journal of the mechanical behavior of biomedical materials. 59:197-206.

Forier K, Raemdonck K, De Smedt SC, Demeester J, Coenye T, Braeckmans K. 2014. Lipid and polymer nanoparticles for drug delivery to bacterial biofilms. Journal of Controlled Release. 190:607–623.

Forrester SE, Evans GM. 1997. Computational modelling study of a plane gas jet impinging onto a liquid pool. 1st International Conference on CFD in the Mineral & Metal Processing and Power Generation Industries. p. 313-320.

Geyer WR, Lavery AC, Scully ME, Trowbridge JH. 2010. Mixing by shear instability at high reynolds number. Geophysical Research Letters. 37(22).

He Y, Peterson BW, Jongsma MA, Ren Y, Sharma PK, Busscher HJ, van der Mei HC. 2013. Stress relaxation analysis facilitates a quantitative approach towards antimicrobial penetration into biofilms. PloS one. 8(5):e63750.

Heydorn A, Nielsen AT, Hentzer M, Sternberg C, Givskov M, Ersbøll BK, Molin S. 2000. Quantification of biofilm structures by the novel computer program comstat. Microbiology. 146(10):2395-2407.

Hsu TT, Walker TW, Frank CW, Fuller GG. 2011. Role of fluid elasticity on the dynamics of rinsing flow by an impinging jet. Physics of Fluids (1994-present). 23(3):033101.

Kate RP, Das PK, Chakraborty S. 2007. Hydraulic jumps due to oblique impingement of circular liquid jets on a flat horizontal surface. Journal of Fluid Mechanics. 573:247-263.

Liu X. 1993. The hydraulic jump in circular jet impingement and in other thin liquid films. Experiments in Fluids. 15(2):108-116.

Marsh PD. 2004. Dental plaque as a microbial biofilm. Caries Research. 38:204-211.

Miller JK, Neubig R, Clemons CB, Kreider KL, Wilber JP, Young GW, Ditto AJ, Yun YH, Milsted A, Badawy HT. 2013. Nanoparticle deposition onto biofilms. Annals of biomedical engineering. 41(1):53-67.

Parini MR, Eggett DL, Pitt WG. 2005. Removal of streptococcus mutans biofilm by bubbles. Journal of Clinical Periodontology. 32(11):1151-1156.

Parini MR, Pitt WG. 2006. Dynamic removal of oral biofilms by bubbles. Colloids and Surfaces B: Biointerfaces. 52(1):39-46.

Phares DJ, Smedley GT, Flagan RC. 2000. The wall shear stress produced by the normal impingement of a jet on a flat surface. Journal of Fluid Mechanics. 418:351-375.

Rmaile A, Carugo D, Capretto L, Aspiras M, De Jager M, Ward M, Stoodley P. 2014. Removal of interproximal dental biofilms by high-velocity water microdrops. Journal of dental research. 93(1):68-73.

Rmaile A, Carugo D, Capretto L, Wharton JA, Thurner PJ, Aspiras M, Ward M, De Jager M, Stoodley P. 2015. An experimental and computational study of the hydrodynamics of high-velocity water microdrops for interproximal tooth cleaning. Journal of the Mechanical Behavior of Biomedical Materials. 46:148-157.

Schindelin J, Arganda-Carreras I, Frise E, Kaynig V, Longair M, Pietzsch T, Preibisch S, Rueden C, Saalfeld S, Schmid B et al. 2012. Fiji: An open-source platform for biological-image analysis. Nat Methods. 9(7):676-682.

Stanton DW, Rutland CJ. 1998. Multi-dimensional modeling of thin liquid films and spray-wall interactions resulting from impinging sprays. International Journal of Heat and Mass Transfer. 41(20):3037-3054.

Stoodley P, deBeer D, Lewandowski Z. 1994. Liquid flow in biofilm systems. Applied and Environmental Microbiology. 60(8):2711-2716.

Takenaka S, Pitts B, Trivedi HM, Stewart PS. 2009. Diffusion of macromolecules in model oral biofilms. Applied and Environmental Microbiology. 75:1750-1753.

Tu CV, Wood DH. 1996. Wall pressure and shear stress measurements beneath an impinging jet. Experimental thermal and fluid science. 13:364-373.

Vazquez-Una G, Chenlo-Romero F, Sanchez-Barral M, Perez-Munuzuri V. 2000. Mass transfer enhancement due to surface wave formation at a horizontal gas–liquid interface. Chemical engineering science. 55(23):5851-5856.

Walker TW, Hsu TT, Frank CW, Fuller GG. 2012. Role of shear-thinning on the dynamics of rinsing flow by an impinging jet. Physics of Fluids (1994-present). 24(9):093102.

Zuckerman N, Lior N. 2006. Jet impingement heat transfer: Physics, correlations, and numerical modeling. Advances in heat transfer. 39(06):565-631.

CHAPTER 7

High-velocity microsprays enhance antimicrobial activity in *S. mutans* biofilms

S. Fabbri[1], D.A. Johnston[2], A. Rmaile[3], B. Gottenbos[3], M. De Jager[3], M. Aspiras[4], E. M. Starke[5], M. T. Ward[5] and P. Stoodley[1, 6]

[1]National Centre for Advanced Tribology at Southampton (nCATS), University of Southampton, Southampton SO17 1BJ, United Kingdom.
[2]Biomedical Imaging Unit, School of Medicine, University of Southampton, Southampton SO16 6YD, UK.
[3]Philips Research, High Tech Campus, Eindhoven 5656 AE, The Netherlands.

[4]Wrigley, Chicago, Illinois 60613, USA.

[5]Philips Oral Healthcare, Bothell, Washington 98021, USA.

[6]Department of Microbial Infection and Immunity and the Department of Orthopaedics, Centre for Microbial Interface Biology, The Ohio State University, Columbus, Ohio 43210, USA.

ABSTRACT

Streptococcus mutans in dental plaque biofilms are responsible for caries development. Biofilm complex structure enhances the resistance to antimicrobial agents by limiting the transport of dentifrices inside the biofilm. We assessed the ability of high-velocity microsprays to enhance delivery of antimicrobials into 3-days old *S. mutans* biofilms. Biofilms were exposed to a 90° or 30° impact using a 0.2% chlorhexidine or 0.085% Cetylpyridinium chloride solution. For comparison, a 30 sec diffusive transport was performed. Confocal microscopy was used to determine the penetration depth calculated from the resultant zone of killing detected by live/dead viability staining. Our experiments revealed that the microspray yielded better antimicrobial penetration evidenced by a deeper killing inside the biofilm and a wider killing zone around the zone of clearance than a diffusion transport with the same antimicrobials. Interestingly the 30° impact in the distal position yielded approximately 15% more bacteria killing (for both CHX and CPC) than the 90° impact. These data suggest that high-velocity water microsprays can be used as an effective mechanism for delivering antimicrobials inside *S. mutans* dental biofilms. Further, the impact angle has potential to be optimized both for biofilm removal and dentifrice delivery inside biofilm in those protected areas where some biofilm might remain.

7.1 INTRODUCTION

Biofilms are surface-attached microbial communities surrounded by a self-produced matrix of extracellular polymeric substances (EPS), which conveys to the biofilm a three-dimensional structure (matrix) (Flemming and Wingender 2010). Oral biofilms play an important role in the development and the persistence of caries, gingivitis and periodontitis (Marsh 2004). The addition of antiplaque or antimicrobials (such as fluoride, Chlorhexidine (CHX), Cetylpyridinium chloride (CPC) and essential oils) to toothpastes, mouthwashes and varnishes in order to enhance remineralisation or kill bacteria is one of the most common way to control dental biofilms (Marsh 2006; Marsh et al. 2015). However, biofilms complicated structure increases their resistance to antiplaque and/or antimicrobials by limiting the diffusion of dentifrices inside the biofilm (Stewart 2003; 2015). The heterogeneity of the EPS (ranging from hydrophilic or hydrophobic components to cationic or aniconic ones) not only provide the "scaffold" for the biofilm itself but also a physical barrier to antimicrobial agents (Sutherland 2001). Microelectrodes studies on *in vitro* oral biofilms showed that fluoride and CHX could influence the localized anaerobic environments and attenuate the proliferation of cariogenic bacteria (Aspiras et al. 2010; Stoodley et al. 2008; von Ohle et al. 2010). The role of the hydrodynamic in the enhancement of dentifrices inside the biofilm has become a topic of interest, since it might be utilized to improve delivery to the tooth surface or the cells themselves. Investigators demonstrated that fluid-dynamic activity generated by power toothbrushes can enhance antimicrobials/antiplaque delivery inside any remaining biofilm compared to simple diffusional transport (He et al. 2014; Jongsma et al. 2015; Sjogren et al. 2004; Stoodley et al. 2007). Microsprays have the advantage that they are low volume but also have the air / water interface moving over the solid surface which facilitates biofilm removal (Busscher et al. 2010). We already documented the ability of high-velocity water microsprays to enhance mass transfer inside *S. mutans* dental biofilms using tracer micro beads (see Chapter 6). We related the dynamic of the microspray impact which changed biofilm mechanical properties (through the generation of fast moving ripple-like instabilities and mixing up of the biofilm) with the increase of beads penetration (see Chapter 6). Here we assess the ability of the microspray to improve the delivery of dentifrices into the biofilm, and specifically into the EPS matrix, using chlorhexidine or Cetylpyridinium chloride and measuring depth and the zone of killing. Delivery into the biofilm by the high-velocity water microspray was compared with a static (diffusion only) delivery.

7.2 MATERIALS AND METHODS

7.2.1 Biofilm growth conditions

Streptococcus mutans biofilms UA159 (ATCC 700610) were grown for 72 hrs. on microscope glass slides as previously described (see paragraph 4.2.1). After the growth period biofilm covered-slides were gently rinsed in 1 % (wt/vol) phosphate-buffered saline (1% PBS) solution (Sigma-Aldrich) before placing them in petri plates.

7.2.2 Antimicrobials delivery

The CHX and CPC stock solutions (Sigma-Aldrich) were diluted to 0.2% (wt/vol) (CHX working solution) and 0.085% (wt/vol) (CPC working solution) respectively. A Philips Sonicare AirFloss (AF) commercially available oral hygiene device was used to generate high-velocity microsprays. A micromanipulator was used in order to hold the Airfloss device in a vertical position. The AF device was filled with 3 mL of the CHX or CPC working solution. The biofilms were then exposed to a single 90° or a 30° microspray shot (microspray experiments) or a 30 sec static incubation for each antimicrobial. As untreated assays, the experiments were also performed using 1% phosphate buffered saline (1% PBS) solution (Sigma-Aldrich). Three independent replicates were performed for each experiment.

7.2.3 Confocal microscopy

Control biofilms (prior the experiments) and those biofilms immediately after the antimicrobials experiments were carefully transferred to petri plates filled with 1 % (wt/vol) phosphate-buffered saline (PBS) solution (Sigma-Aldrich). Live/dead staining (BacLight, Invitrogen) was performed immediately after microburst or static exposure. Samples were imaged by confocal laser scanner microscope (CLSM, Leica TCS SP5). Three random 3D stacks were taken on each of three independent replicate for the diffusion experiments (Figure 7.1D). The microsprays generated a zone of clearance (ZOC) in the area where the biofilm was removed (Figure 7.1A). The 90° impact generated a circular ZOC of approximately 300 mm^2, as the flow pattern was axisymmetric. Instead, the 30° impact created an elliptical ZOC of approximately 450 mm^2 because the liquid flow over the surface became asymmetric and less biofilm was removed behind the point of impact (proximal zone, with respect to the direction of the flow). For the independent triplicate spray-exposed biofilm slides (90° and 30° microsprays) confocal images were taken 1-2 mm outside the zone of clearance to represent the unimpacted biofilm. For the 90° microspray, three random images where taken around the circular zone (Figure 7.1B). Instead for the 30° microspray, to assess whether the symmetry of the flow influenced beads and/or antimicrobial penetration three random images were taken at the proximal and at the distal positions (Figure 7.1C). Three random images were also taken inside the zone of clearance (interior zone). To establish the thickness of the biofilm prior the experiments, three random confocal images were taken on each of three independent replicate control biofilm slides. The thickness of the control biofilms was measured by COMSTAT from the confocal images. The experiments were replicated three times with triplicate repeated confocal images for each replicate.

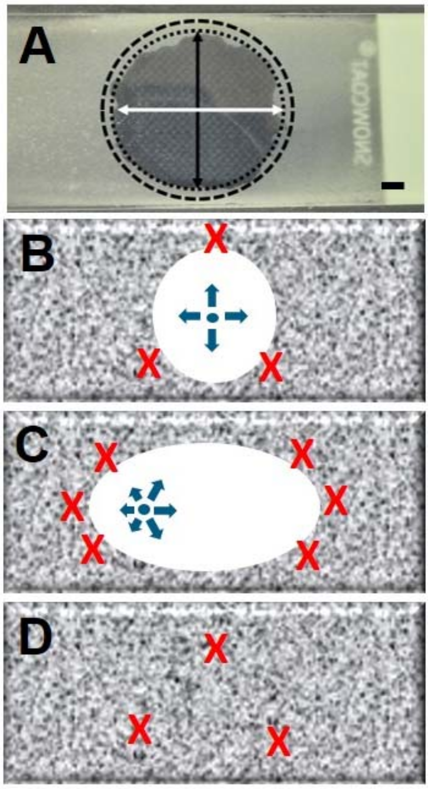

Figure 7.1. A) Microscope slide covered with S. mutans biofilm (light grey) after being exposed to a high velocity PBS microspray at 90^{o} impact. A well-defined circular shaped zone of clearance (ZOC) in the area where biofilm was removed reveals the darker background surface. The black and white arrows show the diameters of the ZOC in the x- and y-axes respectively (major and minor axes lengths for the 30^{o} impact). The dotted circle marks the edge of the ZOC and the measurements of transport and killing in the remaining biofilm were made no further than 200 µm from outside this edge (dashed circle). Scale bar is 5 mm. Representation of one biofilm-covered slide (biofilm depicted as grey and the zone of clearance as white) showing the confocal images positions taken after the 90° microspray shot (B), the 30° microspray shot (C) the diffusion experiment (D). Images were taken 1-2 mm after the edge of the zone of clearance. Blue arrows show the direction of the flow from the impact centre.

7.2.4 Quantification of antimicrobials killing

Bacterial killing, measured from live/dead staining was taken as an indicator for the degree of CHX or CPC penetration into the biofilm as explained previously (He et al. 2014). Confocal images were analysed with Fiji software (Schindelin et al. 2012). Using the Plot Profile function on an x–z cross section view we obtained the ratio of the intensity of red to green (R/G) as a function of the biofilm thickness. Five random measurements were taken on each cross-section for the diffusion and the microbursts experiments. Then a biofilm dead band was defined as the biofilm thickness until when R/G became less than 1.5 (He et al. 2014). Next, CHX and CPC killing depth ratios (KD_{CHX} and KD_{CPC}) were calculated as:

$$\mathrm{KD} = \frac{\text{dead band thickness}}{\text{biofilm thickness}} \times 100\% \qquad (7.1)$$

The x-y plan views of the confocal images were also analysed with Fiji measuring the averaged R/D ratio using the z-project Function. Then using the Plot Profile function we obtained R/G as a function of the distance from the edge of the zone of clearance (Figure 7.1A). Three random measurements were taken on each x-y image for the diffusion and the microspray experiments. Then the length of the antimicrobial killing zone for each antimicrobial (l_{CHX} and l_{CPC}) was defined as the distance from the point of impact where R/G dropped to less than 1.5. Statistical comparisons were performed using unpaired two samples t-test for normally distributed data and difference considered significant where $p < 0.05$.

7.3 RESULTS

7.3.1 Biofilm structure and thickness

Biofilm samples imaged by confocal microscopy were heterogeneous in the structure showing channels and voids (Figure 7.2). The thickness of the control biofilm was 51.8±4.9 μm (Figure 6.2). The static incubation of antimicrobials and 1% PBS did not significantly change the biofilm thickness (t_{CHX}=47.1±7.1 μm, t_{CPC}=50.1±8.5 μm and t_{PBS}=48.9±6.4 μm) compared to the control sample, but the 30° and 90° microspray shots reduced it a further t_{CHX}=28.6±7.3 μm and t_{CPC}=29.6±7.3 μm for CHX and CPC respectively. Statistical difference was found between the biofilm thickness after the 90° microspray (t_{CHX} =32.1±5.6 μm, t_{CPC}=30.1±4.6 μm and t_{PBS}=28.6±2.1μm) and the biofilm thickness after a 30° microspray in the distal position (t_{CHX} =18.2±2.5 μm, t_{CPC}=19.1±3.4 μm and t_{PBS}=20.6±4.7μm) but not in the proximal one (t_{CHX} =33.5±3.5 μm, t_{CPC}=28.2±1.4 μm and t_{PBS}=26.1±3.9μm). All the thicknesses were statistically different from the biofilm thickness in the interior zone (t=0.005±0.003 μm).

7.3.2 Antimicrobial delivery

Confocal images of biofilms samples exposed to 0.02% Chlorhexidine and 0.085% Cetylpyridinium chloride revealed that both 30° and 90° microsprays (Figure 7.2A-C and

Figure 7.2E-G) caused an increase of biofilm red zones (dead biofilm) compared to a static transport of the same antimicrobial (Figure 7.2D and Figure 7.2E).

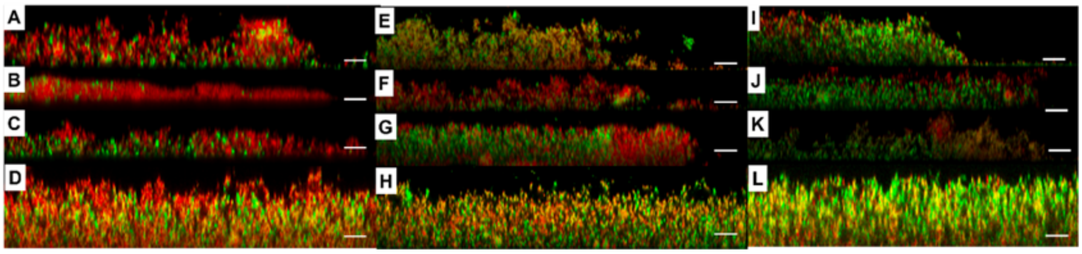

Figure 7.2. Confocal images in x–z cross section view showing S. mutans biofilms after a 90° shooting (A), 30° shooting in the distal zone (B), 30° shooting in the proximal zone (C), static assay (D) with 0.085% CPC. 90° shooting (E), 30° shooting in the distal zone (F), 30° shooting in the proximal zone (G), static assay (H) with 0.2% CHX. 90° shooting (I), 30° shooting in the distal zone (J), 30° shooting in the proximal zone (K), static assay (L) with 1% PBS. Dead biofilm was stained red (Propidium Iodide) and live biofilm green (Syto 9). Scale bar is 20 µm.

In particular, CHX and CPC killing depth after a 90° microspray exposure ($KD_{CHX,90}$=51.8±10.2% and $KD_{CPC,90}$=66.1±5.5%), a 30° microspray exposure in the proximal ($KD_{CHX,30p}$=39.9±9.6% and $KD_{CPC,30p}$=54.5±14.8%) and in the distal position ($KD_{CHX,30d}$=76.6±10.6% and $KD_{CPC,30d}$=87.9±13.9%) were higher than the ones after static transport (KD_{CHX}=4.7±1.1% and KD_{CPC}=21.1±6.4%) (Figure 7.3A-B). When the biofilm was exposed to 30° microspray, both antimicrobials generated a significantly higher killing penetration in the distal position than in the proximal position. In addition, a CHX and CPC 30° microspray exposure resulted in a higher KD in the distal position compared to a 90° microspray, but not in the proximal one.

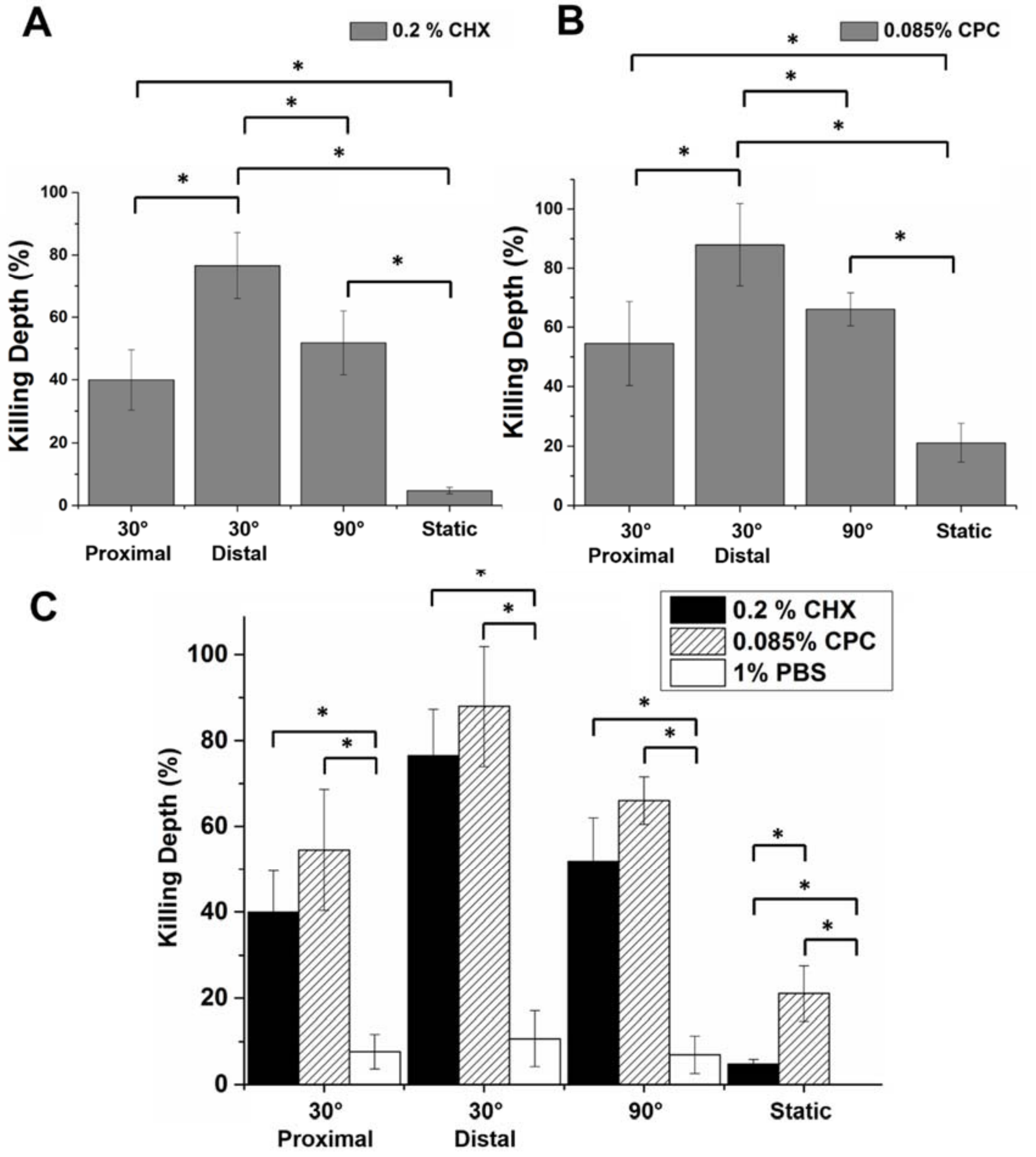

*Figure 7.3. Biofilm killing depth caused by 0.2% CHX (A) or 0.085% CPC (B) after the 30° microspray, 90° microspray and the static experiment. C) Biofilm killing depth caused by 0.2% CHX or 0.085% compared with the untreated samples (1% PBS) after the 30° microspray, 90° microspray and the static experiment. Data represented as mean and 1SD from three independent replicates. Asterisks represent statistical significance, as calculated by unpaired t-test test (*p<0.05).*

Confocal images of biofilm exposed to a static assay showed that a 0.085% Cetylpyridinium chloride solution (Figure 7.2D) presented more dead bacteria compared to a 0.02% Chlorhexidine solution (Figure 7.2H**).** Quantification of the bacterial killing resulted in a significantly higher CPC killing penetration (KD_{CPC}=20.1±5.8%, n=3) compared to CHX

(KD_{CHX}=2.2%±1.6%, n=3) (Figure 7.3C). No dead zones instead were observed in the 1% PBS exposed samples (untreated samples, Figure 7.2L and Figure 7.3C).

The microspray without antimicrobials (Figure 7.2I-L**)** yielded a significantly lower killing penetration (KD_{90}=6.9%±4.3%, KD_{30p}=7.6%±3.9% and KD_{30d}=10.6%±6.4%) compared with antimicrobials but a higher killing penetration compared with the simple diffusion (Figure 7.3C).

The length of the antimicrobial killing zone was measured as the distance from the clearance zone when the biofilm dead/live ratio became less than 1.5. The killing zone lengths of both Chlorhexidine and Cetylpyridinium chloride when shot with a 30° microspray were significantly higher in the distal position ($l_{CHX30°,D}$=196±4.7 µm and $l_{CPC30°,D}$>200µm) compared to a 90° microspray of the same antimicrobials ($l_{CHX90°}$=155.4±13.9 µm and $l_{CPC90°,D}$=170.3±37.6µm), but not in the proximal one ($l_{CHX30°,P}$=110±38.1 µm and $l_{CPC30°,P}$=152.7±30.8µm) (Figure 7.4A-B). The 30° and 90° microsprays without antimicrobials yielded a significantly narrower killing zone ($l_{30°,PBS}$=18.9±6.7 µm and $l_{90°,PBS}$=15.4±8.5 µm) compared with antimicrobials. A simple diffusion of CPC generated a constant dead/live ratio over a distance of 200 µm (D/L_{CPC}=1.5±0.03 µm) which was significantly different from the D/L caused by the diffusion of CHX (D/L_{CHX}=1.2±0.05 µm, Figure 7.4C). No dead zones instead were observed in the 1% PBS exposed samples (D/L_{PBS}=0.7±0.08 µm).

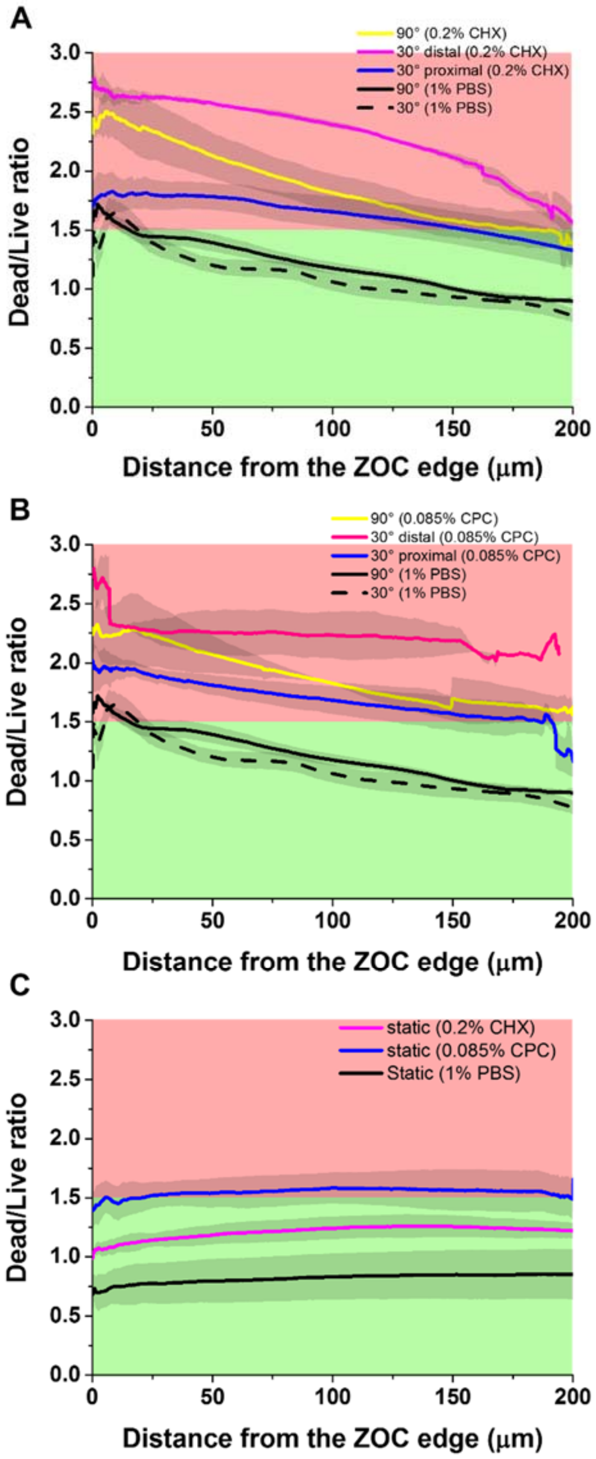

Figure 7.4. Biofilm dead/live ratio as a function of distance moving outwards from the edge of the ZOC in the x or y axis (see Figure 7.1A) caused by a 30° or a 90° microspray when using 0.2% CHX (A) or 0.085% CPC (B) and caused by 0.2% CHX or 0.085% CPC compared with the untreated samples (1% PBS) (C). The solid lines are the average dead/live ratio and the coloured areas are SD intervals from three independent replicates. Below the threshold ratio of 1.5 biofilm was considered "alive" (green background) while above 1.5, biofilm was considered "dead" (red background).

7.4 DISCUSSION

The purpose of this study was to assess whether a high-velocity microspray might enhance the penetration of dentifrices into dental biofilms using laboratory-grown *Streptococcus mutans* biofilms and 0.2% Chlorhexidine or 0.085% Cetylpyridinium chloride solutions. We then compared microspray-induced delivery with a 30-sec diffusion transport. The bacterial killing depths yielded by CPC and CHX after diffusion were approximately 5% and 20% respectively. These data are consistent with previous studies on oral biofilms showing that CHX and CPC antimicrobial efficacy decreased in biofilm deep layers (Hope and Wilson 2004; Vitkov et al. 2005; von Ohle et al. 2010) with penetration timescales up to 20 mins to reach half of the biofilm thickness (Corbin et al. 2011). The retarded penetration is related with the EPS matrix structure which acts as a barrier towards the diffusion of particles and free antimicrobial agents into the biofilm (Flemming and Wingender 2010). Cetylpyridinium chloride and Chlorhexidine are positively-charged molecules which likely bind to negatively charged EPS matrix polymers or to cell surfaces, delaying penetration. In particular *S. mutans* biofilms matrix is mainly formed of α-Dglucans which are known to limit diffusion of charged ions inside dental plaque biofilms (Bowen and Koo 2011).

Next, our experiments revealed that the microspray yielded better antimicrobial penetration evidenced by a deeper killing inside the biofilm (Figure 7.3A-B) and a wider killing zone around the zone of clearance (Figure 7.4) than a diffusion transport with the same antimicrobials. Viscoelasticity has been linked to the antibiotic tolerance of biofilm-associated cells (He et al. 2013). Recent studies on biofilms exposed to a non-contact brushing showed a change in viscoelastic properties linked with an increase of antimicrobials penetration (He et al. 2013; He et al. 2014; Jongsma et al. 2015). Moreover, advection alone with no significant mechanical perturbation of the biofilm structure was not enough to increase mass transfer inside the biofilm (de Beer et al. 1996; Stoodley et al. 1994). The microspray 90° impact on the biofilm can be simplified by modelling as a spray impingement on a flat surface covered with a thin film layer (Stanton and Rutland 1998). Studies on rinsing flows where a water jet impinges on a flat surface coated with a second fluid at higher viscosity, demonstrated the formation of recirculation zones downstream at the interface between the two liquids (Hsu et al. 2011; Walker et al. 2012) possibly increasing mass transfer (Zuckerman and Lior 2006**.** We previously showed the ability of high-velocity water microsprays to enhance micro beads delivery in *S. mutans* biofilms (see Chapter 6). We related the dynamic of the microspray impact which changed biofilm mechanical properties (through the generation of fast moving ripple-like instabilities and mixing up of the biofilm) with the increase of beads penetration (see Chapter 6). We hypothesize that a combined effect of shear, which left the unremoved biofilm structure in a more open state enabling better antibacterial penetration, and antimicrobial delivery yielded an increase in bacteria killing.

Interestingly, a nozzle 30° inclination was more powerful (in terms of beads delivery and bacterial killing caused by the antimicrobials) in the distal part of the exposed area compared to the proximal part and to a 90° microspray. In the 30° microspray shooting there is an increase in the velocity in the direction of which the nozzle is inclined (i.e., distal position) and a reduction in the opposite direction (i.e., proximal position)(Kate et al. 2007). Such asymmetrical velocity distribution can have possibly enhanced microspray power in the distal position.

Finally, our data showed that the microspray alone (without any antimicrobial) resulted in killing biofilm bacteria in the remaining biofilm outside the zone of clearance (Figure 7.4). It is not clear why this is. Powered and mechanical toothbrushes caused damage to cell surface structures but did not affected cell viability (MacNeill et al. 1998; McInnes et al. 1993). However, no studies examined viability of biofilm-associated bacteria when exposed to hydrodynamic phenomena. It is possible that the remaining cells could be not completely dead but metabolically compromised and not have the necessary energy reserves to repair essential channels/walls/membranes/receptors. Another possibility is that the microspray could have introduced oxygen into the biofilm causing oxidative stresses. It has been recently demonstrated that presence of oxygen can alter cell surface composition in *S. mutans* biofilms (Ahn et al. 2007).

In conclusion, low volume high-velocity water microsprays are effective at removing *S. mutans* biofilms from areas relevant to that of a tooth surface and has the additional benefit as a potential delivery method for antimicrobials inside dental biofilm that might remain in or adjacent to the zone of clearance. There are other potential clinical benefits that we did not test but might explain the clinical efficacy in reducing inflammation. It is reasonable to assume that if the microspray is effectively mixing the biofilm up to drive things into the biofilm then potentially proinflammatory mediators such as bacterial toxins would get driven out. It is not still clear how powerful needs to be the air spray or the waterjet in the microspray. The further improvement of the synergy between microsprays and antibacterial activity, either by changing the design of the dental device or the use of different drug-delivery methods such as antimicrobial coated nanoparticles or micro/nano emulsions is of interest in future research.

7.5 REFERENCES

Ahn S-J, Wen ZT, Burne RA. 2007. Effects of oxygen on virulence traits of *Streptococcus mutans*. Journal of bacteriology. 189(23):8519-8527.

Aspiras M, Stoodley P, Nistico L, Longwell M, de Jager M. 2010. Clinical implications of power toothbrushing on fluoride delivery: Effects on biofilm plaque metabolism and physiology. International journal of dentistry. 2010:651869.

Bowen WH, Koo H. 2011. Biology of *Streptococcus mutans*-derived glucosyltransferases: Role in extracellular matrix formation of cariogenic biofilms. Caries Research. 45:69-86.

Busscher HJ, Jager D, Finger G, Schaefer N, Van Der Mei HC. 2010. Energy transfer, volumetric expansion, and removal of oral biofilms by non-contact brushing. European Journal of Oral Sciences. 118(2):177-182.

Corbin A, Pitts B, Parker A, Stewart PS. 2011. Antimicrobial penetration and efficacy in an in vitro oral biofilm model. Antimicrobial agents and chemotherapy. 55(7):3338-3344.

de Beer D, Stoodley P, Lewandowski Z. 1996. Liquid flow and mass trasport in heterogeneous biofilms. Biotechnology and Bioengineering. 44:636-641.

Flemming H-C, Wingender J. 2010. The biofilm matrix. Nature Reviews Microbiology. 8:623-633.

He Y, Peterson BW, Jongsma MA, Ren Y, Sharma PK, Busscher HJ, van der Mei HC. 2013. Stress relaxation analysis facilitates a quantitative approach towards antimicrobial penetration into biofilms. PloS one. 8(5):e63750.

He Y, Peterson BW, Ren Y, van der Mei HC, Busscher HJ. 2014. Antimicrobial penetration in a dual-species oral biofilm after noncontact brushing: An in vitro study. Clinical Oral Investigations. 18:1103-1109.

Hope C, Wilson M. 2004. Analysis of the effects of chlorhexidine on oral biofilm vitality and structure based on viability profiling and an indicator of membrane integrity. Antimicrobial agents and chemotherapy. 48(5):1461-1468.

Hsu TT, Walker TW, Frank CW, Fuller GG. 2011. Role of fluid elasticity on the dynamics of rinsing flow by an impinging jet. Physics of Fluids (1994-present). 23(3):033101.

Jongsma MA, van de Lagemaat M, Busscher HJ, Geertsema-Doornbusch GI, Atema-Smit J, van der Mei HC, Ren Y. 2015. Synergy of brushing mode and antibacterial use on in vivo biofilm formation. Journal of dentistry. 43(12):1580-1586.

Kate RP, Das PK, Chakraborty S. 2007. Hydraulic jumps due to oblique impingement of circular liquid jets on a flat horizontal surface. Journal of Fluid Mechanics. 573:247-263.

MacNeill S, Walters DM, Dey A, Glaros AG, Cobb CM. 1998. Sonic and mechanical toothbrushes. Journal of clinical periodontology. 25(12):988-993.

Marsh PD. 2004. Dental plaque as a microbial biofilm. Caries Research. 38:204-211.

Marsh PD. 2006. Dental plaque as a biofilm and a microbial community - implications for health and disease. BMC Oral Health. 6 Suppl 1:S14.

Marsh PD, Head DA, Devine DA. 2015. Dental plaque as a biofilm and a microbial community—implications for treatment. Journal of Oral Biosciences. 57(4):185-191.

McInnes C, Engel D, Martin RW. 1993. Fimbria damage and removal of adherent bacteria after exposure to acoustic energy. Oral microbiology and immunology. 8(5):277-282.

Schindelin J, Arganda-Carreras I, Frise E, Kaynig V, Longair M, Pietzsch T, Preibisch S, Rueden C, Saalfeld S, Schmid B et al. 2012. Fiji: An open-source platform for biological-image analysis. Nat Methods. 9(7):676-682.

Sjogren K, Lundberg AB, Birkhed D, Dudgeon DJ, Johnson MR. 2004. Interproximal plaque mass and fluoride retention after brushing and flossing--a comparative study of powered toothbrushing, manual toothbrushing and flossing. Oral health & preventive dentistry. 2(2):119-124.

Stanton DW, Rutland CJ. 1998. Multi-dimensional modeling of thin liquid films and spray-wall interactions resulting from impinging sprays. International Journal of Heat and Mass Transfer. 41(20):3037-3054.

Stewart PS. 2003. Diffusion in biofilms. Journal of Bacteriology. 185(5):1485-1491.

Stewart PS. 2015. Antimicrobial tolerance in biofilms. Microbiology spectrum. 3(3):10.1128/microbiolspec.MB-0010-2014.

Stoodley P, A Nguyen D, A Longwell M, A Nistico L, A von Ohle C, A Milanovich N, A de Jager M. 2007. Effect of the sonicare flexcare power toothbrush on fluoride delivery through *Streptococcus mutans* biofilms. Compendium of Continuing Educationin Dentistry. 28:15-22.

Stoodley P, deBeer D, Lewandowski Z. 1994. Liquid flow in biofilm systems. Applied and Environmental Microbiology. 60(8):2711-2716.

Stoodley P, Wefel J, Gieseke A, deBeer D, von Ohle C. 2008. Biofilm plaque and hydrodynamic effects on mass transfer, fluoride delivery and caries. The Journal of the American Dental Association. 139(9):1182-1190.

Sutherland IW. 2001. Biofilm exopolysaccharides: A strong and sticky framework. Microbiology. 147:3-9.

Vitkov L, Hermann A, Krautgartner WD, Herrmann M, Fuchs K, Klappacher M, Hannig M. 2005. Chlorhexidine-induced ultrastructural alterations in oral biofilm. Microsc Res Tech. 68(2):85-89.

von Ohle C, Gieseke A, Nistico L, Decker EM, deBeer D, Stoodley P. 2010. Real-time microsensor measurement of local metabolic activities in ex vivo dental biofilms exposed to sucrose and treated with chlorhexidine. Applied and Environmental Microbiology. 76(7):2326-2334.

Walker TW, Hsu TT, Frank CW, Fuller GG. 2012. Role of shear-thinning on the dynamics of rinsing flow by an impinging jet. Physics of Fluids (1994-present). 24(9):093102.

Zuckerman N, Lior N. 2006. Jet impingement heat transfer: Physics, correlations, and numerical modeling. Advances in heat transfer. 39(06):565-631.

CHAPTER 8

General conclusion and future perspectives

Although a set of comprehensive conclusions were provided at the end of each chapter, this section intends to draw together the key findings in order to establish a general overview of the experimental discussion and outline future directions.

In Chapter 4 it was concluded that *Streptococcus mutans* biofilm was able to flow over the surface in response to high-velocity water microsprays. We also documented the formation of turbulent vortices and waves occurring at the biofilm/fluid interface. These phenomena suggest that biofilm fluidification can be the result of mixing processes occurring between the water and the biofilm structure. Chapter 5 represents a follow up of Chapter 4 where we reported the discovery of high-speed ripple formation by overlying water spray and air flows in *S. mutans* biofilms. This phenomenon was only revealed using high speed imaging. Classical linear stability analysis suggested that the ripples were Kelvin-Helmholtz Instabilities implying the onset of turbulence in the flowing biofilm. Fluid/structure interactions in biofilms are known to modulate the dynamics of biofilm growth, tolerance to antibiotics, and virulence. We believe that the fact that biofilm exposure to the high-velocity microsprays happened in a very short time interval (ms), the biofilm didn’t have time to adapt and resist to the hydrodynamic stress. As a result, biofilms started to flow, migrate in ripples and mix with the overlying fluid flow. We hypothesized that the high-velocity microspray by generating such interaction can induce dentifrice delivery inside remaining biofilm. In Chapter 6 and 7 we demonstrated our hypothesis showing that microsprays where able to deliver fluorescent tracer beads and antimicrobials activity (CHX and CPC) up to 90% of the biofilm thickness. In addition, we found that the penetration efficacy was dependent on the angle of impact. In particular, a 30º inclination yielded a better microbeads and antimicrobials penetration inside the remaining biofilm located in front of the point of impact (with respect to the direction of motion) but not inside the remaining biofilm located behind the point of impact. Decreasing the angle of impact causes the liquid flow over the surface to become asymmetric which will influence the removal and also a potential mass transfer. Therefore, future work should focus on designing impact angle of the head to optimize biofilm removal and dentifrice delivery into any biofilm that may remain in protected areas. It is not still clear what force threshold is required by interdental cleaning devices to produce advective mixing nor what force is required to eliminate biofilms. Surely, droplet velocity and droplet size of the microspray play a key role and need to be taken in consideration for a further improvement of the synergy between microsprays and antibacterial activity.

Although we have focused on the removal of dental plaque, the results of this work can be applied to biofilms in general. In Chapter 5 we also discovered that ripples can also form in *Staphylococcus epidermidis* biofilms and wrinkle-like structures in *Pseudomonas aeruginosa* biofilms suggesting that the formation of interfacial instabilities could be a general phenomenon given the conserved nature of biofilm viscoelasticity (Figure 8.1). Whether a biofilm is more likely to flow in ripples or form more solid-like wrinkles is likely a function of a number of factors including adhesion strength, density, surface tension and viscoelastic moduli.

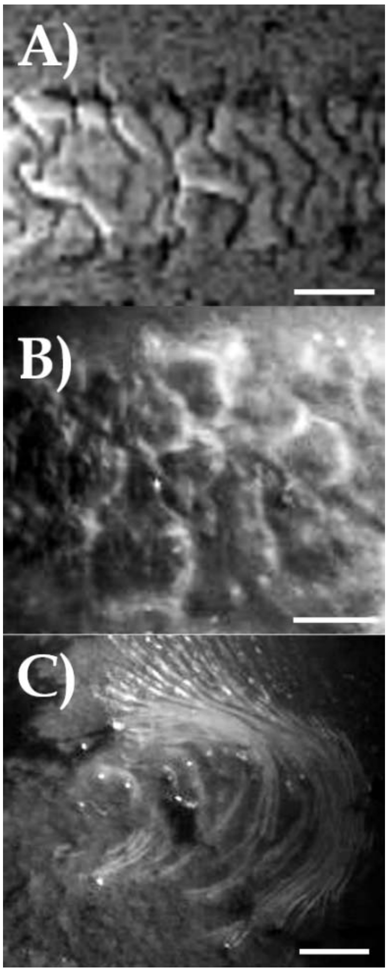

Figure 8.1. High magnification pictures of different ripples morphologies generated at the surface of 3-days old S. mutans (A), 3-days old S. epidermidis (B) and 7-days old P. aeruginosa (C) biofilms during the exposure to high-velocity microsprays. Flow was left to right. Scale bar = 2 mm. Showing that high-velocity biofilm-fluid interactions can cause the generation of high-velocity ripples provides further insight into the mechanical behaviour of biofilms as viscoelastic complex liquids (Original Data. The experimental details can be found in Chapter 5).

We have seen that there is compelling evidence which shows biofilms are complex biological materials composed by bacteria and hydrated polymeric substances in water. The matrix is itself a multi-component element which gives flexibility to the biofilm structure by changing shape in response to an applied force. As a result, biofilms behave as non-linear viscoelastic materials whose viscous or elastic responses dominates depending on the environmental and growth conditions. Reviews of the literature on biofilm mechanics showed that changes in the EPS composition caused by various external factors (such as change in the nutrient intake, temperature shift, enzyme exposure or a specific gene knock-out) considerably change biofilm mechanical behaviour (sometimes from viscoelastic fluids they became solid elastic) or increase/decrease biofilm detachment. In addition, in the natural, industrial and medical environment biofilms are often exposed to a wide range of hydrodynamic forces (compressive, tensile or shear) which significantly alter biofilm physical morphology. Wave-like pattern biofilms have been found inside endotracheal tubes (Inglis 1993) and venous catheter (Rusconi et al. 2010). Flow-induced slow-moving ripples-like structures (Stoodley et al. 1999) have been discovered at the surface of in vitro biofilms as well as similar ripples marks have been observed in modern streams (Battin et al. 2003) and in ancient fossils (Noffke 2011; Thomas et al. 2013). It has been hypothesized that these structures are related to biofilm viscoelasticity as an adapted trait that allows bacteria to flows and remain attached to surfaces when subjected to steady or transient overlying shear forces. Herewith, mechanical properties are determined by an interaction between a structure's composition and external environmental changes which may have a possible survival meaning. Viscoelasticity may be considered an emergent property of populations of prokaryotes when in biofilms and its commonality to a diverse range of bacterial species with different EPS polymers suggests a highly conserved trait and thus an integral fitness component for survival on surfaces. Biofilm adaptation to persist on surfaces involves structural and physiological changes which are represented in the viscoelasticity of a biofilm. This has important consequences for mechanical removal control strategies in the medical and industrial fields. Moreover, recent studies on infectious and oral biofilms also related viscoelastic behaviour with antimicrobial/chemicals penetration in biofilms (Peterson et al. 2015). This means that the mechanical behaviour allows biofilm not only to withstand physical stresses but also chemical ones, possibly increasing their chance of survival. This hypothesis opens up new research paths on biofilm mechanical properties which might help the designing of new strategies for controlling and preventing biofilms, as well as revealing new insights into the role of biofilm formation in prokaryotic biology. Our observations can explain the high pressure drops exerted by biofilms in pipelines and ship hulls and also supports the hypothesis that interfacial instabilities are responsible for forming Kinneyia ripple structures in fossilized microbial mats. In addition, we believe that ripples phenomenon may have important implications for biofilm ecology by disrupting gradients of nutrients (i.e. DO), metabolites (i.e. pH) and diffusible signals. In our experiments we used a pure culture of *S. mutans* as representing the initial colonizing stages of biofilm plaque, but biofilms in the real word such as dental plaque contain many different species of bacteria. Future studies should focus on mixed species biofilms since biofilm complexity will be expected to change the mechanical properties and therefore biofilm response to external stresses. This is important for testing our hypothesis that by disrupting biofilm microenvironments, the microbial community will be influenced. Finally, our observations increase biofilm understanding of the biophysics of bacterial biofilms and opens up a potentially new area of interdisciplinary research between microbiologists, physicists and computational modellers in order to develop a better mechanistic understanding of such high velocity biofilm-fluid interactions. These observations also provide the basis for future investigations into biofilm removal methods that can be developed and optimized with validated modeling coupled with state-of-the art experimentation.

8.1 REFERENCES

Battin TJ, Kaplan LA, Newbold JD, Cheng X, Hansen C. 2003. Effects of current velocity on the nascent architecture of stream microbial biofilms. Applied and Environmental Microbiology. 69(9):5443-5452.

Inglis T. 1993. Evidence for dynamic phenomena in residual tracheal tube biofilm. British journal of anaesthesia. 70(1):22-24.

Noffke N. 2011. Microbially induced sedimentary structures. Encyclopedia of Astrobiology.1045-1048.

Peterson BW, He Y, Ren Y, Zerdoum A, Libera MR, Sharma PK, van Winkelhoff A-J, Neut D, Stoodley P, van der Mei HC. 2015. Viscoelasticity of biofilms and their recalcitrance to mechanical and chemical challenges. FEMS microbiology reviews. 39(2):234-245.

Rusconi R, Lecuyer S, Guglielmini L, Stone HA. 2010. Laminar flow around corners triggers the formation of biofilm streamers. Journal of The Royal Society Interface. 7(50):1293-1299.

Stoodley P, Lewandowski Z, Boyle JD, Lappin-Scott HM. 1999. The formation of migratory ripples in a mixed species bacterial biofilm growing in turbulent flow. Environmental microbiology. 1(5):447-455.

Thomas K, Herminghaus S, Porada H, Goehring L. 2013. Formation of kinneyia via shear-induced instabilities in microbial mats. Philosophical Transactions of the Royal Society A: Mathematical, Physical and Engineering Sciences. 371(2004):20120362.

APPENDIX A

QUANTIFICATION OF BEADS PENETRATION

Imagej: z_{BEAD} values

Each confocal stack was imported in FIJI then the following steps were made:

- The dimensionality of the stack was reduced and only the channel representing the beads was considered.
- Transform → Flip z.
- Adjust → auto threshold ("internodes", "stack", and "use stack histogram").

The plugin 3D object counter was used. This plugin saved in a .txt file the coordinates (x, y, and z) of the beads found in the stack. The dimensional scale was in µm.

COMSTAT: $z_{BIOFILM}$ values

The $z_{BIOFILM}$ values of each stack were obtained from the COMSTAT function # 3. The function # 3 gave as output a topography of the biofilm thickness distribution – i.e. $z_{BIOFILM}$ (Figure A.1a). This image was related to the matrix named "height_matrix" in which all the $z_{BIOFILM}$ values were found (the relation is explained in Figure A.1b).

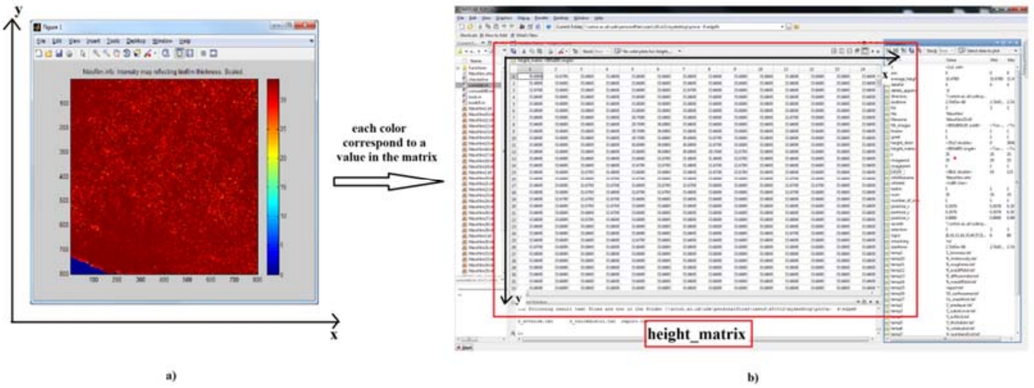

a)

b)

Figure A.1. a) The thickness distribution of a confocal stack analysed with the COMSTAT function # 3. Each colour corresponds to a different thickness value. b) The matrix ("height_matrix") contains all the thickness values are related to the x and y coordinates.

At this point, the .txt file with the coordinates (x, y, and z) of the beads was imported in MATLAB (Import Data). The file was automatically converted as a matrix (named "data") and the first columns with zero values were deleted. In this way the x, y and z values for each bead were represented by the columns 1, 2 and 3 (Figure A.2). The column 3 is the one which contained the z_{BEAD} values.

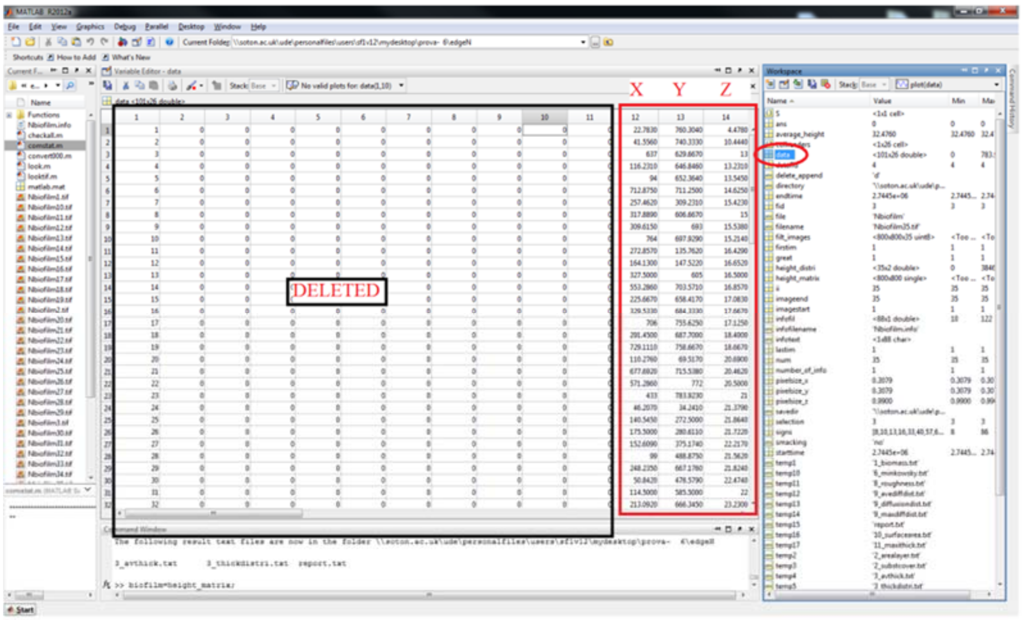

	1	2	3	4	5	6	7	8	9	10	11	12	13	14
1	1	0	0	0	0	0	0	0	0	0	0	22.7830	760.3040	4.4780
2	2	0	0	0	0	0	0	0	0	0	0	41.5560	740.3330	10.4440
3	3	0	0	0	0	0	0	0	0	0	0	637	629.6670	13
4	4	0	0	0	0	0	0	0	0	0	0	116.2310	646.8460	13.2310
5	5	0	0	0	0	0	0	0	0	0	0	94	652.3640	13.5450
6	6	0	0	0	0	0	0	0	0	0	0	712.8750	711.2500	14.6250
7	7	0	0	0	0	0	0	0	0	0	0	257.4620	309.2310	15.4230
8	8	0	0	0	0	0	0	0	0	0	0	317.8890	606.6670	15
9	9	0	0	0	0	0	0	0	0	0	0	309.6150	693	15.5380
10	10	0	0	0	0	0	0	0	0	0	0	764	697.9290	15.2140
11	11	0	0	0	0	0	0	0	0	0	0	272.8570	135.7620	16.4290
12	12	0	0	0	0	0	0	0	0	0	0	164.1300	147.5220	16.6520
13	13	0	0	0	0	0	0	0	0	0	0	327.5000	605	16.5000
14	14	0	0	0	0	0	0	0	0	0	0	553.2860	703.5710	16.8570
15	15	0	0	0	0	0	0	0	0	0	0	225.6670	658.4170	17.0830
16	16	0	0	0	0	0	0	0	0	0	0	329.5330	684.3330	17.6670
17	17	0	0	0	0	0	0	0	0	0	0	706	755.6250	17.1250
18	18	0	0	0	0	0	0	0	0	0	0	201.4500	687.7000	18.4000
19	19	0	0	0	0	0	0	0	0	0	0	729.1110	758.6670	18.6670
20	20	0	0	0	0	0	0	0	0	0	0	110.2760	69.5170	20.6900
21	21	0	0	0	0	0	0	0	0	0	0	677.6920	715.5380	20.4620
22	22	0	0	0	0	0	0	0	0	0	0	571.2860	772	20.5000
23	23	0	0	0	0	0	0	0	0	0	0	433	783.8230	21
24	24	0	0	0	0	0	0	0	0	0	0	46.2070	34.2410	21.3790
25	25	0	0	0	0	0	0	0	0	0	0	140.5450	272.5000	21.8640
26	26	0	0	0	0	0	0	0	0	0	0	175.5000	280.6110	21.7220
27	27	0	0	0	0	0	0	0	0	0	0	152.6090	375.1740	22.2170
28	28	0	0	0	0	0	0	0	0	0	0	99	488.8750	21.5620
29	29	0	0	0	0	0	0	0	0	0	0	248.2350	667.1760	21.8240
30	30	0	0	0	0	0	0	0	0	0	0	50.8420	478.5790	22.4740
31	31	0	0	0	0	0	0	0	0	0	0	114.5000	585.5000	22
32	32	0	0	0	0	0	0	0	0	0	0	213.0920	666.3450	23.2300

```
The following result text files are now in the folder \\soton.ac.uk\ude\personalfiles\users\sf1v12\mydesktop\prova-  6\edgeN

3_avthick.txt      3_thickdistri.txt  report.txt

>> biofilm=height_matrix;
```

Figure A.2. A MATLAB screenshot showing an imported .txt file containing the beads coordinates of one confocal stack. The columns containing zero were deleted (black rectangle) in order to have as first columns the x, y and z coordinates (red rectangle).

Hence, both the $z_{BIOFILM}$ and z_{BEAD} values were saved in two matrixes in MATLAB. In order to be able to find for each z_{BEAD} values the relative $z_{BIOFILM}$ values – i.e. $x_{BEAD}=x_{BIOFILM}$ and $y_{BEAD}=y_{BIOFILM}$, a MATLAB function was created and it is explained in the following sub-paragraph.

MATLAB function

The function script is shown in Figure A.3.

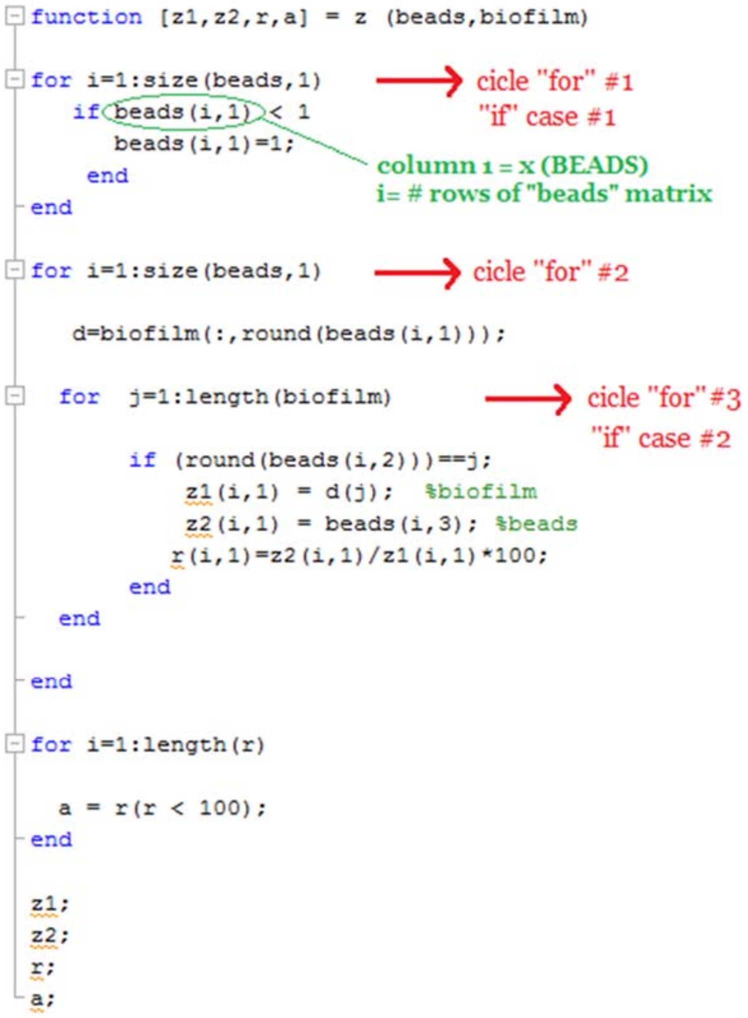

```
function [z1,z2,r,a] = z (beads,biofilm)

for i=1:size(beads,1)
    if beads(i,1)< 1
       beads(i,1)=1;
     end
end

for i=1:size(beads,1)

    d=biofilm(:,round(beads(i,1)));

  for  j=1:length(biofilm)

       if (round(beads(i,2)))==j;
           z1(i,1) = d(j);  %biofilm
           z2(i,1) = beads(i,3); %beads
          r(i,1)=z2(i,1)/z1(i,1)*100;
       end
  end

end

for i=1:length(r)

  a = r(r < 100);
end

z1;
z2;
r;
a;
```

Figure A.3. The MATLAB script of the function "z".

As input it had the two matrixes containing the z_{BEAD} and $z_{BIOFILM}$ values (the names were previously changed in MATLAB as "height_matrix"="biofilm" and "data"="beads"). Figure A.4 shows a schematic representation of how the function worked.

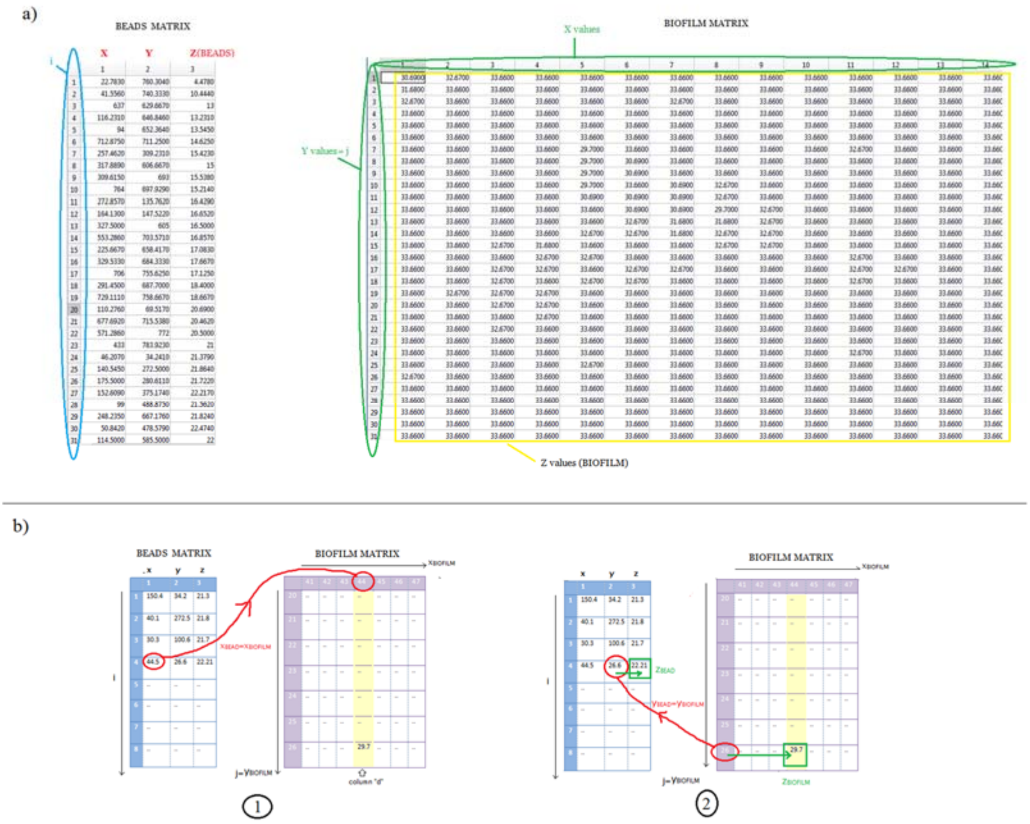

Figure A.4. a) Representation of the "beads" and the "biofilm" matrixes of one analysed confocal stack. The columns 1, 2 and 3 of the beads matrix represented the x_{BEAD}, y_{BEAD} and z_{BEAD} coordinates. Instead, the number of columns of the "biofilm" matrix represented the x_{BIFILM} coordinates while the number of rows (j) represented the $y_{BIOFILM}$ values. b) a schematic representation of the "z" function's total process.

The number of columns of the "biofilm" matrix represented the x_{BIFILM} values while the number of rows (j) represented the $y_{BIOFILM}$ values. The $x_{BIOFILM}$ values were integer and they started from 1. Because of that, some approximations had to be made. Therefore, in order to find the same x_{BEAD} value (column 1), we had to assume that all the x_{BEAD} were integer and equal to 1. Hence, the cycle "for" #1 and the "if" case # 1 (Figure A.3) changed in 1 each x_{BEAD} value which was less than 1. Moreover, also the floating part of x_{BEAD} was not considered ("round" function). Then, the cycle "for" #2 (Figure A.3), for each x_{BEAD}, found the same $x_{BIOFILM}$ value in the "biofilm" matrix (Figure A.4b, number 1), which is the column number, and then the entire column was considered. The cycle "for" # 3 and the "if" case #2 (Figure A.3) checked for each d row number (i.e. j=$y_{BIOFILM}$) the same y_{BEAD} value in the column 2 of the "bead" matrix (Figure A.4b, number 2). Finally, the relative z_{BEAD} and $z_{BIOFILM}$ values (Figure A.4b), number 2, green squares) were saved in two arrays (z1 and z2 respectively, Figure A.3). Then the function measured the relative depth ratio (named "r" in the script, Figure A.3) and gave as output only the relative depth ratio which was less than 100 (named “a” in the script, Figure A.3). An RD ratio greater than 100% meant the beads were located above the biofilm surface (Miller et al. 2013) .

REFERENCES

Miller J, Neubig R, Clemons C, Kreider K, Wilber J, Young G, Ditto A, Yun Y, Milsted A, Badawy H. 2013. Nanoparticle deposition onto biofilms. Annals of biomedical engineering. 41(1):53-67.

APPENDIX B

Journal of Dental Research
2015, Vol. 94(9) 1303–1309
© International & American Associations
for Dental Research 2015
Reprints and permissions:
sagepub.com/journalsPermissions.nav
DOI: 10.1177/0022034515589284
jdr.sagepub.com

Removal of Dental Biofilms with an Ultrasonically Activated Water Stream

R.P. Howlin[1,2], S. Fabbri[3], D.G. Offin[4], N. Symonds[3], K.S. Kiang[5], R.J. Knee[2], D.C. Yoganantham[2], J.S. Webb[1,2], P.R. Birkin[4], T.G. Leighton[6,7], and P. Stoodley[3,8]

Abstract

Acidogenic bacteria within dental plaque biofilms are the causative agents of caries. Consequently, maintenance of a healthy oral environment with efficient biofilm removal strategies is important to limit caries, as well as halt progression to gingivitis and periodontitis. Recently, a novel cleaning device has been described using an ultrasonically activated stream (UAS) to generate a cavitation cloud of bubbles in a freely flowing water stream that has demonstrated the capacity to be effective at biofilm removal. In this study, UAS was evaluated for its ability to remove biofilms of the cariogenic pathogen *Streptococcus mutans* UA159, as well as *Actinomyces naeslundii* ATCC 12104 and *Streptococcus oralis* ATCC 9811, grown on machine-etched glass slides to generate a reproducible complex surface and artificial teeth from a typodont training model. Biofilm removal was assessed both visually and microscopically using high-speed videography, confocal scanning laser microscopy (CSLM), and scanning electron microscopy (SEM). Analysis by CSLM demonstrated a statistically significant 99.9% removal of *S. mutans* biofilms exposed to the UAS for 10 s, relative to both untreated control biofilms and biofilms exposed to the water stream alone without ultrasonic activation ($P < 0.05$). The water stream alone showed no statistically significant difference in removal compared with the untreated control ($P = 0.24$). High-speed videography demonstrated a rapid rate (151 mm^2 in 1 s) of biofilm removal. The UAS was also highly effective at *S. mutans, A. naeslundii*, and *S. oralis* biofilm removal from machine-etched glass and *S. mutans* from typodont surfaces with complex topography. Consequently, UAS technology represents a potentially effective method for biofilm removal and improved oral hygiene.

Keywords: bacteria, caries, dental hygiene, infection control, microbiology, *Streptococcus mutans*

Introduction

The oral cavity provides an optimal environment for the colonization and proliferation of a diverse array of microorganisms (Aas et al. 2005; Zaura et al. 2009). The most prevalent are bacteria, which exist primarily as a biofilm, commonly known as dental plaque, on the tooth surface. The accumulation of dental biofilm plays a key role in the pathogenesis of a range of oral diseases, including gingivitis, periodontitis, and caries (Aspiras et al. 2010).

Streptococcus mutans is a major cariogenic constituent of the supragingival biofilm due, in part, to its ability to grow and metabolize optimally at low pH (von Ohle et al. 2010). This gives it the ability to outcompete noncariogenic commensal species, thus altering microbial homeostasis in favor of the proliferation of acidogenic and aciduric microbial species and the establishment of a disease state (Marsh 2003; Falsetta et al. 2012; Lemos et al. 2013). Most control strategies, therefore, focus on preventing the proliferation of dental biofilm through frequent removal by mechanical oral hygiene procedures, usually in combination with chemical detrifrices (Brading and Marsh 2003; Forssten et al. 2010; Marsh 2010). However, even with good oral hygiene practices, such as regular brushing, flossing, water jets, and high-velocity water drops, biofilms can still accumulate on hard-to-reach places on the tooth surface.

Studies have previously demonstrated that the passage of a water-air interface over a solid surface can entrain bacteria and

---

[1] National Institute for Health Research Southampton Respiratory Biomedical Research Unit, Southampton Centre for Biomedical Research, University Hospital Southampton NHS Foundation Trust, Southampton, UK
[2] Centre for Biological Sciences, Faculty of Natural and Environmental Sciences and Institute for Life Sciences, University of Southampton, Southampton, UK
[3] National Centre for Advanced Tribology, Faculty of Engineering and Institute for Life Sciences, University of Southampton, Southampton, UK
[4] Chemistry, University of Southampton, Southampton, UK
[5] Southampton Nanofabrication Centre Electronics & Computer Science, University of Southampton, Southampton, UK
[6] Faculty of Engineering and the Environment, University of Southampton, Southampton, UK
[7] Institute of Sound and Vibration Research, University of Southampton, Southampton, UK
[8] Departments of Microbial Infection and Immunity and Orthopaedics, Center for Microbial Interface Biology, The Ohio State University, Columbus, OH, USA

A supplemental appendix to this article is published electronically only at http://jdr.sagepub.com/supplemental.

Corresponding Author:
P. Stoodley, Center for Microbial Interface Biology, The Ohio State University, 716 Biomedical Research Tower, 460 West 12th Ave, Columbus, OH 43210, USA.
Email: pstoodley@gmail.com

provide effective biofilm cleaning (Gomez-Suarez et al. 2001; Parini and Pitt 2006). This can be achieved with the passage of a microbubble stream, occasionally combined with ultrasonic agitation, to generate significant surface tension and shear forces for mechanical-based cleaning (Parini and Pitt 2005; Halford et al. 2012). Recently, a novel cleaning system has been developed that uses the acoustic activation of bubbles within a free flow of water to generate an ultrasonically activated stream (UAS) (Leighton et al. 2011). The forces acting on individual gas bubbles cause them to coalesce and move over the surface or be trapped within pits and fissures within the substratum (Leighton 1994; Doinikov 2001; Stricker et al. 2013), where the motion and cavitation dynamics of the bubbles create local shear and pressure, contributing to cleaning efficacy (Rooney 1970). This has been demonstrated in oral models (Leighton 1994; O'Leary et al. 1997; Lea et al. 2005) using standard dental ultrasonic equipment but never with contact-free technologies such as UAS. Particularly with respect to the pits and recesses of a surface, the entrapment of dynamic gas bubbles produces highly effective cleaning that may not be achieved with a normal water stream (Offin et al. 2014). This study aims to evaluate the efficacy of UAS as a novel approach to dental biofilm removal.

Materials and Methods

Bacteria and Biofilm Growth Conditions

Overnight cultures of *S. mutans* UA159 (ATCC 700610), *Actinomyces naeslundii* ATCC 12104, and *Streptococcus oralis* ATCC 9811 were grown in brain heart infusion (BHI; Sigma-Aldrich, St. Louis, MO, USA) broth at 37 °C (for *S. mutans*, BHI was supplemented with 2% sucrose [Sigma-Aldrich] and cultures were grown at 5% CO_2). Each culture was diluted in fresh media to an optical density value corresponding to 10^6 colony-forming units (CFU)/mL. The adjusted culture was used as an inoculum to assess UAS cleaning on a variety of increasingly complex surfaces with different roughness and material properties. Biofilms were grown on all surfaces for 72 h at 37 °C (with 5% CO_2 for *S. mutans* biofilm growth) in a humidified incubator with media changes performed every 24 h.

The UAS Device

We used a benchtop prototype of the StarStream UAS device (Leighton 2011) (Ultrawave Precision Ultrasonic Cleaning Equipment, Cardiff, UK). The device generates a stream of water at 2.1 L/min (±0.2 L/min) from a 10-mm diameter circular orifice, down which an ultrasonic field is projected. The device also creates bubble clouds, which impinge on the sample and spread laterally, and clean from the shear they generate (Leighton 1994). Biofilms were positioned 1 cm downstream from the orifice and exposed to a continuous stream of UAS for 10 s at room temperature.

Removal of Biofilms from Flat Surfaces Using an UAS

Glass slides were sterilized by autoclaving at 121 °C for 20 min. The slides were immersed vertically in a tube containing 40 mL of a 10^6 CFU/mL culture of either *S. mutans, A. naeslundii*, or *S. oralis*, and biofilms were grown as described above.

Following UAS exposure with the water stream positioned perpendicular to the surface, the slides were fluorescently stained with Live/Dead Baclight (Invitrogen, Carlsbad, CA, USA) in the dark for 20 min. Following a rinse in Hank's buffered salt solution (HBSS; Sigma-Aldrich) for 5 s, the slides were imaged using an inverted Leica DMI600 SP5 confocal scanning laser microscope (CSLM; Leica Microsystems, Milton Keynes, UK). Image analysis was carried out using the image analysis package COMSTAT (www.comstat.dk) (Heydorn et al. 2000). Assays were performed in duplicate (n = 4 image stacks per repeat) and statistical analysis performed using the Mann-Whitney rank sum tests for nonnormally distributed data and difference considered significant where $P < 0.05$.

In addition, *S. mutans* biofilms were grown in 9-cm, presterilized Petri dishes as described above. The UAS device was positioned centrally over the Petri dish and the biofilm exposed to UAS action or the water stream alone without ultrasonic activation with the water flow perpendicular to the surface. Representative photographs were taken for observation of gross biofilm removal. Each assay was performed in duplicate.

High-Speed Camera Assessment of S. mutans Removal Using an UAS from an Interproximal Space Model

To simulate the interproximal (IP) space of the teeth, 2 *S. mutans* biofilm-colonized slides were placed inside a rectangular plastic holder in parallel with a gap of 1 mm. The IP space holder was then placed under the device, and a high-speed camera (1,000 f/s; Motion Pro X3, IDT, Tallahassee, FL, USA) equipped with a Nikon (Tokyo, Japan) 105-mm f/2.8 VR G lens was used to capture the removal of the biofilm due to the UAS and the water stream alone without ultrasonic activation. In this assay, the water flow was run parallel to the biofilm. Representative videos can be found in the online supplementary material. Each experiment was performed in duplicate. High-speed videos were postprocessed with ImageJ software (National Institutes of Health, Bethesda, MD, USA). *S. mutans* biofilm clearance zone (CZ) was quantified by measuring the CZ area (A_{CZ}) in each frame every 300 ms. Then, the averaged A_{CZ} values (n = 2) with the relative SD were plotted as a function of the time. Statistical analysis was performed using an unpaired t test to compare normally distributed data means and difference considered significant where $P < 0.05$.

Surface Roughness Following UAS Exposure

Glass slides and hydroxyapatite (HA) coupons were exposed to the UAS for 10 s and 10 min continuously under the same conditions described above. Following exposure, the surface profiles were measured 2-dimensionally using the contact tracing system provided by the Taylor Hobson Talysurf 120L (Leicester, UK). The evaluation lengths were set at 5 and 40 mm for the HA coupons and glass slide, respectively, with a measurement speed of 0.5 mm/s. The primary raw data were filtered following the rules and procedures given in BS EN ISO 4288:1998. The characteristic wavelength of the profile filter λ_c was set at 0.8 and 0.08 mm for the HA coupons and glass slides, respectively. Surface roughness (R_a/µm) was determined in experimental triplicate, and statistical analysis was performed using an unpaired *t* test to compare normally distributed data means and difference considered significant where $P < 0.05$.

Removal of Biofilm from Artificial Rough Surface Using an UAS

Using a Loadpoint Microace 3 dicing saw (Swindon, UK), micro-grooves were cut into standard microscope glass slides to a uniform depth of 150 µm to a lattice configuration (period spacing: 500 µm × 760 µm, 760 µm × 1 mm, and 500 µm × 1 mm). The glass slides were then reduced in size to 15 mm × 15 mm using the dicing saw and rinsed in acetone and isopropanol to remove any organic residues, followed by dehydration at 200 °C for 30 min using a conventional oven. Following autoclaving at 121 °C for 20 min to sterilize, the slides were immersed in 4 mL of 10^6 CFU/mL and *S. mutans, A. naeslundii*, and *S. oralis* biofilms grown as described previously.

Following exposure to the UAS or water stream alone with the water flow positioned perpendicular to the surface, the slides were immersed in a primary fixative of 0.15 M sodium cacodylate buffer (pH 7.2) containing 3% glutaraldehyde and 0.15% Alcian blue 8GX for 24 h at 4 °C. A 1-h rinse in 0.15 M cacodylate buffer was performed at room temperature, and the biofilms were then postfixed in a secondary fixative containing 1% osmium tetraoxide in 0.15 M cacodylate buffer (pH 7.2) for 1 h. Following a further 1-h rinse in cacodylate buffer, the biofilms were dehydrated through an ascending ethanol series (50%, 70%, 80%, 95%, and 100% [twice]) prior to critical point drying and gold-palladium sputter coating and imaged using an FEI Quanta 200 Scanning Electron Microscope (Hillsboro, OR, USA).

Removal of S. mutans Biofilms from a Typodont Model Using an UAS

To re-create a realistic anatomical geometry of patient dental architecture in vitro, *S. mutans* biofilms were grown on the molars of a training typodont (A-PZ periodontal dental model 4030025; Frasaco GmbH, Tettnang, Germany) (Rmaile et al. 2014). The typodont teeth were autoclave sterilized and immersed in 5 mL of a 10^6 CFU/mL culture of *S. mutans* and biofilms grown as described previously. After this time, the teeth were removed using sterile tweezers and repositioned into the typodont and exposed to the UAS and water stream alone without ultrasonic activation with the water flow positioned perpendicular to the tooth crown. Following this, the teeth were removed from the typodont and immersed in 0.5% crystal violet (Sigma-Aldrich) for 10 min. Poststaining, the surface was dipped and gently rinsed in deionized water to remove excess stain prior to photographing to observed gross biofilm removal. To visualize removal from the teeth at the micro-scale, subsequent repeats were performed where the teeth were fixed as described above for scanning electron microscopy (SEM).

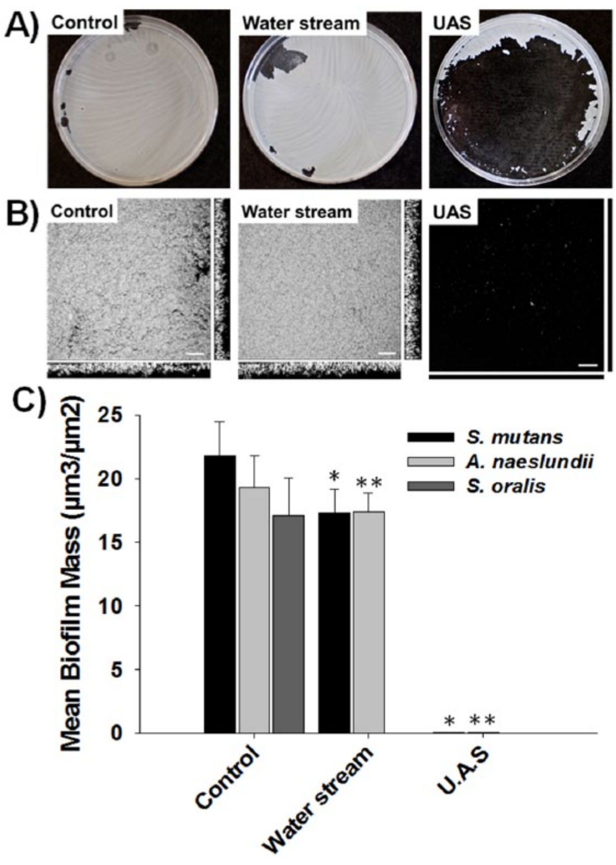

Figure 1. Removal of oral biofilms using an ultrasonically activated water stream (UAS). (**A**) Images show the zone of clearing of *Streptococcus mutans* UA159 biofilms grown in Petri dishes following 10-s exposure using the water stream alone without ultrasonic activation and the UAS, relative to an untreated control. In both cases, the water stream was positioned in the center of the plate. (**B**) Representative confocal scanning laser microscopy (CSLM) images of residual *S. mutans* UA159 biofilms following exposure to the UAS and water stream alone for 10 s, relative to an untreated control following Live/Dead Baclight fluorescent staining. Scale bars: 25 µm. (**C**) Graph shows COMSTAT analysis of residual mean biofilm mass with standard error bars of *S. mutans* UA159, *Actinomyces naeslundii* ATCC 12104, and *Streptococcus oralis* ATCC 9811 biofilms following a 10-s exposure to the UAS and the water stream alone as identified by Live/Dead Baclight fluorescent staining and CSLM ($n = 8$ with assay performed in duplicate). * and ** indicate corresponding data showing a statistically significant difference ($P < 0.01$).

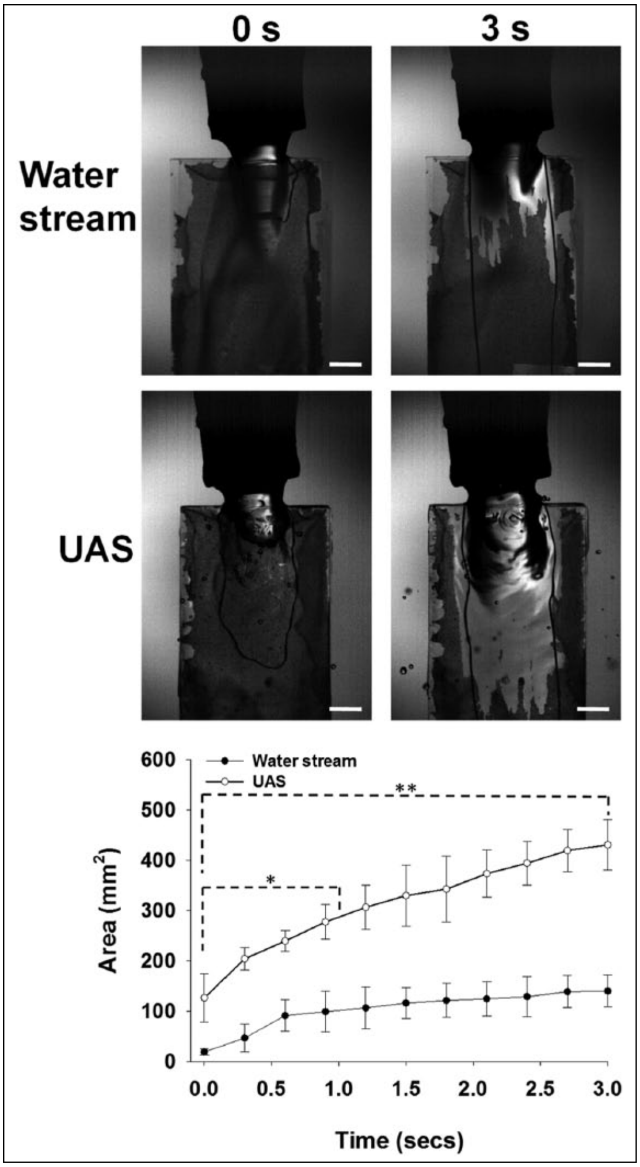

Figure 2. High-speed camera (1,000 f/s) imaging of *Streptococcus mutans* UA159 biofilm removal, using a ultrasonically activated water stream (UAS) and water stream alone, from glass slides placed in an interproximal space model. Images show representative frames from the high-speed camera at 0- and 3-s intervals. Scale bars: 5 mm. Graph shows the mean area of biofilm clearance against time following high-speed camera imaging of *S. mutans* biofilm removal using the UAS and water stream alone. Data points represent the mean of duplicate experimental repeats with standard error bars. * and ** represent data ranges of 0 to 1 s and 0 to 3 s, showing a statistically significant difference ($P < 0.5$).

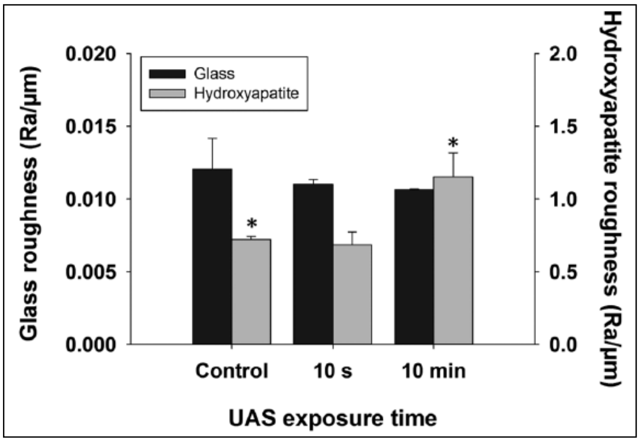

Figure 3. Surface profile (R_a/µm) following exposure of clean glass and hydroxyapatite surfaces to an ultrasonically activated water stream (UAS) for 10 s and 10 min. Data represent the mean of assays performed in experimental triplicate with standard deviation bars. Data points represent the mean of duplicate experimental repeats with standard error bars. * represents data showing a statistically significant difference ($P < 0.5$).

Results

Gross *S. mutans* biofilm removal from Petri dishes was demonstrated as a larger (50.8-cm^2) zone of clearing from the center of the plate covering almost the entire plate diameter following 10-s exposure to the UAS, relative to the water stream alone without ultrasonic activation (3.5 cm^2; Fig. 1A). The water stream alone showed no removal of biofilm from the center of the plate at the initial water stream impact site and was indistinguishable from untreated controls. Biofilm removal with the water stream alone was noted only at the edge of the plate, possibly due to water streaming around the plate edge.

A more detailed inspection by confocal microscopy showed that the UAS was significantly more effective at removing biofilms grown on simple flat surfaces (Fig. 1B) than the water stream alone. COMSTAT analysis of *S. mutans* biofilm removal showed that water stream treatment alone caused a 0.10 log reduction (20.7%) in biomass from 21.8 µm^3/µm^2 to 17.3 µm^3/µm^2 and a 0.17 log reduction (33.8%) in average thickness from 25.3 µm to 16.7 µm, although these reductions were not statistically different ($P = 0.24$). The UAS caused a further 2.3 log reduction in biomass to 0.08 µm^3/µm^2 (99.5% reduction compared with the untreated control) and a 2.9 log reduction in thickness to 0.02 µm (99.9% reduction), which was statistically significant ($P = 0.002$). Similarly, the water stream alone was unable to elicit a statistically significant reduction of *A. naeslundii* biofilms ($P = 0.645$) compared with the control, while biofilm removal with the UAS was significantly greater than the water stream alone ($P < 0.001$). However, the water stream alone, without UAS activation, resulted in a significant reduction in mean *S. oralis* biofilm mass relative to controls ($P = 0.001$), equivalent to a 99.95% reduction, suggesting weak surface attachment of *S. oralis* in this assay.

Further analysis using a high-speed camera of *S. mutans* biofilm removal from glass slides in a model mimicking the interproximal space showed a more rapid rate of biofilm removal during 0 to 3 s of UAS exposure relative to the water stream alone (Fig. 2; $P < 0.5$, $n = 2$). Within the first second of exposure, the biofilm clearance zone area (A_{CZ}) was 151 mm^2, relative to 80 mm^2 with the water stream alone. The A_{CZ} after a period of 3 s was 139.5 mm^2 (±32.03 mm^2, $n = 2$) and 430.4 (±50.34 mm^2, $n = 2$) for the water stream alone and the UAS, respectively. Representative high-speed camera videos can be found in the online supplementary material.

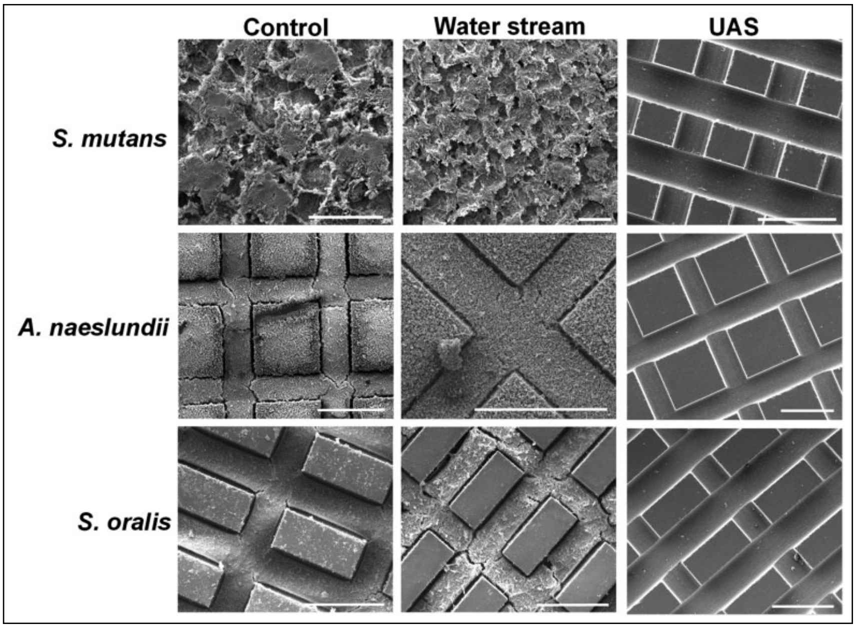

Figure 4. Scanning electron microscopy imaging of residual *Streptococcus mutans* UA159, *Actinomyces naeslundii* ATCC 12104, and *Streptococcus oralis* ATCC 9811 biofilms, grown on machine-etched glass slides to artificially and reproducibly mimic a rough surface, following exposure to the ultrasonically activated water stream (UAS) and water stream alone for 10 s, relative to untreated controls. Scale bars: 500 μm.

Analysis of the effect of a UAS on the underlying substratum was determined by 10-s and 10-min exposure to glass slides (used in Figs. 1 and 2) and HA coupons (Fig. 3). Exposure of glass slides to the UAS had no significant effect on R_a relative to the control (10 s: $P = 0.246$; 10 min: $P = 0.468$). There was also no statistically significant difference in R_a relative to controls of HA coupons exposed to the UAS for 10 s ($P = 0.544$). However, a 10-min exposure did elicit a significant increase in R_a ($P = 0.011$) from 0.72 to 1.15, equivalent to a 62.5% increase in surface R_a.

To further evaluate the effectiveness of UAS biofilm removal from a more complex surface, rough surfaces were created with various microgroove configurations and *S. mutans, A. naeslundii*, and *S. oralis* biofilms grown to demonstrate broad-spectrum bacterial species removal. SEM imaging following exposure to the water stream alone without ultrasonic activation showed no difference in residual biofilm relative to untreated controls (Fig. 4). However, a dramatic reduction in residual biofilm of all 3 bacterial strains was observed following treatment with the UAS relative to the water stream and untreated controls, with the rough surface showing no reduction in the efficacy of UAS mediated removal compared with previous assays on flat surfaces. Importantly, for *S. oralis*, this is in contrast to Figure 1, where the water stream alone was highly effective at biofilm removal, confirming UAS efficacy of hard-to-clean surfaces where the water stream alone was inefficient.

Similarly, the UAS was also effective at removing biofilm from teeth in a typodont training model representing a realistic patient dental architecture (Fig. 5). Crystal violet (CV) staining to assess gross biofilm removal again showed no noticeable difference between the water stream alone and control treatment groups, with a marked reduction in CV staining noted on teeth exposed to the UAS. SEM analysis imaging of the teeth to assess micro-scale removal of *S. mutans* biofilm revealed only occasional single cells visible in the areas exposed to the UAS. In contrast, the water stream alone showed comparable residual biofilm to the untreated control.

Discussion

As a key cariogenic species and a major risk factor for early childhood caries and future caries development, as well as its propensity to form biofilms, both in vitro and in vivo in the oral cavity, *S. mutans* was chosen as the model organism for the study (García-Godoy and Hicks 2008), in addition to *A. naeslundii* and *S. oralis*, to demonstrate broad-spectrum biofilm cleaning. Relative to a water stream flow of 2.1 L/min (±0.2 L/min), ultrasonic activation of the same stream at the same flow rate demonstrated a greater efficiency and rate of biofilm removal from a variety of increasingly complex surfaces, including, importantly, machine-etched slides to provide a consistent "rough" surface and molar teeth from a typodont model. Importantly, typodont model teeth effectively reproduce the normal dental architecture, including the complexity of the crown fissures where mechanical biofilm removal is more challenging and, combined with the IP space, are the most at-risk sites for caries development (Rugg-Gunn 2013).

UAS in a free water stream has several key and beneficial features that make it effective at biofilm removal (Leighton et al. 2011). First, effective cleaning can be achieved through pure water alone under ambient conditions and does not require chemical additives or the generation of high temperature. This is of added benefit as the lack of antimicrobial additives reduces the risk of antibiotic resistance developing and the risk to patient health due to the high doses of antimicrobials sometimes required to clear oral biofilm infections (Larsen and Fiehn 1996; Shani et al. 2000). Instead, the effectiveness of the UAS is achieved due to the utilization of the ultrasonically induced bubble activity and shear (Leighton et al. 2011). While it is known that, for some substrates and some bacterial species, the simple proximity of the passage of a nearby gas bubble (e.g., rising under buoyancy) can cause detachment (Gomez-Suarez et al. 2001), in this study, it is the ultrasonically induced volume and shape oscillations in the bubbles, as well as the associated shear, that produce the significant

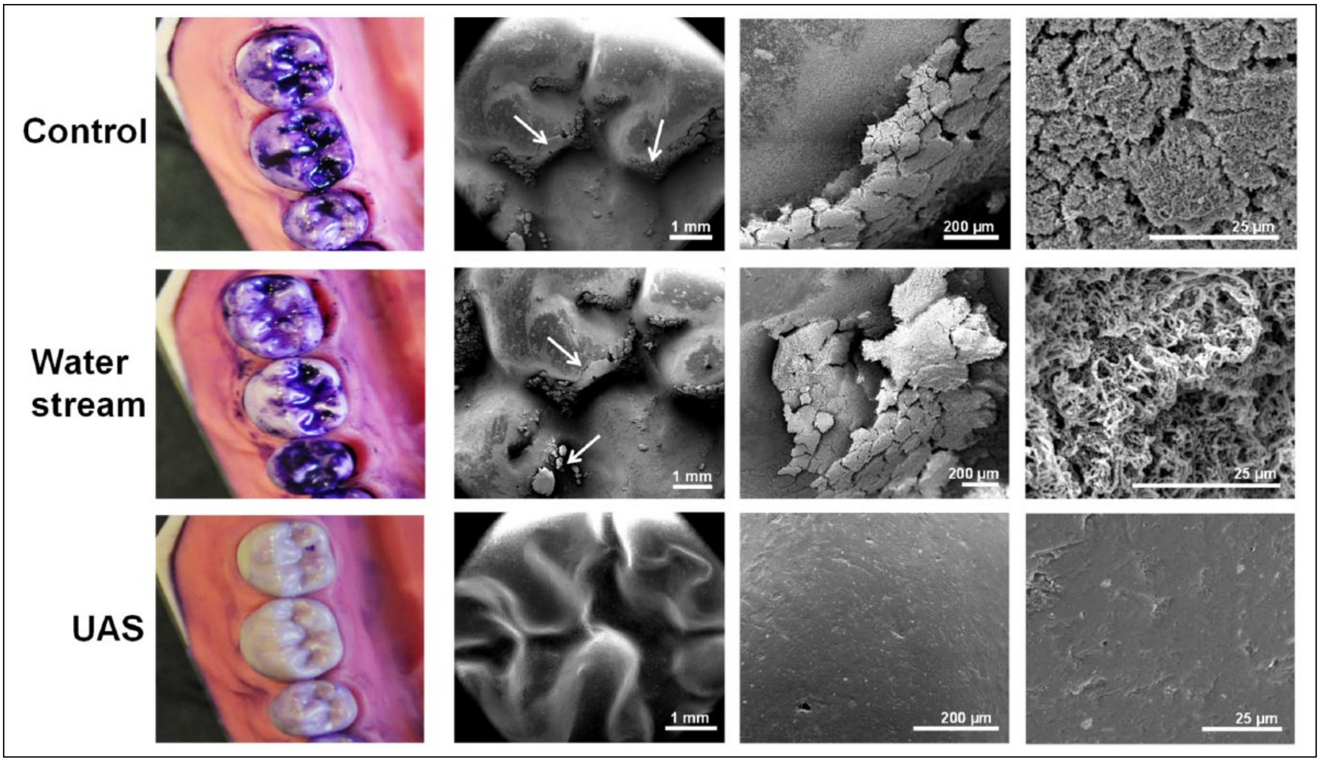

Figure 5. Representative images showing removal of *Streptococcus mutans* UA159 biofilms from molar teeth in a typodont training model, following a 10-s exposure to the ultrasonically activated water stream (UAS) and water stream alone, relative to untreated controls. Left-hand column panels show total residual biomass (blue/purple) as identified by crystal violet staining. Remaining panels show increasingly higher magnification scanning electron microscopy images of the crown surface. White arrows indicate residual *S. mutans* biofilm on low-magnification images. This figure is available in color online at http://jdr.sagepub.com.

removal effect (Leighton et al. 2011). Importantly, since the activated bubbles are in a free water stream, no direct contact between the device and the oral surface is required, facilitating access to hard-to-reach places. Second, the acoustic field causes the bubbles to move to crevices and such surface structures, preferentially cleaning features that are normally more difficult to clean (Leighton 1994; Offin et al. 2014). Consequently, due to the complex oral cavity topography, this approach has the potential to greatly contribute to improved oral hygiene. Third, the area of biofilm removal in this study was relevant in the context of dental hygiene and was achieved over the relatively short time period of a few seconds. The removal efficacy of laboratory-grown biofilms by UAS was similar to that of microburst technology in which high-velocity micro water drops generate high enough fluid shear to remove significant amounts of biofilm from an interproximal space model (Rmaile et al. 2014). However, the microdrops have the advantage of using minimal volumes of water. In addition, while not required for efficacy in this study, additives to the water reservoir, such as fluoride with proven anticaries properties, may further enhance not just the immediate cleaning efficacy but also long-term oral hygiene (Aspiras et al. 2010).

However, issues will need to be addressed regarding application of UAS to oral health care. Future work should address the influence of different surface materials (e.g., dental enamel and dentin) on UAS efficacy. In addition, the influence of the pellicle and salivary coating of a surface on UAS-mediated biofilm clearance needs to be assessed. Existing studies suggest that salivary mucins such as MUC5B decrease surface attachment and biofilm formation of *S. mutans*, and so UAS removal could be enhanced with a more representative oral environment (Frenkel and Ribbeck 2015). Careful consideration and future work will also be needed to assess the potential for tissue damage to the surrounding gingiva, but it is expected that these can be overcome by optimizing exposure time and power output to settings capable of maintaining the efficacy of the device and alleviating the risk of damage to the surrounding tissue. This is corroborated by data from this study where effective biofilm removal without a detrimental effect to the substratum was observed at short exposure times (10 s). Longer exposure times of 10 min did cause an increase in surface roughness on a hydroxyapatite surface; however, this should be put into context of other studies where exposure of 2 min to toothbrushing using certain dentrifices produced a much greater surface abrasion than observed with a 10-min UAS exposure (Pascaretti-Grizon et al. 2013). In addition, while the flow rate of 2.1 L/min used in this study provides good surface area coverage, there is the issue of requiring relatively large volumes of water, and thus miniaturization would be desirable. The current flow rate is higher than commercially available continuous or pulsed water irrigation shear-based removal devices that generally operate on the order of a few hundreds of mL/min (Rmaile et al. 2014). However, the use of a UAS represents a potentially practical and effective method for oral biofilm removal with the capacity to improve oral hygiene.

Author Contributions

R.P. Howlin, contributed to conception, design, data acquisition, analysis, and interpretation, drafted and critically revised the manuscript; S. Fabbri, contributed to data acquisition, analysis, and interpretation, critically revised the manuscript; D.G. Offin, N. Symonds, K.S. Kiang, R.J. Knee, D.C. Yoganantham, contributed to data acquisition, critically revised the manuscript; J.S. Webb, contributed to conception, critically revised the manuscript; P.R. Birkin, T.G. Leighton, contributed to conception, design, and data interpretation, critically revised the manuscript; P. Stoodley, conception, design, data analysis, and interpretation, critically revised the manuscript. All authors gave final approval and agree to be accountable for all aspects of the work.

Acknowledgments

This work was funded by the Royal Society Brian Mercer Award scheme. The authors thank Prof. J. Barton from The University of Southampton. Leighton and Birkin are named inventors of the ultrasonically activated water stream technology on the patent and on a standard licence deal between the University of Southampton and Ultrawave Ltd. The other authors declare no potential conflicts of interest with respect to the authorship and/or publication of this article.

References

Aas JA, Paster BJ, Stoke LN, Olsen I, Dewhirst FE. 2005. Defining the normal bacterial flora of the oral cavity. J Clin Microbiol. 43(11):5721–5732.

Aspiras M, Stoodley P, Nistico L, Longwell M, de Jager M. 2010. Clinical implications of power toothbrushing on fluoride delivery: effects on biofilm plaque metabolism and physiology. Int J Dent. 2010:651869.

Brading MG, Marsh PD. 2003. The oral environment: the challenge for antimicrobials in oral care products. Int Dent J. 53(6 Suppl 1):353–362.

Doinikov AA. 2001. Translational motion of two interacting bubbles in a strong acoustic field. Phys Rev E Stat Nonlin Soft Matter Phys. 64(2 Pt 2):026301.

Falsetta ML, Klein MI, Lemos JA, Silva BB, Agidi S, Scott-Anne KK, Koo H. 2012. Novel antibiofilm chemotherapy targets exopolysaccharide synthesis and stress tolerance in Streptococcus mutans to modulate virulence expression in vivo. Antimicrob Agents Chemother. 56(12):6201–6211.

Forssten SD, Björklund M, Ouwehand AC. 2010. *Streptococcus mutans*, caries and simulation models. Nutrients. 2(3):290–298.

Frenkel ES, Ribbeck K. 2015. Salivary mucins protect surfaces from colonization by cariogenic bacteria. Appl Environ Microbiol. 81(1)332–338.

García-Godoy F, Hicks MJ. 2008. Maintaining the integrity of the enamel surface: the role of dental biofilm, saliva and preventive agents in enamel demineralization and remineralization. J Am Dent Assoc. 139(Suppl 2):25S–34S.

Gomez-Suarez C, Busscher HJ, van der Mei HC. 2001. Analysis of bacterial detachment from substratum surfaces by the passage of air-liquid interfaces. Appl Environ Microbiol. 67(6):2531–2537.

Halford A, Ohl CD, Azarpazhooh A, Basrani B, Friedman S, Kishen A. 2012. Synergistic effect of microbubble emulsion and sonic or ultrasonic agitation on endodontic biofilm in vitro. J Endod. 38(11):1530–1534.

Heydorn A, Nielsen AT, Hentzer M, Sternberg C, Givskov M, Ersbøll BK, Molin S. 2000. Quantification of biofilm structures by the novel computer program COMSTAT. Microbiology. 146(10):2395–2407.

Larsen T, Fiehn NE. 1996. Resistance of *Streptococcus sanguis* biofilms to antimicrobial agents. Apmis. 104(4):280–284.

Lea SC, Price GJ, Walmsley AD. 2005. A study to determine whether cavitation occurs around dental ultrasonic scaling instruments. Ultrason Sonochem. 12(3):233–236.

Leighton TG. 1994. The acoustic bubble. New York (NY): Academic Press.

Leighton TG, Vian CJB, Birkin PR, inventors; University of Southampton, assignee. 2011. Cleaning apparatus and method, and monitoring thereof. Patent PCT/EP2010/062448.

Lemos JA, Quivey RG Jr, Koo H, Abranches J. 2013. *Streptococcus mutans:* a new Gram-positive paradigm? Microbiology. 159(Pt 3):436–445.

Marsh PD. 2003. Are dental diseases examples of ecological catastrophes? Microbiology. 149(Pt 2):279–294.

Marsh PD. 2010. Controlling the oral biofilm with antimicrobials. J Dent. 38(Suppl 1):S11–S15.

Offin DG, Birkin PR, Leighton TG. 2014. An electrochemical and high-speed imaging study of micropore decontamination by acoustic bubble entrapment. Phys Chem Chem Phys. 16(10):4982–4989.

O'Leary R, Sved AM, Davies EH, Leighton TG, Wilson M, Kieser JB. 1997. The bactericidal effects of dental ultrasound on *Actinobacillus actinomycetemcomitans* and *Porphyromonas gingivalis*. J Clin Periodontol. 24(6):432–439.

Parini MR, Pitt WG. 2005. Removal of oral biofilms by bubbles: the effect of bubble impingement angle and sonic waves. J Am Dent Assoc. 136(12):1688–1693.

Parini MR, Pitt WG. 2006. Dynamic removal of oral biofilms by bubbles. Colloids Surf B Biointerfaces. 52(1):39–46.

Pascaretti-Grizon F, Mabillaeu G, Chappard D. 2013. Abrasion of 6 dentrifices measured by vertical scanning interference microscopy. J Appl Oral Sci. 21(5):475–481.

Rmaile A, Carugo D, Capretto L, Aspiras M, De Jager M, Ward M, Stoodley P. 2014. Removal of interproximal dental biofilms by high-velocity water microdrops. J Dent Res. 93(1):68–73.

Rooney JA. 1970. Hemolysis near an ultrasonically pulsating gas bubble. Science. 169(3948):869–871.

Rugg-Gunn A. 2013. Dental caries: strategies to control this preventable disease. Acta Med Acad. 42(2):117–130.

Shani S, Friedman M, Steinberg D. 2000. The anticariogenic effect of amine fluorides on *Streptococcus sobrinus* and glucosyltransferase in biofilms. Caries Res. 34(3):260–267.

Stricker L, Dollet B, Fernandez Rivas D, Lohse D. 2013. Interacting bubble clouds and their sonochemical production. J Acoust Soc Am. 134(3):1854–1862.

von Ohle C, Gieseke A, Nistico L, Decker EM, deBeer D, Stoodley P. 2010. Real-time microsensor measurement of local metabolic activities in ex vivo dental biofilms exposed to sucrose and treated with chlorhexidine. Appl Environ Microbiol. 76(7):2326–2334.

Zaura E, Keijser BJ, Huse SM, Crielaard W. 2009. Defining the healthy "core microbiome" of oral microbial communities. BMC Microbiol. 15(9):259.

APPENDIX C

JOURNAL OF THE MECHANICAL BEHAVIOR OF BIOMEDICAL MATERIALS 59 (2016) 197–206

Available online at www.sciencedirect.com

ScienceDirect

www.elsevier.com/locate/jmbbm

Research Paper

Streptococcus mutans biofilm transient viscoelastic fluid behaviour during high-velocity microsprays

S. Fabbri[a,*], D.A. Johnston[b], A. Rmaile[c], B. Gottenbos[c], M. De Jager[c], M. Aspiras[d], M.E. Starke[e], M.T. Ward[e], P. Stoodley[a,f]

[a]National Centre for Advanced Tribology at Southampton (nCATS), University of Southampton, Southampton SO17 1BJ, UK
[b]Biomedical Imaging Unit, School of Medicine, University of Southampton, Southampton SO16 6YD, UK
[c]Philips Research, High Tech Campus, Eindhoven 5656 AE, The Netherlands
[d]Wrigley, Chicago, IL 60613, USA
[e]Philips Oral Healthcare, Bothell, WA 98021, USA
[f]Department of Microbial Infection and Immunity and the Department of Orthopaedics, Centre for Microbial Interface Biology, The Ohio State University, Columbus, OH 43210, USA

ARTICLE INFO

Article history:
Received 18 August 2015
Received in revised form
12 December 2015
Accepted 14 December 2015
Available online 23 December 2015

Keywords:
Biofilm
Oral hygiene
High-speed camera
Fluid dynamics
Mechanical properties
Viscoelasticity

ABSTRACT

Using high-speed imaging we assessed *Streptococcus mutans* biofilm–fluid interactions during exposure to a 60-ms microspray burst with a maximum exit velocity of 51 m/s. *S. mutans* UA159 biofilms were grown for 72 h on 10 mm-length glass slides pre-conditioned with porcine gastric mucin. Biofilm stiffness was measured by performing uniaxial-compression tests. We developed an in-vitro interproximal model which allowed the parallel insertion of two biofilm-colonized slides separated by a distance of 1 mm and enabled high-speed imaging of the removal process at the surface. *S. mutans* biofilms were exposed to either a water microspray or an air-only microburst. High-speed videos provided further insight into the mechanical behaviour of biofilms as complex liquids and into high-shear fluid–biofilm interaction. We documented biofilms extremely transient fluid behaviour when exposed to the high-velocity microsprays. The presence of time-dependent recoil and residual deformation confirmed the pivotal role of viscoelasticity in biofilm removal. The air-only microburst was effective enough to remove some of the biofilm but created a smaller clearance zone underlying the importance of water and the air–water interface of drops moving over the solid surface in the removal process. Confocal and COMSTAT analysis showed the high-velocity water microspray caused up to a 99.9% reduction in biofilm thickness, biomass and area coverage, within the impact area.

---

[*]Correspondence to: National Centre for Advanced Tribology at Southampton (nCATS), Faculty of Engineering and the Environment, University of Southampton, Southampton SO17 1BJ, UK.
E-mail address: stefaniafabbri1987@gmail.com (S. Fabbri).

http://dx.doi.org/10.1016/j.jmbbm.2015.12.012
1751-6161/

1. Introduction

Dental plaque biofilms are the heterogeneous bacterial communities attached to teeth and soft tissues and embedded in a matrix composed mainly of extracellular DNA, proteins, and polysaccharides (Marsh and Bradshaw, 1995). Oral biofilms are associated with the development of caries, gingivitis and periodontitis (Costerton et al., 1995; Donlan and Costerton, 2002). Dental caries occurs through the dissolution of the enamel by acidogenic bacteria such as *Streptococcus mutans*, *Streptococcus sobrinus*, and lactobacilli (Featherstone, 1999). Biofilm complex structure makes dental diseases difficult to control and to eradicate, thus becoming a worldwide public health problem (Selwitz et al., 2007). When biofilms are subjected to different flow conditions, they mechanically behave as viscoelastic fluids (Klapper et al., 2002; Peterson et al., 2015; Towler et al., 2003; Wilking et al., 2011). This means that at low-shear rates biofioms have a "solid-like" behaviour and are able to store energy, while at high-shear rates they become "fluid-like" and lose their ability to store elastic energy. Energy dissipation through viscoelasticity is an important characteristic because it allows biofilms to tolerate rapidly-changing shear stresses without detaching from the surface. In dentistry, fluid shear stresses generated via either non-contact toothbrushing or fluid flow play a major role in biofilm detachment (Hope et al., 2003; Hope and Wilson, 2003; Paramonova et al., 2009) since dental plaque mainly accumulates in particular areas inside the mouth (such as pits, fissures, interproximal (IP) spaces and subgingival areas) inaccessible for toothbrush bristles and dentifrices (Fried, 2012). Therefore, the understanding of biofilm mechanical properties under various hydrodynamic flows represents an important part for the design of more effective strategies to remove and to control dental plaque biofilms. Oral irrigators, which generate a continuous pulsating or steady water jet designed to remove interdental and subgingival plaque are widely used as a supplement to toothbrushing, or to replace traditional flossing (Barnes et al., 2005; Jahn, 2010). More recently, mechanical biofilm removal either using low volume, high-velocity water droplets (Cense et al., 2006) or by entrained air bubbles (Parini and Pitt, 2006; Sharma et al., 2005b) has shown positive results due to the droplets' impact pressure, hydrodynamic shear stresses and the surface tension effects of the passage of an air–water interface over a solid surface (Busscher et al., 2010b).

In previous studies we grew *S. mutans* biofilms on and between two central incisors of a periodontal model to recreate the realistic geometry of the IP space (Rmaile et al., 2012). Then we performed high-speed imaging to assess biofilm removal and viscoelastic behaviour during the exposure to high-velocity microbursts (Rmaile et al., 2014). We also performed Computational Fluid Dynamics (CFD) simulations to predict wall shear stresses generated over the tooth surface during the burst (Rmaile et al., 2015). However, due to the opaque nature of the surface we could not see the details of biofilm removal process at the surface. Here we developed an in vitro IP model allowing the parallel insertion of two biofilm-colonized glass slides which could be monitored through the side of the slide by a high-speed camera. Biofilms were exposed to high-velocity water microsprays or air-only microbursts to assess the effects of these different fluid flows on the biofilm–burst interactions and biofilm viscolastic mechanical behaviour with respect to the removal process.

2. Materials and methods

2.1. Bacteria and growth media

Biofilms were inoculated with a *S. mutans* UA159 (ATCC 700610) adjusted overnight culture (10^6 cfu/mL) grown in a 2% sucrose-supplemented brain-heart infusion (BHI+S medium) (Sigma-Aldrich). Type II porcine gastric mucin (Sigma-Aldrich) was added to the BHI+S medium (BHI+SM medium). Petri plates or microscope glass slides were conditioned with 10 mL of the BHI+SM medium for 24 h to allow mucins to cover the surface. Then, biofilms were grown in static conditions for 72 h at 37 °C and 5% CO_2 with BHI+SM medium replacement every 24 h. We also grew biofilms on non-mucin conditioned plates and in BHI+S medium (control *S. mutans* biofilms) to assess the influence of mucin on the mechanical properties.

2.2. Uniaxial compression tests

Uniaxial compression experiments were performed on control *S. mutans* biofilms and on *S. mutans* biofilms grown on mucin-conditioned petri plates and with mucin-supplemented medium using an Electroforce 3200 testing instrument (Bose). Since biofilms are known to be viscoelastic materials and their mechanical behaviour varies with the strain rate applied, we performed uniaxial compression experiments at a constant rate of 0.05 mm/s. An upper cylindrical plunger of a diameter (D) of 7.75 mm compressed the biofilm and a 5 N capacity load cell (Honeywell Sensotec, Columbus, OH, USA) recorded the resulted force. Biofilm stiffness under constant strain rate was measured calculating the Young's modulus (E) from the stress–strain curves as previously described (Rmaile et al., 2012). Six independent replicate experiments were performed ($n=6$). Statistical analysis was performed using unpaired two samples t-test for normally distributed data and difference considered significant where $p<0.05$.

2.3. In vitro IP model and high-velocity microsprays

To allow high-speed camera imaging at the surface we developed an in vitro IP model (Fig. 1). The model consisted of a rectangular clear plastic holder, in which two grooves were made for the parallel insertion of two *S. mutans* biofilm-colonized slides at a distance of 1 mm. Slides were cut at 10 mm (10 mm-length slice) as a representative length, in the outside-in direction, of the proximal surface of the human molars. Since most of the biofilm was rapidly cleared from the 10 mm length of the slide we also grew *S. mutans* biofilms on full-length slides (75 mm × 25 mm) in order to more clearly assess the fluid nature of the biofilm which was most evident at the interface between the spray and the biofilm. Prior to the insertion into the IP model, the initial thickness of the

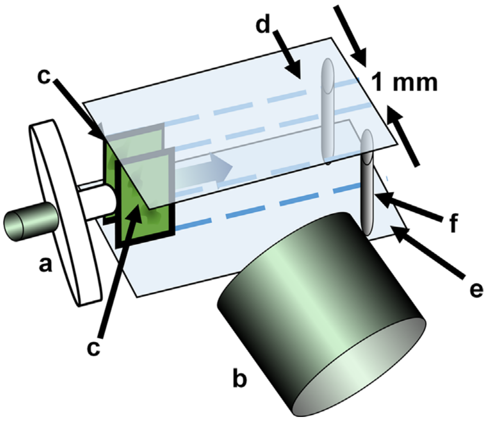

Fig. 1 – Schematic showing the juxtaposition of the IP model, the tip of the AirFloss (a) and the lens of the hyperspectral camera (b). The IP model was made up of two biofilm-colonized microscope slides (in green) (c) held in parallel grooves in top and bottom plates (d and e) to make a 1-mm gap. The slides length represented in this schematic is 10 mm. Two support pillars were placed at the back of the holder (f). The collar holding the AirFloss neck to the bottom plate (e) so that the tip was firmly abutted to the IP gap is not shown for clarity. The direction of the microspray though the IP space is indicated by the blue arrow. (For interpretation of the references to color in this figure legend, the reader is referred to the web version of this article.)

biofilm was 51.8±9.1 μm (mean±1 SD, $n=9$), measured by COMSTAT from 3D confocal images (see Section 2.6). A Philips Sonicare AirFloss HX8111 commercially available oral hygiene device was used to generate high-velocity microsprays. The device was filled either with water to generate a water microspray, as per normal use of the device, or was left empty in order to generate an air-only microburst.

2.4. *S. mutans biofilms exposure to high-speed microsprays*

The dental cleaning device was positioned in order to have the tip centred between the two biofilm-covered slides inside the IP model (Fig. 1). The shooting was recorded at 8000 frames per seconds (fps) with a high-speed camera MotionPro X3 (IDT) equipped with a Sigma 105 mm f/2.8 EX DG Macro lens. To characterize the hydrodynamic of the flow during the water microspray, high-speed images were also taken of the burst into open air.

2.5. *High-speed video post-processing*

The HSC videos were converted in Fiji (http://fiji.sc/Fiji) (Schindelin et al., 2012) to a stack with each frame in the stack being a different time (T) so that the volume could be represented as XYT co-ordinates. The external diameter of the nozzle tip ($d_{AF}=2$ mm) was used as an internal scale to calibrate pixels with microns.

In order to characterize the water microspray hydrodynamic, a water microspray average velocity (u) was defined as $u=\Delta X/\Delta T$ (1), where ΔX is the microspray length variation along the X axis and ΔT is the time interval between the two adjacent frames. A Reynolds number (Re) was also measured using the Reynolds equation for free jets:

$$\mathrm{Re} = \frac{u\rho D}{\mu} \tag{1}$$

where ρ and μ are the density (998 kg/m^3) and the viscosity (1.003×10^{-3} Pa s) of water at 20 °C and D is the Airfloss tip internal diameter (1 mm). Videos were analysed from five independent experiments ($n=5$).

Regarding biofilms exposure to high-speed microsprays, the area of the biofilm cleared zone caused by the microsprays (A) was measured as a function of the time in each frame every 5 ms. Using the Threshold function in Fiji only the cleared zone was selected in each frame. Then A was measured using the Measure function. Videos were analysed from three independent experiments ($n=3$). Statistical analysis was performed using unpaired two samples t-test for normally distributed data and difference considered significant where $p<0.05$.

Biofilm recoil was measured using the reslice function which creates a time-trace along a defined line. As the biofilm recoiled towards the cleared zone it makes a continuous curve from the left to the right. Biofilm total recoil was defined as the difference between the final and initial length. Videos were analysed from three independent experiments ($n=5$ measurements per repeat). Statistical analysis was performed using unpaired two samples t-test for normally distributed data and difference considered significant where $p<0.05$.

2.6. *Confocal and scanning electron microscope analysis*

The thickness of the control biofilms (unexposed to a spray or air jet) and those biofilms on the 1 cm slide immediately after the shooting were carefully transferred to petri plates filled with 1% (wt/vol) phosphate-buffered saline (PBS) solution (Sigma-Aldrich). Then, the samples were fixed by the addition of 100 μL of 4% (wt/vol) paraformaldehyde (PFA) solution (Agar Scientific) and left for 1 h inside the fridge. Afterwards, the biofilm slides were rinsed twice with 1% PBS in order to disrupt loosely-adherent bacteria. To visualize dead cells in the biofilm, slides were immersed in a 0.2% solution of Propidium iodide (PI, Live/Dead BacLight Bacterial Viability Kit, Invitrogen) for 30 min, washed three times with 1% PBS and then covered immediately with mowiol mounting medium (20 gr of mowiol powder, 88 mL of 1% PBS solution, 40 mL of Glycerol and 2.4 mL of 5% Citifluor solution). Mowiol mounting medium is not only optically appropriate (non-absorbing, containing no autofluorescence, or light scattering), but also has an anti-fade agent which is capable of reducing light-induced fading of the fluorophore. Immediately after, the samples slides were covered with a microscope coverslip and left in the fridge for 24 h in order to settle the mountant uniformly over the whole slide. Then, the samples were imaged using an inverted Leica DMI600 SP5 confocal scanning laser microscope (CSLSM, Leica Microsystems) using a HCX PL APO CS 63x/1.3 NA glycerol immersion lens. Three random confocal images were taken on each of three independent replicate control (not exposed to the

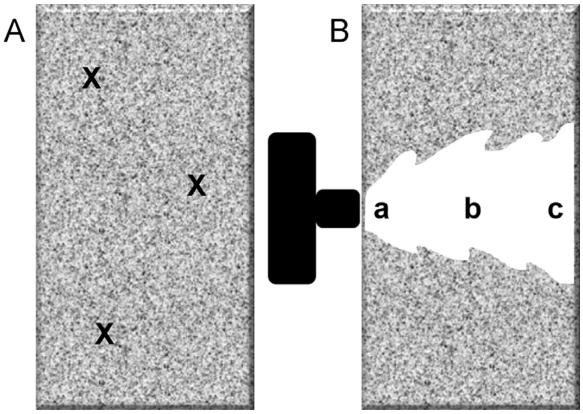

Fig. 2 – (A) Schematic illustrating a *S. mutans* biofilm covered slide (10 mm × 25 mm) prior the shooting. Three random confocal images (X) were taken on the non-exposed slide. (B) Schematic illustrating a *S. mutans* biofilm covered slide (10 mm × 25 mm) after the shooting. Confocal images were taken at 1 mm (a), 5 mm (b) and 8 mm (c) from the leading edge of the slide. Biofilm is depicted grey while the biofilm clearance zone white.

spray) biofilm slides to establish the thickness of the biofilm prior to the shooting (Fig. 2A). For the independent triplicate spray-exposed biofilm slides, confocal images were taken inside the clearance zone, at 1, 5 and 8 mm distances directly downstream from the nozzle, from the leading edge of the slide (Fig. 2B). Thus the experiments were replicated three times with triplicate repeated confocal images for each position within each replicate.

The amount of biofilm removed by the water microspray was quantified by comparing biofilm thickness (*T*), surface area (*A*) and biomass (*B*) of non-exposed control slides and slides after the shooting by analysing the confocal images with the Matlab plugin COMSTAT (Heydorn et al., 2000). The percent reduction in biofilm thickness (%RT), biomass (%RB) and surface area (%RA) were also measured as:

$$\%\mathrm{RT} = \frac{T_0 - T_{CZ}}{T_0} \times 100 \tag{2}$$

$$\%\mathrm{RB} = \frac{B_0 - B_{CZ}}{B_0} \times 100 \tag{3}$$

$$\%\mathrm{RA} = \frac{A_0 - A_{CZ}}{A_0} \times 100 \tag{4}$$

where T_0, B_0, A_0 and T_{CZ}, B_{CZ}, A_{CZ} are biofilm thickness, surface area and biomass prior the and after the shooting respectively.

We compared the thickness of the control (un-shot) biofilm with that at each of these distances using a *t*-test on an $n=3$ for the control and an $n=3$ for the experiment biofilms. In addition we did a *t*-test to establish that there was no significant difference between the biofilm thicknesses at the three different distances from the nozzle after shooting ($P>0.05$) and so also grouped these values to compare the mean thickness within the cleared area with that of the thickness in the unexposed control biofilm ($n=9$).

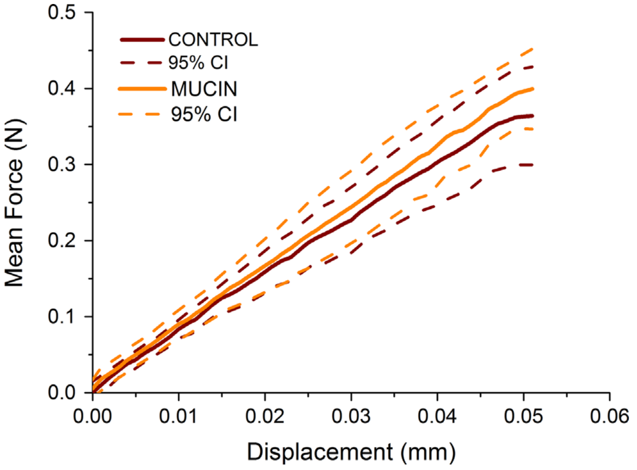

Fig. 3 – Load-versus-displacement curves of 3-days old *S. mutans* biofilms grown on mucin-conditioned plates or non-mucin conditioned plate from uniaxial compression experiments performed under a contant strain rate of 0.05 mm/s. The solid lines are the average of 5 mechanical tests and the dashed lines are the 95% confidence intervals.

A Scanning Electron Microscope (SEM, FEI Quanta-200) was also used to qualitatively assess biofilm removal in high resolution.

3. Results

3.1. *S. mutans* biofilm structure and mechanical properties

The biofilm structure was similar to that reported previously (Rmaile et al., 2014, 2012) and consisted of a dense base layer of cells interspersed with prominent clusters separated by water channels. At 3 days, the unexposed *S. mutans* biofilm was 51.8±4.9 μm ($n=9$) thick. The load–displacement curves under constant strain rate showed a linear behaviour (Fig. 3) with a Young's modulus of 760±201 kPa for the mucin grown biofilm and 800±200 kPa for the non-mucin grown biofilm. These differences were not significant ($p<0.05$, $n=6$).

3.2. *High-velocity water microspray hydrodynamics*

High-speed videos of the water microspray into air showed two distinct phases (**Supplemental** Movie 1). The first phase was a 10.5 ms (±0.3 ms, $n=5$) water jet, while the second phase was a 45.9 ms (±0.8 ms, $n=5$) water spray (Fig. 4A). The total microspray time interval (Δt) was 56.8 ms (±0.6 ms, $n=5$). For the jet phase, the water microspray average velocity (u) started from a value of 36.6 m/s (±6.2 m/s, $n=5$) and decreased to a minimum value of 31.7 m/s (±6.8 m/s, $n=5$) before increasing to a maximum value of 51.1 m/s (±6.3 m/s, $n=5$) (Fig. 4B). The exit-velocity profile of the spray phase was less variable over time, and started from a maximum of 12.9 m/s (±1.7 m/s, $n=5$) decreasing to 10.9 m/s (±3.9 m/s, $n=5$). The Re number calculated for the jet phase ranged from 30,000 to 50,000 predicting fully-developed turbulent flow.

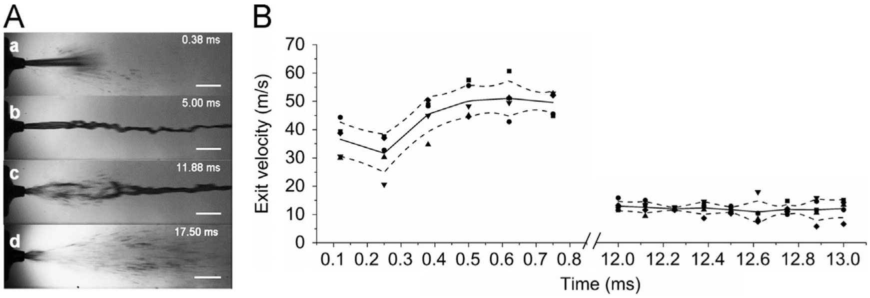

Fig. 4 – (A) Individual frames from a high-speed camera video of the AirFloss water microspray as a free-jet into air at different time points. (a) Initiation of the burst. (b) Fully-developed jet phase. (c) Transition phase from water jet to water spray. (d) Spray phase. Scale bar=5 mm. (B) Water microspray exit velocity as a function of the time for the first part of the jet phase (0–0.8 ms) and the spray phase (12–13 ms). The solid lines is the average exit velocity and the dashed lines are 95% confidence intervals. Individual data from 5 independent runs shown as various symbols.

3.3. *S. mutans biofilm transient viscoelastic fluid behaviour*

High-speed videos of biofilms exposed to high-velocity microsprays revealed that the water microspray and the air-only microburst rapidly entered the IP channel pushing the biofilm outwards towards the distal end of the slide, creating a biofilm cleared zone. The microsprays appeared to cause the biofilms to liquefy and flow over the slide in an extremely short period of time (<60 ms). We observed wave-like structures forming at the biofilm/fluid interface for the entire burst duration (Fig. 5A and **Supplemental** Movie2). Also vortices were seeing developing in a very short time (<5 ms) at the edges of the remaining biofilm (Fig. 5B and **Supplemental** Movie 3). When the microspray ended, these structures disappeared and left no trace of their formation on the slide surface, suggesting biofilm fluidisation can be an extremely transient mechanical behaviour.

Biofilm fluid behaviour was also observed at the edge of the microscope slides where biofilm was seen dripping out and creating droplets which where pushed out of the IP space (Fig. 6 and **Supplemental** Movie 4). Biofilm drops were seen first stretching and then breaking off.

Immediately after the microspray ended, the biofilms exhibited viscoelastic behaviour by undergoing a time-dependant elastic recoil, which caused a the reduction in the width of the cleared channel (Fig. 7A and **Supplemental** Movie 5). Reslice graphs showed an exponential increase in biofilm elongation (recoil) across the spray direction (Fig. 7B). The rate of recoil was similar to that of a viscoelastic creep recovery (Towler et al., 2003). Biofilm total recoil was 0.41 mm (±0.22, $n=15$ from three independent replicates) in aproximately 15 ms.

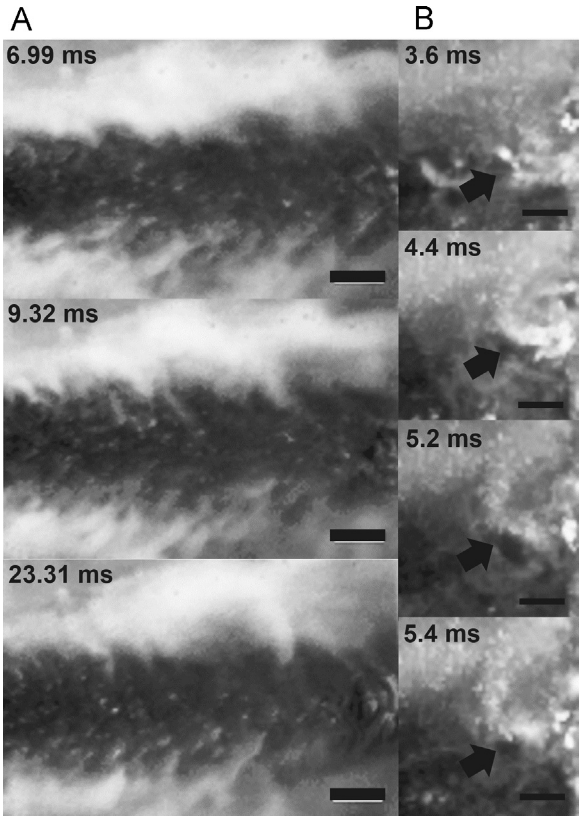

Fig. 5 – Cropped areas from individual frames from two high-speed camera videos showing *S. mutans* biofilm fluid behaviour when exposed to a high-velocity water microspray. The *S. mutans* biofilmappeared whitish grey and the clearance zone was black. The flow was left to right. The microspray caused the transient formation of wave-like patterns (A) or vortices (B) at the biofilm/fluid interface. Scale bars are 1 mm and 0.5 mm for panels A and B respectively.

3.4. *S. mutans biofilm removal*

High-speed camera videos of *S. mutans* biofilms removal from the 1-cm length slides showed a different removal process when exposed to a water microspray or an air-only microburst (Fig. 8A–C and **Supplemental** Movie 6 and Movie 7). Biofilm cleared area caused by the water microspray initial "jet" phase ($\Delta t \sim 10$ ms) created a relatively straight channel through the biofilm clearing an area of 32.6 mm^2 (±6.3 mm^2, $n=3$) at a constant rate of removal. In the second "spray" phase ($\Delta t \sim 45$ ms) the zone of clearance flared out thus that a further area of 8.2 mm^2 (±2.1 mm^2, $n=3$) was removed over an additional 20 ms. There was little further clearance over the remaining 25 ms of the burst. A total area of 40.8 mm^2 (±0.9 mm^2, $n=3$) was cleared of biofilm at the end of the water microspray ($\Delta t \sim 55$ ms). In contrast, the air-only

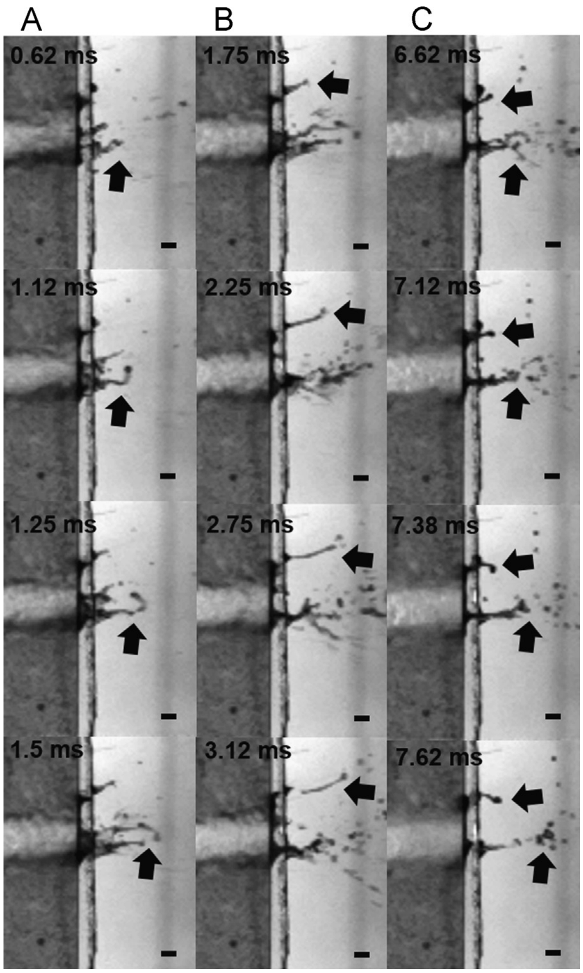

Fig. 6 – Cropped area from individual frames from a high-speed camera video showing three different sequences (A, B and C) of *S. mutans* biofilm fluid behaviour during the exposure to an air-only microburst. The flow was left to right. As the biofilm was pushed out of the IP space, it formed droplets which first elongated and then broke off (white arrows). Scale bar is 1 mm.

microburst only generated a straight channel through the biofilm, with less biofilm being “forced” off the edge of the slide, resulting in a cleared area of 11.7±0.9 mm^2 after approximately 30 ms (Fig. 8D). The final biofilm clearance zone generated by the water microspray was approximately 20 times greater than the one created by the air-only microburst ($p<0.05$, $n=3$).

3.5. *Microscopic evaluation of biofilm removal*

SEM micrographs of biofilms grown on a 1-cm length slide and exposed to a single microburst revealed a clearance zone with well-defined edges (Fig. 9A). Higher magnification revealed that there were some small clusters and single bacterial cells remaining on the surface in the centre of the cleared area. Confocal micrographs were in agreement with SEM images and allowed the remaining biofilm to be quantified from the 3D stack (Fig. 9B).

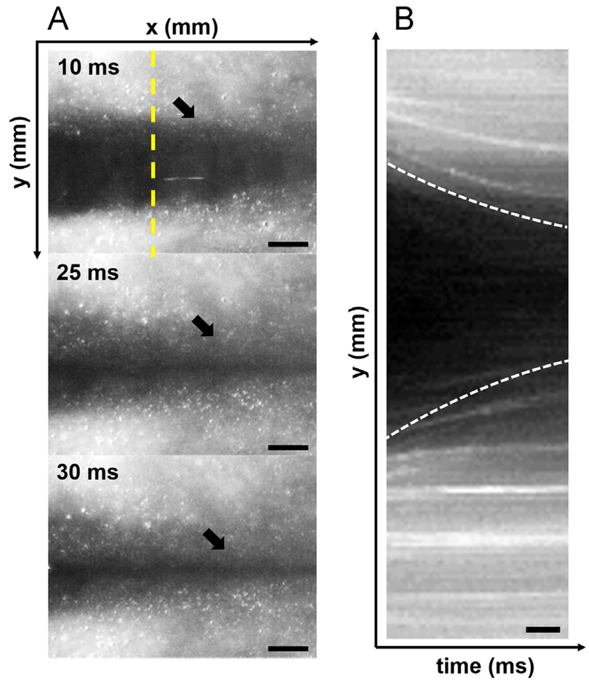

Fig. 7 – Images from a high-speed camera video showing biofilm viscoelastic recoil after a the air-only microburst spray. (A) Subsequent frames show the biofilm move back into back into the previously cleared channel. Scale bar=1 mm. (B) Time trace using the FIJI “reslice function” taken perpendicularly across the cleared channel (indicated by the yellow dashed line in panel (A) showing the time-dependant biofilm recoil. Scale bar=10 mm. The recovery of back into the cleared channel from both sides of the channel is indicated by the white-dashed lines and appears similar to that of an exponential decay function characteristic of viscoelastic creep recovery. (For interpretation of the references to color in this figure legend, the reader is referred to the web version of this article.)

Quantification of *S. mutans* biofilms removal in the exposed area caused by the high-speed water microspray showed a significant reduction in terms of thickness, biomass and surface area compared to the unshot sample (Table 1). No statistical difference was observed between the 1 mm, 5 mm and 8 mm positions in terms of biofilm thickness, biomass and area coverage ($p<0.05$, $n=3$). Therefore we measured thickness, biomass and surface area in the exposed zone by grouping together the data from the different positions ($n=9$ from three independent replicates).

4. Discussion

The in vitro IP model successfully simulated a simplified geometry of an interproximal biofilm and allowed high-speed imaging of the biofilm on the surface during the shooting. We are aware that this model represents a departure from a dental clinical relevant model; however, it allowed us to add a direct real-time biofilm imaging at the surface to the previous tests on typodonts (Rmaile et al., 2015', 2014). In particular, here we show that high-speed microsprays caused biofilm

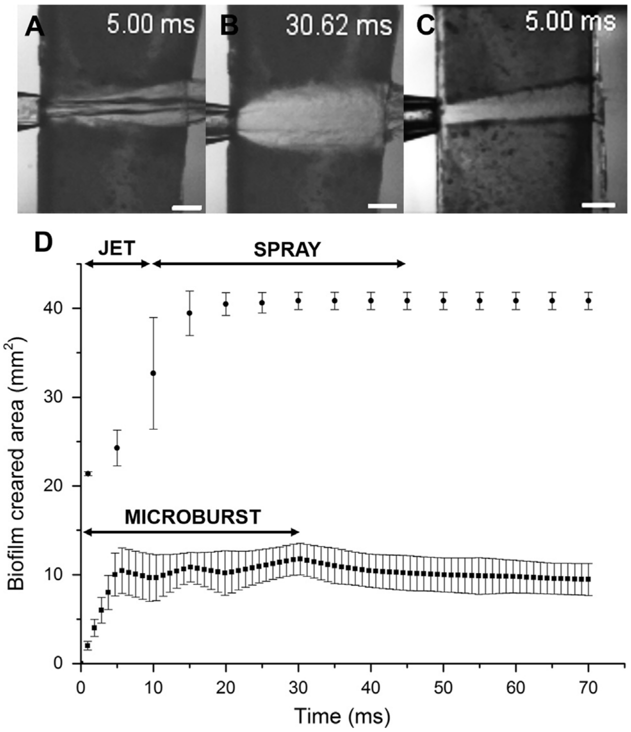

Fig. 8 – Individual frames showing *S. mutans* biofilm exposure to a high-speed water microspray (A and B) or air-only microburst (C) into the IP model space. Frames show *S. mutans* biofilm-colonized slide proximal to the camera (biofilm depicted as dark grey and biofilm clearance zone depicted as white). The AirFloss nozzle tip was located at the left edge of the slide. (A) Jet phase creating a straight clearance zone. (B) Spray phase generating a conical clearance zone. (C) Air-only microburst generating a straight clearance zone. Scale bar = 2 mm. (D) Mean biofilm cleared area as a function of the time during the water microspray (dots) and the air-only microburst (squares). Data points represent the mean of triplicate experimental repeats with standard error bars. Data were statistically different in each time point ($p < 0.05$, $n = 3$).

fluidisation on the surface in a highly transient manner (Figs. 5 and 6). This phenomenon was extremely quick (<60 ms) and cannot be seen with regular videography or microscopic imaging techniques. Biofilm fluidification can be the result of mixing processes occurring between the water and the biofilm structure. Since high Re numbers measured for the water-jet phase suggested turbulent behaviour, it might be possible that the vortices observed at the edges of the remaining biofilm can be turbulent eddies. Turbulent mixing together with biofilm fluid behaviour could possibly enhance the mass transfer inside the unremoved biofilm. This phenomenon could, in future, help antimicrobial delivery inside dental biofilms for a better therapeutical effect. In the oral cavity, dental biofilm removal under non-contact brushing is subjected to different shear forces which can cause an expansion in the structure of unremoved biofilms due to its viscoelastic nature (Busscher et al., 2010a; Peterson et al., 2015). Investigators demonstrated that fluid-dynamic activity generated by power toothbrushes can change biofilm viscoelastic properties which in turn enhance antimicrobials penetration inside the remaining biofilm (He et al., 2014; Sjogren et al., 2004; Stoodley et al., 2007).

In addition to fluid behaviour we also demonstrated biofilm viscoelastic behaviour showing biofilm time-dependent recoil and residual strain when the shear-stress caused by the microsprays was removed (Fig. 7). Other studies have reported that biofilms exhibit both elastic recoil and residual strain caused by viscous flow (Klapper et al., 2002; Rupp et al., 2005; Shaw et al., 2004; Towler et al., 2003). Conventional "before" and "after" imaging would not have revealed this behaviour and the drawn conclusion would be that a device had failed to remove biofilm from the surface in the first place. Thus, when dealing with dental biofilm removal, the shear forces should be high enough and sustained for a sufficient time to overcome the recoil effect and be able to detach the biofilm completely off the surface.

It is known from the literature that *S. mutans* specifically bind salivary mucins present in the dental pellicle which cover the tooth surface (Gibbons and Hay, 1989). Therefore, we added type II porcine gastric mucin to the biofilm growth medium as a substitute for salivary mucin (Kolenbrander, 2011). The we conditioned microscope slides with the mucin medium prior the inoculation in order to simulate *S. mutans*/mucin interactions. We then performed uniaxial compression test to assess how mucin in the medium might influence biofilm mechanical properties and thus biofilm behaviour. Although mucins have been shown to be important in the adhesion of *S. mutans*, in both promoting attachment (Kishimoto et al., 1989) or inhibiting attachment and biofilm formation (Frenkel and Ribbeck, 2015; Marsh et al., 2009) we found the presence of mucin as a slide preconditioned pellicle or in the growth medium had no significant effect on rigidity ($p > 0.05$), suggesting that it did not influence matrix production, or was not incorporated at all into the matrix. It is important to mention that mucin in the growth medium was a simplified model of the dental pellicle. Human saliva contains not only mucins but a complex mixture of proteins, electrolytes and antibacterial compounds. For our work we used commercially available mucin since it is more consistent and easier to work with than high viscosity human saliva, but in order to have a more complete picture, mechanical experiments should be performed with human saliva as the growth medium. However, we also discovered that increasing the growth period from 2 days in previous studies (Rmaile et al., 2012) to 3 days significantly increased the rigidity of the biofilm from 0.280 kPa to 760 kPa, a factor of $\sim 10^3$. This is consistent with findings showing that the elastic modulus of dental biofilms is positively correlated with the amount (and density) of matrix components (Hwang et al., 2014; Klein et al., 2015; Waters et al., 2013), and stresses the importance of frequent and consistent oral hygiene to continually remove and disrupt plaque biofilm before it gets stiffer.

The initial jet phase blasted a channel through the biofilm and the second spray phase extended the zone of clearance, thus the combination of these two phases appear complimentary. The water microspray cleared proximally four times of the area of biofilm than the air-only microburst ($p < 0.05$) (Fig. 8B). Although interestingly the force of the air alone was strong enough to remove some biofilm. This suggests that

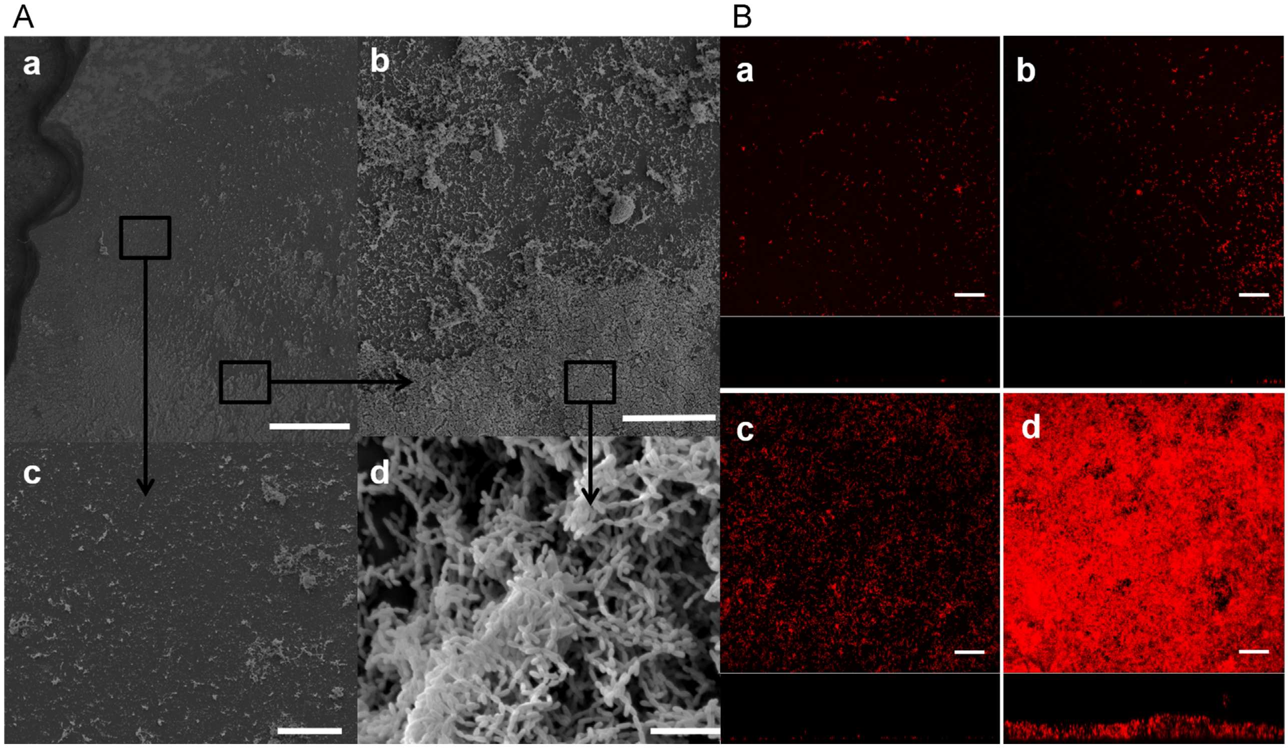

Fig. 9 – (A) Scanning electron microscopy images of a representative slide exposed to a single water microspray burst. (a) Lower magnification of the clearance zone. The leading edge of the slide was located at the left as presented in Fig. 2. Scale bar=500 μm. (b) Higher magnification SEM of the edge delimiting the clearance zone showing a reduction of biofilm but with remaining clusters and single cells. Scale bar=100 μm. (c) Inside the clearance zone only small clusters and single cells remained. Scale bar=100 μm. (d) Biofilm composed of dense clusters and chains of cocci in the unexposed area away from the microburst. Scale bar=50 μm. (B) Confocal images in *x*–*y* plan view with *x*–*z* cross section below at distances of (a) 1 mm, (b) 5 mm and (c) 8 mm from the microspray inlet (see Fig. 2). (d) An image of the biofilm in an unexposed area. Scale bar=100 μm.

Table 1 – Thickness, biomass, surface area and relative percent reductions of *S. mutans* biofilms prior and after the high-speed microspray exposure. Experimental data reported as mean and 1 standard deviation. Values marked in bold were statistically different from the unexposed controls ($p<0.05$).

Sample	Location	Thickness (μm)	Biomass ($\mu m^3/\mu m^2$)	Area ($10^5 \times \mu m^2$)	RT (%)	RB (%)	RA (%)
Unexposed control	Random (*n*=9)	51.79±9.01	28.53±5.86	0.41±0.14	–	–	–
Exposed	1 mm from nozzle (*n*=3)	0.38±0.49	0.25±0.29	0.11±0.10	99.2±0.9	99.1±1.0	99.4±0.4
	5 mm from nozzle (*n*=3)	0.03±0.03	0.03±0.02	0.25±0.21	99.9±0.1	99.9±0.1	99.7±0.2
	8 mm from nozzle (*n*=3)	0.13±0.14	0.07±0.06	41.05±13.22	99.7±0.26	99.7±0.2	99.3±0.5
	Combined (*n*=9)	0.16±0.24	0.10±0.15	0.20±0.15	99.7±0.5	99.6±0.5	99.5±0.4

water inside the microspray plays a crucial role in the detachment mechanisms possibly because of the higher shear stresses caused by the more viscous water drops as well as the surface tension effect of the moving air–water interface of the drop over the biofilm-colonized surface (Sharma et al., 2005a). Previous studies demonstrated that, when water shear stresses inside flow cells reached a critical value between 5 and 12 Pa, biofilm macroscopic clusters detached from the surface (Ohashi and Harada, 1994; Stoodley et al., 2002). Although high-speed camera videos of the water microspray developing inside the IP space model demonstrated the complexity and the turbulence of the flow (**Supplementary** Movie 1), we made a rough estimate of the magnitude of the shear stresses (τ_w) acting over the surface of the biofilm for the water microspray first phase (i.e. water jet) and the air-only microburst, making two simplifying assumptions: a) when bursts developed inside the channel formed by the two *S. mutans* biofilm slides, the biofilm exposed area can be approximated to a square channel having a depth and a width of 1 mm; b) the air-only microburst had the same maximum velocity as the water jet (51.1 m/s). The corresponding wall shear stresses values were 7.4 kPa and 0.016 kPa for the water microspray and air-only microburst, respectively. These results were consistent with the values found by Rmaile et al. (2014) where a computed $\tau_w = 3$ kPa was required to remove 95% of the biofilm by shooting water micro-drops from a prototype AirFloss at a velocity of 60 m/s. Quantification of *S. mutans* biofilm removal in different positions along the 10-mm slide showed a reduction in biofilm thickness, biomass and area covelage up to 99.9% (Table 1), similar to our previous studies (Rmaile, 2015, 2014, 2012). We are aware that one of the limitations of confocal analyisis is that it is limited in being able to map in high resolution over larger areas. In this case the relevant areawould be that of the tooth surface in the IP space which will be on the order of 0.5–1 cm^2. Future work will considere Optical Coherence Tomography would as a complimentary technology to achieve both high resolution and a more complete mapping of the zone of clearance.

SEM images indicated that there was still some biofilm remaining in the clearance zone (Fig. 9A), underlining the importance of the adhesive viscoelastic forces which develop between the biofilm and the surface. Similar findings were obtained in a recent study on shear-induced detachment of 64 h *S. mutans* biofilms which showed a decrease in the biomass removal rate close to the surface because of the presence of a dense layer of EPS (Hwang et al., 2014). In addition, the authors also demonstrated that biofilm treated with EPS-digesting dextranase were easier to detach. Therefore, a possible new therapeutical approach can be the combination of high-speed fluid forces with specific matrix-digesting agents that facilitate the mechanical cleaning of dental biofilms.

5. Conclusions

High-speed videography revealed that high-velocity fluid-biofilm interactions can cause the biofilm to behave like a viscoelastic fluid over very short times-scales (ms). The ability of the biofilm to liquefy and flow over surfaces when exposed to mechanical forces is an important consideration in the future designs of oral hygiene devices. It also opens new opportunities to exploit this phenomenon with the aim of enhancing transport of dentifrices inside dental biofilms for increasing antimicrobials or anticaries therapeutical effects.

Acknowledgements

This work was financially funded in part by EPSRC DTP EP/K503130/1 award and in part by Philips Oral Helathcare, Bothell, WA, USA. M. Starke and M. Ward are employed by Philips Oral Healthcare, Bothell, WA, USA. The other authors declare no potential conflicts of interest with respect to the authorship and/or publication of this article. We also thank Dr. Janice M. Barton and Dr. Marco Longana from the Testing and Structures Research Laboratory (TSRL, University of Southampton) for providing the high-speed camera set up. All data supporting this study are openly available from the University of Southampton repository at http://dx.doi.org/10.5258/SOTON/384985.

REFERENCES

Barnes, C.M., Russell, C.M., Reinhardt, R.A., Payne, J.B., Lyle, D.M., 2005. Comparison of irrigation to floss as an adjunct to tooth brushing: effect on bleeding, gingivitis, and supragingival plaque. J. Clin. Dent. 16, 71.

Busscher, H., Jager, D., Finger, G., Schaefer, N., Van der Mei, H., 2010a. Energy transfer, volumetric expansion, and removal of oral biofilms by non-contact brushing. Eur. J. Oral Sci. 118, 177–182.

Busscher, H.J., Jager, D., Finger, G., Schaefer, N., Van der Mei, H.C., 2010b. Energy transfer, volumetric expansion, and removal of oral biofilms by non-contact brushing. Eur. J. Oral Sci. 118, 177–182.

Cense, A.W., Van Dongen, M.E.H., Gottenbos, B., Nuijs, A.M., Shulepov, S.Y., 2006. Removal of biofilms by impinging water droplets. J. Appl. Phys. 100 124701-124701-124708.

Costerton, J.W., Lewandowski, Z., Caldwell, D.E., Korber, D.R., Lappin-Scott, H.M., 1995. Microbial biofilms. Annu. Rev. Microbiol. 49, 711–745.

Donlan, R.M., Costerton, J.W., 2002. Biofilms: survival mechanisms of clinically relevant microorganisms. Clin. Microbiol. Rev. 15, 167–193.

Featherstone, J.D.B., 1999. Prevention and reversal of dental caries: role of low level fluoride. Community Dent. Oral Epidemiol. 27, 31–40.

Frenkel, E.S., Ribbeck, K., 2015. Salivary mucins protect surfaces from colonization by cariogenic bacteria. Appl. Environ. Microbiol. 81, 332–338.

Fried, J.L., 2012. Interdental cleansing. Access 2, 22–25.

Gibbons, R., Hay, D., 1989. Adsorbed salivary acidic proline-rich proteins contribute to the adhesion of *Streptococcus mutans* JBP to apatitic surfaces. J. Dent. Res. 68, 1303–1307.

He, Y., Peterson, B.W., Ren, Y., van der Mei, H.C., Busscher, H.J., 2014. Antimicrobial penetration in a dual-species oral biofilm after noncontact brushing: an in vitro study. Clin. Oral Investig. 18, 1103–1109.

Heydorn, A., Nielsen, A.T., Hentzer, M., Sternberg, C., Givskov, M., Ersbøll, B.K., Molin, S., 2000. Quantification of biofilm structures by the novel computer program COMSTAT. Microbiology 146, 2395–2407.

Hope, C.K., Wilson, M., 2003. Effects of dynamic fluid activity from an electric toothbrush on in vitro oral biofilms. J. Clin. Periodontol. 30, 624–629.

Hope, C.K., Petrie, A., Wilson, M., 2003. In vitro assessment of the plaque-removing ability of hydrodynamic shear forces produced beyond the bristles by 2 electric toothbrushes. J. Periodontol. 74, 1017–1022.

Hwang, G., Klein, M.I., Koo, H., 2014. Analysis of the mechanical stability and surface detachment of mature *Streptococcus mutans* biofilms by applying a range of external shear forces. Biofouling 30, 1079–1091.

Jahn, C.A., 2010. The dental water jet: a historical review of the literature. Am. Dent. Hyg. Assoc. 84, 114–120.

Kishimoto, E., Hay, D.I., Gibbons, R.J., 1989. A human salivary protein which promotes adhesion of *Streptococcus mutans* serotype c strains to hydroxyapatite. Infect. Immun. 57, 3702–3707.

Klapper, I., Rupp, C.J., Cargo, R., Purvedorj, B., Stoodley, P., 2002. Viscoelastic fluid description of bacterial biofilm material properties. Biotechnol. Bioeng. 80, 289–296.

Klein, M., Hwang, G., Santos, P., Campanella, O., Koo, H., 2015. *Streptococcus mutans*-derived extracellular matrix in cariogenic oral biofilms. Front. Cell. Infect. Microbiol. 5, 5.

Kolenbrander, Paul, E., 2011. Multispecies communities: interspecies interactions influence growth on saliva as sole nutritional source. Int. J. Oral Sci. 3.2, 49–54.

Marsh, P.D., Bradshaw, D.J., 1995. Dental plaque as a biofilm. J. Ind. Microbiol. 15, 169–175.

Marsh, P.D., Martin, M.V., Lewis, M.A., Williams, D., 2009. Oral Microbiology. Elsevier Health Sciences.

Ohashi, A., Harada, H., 1994. Adhesion strength of biofilm developed in an attached-growth reactor. Water Sci. Technol. 29, 281–288.

Paramonova, E., Kalmykowa, O.J., van der Mei, H.C., Busscher, H.J., Sharma, P.K., 2009. Impact of hydrodynamics on oral biofilm strength. J. Dent. Res. 88, 922–926.

Parini, M.R., Pitt, W.G., 2006. Dynamic removal of oral biofilms by bubbles. Colloids Surf. B: Biointerfaces 52, 39–46.

Peterson, B.W., He, Y., Ren, Y., Zerdoum, A., Libera, M.R., Sharma, P.K., van Winkelhoff, A.-J., Neut, D., Stoodley, P., van der Mei, H.C., 2015. Viscoelasticity of biofilms and their recalcitrance to mechanical and chemical challenges. FEMS Microbiol. Rev. 39, 234–245.

Rmaile, A., Carugo, D., Capretto, L., Aspiras, M., De Jager, M., Ward, M., Stoodley, P., 2014. Removal of Interproximal dental biofilms by high-velocity water microdrops. J. Dent. Res. 93, 68–73.

Rmaile, A., Carugo, D., Capretto, L., Zhang, X., Wharton, J.A., Thurner, P.J., Aspiras, M., Ward, M., Stoodley, P., 2012. Microbial tribology and disruption of dental plaque bacterial biofilms. Wear 306, 276–284.

Rmaile, A., Carugo, D., Capretto, L., Wharton, J.A., Thurner, P.J., Aspiras, M., Ward, M., De Jager, M., Stoodley, 2015. An experimental and computational study of the hydrodynamics of high-velocity water microdrops for interproximal tooth cleaning. J. Mech. Behav. Biomed. Mater. 46, 148–157.

Rupp, C.J., Fux, C.A., Stoodley, P., 2005. Viscoelasticity of *Staphylococcus aureus* biofilms in response to fluid shear allows resistance to detachment and facilitates rolling migration. Appl. Environ. Microbiol. 71, 2175–2178.

Schindelin, J., Arganda-Carreras, I., Frise, E., Kaynig, V., Longair, M., Pietzsch, T., Preibisch, S., Rueden, C., Saalfeld, S., Schmid, B., Tinevez, J.Y., White, D.J., Hartenstein, V., Eliceiri, K., Tomancak, P., Cardona, A., 2012. Fiji: an open-source platform for biological-image analysis. Nat. Methods 9, 676–682.

Selwitz, R.H., Ismail, A.I., Pitts, N.B., 2007. Dental caries. The Lancet 369, 51–59.

Sharma, P.K., Gibcus, M.J., van der Mei, H.C., Busscher, H.J., 2005a. Influence of fluid shear and microbubbles on bacterial detachment from a surface. Appl. Environ. Microbiol. 71, 3668–3673.

Sharma, P.K., Gibcus, M.J., Van Der Mei, H.C., Busscher, H.J., 2005b. Microbubble-induced detachment of coadhering oral bacteria from salivary pellicles. Eur. J. Oral Sci. 113, 326–332.

Shaw, T., Winston, M., Rupp, C.J., Klapper, I., Stoodley, P., 2004. Commonality of elastic relaxation times in biofilms. Phys. Rev. Lett. 93, 098102.

Sjogren, K., Lundberg, A.B., Birkhed, D., Dudgeon, D.J., Johnson, M.R., 2004. Interproximal plaque mass and fluoride retention after brushing and flossing – a comparative study of powered toothbrushing, manual toothbrushing and flossing. Oral Health Prev. Dent. 2, 119–124.

Stoodley, P., Cargo, R., Rupp, C.J., Wilson, S., Klapper, I., 2002. Biofilm material properties as related to shear-induced deformation and detachment phenomena. J. Ind. Microbiol. Biotechnol. 29, 361–367.

Stoodley, P., Nguyen, D., Longwell, M., Nistico, L., von Ohle, C., Milanovich, N., de Jager, M., 2007. Effect of the sonicare flexcare power toothbrush on fluoride delivery through *Streptococcus mutans* biofilms. Compend. Contin. Educ. Dent. 28, 15–22.

Towler, B.W., Rupp, C.J., Cunningham, A.B., Stoodley, P., 2003. Viscoelastic properties of a mixed culture biofilm from rheometer creep analysis. Biofouling 19, 279–285.

Waters, M.S., Kundu, S., Lin, N.J., Lin-Gibson, S., 2013. Microstructure and mechanical properties of in situ *Streptococcus mutans* biofilms. ACS Appl. Mater. Interfaces 6 (1), 327–332.

Wilking, J.N., Angelini, T.E., Seminara, A., Brenner, M.P., Weitz, D.A., 2011. Biofilms as complex fluids. MRS Bull. 36, 385–391.